Tumor necrosis factor-α receptor 1 mediates BoDV1-driven changes in mitochondrial and peroxisomal dynamics in neurons

Inaugural dissertation

submitted to the

Faculty of Veterinary Medicine

in partial fulfillment of the requirements

for the **PhD (Doctor of Philosophy) degree**

of the Faculties of Veterinary Medicine and Medicine

of the Justus Liebig University Giessen, Germany

By:

Dominic Osei (DVM**)**

Kumasi, Ghana.

Gießen, 2024

From the: (i) Institute of Veterinary Pathology

Faculty of Veterinary Medicine

Justus Liebig University Giessen, Germany

(ii) Institute for Anatomy and Cell Biology,

Faculty of Medicine

Justus Liebig University Giessen, Germany

First Reviewer and Supervisor:

Prof. Dr. habil. Christiane Herden

Second Reviewer:

Prof. Dr. Georg Lüers

Vice Chair/Co-supervisor:

PD Dr. Barbara Ahlemeyer

Chairperson of the Examination Committee:

Prof. Dr. Klaus-Dieter Schlüter

Date of Doctoral Defense:

4th November 2024

Declaration

I declare that I have completed this dissertation single-handedly without the unauthorized help of a second party and only with the assistance acknowledged therein. I have appropriately acknowledged and referenced all text passages that are derived literally from or based on the content of published or unpublished work of others, and all information that relates to verbal communications. I have abided by the principles of good scientific conduct laid down in the charter of the Justus Liebig University Giessen in carrying out the investigations described in the dissertation.

Dominic Osei

Parts of the present work are related to the following contributions:

Publication:

Osei, D., Baumgart-Vogt, E., Ahlemeyer, B. & Herden, C. (2024). Tumor necrosis factor-α receptor 1 mediates BoDV1-driven changes in mitochondrial and peroxisomal dynamics in neurons. *Int. J. Mol. Sci.*, *25*(3), 1849. https://doi.org/10.3390/ijms25031849

Conference abstracts:

Osei, D., Baumgart-Vogt, E., Ahlemeyer, B. & Herden, C. (2023). Tumor necrosis factor-α receptor 1 mediates changes in mitochondrial and peroxisomal dynamics in neurons – a mechanism contributing to Borna disease virus 1 persistence in the brain. *Center for mind, brain, and behavior (CMBB) Day 2023*; A138 (Poster presentation).

Osei, D., Baumgart-Vogt, E., Ahlemeyer, B. & Herden, C. (2024). Tumor necrosis factor-α receptor 1 mediates changes in mitochondrial and peroxisomal dynamics in neurons – a mechanism contributing to Borna disease virus 1 persistence in the brain. *DVG-Fachgruppe Pathologie 2024, Fulda (67. Jahrestagung und 29. Schnittseminar)*; P58 (Poster presentation).

This study was supported financially by the German Academic Exchange Service (DAAD).

To my parents, siblings, beloved wife,

and three adorable daughters

"I can do all things through Christ who strengthens me."

(**Philippians 4:13** NKV)

Table of Contents

Table of Contents

Table of Contents

Table of Contents

List of figures

List of figures

List of figures

List of figures

List of figures

List of figures

List of tables

Abbreviations

ABCD	adenosine triphosphate-binding cassette transporter type D
AP-1	activator protein 1
ATP	adenosine triphosphate
ATP5B	adenosine triphosphate synthase F1 subunit beta
BD	borna disease
BoDV1	borna disease virus 1
BSA	bovine serum albumin
CA	cornu ammonis
Cb	cerebellar cortex
cIAP	cellular inhibitor of apoptosis protein
CNS	central nervous system
CoA	coenzyme A
Cx	cerebral cortex
DAPI	4′,6-diamidino-2-phenylindole
DG	dentate gyrus
DNA	deoxyribonucleic acid
DNM1L	dynamin 1-like protein
FFPE	formalin-fixed, paraffin-embedded
GDAP1	ganglioside-inducing differentiation-associated protein 1
gRNA	genomic ribonucleic acid
GTPase	guanidine triphosphatase
H_2O_2	hydrogen peroxide
HIV	human immuno-deficiency virus
IF	indirect immunofluorescence
IFN	interferon
IL	interleukin
IRD	infantile Refsum disease
IRF	interferon regulatory factor
MAPK	mitogen-activated protein kinase
MAVS	mitochondrial antiviral signaling protein
MDA5	melanoma differentiation-associated protein 5
MFF	mitochondrial fission factor
mRNA	messenger ribonucleic acid
mtDNA	mitochondrial deoxyribonucleic acid

Abbreviations

NAD^+	oxidized nicotinamide dehydrogenase
NADH	reduced nicotinamide dehydrogenase
NALD	neonatal adrenoleukodystrophy
NF-κB	nuclear factor-kappa B
NM	nutrient medium
NMDA	n-methyl-D-aspartate
NRF	nuclear respiratory factor
$O_2^{\cdot -}$	superoxide
OXPHOS	oxidative phosphorylation
PBD	peroxisomal biogenesis disorder
PBS	phosphate-buffered saline
PEX	peroxin
PGC-1α	peroxisome proliferator-activated receptor gamma coactivator 1 alpha
p.i.	post infection
PMP	peroxisomal membrane protein
PPAR	peroxisome proliferator-activated receptor
PRR	pattern recognition receptor
PTS	peroxisomal targeting signal
RIG-I	retinoic acid inducible gene I
RLR	retinoic acid inducible gene I-like receptors
RNA	ribonucleic acid
ROS	reactive oxygen species
RT	room temperature
SCM	slice culture medium
SOD	superoxide dismutase
SPED	specific peroxisomal enzyme deficiency
sTNF-α	soluble TNF-alpha
TCA	tricarboxylic acid
TLR	toll-like receptor
mTNF-α	transmembrane tumor necrosis factor-alpha
TNFR	tumor necrosis factor-alpha receptor
TNFR1ko	tumor necrosis factor-alpha receptor 1 knockout
TNFR2ko	tumor necrosis factor-alpha receptor 2 knockout
TNFTg	tumor necrosis factor-alpha transgenic

Abbreviations

TNF-α	tumor necrosis factor-alpha
TRAF	tumor necrosis factor receptor-associated factor
VLCFA	very long chain fatty acid
Wt	wild-type
X-ALD	X-linked adrenoleukodystrophy
ZS	Zellweger sydrome
ZSS	Zellweger syndrome spectrum

Introduction

1. Introduction

Borna disease virus 1 (BoDV1) causes a persistent, non-cytolytic infection in the central nervous system (CNS), resulting in the release of pro-inflammatory cytokines like tumor necrosis factor-alpha (TNF-α), interleukin (IL)-1 and IL-2 (Stitz et al., 2002; Kramer et al., 2012; Herden et al., 2013). BoDV1 infects a wide range of warm-blooded animals including humans, and causes Borna disease (BD) – a severe disease that occurs mainly in sheep and horses with about 90% fatality rate in horses, characterized by a T cell-mediated meningo-encephalitis (Richt et al., 2000; Stitz et al, 2002; Kramer et al., 2012; Herden et al., 2013; Lipkin et al., 2023). BoDV1 can infect humans leading to fatal encephalitis; so far, more than 45 human cases have been diagnosed in Germany alone (Schlottau et al., 2018; Korn et al., 2018; Tappe et al., 2019; Liesche et al., 2019; Nobach et al., 2020; Niller et al., 2020; Tappe et al., 2021).

BoDV1 infection of laboratory animals offers important opportunities for the extensive study of virus-induced, immune-mediated neuropathologic diseases (Richt et al., 2000; Stitz et al., 2002; Kramer et al., 2012; Herden et al., 2013; Nobach et al., 2020; Lipkin et al., 2023). Experimental BoDV1 infection of susceptible neonatal mouse strains causes neurological signs by 28–42 days post-infection, characterized by weight loss, ataxia, paraparesis, torticollis, nervous ticks, coarse fur and death, associated with a non-purulent meningoencephalitis (Hallensleben et al., 1998; Kramer et al., 2012; Tizard et al., 2016). After experimental exposure of neonatal rats to BoDV1, brain areas – such as the hippocampus, cerebral and cerebellar cortices –, which mature in the postnatal period, are infected; therefore, abnormalities in learning and behavior are observed (Richt et al., 2000; Stitz et al., 2002; Herden et al., 2013). Other rodents and non-human primates also succumb to experimental infection with BoDV1; unlike in mice, experimental exposure of rats to BoDV1 causes BD in adults only (Narayan et al., 1983; Staeheli et al., 2000; Herden et al., 2013). Susceptibility of mouse strains to BoDV1 was in the case of wild-type (Wt) mice highest for Murphy Roth large (MRL) mice, medium for Balb/c mice, and lowest for C57/Bl6 mice, where 83%, 37% and 13% of infected animals developed neurological symptoms, respectively. In the less susceptible C57/Bl6 mice, this percentage increased up to 100% and 30% after changes in the immune system were induced via IL-12 (Hofer et al., 2004) and TNF-α overexpression (Kramer et al., 2012), respectively. In our study, a mouse-adapted virus strain was injected into the brain of C57/Bl6 mice with an altered TNF system, which is reliably able to induce disease in TNF-α transgenic (TNFTg) mice as shown before (Kramer et al., 2012; Hirz, 2017).

Introduction

TNF-α is a pleiotropic pro-inflammatory cytokine of the immune system and belongs to the TNF/TNF-α receptor (TNFR) superfamily; its effects are mediated via 2 main receptors – i.e. TNFR1 and TNFR2 (McCoy & Tansey, 2008; Muhammad, 2020). TNFR1 is primarily stimulated by soluble TNF-α (sTNF-α), leading to pro-inflammatory and apoptotic signaling, whereas TNFR2 is activated by transmembrane TNF-α (mTNF-α), evoking anti-inflammatory and pro-survival effects in eukaryotic cells (Marchetti et al., 2004; McCoy & Tansey, 2008). Both TNFR1 and TNFR2 signaling induce nuclear factor-kappa B (NF-κB) activation – TNFR1-induced NF-κB activation is short-lived whereas that by TNFR2 is delayed but lasts longer (Naudé et al, 2011). In the normal CNS, TNF-α expression is low and localized mainly in microglia, astrocytes and neurons – it is markedly elevated during and after injuries (e.g. ischemia, trauma, and infection) due to secretion by mainly the microglia (Marchetti et al., 2004; Probert et al., 1997). TNF-α is a crucial mediator of virus-induced activation of the immune system, and its prolonged overexpression in the brain pre-sensitizes neurons and glial cells with consequent damage to the CNS (Marchetti et al., 2004; Kramer et al., 2012). An upregulation of this pro-inflammatory cytokine generates reactive oxygen species (ROS) and has been causally linked to several neurodegenerative diseases like multiple sclerosis, Parkinson's disease, dementia and Ahlzeimer's disease (Frankola et al., 2011; Rauf et al., 2022). Nonetheless, previously elevated levels of TNF-α can exert neuroprotection, and was shown to mitigate glutamate-induced excitotoxicity in primary cortical neurons via TNFR2 signaling (Marchetti et al., 2004).

TNFTg and TNF-α receptor knockout (TNFRko) mouse models have been used to elucidate the roles of TNF-α in several tissues and organs, especially the brain (Marchetti et al., 2004; McCoy & Tansey, 2008), and these model systems are well established in our laboratory. In TNFTg mice, TNF-α is moderately overexpressed in the forebrain regions (Probert et al., 1997; Kramer et al., 2012; Hirz, 2017); and, the overexpression of TNF-α transgenes by neurons in the CNS of mice is sufficient to cause epileptic seizures (Kramer et al., 2012), ataxia, seizures and paresis depending on the TNF levels, thereby, mimicking chronic CNS inflammation (Probert et al., 1997). Thus, in this study, we used three different mouse models, including TNFTg, TNFR1ko and TNFR2ko, to investigate the role(s) of TNF-α and its receptors. TNFTg mice were used to investigate the effect of prolonged *in vivo* exposure of several neuronal cell types to moderately overexpressed TNF-α on the peroxisomal and mitochondrial compartments, before and after BoDV1 infection. Furthermore, TNFR1ko and TNFR2ko mouse lines were used to address the same question concerning TNFR1 and TNFR2 signaling.

Introduction

Besides the typical antiviral pathways and molecules of the innate immune system, virus-induced changes in subcellular organelles such as peroxisomes and mitochondria remain largely unexplored. Both subcellular organelles influence intracellular redox homeostasis by generating and detoxifying ROS (Terlecky et al., 2012; Trompier et al., 2014; Wang et al., 2018). Mitochondria produce adenosine triphosphate (ATP) via the tricarboxylic acid (TCA) cycle and oxidative phosphorylation – these processes generate ROS (OXPHOS) (Kalinina et al., 2008). Mitochondria possess superoxide dismutase type-2 (SOD2), located mainly within the mitochondrial matrix, which converts a particular ROS [i.e. superoxide ($O_2^{\cdot -}$)] into oxygen and hydrogen peroxide molecules (Wang et al., 2018). Peroxisomes on the other hand generate the ROS, hydrogen peroxide (H_2O_2), during β-oxidation of very long chain fatty acids (VLCFAs); afterwards, H_2O_2 is detoxified by the peroxisomal matrix enzyme, catalase, and converted into water and oxygen (Terlecky et al., 2012; Trompier et al., 2014; Cipolla & Lodhi, 2017).

Oxidative stress and inflammation are two inseparable processes (Terlecky et al., 2012; Singh & Pujol, 2010). Peroxisomes synthesize pro-inflammatory (prostaglandins, leukotrienes, thromboxanes) and anti-inflammatory lipid derivatives (resolvins, maresins and protectins) (Terlecky et al., 2012). In addition, peroxisomal-derived ROS and other molecules (e.g. free FAs and polyamines) stimulate immune cells; others (oxysterols) suppress inflammation (Terlecky et al., 2012). Recent evidence depict some form of crosstalk between peroxisomes and mitochondria (Fransen et al., 2017; Ferreira et al., 2019). For instance, the activation of mitochondrial antiviral signaling proteins (MAVS) – located on the outer membranes of both organelles – leads to the release of cytokines, which aid in the recruitment of immune cells and the creation of an antiviral state within host cells (Fransen et al., 2017; Jean et al., 2018; Ferreira et al., 2019).

Viral proteins have evolved in their interactions with cellular organelles and components to escape the innate antiviral immune defenses and enhance their replication (Ferreira et al., 2019). Some viruses have developed strategies to target and evade peroxisomal- and mitochondrial-dependent antiviral signaling (Jean et al., 2018; Ferreira et al., 2019; Elesela & Lukacs, 2021). Until now, there are no comprehensive studies analyzing the numerical abundances of both subcellular compartments and their respective main antioxidant enzymes, catalase and SOD2, after BoDV1 infection. Using our mouse models, we analyzed peroxisomal and mitochondrial abundances and their main antioxidant enzymes (i.e. catalase and SOD2) in the hippocampus, cerebral, and cerebellar cortices of non-infected and BoDV1-infected mice of four different

mouse lines [i.e. Wt, TNFTg, TNFR1ko and TNFR2ko mice]. Our study aimed to understand the effects of BoDV1 infection on the abundances of both subcellular compartments as well as their respective main antioxidant enzymes, whilst observing the role(s) of the TNF system in BoDV1 infection events of the brain. This study provides more insight into the interactions between BoDV1 and distinct neuronal cell types under different TNF-α/TNFR-signaling conditions with special emphasis on the peroxisomal and mitochondrial reaction patterns.

2. Literature review

2.1 TNF, TNF-α receptors (TNFRs) and TNFR signaling in the brain

The tumor necrosis factor family, including TNF-α and TNF-β (lymphotoxin-β), is one of the 19 members of the TNF superfamily of type II transmembrane proteins, and is a key player in the immune regulatory functions of the CNS, in both health and disease (McCoy & Tansey, 2008; Muhammad, 2020). Under physiological conditions, TNF-α is mainly synthesized and released by microglia, astrocytes, and some population of neurons, but during/after neuronal injury this potent cytokine can be released also by macrophages, monocytes, T and B cells, and natural killer cells (Figiel, 2008; McCoy & Tansey, 2008; Dong, et al, 2015; Muhammad, 2020). TNF-α is crucial for the maintenance of synaptic transmission at excitatory synapses, and decreases the transmission strength at inhibitory synapses by enhancing the endocytosis of gamma (γ)-amino butyric acid (Beattie et al., 2010). The enhanced secretion of TNF-α by glial cells and infiltrating immune cells is a hallmark of pathological conditions such as cerebral ischemia, infections, convulsion/epilepsy, as well as numerous neurodegenerative conditions including Ahlzeimer's disease, ischemic stroke, Parkinson's disease, multiple sclerosis, and amyotrophic lateral sclerosis (McCoy & Tansey, 2008; Frankola et al., 2011; Rauf et al., 2022).

TNF-α is a 26 kDa precursor polypeptide, bound to the cytoplasmic membrane (Figiel, 2008; Dong, et al, 2015). Upon proteomic cleavage by TNF-α converting enzyme (TACE/ADAM17), a 17 kDa monomeric soluble protein (sTNF-α) is released, leaving behind a membrane-bound form of TNF-α (i.e. mTNF-α) (Figiel, 2008; Dong, et al, 2015). TNF-α produces its biological effects via two main distinct cell surface receptors: the 55 kDa TNFR1 and the 75 kDa TNFR2 (Pegoretti et al., 2018). Generally, TNFR1 is ubiquitously expressed in all cell types and tissues, whereas TNFR2 is expressed mainly by immune cells, endothelial cells, microglia, oligodendrocytes, astrocytes, specific neuronal subtypes, thymocytes, and cardiomyocytes (Naudé et al., 2011; Cabal-Hierro & Lazo, 2012). The two forms of TNF-α (sTNF-α and mTNF-α) demonstrate different binding affinities for the two TNFR types. TNFR1 can be activated by both forms of TNF-α, however, with higher affinity for sTNF-α. TNFR2, on the other hand, is primarily activated by mTNF-α. sTNF-α, after being released, forms a bioactive homotrimer which produces its effects in an autocrine and/or paracrine fashion (Figiel, 2008; Pegoretti et al, 2018).

Due to TNFR1/R2 knockout mouse models and agonistic antibody therapies specifically targeted at either one of both receptors, the biological effects of TNFR stimulation are now well

understood (Naudé et al., 2011). TNFR1 is the major mediator of TNF-α-induced signaling. TNFR1 signaling leads to pro-apoptotic, pro-convulsive and inflammatory outcomes (Figiel, 2008; Naudé et al., 2011; Dong et al., 2015; **Figure 1**), whereas that of TNFR2 promotes cellular proliferation and survival (anti-apoptotic), has anti-convulsive effect, and inhibits inflammation (Figiel, 2008; Okamoto et al., 2009; Van Herreweghe et al., 2010; Naudé et al., 2011; Dong et al., 2015; **Figure 2**). TNFR1 and TNFR2 have an extracellular conserved domain of N-terminal repeating cysteine-rich motifs relevant for interaction with TNF-related ligands; nonetheless, the intracellular domain of TNFR1 and TNFR2 lack homologous sequences, which accounts for the differences in their respective downstream signaling pathways (Figiel, 2008; Naudé et al., 2011; Dong et al., 2015; Pegoretti et al, 2018).

Figure 1: Schematic illustration of TNFR1 signaling

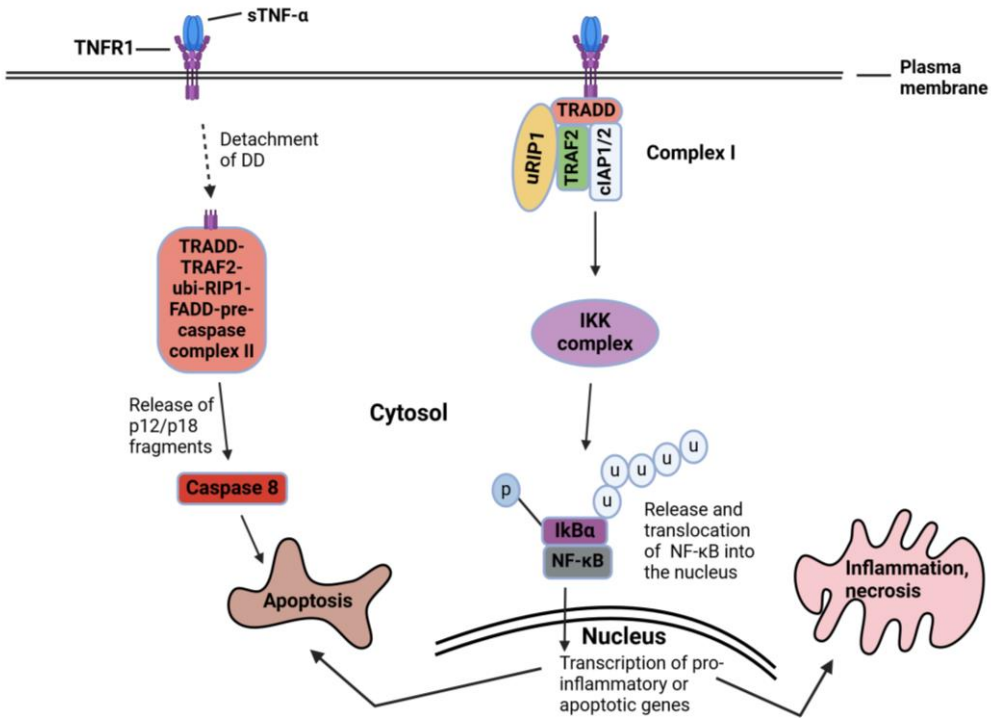

Multiple downstream signaling pathways associated with TNFR1 stimulation by soluble and transmembrane TNF-α, resulting in pro-apoptotic or pro-necrotic outcomes. Receptor interacting protein 1 is modified by the attachment of non-degradative poly-ubiquitin chains (uRIP1) after recruitment by tumor necrosis factor receptor associated death domain (TRADD). Activated IKK complex, which consists of an IKKα subunit and an IKKβ subunit, functions as an essential regulatory subunit of the IKK complex (IKKγ/NEMO), which then phosphorylates the inhibitor of the IκB complex. Via the ubiquitin-proteasome, the IκB complex is then degraded to release NF-κB. If complex I signaling is insufficient to activate NF-κB, the activated TNFR1 can initiate the caspase 8-dependent complex II apoptotic pathway. With this pathway, the death domain (DD) of the activated TNFR1 dissociates and recruits TRADD, RIP1, tumor necrosis factor receptor associated factor 2 (TRAF2), Fas-associated death domain (FADD) and pre-caspase 8, causing the release of p18/p12 fragments to trigger downstream caspase cascades to cause apoptosis. (Image created with Biorender.com, based on Dong et al., 2015).

Figure 2: Schematic illustration of TNFR2 signaling

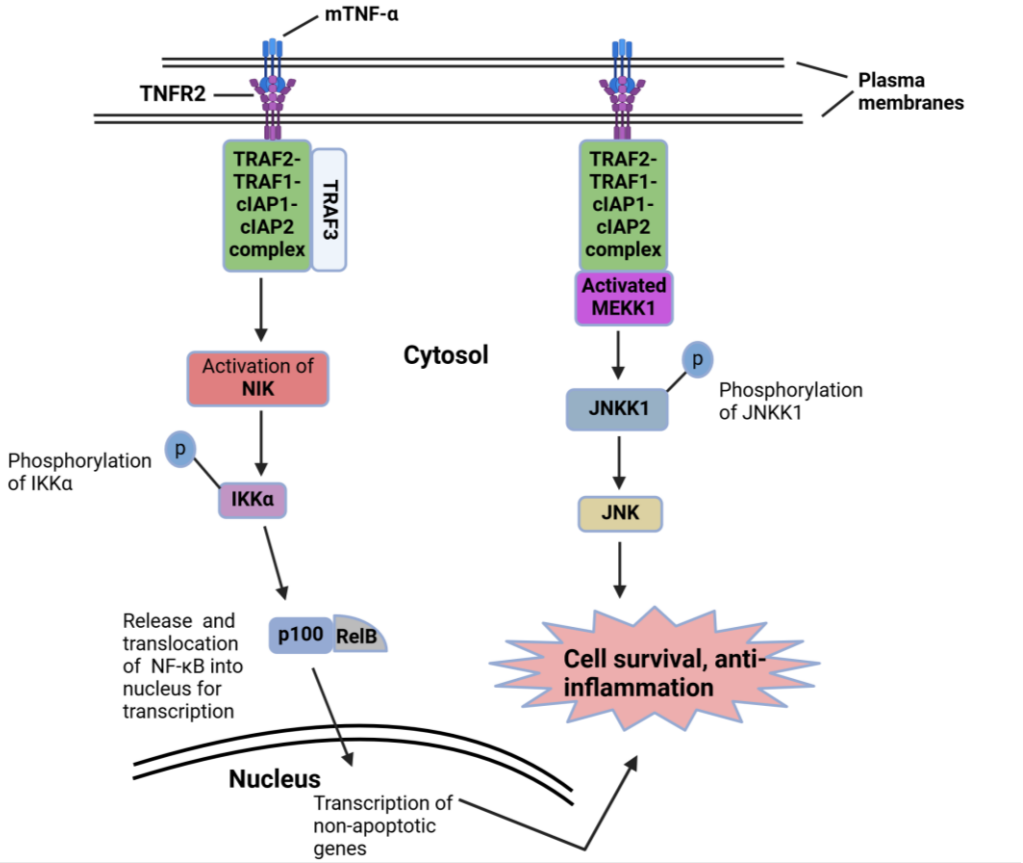

Downstream signaling pathways associated with mTNF-α-activation of TNFR2, leading to cell survival and anti-apoptotic outcomes. Activated TRAF2-TRAF1-cIAP1/2 complex is recruited to NF-κB-inducing kinase (NIK) by TRAF3, resulting in proteosomal degradation of NIK, followed by the phosphorylation and activation of IKKα, and triggering the release of the NF-κB precursor protein, p100/RelB. TNFR2-mediated signaling can also trigger c-Jun N-terminal kinase (JNK) or p38 mitogen-activated protein kinases (MAPKs), depending on the recruitment of TRAF2 to the varied intracellular binding regions of TNFR2. With this pathway, the TRAF2-TRAF1-cIAP1/2 complex binds to and activates a MAPK kinase (MAP3K) protein called MEKK1, leading to the phosphorylation of JNK-activating kinase 1 (JNKK1) and JNK activation – a transient activation of JNK promotes cell survival but prolonged activation may lead to pro-apoptotic signaling (Image created with Biorender.com, based on Dong et al., 2015).

The crosstalk between TNFR1 and TNFR2 depends on the physiologic environment and signaling kinetics between the two receptors (Naudé et al, 2011). Deletion of TNFR2 in mouse brain causes impairment of motor functions, novel object and spatial memory recognition, and, precipitates anxiety-like behavior, whereas the deletion of TNFR1 confers insusceptibility to age-mediated anxiety-like behavior (Naudé et al., 2014). Early phase hyperalgesic responses have dual dependence on both TNFR types (Zhang et al., 2011). Meanwhile, some studies have also shown antagonistic outcomes of TNFR1 and TNFR2 signaling. Unlike TNFR1, TNFR2 signaling was shown to be essential for the regeneration of oligodendrocyte precursor cells; TNFR1 signaling in mice worsened neuronal death whilst TNFR2 guarded against ischemic

retinal tissue damage (Naudé et al, 2011). In an experimental autoimmune encephalomyelitis model, TNFR1 signaling caused damage to microglia, monocytes and macrophages but that of TNFR2 conferred protection on microglia only (Gough et al., 2020). Nonetheless, TNFR2 signaling, after prolonged stimulation, may enhance TNFR1-mediated apoptosis via p38 mitogen-activated protein kinase (MAPK) signaling pathway, which occurs via certain downstream adaptor proteins [e.g. tumor necrosis factor receptor associated factor 1 (TRAF1), TRAF2 and cellular inhibitor of apoptosis proteins (cIAPs)], leading to caspase 8 activation (Koniaris et al., 2001; Naudé et al, 2011; Li et al., 2014; Dong et al., 2015; Fujita et al., 2016). Several studies have demonstrated the involvement of TNFR2 in the pathogenesis of certain disease conditions: the susceptibility of adrenalectomized mice to lipopolysaccharide (Koniaris et al., 2001), the pathogenesis of pulmonary emphysema in TNF-α transgenic mice (Fujita et al., 2016), and the development of drug tolerance by breast cancer cells (Li et al., 2014).

TNF-α plays a major role in immune defense and protection against pathogens such as viruses; and, is one of many cytokine mediators released initially by immune cells after detecting viruses, alerting nearby cells of invading pathogens (Rahman et al., 2006; Oyler-Yaniv et al., 2021). Studies involving TNF or TNFR-deficient mice have shown that TNF-α is essential for cell survival in certain viral infections, including those caused by herpes simplex virus, lymphocytic choriomeningitis virus and mouse cytomegalovirus (Rahman et al., 2006). Although TNF-α is an important antiviral cytokine, it can cause tissue damage via its cell-death pathway inducing effects (Rahman et al., 2006). TNF-α has useful anti-microbial properties [i.e. direct killing of infected cells (cytolysis), induction of apoptosis, inhibition of intracellular viral replication, and upregulation of other diverse host responses]; however, many viruses have developed intervention mechanisms against particular stages of the TNF signaling pathways (Rahman et al., 2006; Oyler-Yaniv et al., 2021). For instance, the human cytomegalovirus downregulated the expression TNFR1 on the cell surface of monocytic (THP1) cells (Baillie et al., 2003). The non-capsid protein 3A of poliovirus also affects the intracellular trafficking of TNFRs and causes TNF-α resistance by removing TNFRs from the plasma membrane (Neznanov et al., 2001). Moreover, the E6 protein of human papilloma virus 16 inhibited TNF-α-induced apoptosis in several tissues of mice and humans (Yuan et al., 2005).

2.2 Borna disease virus 1 and Borna disease

BoDV1 is an enveloped, non-segmented, single-stranded, negative-sense ribonucleic acid (RNA) virus belonging to the Realm *Riboviria*, kingdom *Orthornavirae*, phylum *Negarnaviricota*, subphylum *Haploviricotina*, class *Monjiviricetes*, order *Mononegavirales*, and family *Bornaviridae* (Herden et al., 2013; Kuhn et al., 2015; Korn et al., 2018; Amarasinghe et al., 2019; Rubbenstroth et al., 2021; **Figure 3**). BoDV1 is classified at the species level as a mammalian 1 bornavirus (Amarasinghe et al., 2019; Rubbenstroth et al., 2021). BoDV1 is among the most studied bornaviruses with both veterinary and public health impact (Rubbenstroth et al., 2021). The bicolored white-toothed shrew (*Crocidura leucodon*) is believed to be the natural reservoir of BoDV1 (Hilbe et al., 2006; Bourg et al., 2013; Dürrwald et al., 2014; Nobach et al., 2015). Uniquely, bornaviruses remain one of the few (including Influenza viruses) single-stranded, negative-sense RNA viruses that transcribe and replicate in the nucleus of host cells (Honda & Tomonaga, 2013). BoDV1 is a highly neurotropic virus, and is able to maintain a non-cytolytic persistent infection of the CNS in a wide variety of vertebrate host species (Herden et al., 2013). BoDV1 consists of an 8.9 Kb genomic RNA (gRNA), encoding six proteins [nucleoprotein (N); regulatory protein X; phosphoprotein (P); matrix protein (M); glycoprotein (G); and a large protein (L)] with overlapping reading frames which have no intergenic regions (Carbone et al., 1993; Herden et al., 2013; Honda & Tomonaga, 2013; **Figure 3**).

Figure 3: Genome structure of Borna disease virus

Negative sense, linear, single-stranded RNA genome of BoDV1 showing genes that encode the nucleoprotein (N), regulatory protein (X), phosphoprotein (P), matrix protein (M), glycoprotein (G) and the large polymerase protein (L). The X overlaps with P, and M with the type I surface of G (Image created with Biorender.com, based on Herden et al., 2013).

The gRNA, N, P and L proteins together make up the ribonucleoprotein complexes of BoDV1 (Carbone et al., 1993; Schwemmle et al., 1998). The interaction between N, P and X proteins regulate the transcription and replication of BoDV1 (Schwemmle et al., 1998). Further, the X protein has a non-apoptotic, non-cytolytic effect on host cells via interactions with MAVS,

thereby contributing to viral persistence within the CNS (Poenisch et. al, 2009). BoDV1 uses its cell surface G protein to enter host cells (especially brain cells); and, the expression and precise processing of the G protein are required for efficient dissemination of the virus in the CNS (Richt et al., 1997; Bajramovic et al., 2003; Werner-Keiss et al., 2008). The P protein of BoDV1 was shown to bind TANK-binding kinase 1, resulting in the suppression of interferon (IFN) type I production and stifling innate antiviral responses (Staeheli et al., 2001). In addition, the BoDV1 X protein can inhibit rotenone-induced axonal fragmentation, protecting neurons from degeneration and enhancing viral replication and spread (Szelechowski et al., 2014). Further, the BoDV1 N protein inhibited NF-κB processing by the 20S proteasome, resulting in the suppression of IKK/NF-κB pathway activation and viral persistence (Makino et al., 2015).

BoDV1 infection occurs in endemic areas affecting mainly horses, sheep, and rabbits with an incubation period of two weeks to several months; other animals at risk of BD include donkeys, cattle, goats, and alpacas (Staeheli et al., 2000; Herden et al., 2013; Schulze et al., 2020). The disease is endemic in Germany, Austria, Switzerland and Lichtenstein. Natural BoDV1 transmission occurs mainly via the intranasal route, and viral spread through saliva, nasal and lacrimal secretions and urine shed by reservoir hosts has been assumed (Nobach et al., 2015; Kupke et al., 2019). Once inside the nasal cavity, the virus travels retrograde along sensory tracts of the olfactory nerve into the limbic system and subsequently to the entire brain (Morales et al., 1988; MacLachlan & Dubovi, 2011; Kupke et al., 2019), infecting all neural cell types with prolonged activation of microglia and astrocytes (Herden et al., 2013). This provokes a T-cell mediated, non-cytolytic inflammation with no elimination of the virus. BoDV1 spreads to peripheral tissues as well in reservoir species or immunotolerant animals (Stitz et al., 2002; Herden et al., 2013). In mice, intracerebral BoDV1 infection causes disease in neonates only, especially in MRL mice due to their expression of an H-2^k haplotype of the major histocompatibility complex class I antigen – neonates of Balb/c and C57BL/6 mice are relatively less susceptible (Hallensleben et al., 1998). Infected neonatal mice may develop weight loss, torticollis, nervous ticks, coarse fur and death (Hallensleben et al., 1998; Kramer et al., 2012), and in the case of TNFTg mice, where TNF-α is overexpressed, epileptic seizures and a non-purulent meningoencephalitis occur (Kramer et al., 2012). Adult mice are not susceptible to clinical BD but can be infected (Rubin et al., 1993). Experimental BoDV1 infection in mice can induce IFN-γ and TNF-α production, followed by a type 1 T cell response with the release of IFN-β, IL-10, IL-12 and ROS from microglial cells (Kramer et al., 2012; Tizard et al., 2016).

The zoonotic potential of BoDV1 has been demonstrated in acute fatal human bornavirus infections (Schlottau et al., 2018; Liesche et al., 2019; Niller et al., 2020). BD in humans may present with flu-like symptoms, followed by neurological symptoms (e.g. paresis, ataxia, tetraplegia, cranial nerve paralysis etc.), which can progress to coma and death (Schlottau et al., 2018; Liesche et al., 2019). The novel bornavirus of different squirrel species (i.e. variegated squirrel 1 bornavirus) contribute to lethal human bornavirus infections as well (Hoffmann et al., 2015). In humans, BoDV1 infection lead to a non-purulent panencephalomyelitis with identification of BoDV1-characteristic eosinophilic, spherical intranuclear Joest-Degen inclusion bodies in the CNS (Schlottau et al., 2018; Liesche et al., 2019).

2.3 Peroxisomes: morphology, metabolism, biogenesis, and pexophagy

2.3.1 Morphology of the peroxisome

Peroxisomes are multifunctional organelles present in all eukaryotic cells except sperm cells and erythrocytes (Wiese et al., 2007; Waterham & Ebberink, 2012; Islinger et al., 2018). The morphology, composition, and metabolic functions of peroxisomes vary depending on the cell type, tissue or organism (Berger et al., 2016; Jean et al., 2018). Peroxisomes have a single membrane, a fine granular matrix and no deoxyribonucleic acid (DNA) (Trompier et al., 2014; Berger et al., 2016; Islinger et al., 2018). Their sizes range from 0.1 to 1 µm in diameter and occur in round to tubular forms (Trompier et al., 2014). In eukaryotic cells, peroxisome numbers are between 100 and 1000 per cell, and are most abundant in the liver, kidney and brain (Huybrechts et al., 2009; Grant et al. 2013).

2.3.2 Metabolism of peroxisomes

In the brain, peroxisomes are highly abundant in neurons, and ependymal cells, but less present in microglial cells, astrocytes, oligodendrocytes (Ahlemeyer et al., 2007). They are pivotal for neuronal migration, myelination and neurotransmission (Trompier et al., 2014). This organelle undertakes several metabolic activities: the degradation of VLCFAs via α- and β-oxidation, detoxification of ROS and reactive nitrogen species, amino acid and polyamine metabolism, and the synthesis of ether-phospholipids in mammalian cells (Wiese et al., 2007; Waterham et al., 2016; Fransen et al., 2017). During inflammation, peroxisomes break down saturated VLCFAs like arachidonic acid, whose eicosanoid derivatives have a plethora of roles depending

on their location and concentration within cells (Terlecky et al., 2012). Furthermore, peroxisomes biosynthesize docosahexanoic acid, an essential precursor for the production of anti-inflammatory molecules such as resolvins, maresins and protectins (Terlecky et al., 2012). They synthesize plasmalogens and cholesterol, which contribute to plasma membrane fluidity and minimize oxidative stress (Braverman et al., 2012).

Peroxisomes harbor enzymes such as catalase, SOD1, glutathione peroxidase and glutathione S-transferase for combatting oxidative stress to maintain intracellular redox homeostasis (Schrader & Fahimi, 2006; Del Río, 2011). Most enzymes imported into the peroxisomal matrix are involved in oxidative or nitrosative activities (Trompier et al., 2014; Berger et al., 2016). Peroxisome-induced oxidative stress, due to deficient antioxidant enzymes, is associated with cancer pathogenesis, as well as other neuroinflammatory and degenerative CNS diseases (Schrader & Fahimi, 2006; Terlecky et al., 2012). Under oxidative stress, cells produce redox-signaling molecules such as H_2O_2. Catalase, present predominantly in peroxisomes, is a heme-containing, tetrameric antioxidant enzyme that detoxifies H_2O_2 (Schrader & Fahimi, 2006; Terlecky et al., 2012; Sharma & Ahmad, 2014; Berger et al., 2016). Peroxisomes also contain low molecular weight molecules such as ascorbate, which in addition to plasmalogens act as scavengers of free radicals (Fransen et al., 2012; Lismont et al., 2015).

Catalase removes H_2O_2 via a catalatic ($2\ H_2O_2 \rightarrow 2\ H_2O + O_2$) or peroxidatic ($H_2O_2 + AH_2 \rightarrow A + 2\ H_2O$) reactions. AH_2 are electron donors including low molecular weight alcohols (e.g. ethanol, propanol, butanol etc.), nitrite, formate and formaldehyde (Kirkman & Gaetani, 2007). Catalase is an enzyme with a high turnover number; one molecule of catalase can convert about six million H_2O_2 molecules in the cellular environment of eukaryotic cells (Sharma & Ahmad, 2014). Diminishing cellular levels of catalase is a relevant landmark associated with the onset of diseases. In a rat cell model of Ahlzeimer's disease, catalase supplementation reduced β-amyloid peptide-induced neuronal toxicity (Terlecky et al., 2012). Catalase supplementation also reduced the expression of TNF-α, a pivotal initiator of psoriasis in humans (Young et al., 2008). In addition, inadequate peroxisomal catalase caused developmental anomalies in *Caenorhabditis elegans* (Petriv & Rachubinski, 2004), whereas its overproduction in transgenic mice prolonged their overall lifespan (Schriner et al., 2005; Terlecky et al., 2006). Reduced catalase levels have been identified as one of the key features of hepatocellular tumors and liver cirrhosis (Litwin et al., 1999), and colonic cancers in humans (Lauer et al., 1999).

2.3.3 Peroxisomal biogenesis

Peroxisomes proliferate via (i) de novo budding from endoplasmic reticulum membranes, (ii) and splitting of already existing, mature peroxisomes (Schrader et al., 2003; Islinger et al., 2018). In the latter case, the peroxisomal biogenesis protein, peroxin (PEX) 11, promotes peroxisomal fission (**Figure 6**) (Ahlemeyer et al., 2012; Aubourg & Wanders, 2013). The deletion of PEX11β led to 30% decrease in peroxisomal abundance in mouse brain (Ahlemeyer et al., 2012). In mammalian cells, these organelles move in the cytoplasm in a motor protein-driven fashion along microtubules (Schrader et al., 2003; Islinger et al., 2018). Peroxisomes contain about 50 different proteins. Their expression is tissue- or organ-dependent; some peroxisomal matrix proteins can be found in other subcellular organelles such as mitochondria and nuclei (Schrader & Fahimi, 2006; Wanders & Waterham, 2006). Most of peroxisomal membrane and matrix proteins are produced on polyribosomes; all proteins associated with peroxisomes contain a peroxisomal targeting signal 1 (PTS1) or PTS2, which allows for targeting and subsequent transport to peroxisomes (Trompier et al., 2014).

Peroxisomal biogenesis proteins are essential for the formation and proliferation of peroxisomes (i.e. PEX1, PEX3, and PEX11), insertion of membrane proteins (PEX19) and the import of matrix proteins (i.e. PEX5, PEX7, and a docking complex consisting of PEX13, PEX14, PEX2, PEX10, PEX12, PEX4, PEX17, PEX3, and PEX8) (Jean et al., 2018). PEX3, PEX16, and PEX19 facilitate the formation of pre-peroxisomes from ERs. PEX3, after budding from the ER, forms a docking complex with PEX16 for the subsequent recruitment and integration of other peroxisomal membrane proteins (PMPs) (Lodhi & Semenkovich, 2014; **Figure 4**). PEX19 binds newly synthesized PMPs, safeguards their solubility in the cytoplasm and chaperones them to the PEX3-PEX16 complex (Lodhi & Semenkovich, 2014; Jean et al., 2018; **Figures 4**, **5**). After releasing the PMP cargo into the peroxisomal membrane, PEX19 is recycled back into cytoplasm to scavenge more PMPs (**Figure 5**).

Next, PEX5 and PEX7 bind PTS1 and PTS2 proteins, respectively, and this facilitates their transport from the cytosol to peroxisomes (Aubourg & Wanders, 2013; Lodhi & Semenkovich, 2014). PTS1 consists of three amino acids located at the carboxyl terminal end, whereas PTS2 consists of nine amino acids, located at the amino terminal end of the respective protein (Aubourg & Wanders, 2013). PEX5 recognizes peroxisomal proteins with PTS1 (e.g. catalase), whilst PEX7 recognizes those with PTS2 (e.g. thiolase) (Aubourg & Wanders, 2013; Nakai & Imai, 2019).

Figure 4: Schematic illustration of peroxisomal biogenesis and the essential peroxins involved

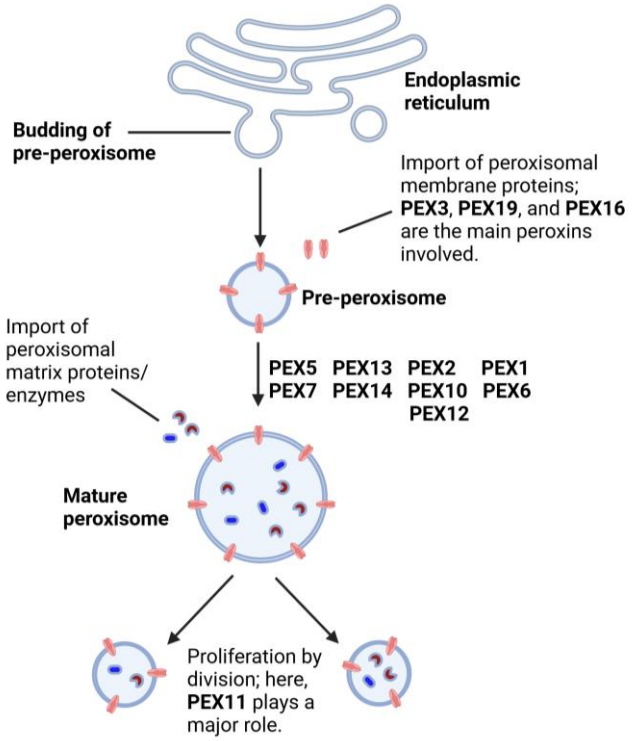

Peroxisomal proteins, peroxins or factors involved in peroxisomal formation, maturation and proliferation (Image created with Biorender.com, based on Aubourg & Wanders, 2013).

Figure 5: Schematic illustration of peroxisomal membrane protein assembly

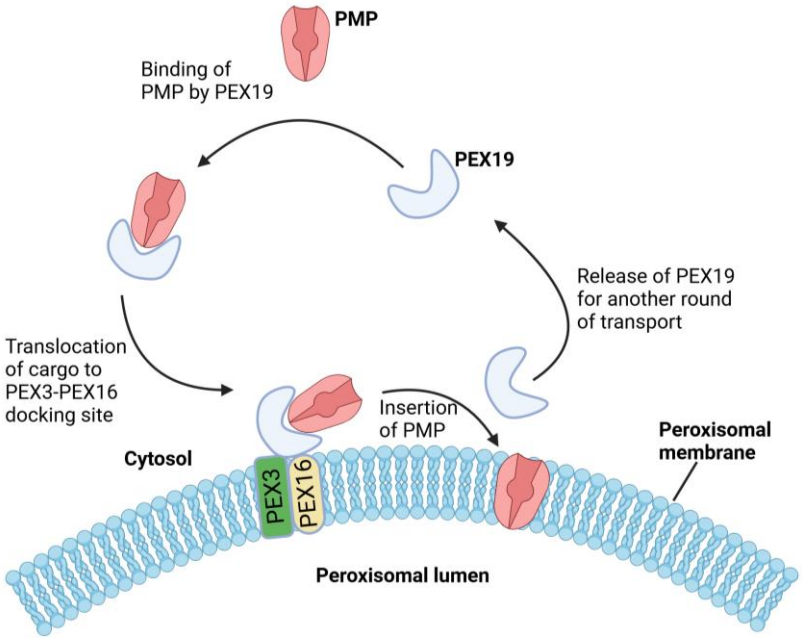

PEX19, a soluble chaperone, acts as a receptor, scavenging PMPs within the cytosol. PEX3 is derived from the endoplasmic reticulum, from which pre-peroxisomes bud (Image created with Biorender.com, based on Lodhi & Semenkovich, 2014).

The import machinery of peroxisomes consists of a docking complex including PEX13 and PEX14 (Aubourg & Wanders, 2013; **Figure 6**). With the aid of PEX2, PEX10 and PEX12, PEX5 forms a pore within the peroxisomal membrane to allow for the release of protein cargos into the peroxisomal matrix (Schrader et al., 2003; Jean et al., 2018; **Figure 6**). Afterwards, PEX1-PEX6 complex, also located in the peroxisomal membrane, in conjunction with PEX26 dissociates PEX5 and PEX7, releasing them into the cytosol to begin another round of transport (Aubourg & Wanders, 2013; **Figure 6**).

Figure 6: Schematic illustration of PEX5 receptor binding to proteins (mainly enzymes) containing peroxisomal targeting signal (PTS) proteins and their subsequent transport into the peroxisomal matrix

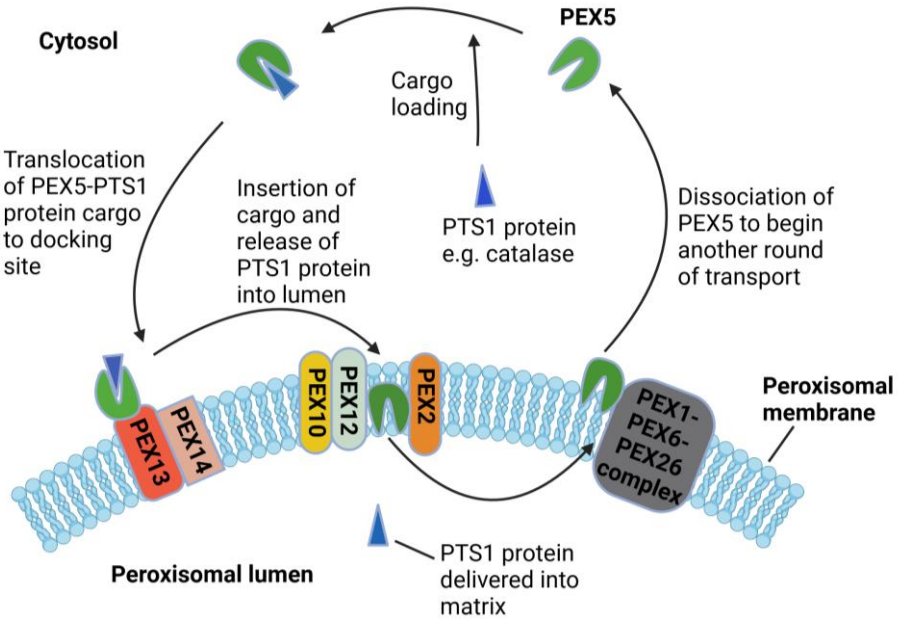

Import of PTS enzymes into the peroxisomal matrix by the cycling receptor, PEX5. A similar pattern of PTS enzyme import is proposed for the receptor, PEX7 (Image created with Biorender.com, based on Aubourg & Wanders, 2013).

Several independent mechanisms are involved in peroxisomal degradation: pexophagy, autolysis and the Lon protease system. Failure of peroxisome functions (mostly due to mutations of PEX genes) causes multiple metabolic, developmental anomalies termed as peroxisomal disorders (Waterham & Ebberink, 2012). Peroxisomal disorders are categorized into peroxisomal biogenesis disorders (PBDs) and single peroxisomal enzyme deficiencies (SPEDs). PBDs result in a total loss of peroxisomal function defined as Zellweger syndrome spectrum (ZSS) (Waterham & Ebberink, 2012; Aubourg & Wanders, 2013). ZSS consists of three different clinical manifestations with Zellweger syndrome (ZS) as the most severe form,

followed by neonatal adrenoleukodystrophy (NALD) and infantile Refsum disease (IRD) with milder symptoms. Rhizomelic chondrodysplasia punctate type 1 belongs to both PBD and SPEDs (Waterham & Ebberink, 2012; Aubourg & Wanders, 2013). Infants with ZS usually die within the first postnatal life; ZS patients develop hypotonia with abnormal craniofacial features (prominent forehead, high arched palate, shallow orbital ridges etc.), ocular abnormalities (glaucoma, cataracts and cloudy cornea), seizures, renal cysts and hepatic dysfunction (Waterham & Ebberink, 2012; Aubourg & Wanders, 2013). Patients with NALD and IRD suffer developmental delays, hypotonia, ocular defects (retinal dystrophy, vision impairment etc.), hearing loss, and hepatic dysfunction. Infants with NALD may reach puberty whereas those with IRD may reach adulthood (Waterham & Ebberink, 2012).

SPEDs result from the deficiency of specific peroxisomal enzymes involved in either α- or β-oxidation of ether lipids (Trompier et al., 2014). For instance, the impairment of β-oxidation of saturated VLCFAs results in their accumulation in plasma and tissues (Trompier et al., 2014; Islinger et al., 2018). Patients with such impairments suffer X-linked adrenoleukodystrophy (X-ALD), a condition that is more common in males. In the brains of X-ALD patients, high levels of VLCFAs affect the cholesterol component of myelin in nerves, leading to demyelination. The childhood cerebral from of X-ALD usually manifests between the ages of four and eight, characterized by progressive behavioral, cognitive and motor function impairments (Trompier et al., 2014; Islinger et al., 2018).

2.4 Mitochondria: morphology, metabolism, biogenesis, and mitophagy

2.4.1 Morphology of mitochondria

Mitochondria are highly dynamic organelles, integral in stress sensing to allow for cellular adaptation to the environment (Fransen et al., 2017). Mitochondria are double-membrane bound, and have their own genomic DNA (mtDNA) (Annesley & Fisher, 2019). mtDNA in different cells of different organisms encode several proteins, mainly involved in TCA cycle and OXPHOS; the rest of mitochondrial proteins (~99%) are encoded by nuclear genes (Annesley & Fisher, 2019; Bouchez & Devin, 2019). Mitochondrial morphology varies from punctate, round, oval, and short/long tubular to reticular shape forms depending on the cell type and metabolic/physiologic state of the cell (Fransen et al., 2017; Kausar et al., 2018; Elesela & Lukacs, 2021). The amount of mitochondria within cells differ based on metabolism and energy demands. For instance, retinal cells (rods and cones), gametes (e.g. oocytes), and striated

muscles have higher mitochondria than fat cells which have very low metabolism (Annesley & Fisher, 2019; Bouchez & Devin, 2019).

2.4.2 Metabolism of mitochondria

Mitochondria produce ATP via the TCA cycle and OXPHOS, which generates ROS – about 90% of ROS within mitochondria arise from ATP production (Annesley & Fisher, 2019). Mitochondria are the primary source of ROS within cells, and ROS production occurs in the mitochondrial intermembrane space or matrix (Fransen et al., 2012; Wang et al., 2018; Annesley & Fisher, 2019). Mitochondria contain a network of enzymatic and non-enzymatic antioxidants that guard against oxidative damage; the major antioxidant enzymes include thioredoxin, peroxiredoxins 3 and 5, SOD1 (contains copper/zinc) and SOD2 (contains manganese) (Kalinina et al, 2008). One particular ROS – i.e. $O_2^{\cdot -}$ – is produced as the main by-product of mitochondrial respiratory chain reaction by complex I and III. SOD1 and SOD2 convert $O_2^{\cdot -}$ to oxygen and hydrogen peroxide ($2\ O_2^{\cdot -} + 2\ H^+ \rightarrow O_2 + H_2O_2$) (Fransen et al., 2012; Lismont et al., 2015; Wang et al., 2018). SOD1 converts $O_2^{\cdot -}$ produced in the intermembrane space, whereas SOD2 converts those produced in the mitochondrial matrix (Diebold & Chandel, 2016). The main non-enzymatic antioxidants include coenzyme A, reduced glutathione, ubiquinol, ascorbate, and α-tocopherol (Fransen et al., 2017). In addition, mitochondria regulate intracellular Ca^{2+} levels, facilitate heme biosynthesis, and β-oxidation of fatty acids (Annesley & Fisher, 2019; Bouchez & Devin, 2019).

2.4.3 Mitochondrial biogenesis and mitophagy

Mitochondrial homeostasis is ensured via mitochondrial dynamics (i.e. biogenesis, fusion and fission) and mitophagy (mitochondrial degradation) (Elesela & Lukacs, 2021). Mitochondria undergo constant turnover, and their half-lives vary from tissue to tissue – in mice, 14 days in heart muscles and 2-4 days in the liver (Gottlieb & Stotland, 2015). Mitochondria are subject to damages, both within and outside the mitochondrial compartment, caused by events such as mutated mitochondrial proteins and ROS (Yoo & Jung, 2018). Mitochondria can change their shape, and number under stress conditions (Meyer et al., 2017). Mitochondrial quality control systems operate, both in physiological and pathological conditions, to safeguard the presence of healthy organelles only. At the organelle level, mitochondrial quality is preserved through biogenesis, fusion, fission and mitophagy (Yoo & Jung, 2018). Mitochondrial biogenesis can

be induced by intra- (e.g. ROS, carbon monoxide etc.) and/or extra-(e.g. viruses, hormones etc.) mitochondrial signals (Yoo & Jung, 2018), and involves the coordinated expression of both mitochondrial and nuclear genomes (**Figure 7**). The major role-players in mitochondrial biogenesis are the nuclear respiratory factors (NRFs; particularly NRF1 and NRF2) and peroxisome proliferator-activator receptor-γ coactivator-1α (PGC-1α) – NRFs and PGC-1α induce the expression of nuclear-encoded mitochondrial proteins, which are delivered to mitochondria to initiate biogenesis (Bouchez & Devin, 2019; Yoo & Jung, 2018; **Figure 7**).

Figure 7: Transcriptional modulation of mitochondrial gene expression and biogenesis

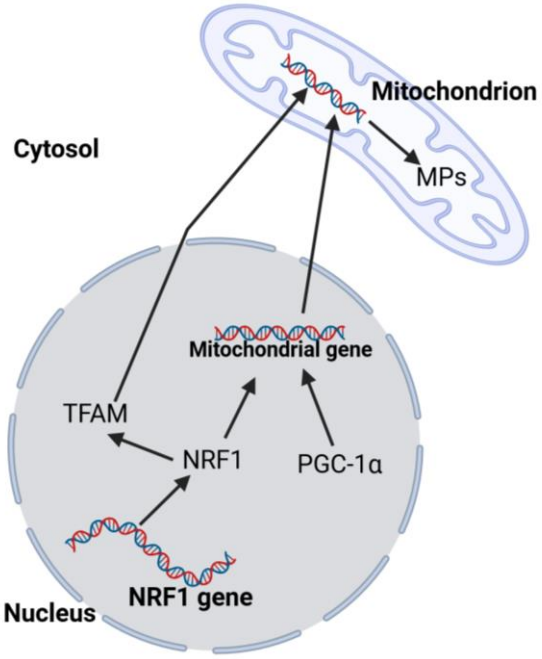

Nuclear respiratory factor 1 (NRF1) and PGC-1α induce mitochondrial genes to synthesize mitochondrial proteins (MPs), some of which are involved in mitochondrial biogenesis. The mitochondrial transcription factor A (TFAM), also implicated in the expression of mitochondrial genes, is regulated by NRF1 (Image created with Biorender.com, based on Bouchez & Devin, 2019).

Mitochondria fusion requires guanidine triphosphatases (GTPases, also known as mitofusins 1 and 2 in humans), which are located in the inner and outer mitochondrial membranes (Meyer et al., 2017). On the other hand, GTPase dynamin related protein 1, in conjunction with several proteins, mediate mitochondrial fission (Meyer et al., 2017; Elesela & Lukacs, 2021). Mitochondrial fission and fusion are perpetual processes; fission helps correct mitDNA mutations while fusion facilitates the exchange and homogenization of matrix metabolites and the recycling of partially impaired mitochondria into fully healthy mitochondrial networks (Elesela & Lukacs, 2021).

Irreparably damaged or redundant mitochondria are degraded primarily by an autophagic process called mitophagy (Elesela & Lukacs, 2021). Dysregulation of mitophagy leads to neuroinflammation and Parkinson's disease. Damaged mitochondria, caused by ageing, infection, stress or ROS, are tagged by PTEN-induced kinase 1 (PINK1), followed by the recruitment of Parkin (an E3 ubiquitin ligase) and ubiquitinization of membrane substrates for recognition and degradation by autophagosomes (Elesela & Lukacs, 2021). In addition, mitochondrial membrane potential ($\Delta\Psi m$) is an essential determinant of mitochondrial health, and aids in the identification and segregation of impaired or damaged mitochondria. Stressors (such as infections) alter $\Delta\Psi m$, resulting in defective antiviral signaling and enhancement of viral replication (Koshiba et al., 2011). The reduction of $\Delta\Psi m$ can lead to damage and loss of mitochondria, promoting immune escape and viral replication in host tissues (Anand & Tikoo, 2013). Human cytomegalovirus infection decreased $\Delta\Psi m$, leading to the accumulation of dysfunctional mitochondria (Anand & Tikoo, 2013). Influenza A virus (PB1-F2 protein), human immunodeficiency virus (HIV; Vpr protein), and Coxsackie virus (2B protein) reduced $\Delta\Psi m$ leading to apoptosis (Anand & Tikoo, 2013). Myxoma poxvirus, however, inhibits $\Delta\Psi m$ loss, halting apoptosis during viral infection (Everett et al., 2002).

2.5 Metabolic and redox interplay between peroxisomes and mitochondria

Peroxisomes and mitochondria share transcriptional regulatory pathways that orchestrate their abundance and functions (Fransen et al., 2017). The concerted metabolic functions of peroxisomes and mitochondria involve α- and β-oxidation of fatty acids, bile acid synthesis and ROS homeostasis (Fransen et al., 2017). β-oxidation of fatty acids is a stepwise process whereby fatty acyl-coenzyme A (CoA) ester chains are shortened between carbons 2 and 3, producing acetyl or propionyl CoA in both peroxisomes and mitochondria (**Figure 8**). Transmembrane transport of molecules (e.g. fatty acids, acetyl CoA, and ATP) occurs across the peroxisomal and mitochondrial membrane via specific transporter proteins – ATP binding cassette-transporters of subfamily D (ABCD; the three family members are ABCD1-3) for substrates involved in peroxisomal fatty acid oxidation, whereas carnitine-acyl carrier (CAC) performs a similar role in the outer membrane of mitochondria. In addition, the re-oxidation of reduced nicotinamide dehydrogenase (NADH) back to NAD^+ requires the interaction between peroxisomes, cytosol, and mitochondria (Wanders et al., 2016; **Figure 8**). Acetyl CoA generated within peroxisomes after β-oxidation is fed into the TCA cycle for ATP synthesis in mitochondria. Defects in peroxisomal β-oxidation enzymes leads to mitochondrial stress with

deleterious injury to the brain and spinal neurons in patients with X-ALD (López-Erauskin et al., 2013; Fourcade et al., 2015).

Figure 8: Interplay between peroxisomal and mitochondrial β-oxidation of fatty acids

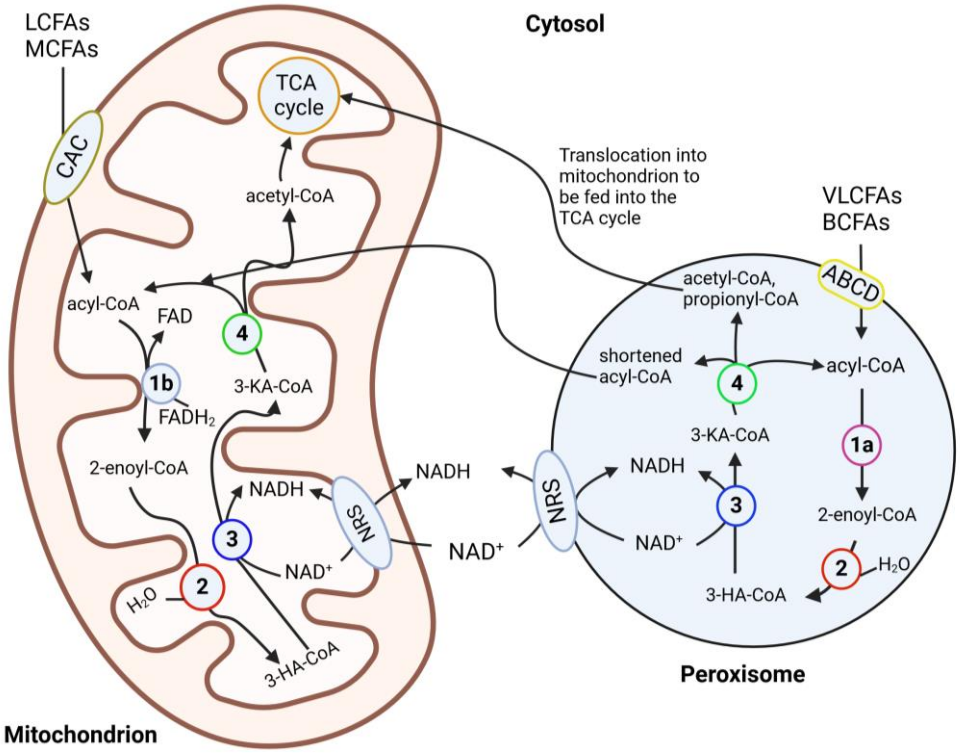

Interplay of peroxisomal and mitochondrial fatty acid β-oxidation. Fatty acid β-oxidation, the NAD(H) redox shuttles (NRS), the tricarboxylic acid (TCA) cycle, and the electron transfer chain are respectively depicted in blue, purple, red, and pink, respectively. 1a, acyl-coenzyme A (CoA) oxidase; 1b, acyl-CoA dehydrogenase; 2, enoyl-CoA hydratase; 3, 3-hydroxyacyl-CoA dehydrogenase; 4, 3-ketoacyl-CoA thiolase. ABCD, ATP-binding cassette transporters of subfamily D; BRCFA, branched-chain fatty acid; CAC, carnitine-acylcarnitine carrier; FAD, flavin adenine dinucleotide; $FADH_2$, reduced FAD; LCFA, long-chain fatty acid; MCFA, medium-chain fatty acid; NAD, nicotinamide adenine dinucleotide; NADH, reduced NAD; VLCFA, very-long-chain fatty acid; 3-HA-CoA, 3-hydroxyacyl-CoA, 3-KA-CoA, 3-ketoacyl-CoA (Image created with Biorender.com, based on Fransen et al., 2017).

Disturbances in peroxisomal catalase activity induces mitochondrial stress and oxidative damage in various organs (Koepke et al., 2008; Ivashchenko et al., 2011; Walton & Pizzitelli, 2012; Hwang et al., 2012). H_2O_2, which is metabolized by catalase, plays a central role in cellular redox signaling, and can easily cross peroxisomal (Boveris et al., 1972) and mitochondrial membranes (Bienert & Chaumont, 2014). Hence, mitochondrial redox balance primarily deranges upon the accumulation or generation of excess ROS within peroxisomes (Fransen et al., 2017). Genes involved in peroxisomal fatty acid metabolism and proliferation are controlled by transcription factors (nuclear receptors) known as peroxisome proliferator-

activated receptors (PPARs). Although PGC-1α (a transcriptional coactivator) serves as the main driver of mitochondrial biogenesis and functions (Fransen et al., 2017), PPARs (such as PPARα, PPARγ, and PPARδ) regulate the expression of genes involved in mitochondrial β-oxidation (Cook et al., 2000; Wang et al., 2003) and biogenesis (Hoivik et al., 2004; Corona et al., 2014). PGC-1α functions together with PPARs to augment the expression of genes encoding mitochondrial OXPHOS subunits, antioxidant enzymes and biogenesis factors (Fransen et al., 2017). Therefore, peroxisomal and mitochondrial abundance and activity are modulated synergistically at the transcriptional level by PPARs and PGC-1α (Fransen et al., 2017).

Moreover, de novo formation of peroxisomes requires mitochondria-derived vesicles (Sugiura et al., 2017; Li & Wang, 2021). Mitochondria communicate with other subcellular compartments via these mitochondria-derived vesicles, which carry cargos to, for instance, a subpopulation of peroxisomes (Neuspiel et al., 2008; Andrade-Navarro et al., 2009). The fission machinery of both organelles share multiple components, which include mitochondrial fission protein 1 (FiS1) (Koch et al., 2005), mitochondrial fission factor (MFF) (Gandre-Babbe & van der Bliek, 2008), ganglioside-induced differentiation-associated protein 1 (GDAP1) (Huber et al., 2013), and dynamin 1-like protein (DNM1L) (Li & Gould, 2003). Defects in DNM1L have been linked to a lethal autosomal dominant disorder, characterized by infantile encephalopathy, optic atrophy and hypoplasia, cerebral dysgenesis, seizures and refractory epilepsy due to aberrant mitochondrial and peroxisomal fission mechanisms (Waterham et al., 2007; Chao et al., 2016; Vanstone et al., 2016). Loss of MFF has been associated with early-onset Leigh-like encephalopathy (Koch et al., 2016) and mitochondrial encephalopathy (Shamseldin et al., 2012); and, mutations in GDAP1 contributes to Charcot-Marie-Tooth disease (Cassereau et al., 2011). Alterations in the abundance and function of peroxisomes and mitochondria markedly affect both their individual and combined outputs (Baumgart et al., 2001; Peeters et al., 2014; Salpietro et al., 2015; Fransen et al., 2017). For example, the loss of PEX5 (which caused dysfunctional peroxisomes) led to severe alterations in mitochondrial ultrastructure and the activities of mitochondrial respiratory chain complexes in organs/tissues such as the liver, kidney, adrenal cortex, heart, skeletal and smooth muscle cells (Baumgart et al., 2001).

2.6 Peroxisome-mitochondria crosstalk in virus-induced neuroinflammation

Multiple cellular processes, including antiviral innate immune signaling, necessitate the synchronized action of subcellular organelles, especially of peroxisomes and mitochondria (Dixit et al., 2010, Fransen, 2017). Pathogen recognition is a crucial component of innate immunity in both the extra- and intracellular compartments (Bowie & Unterholzner, 2008; Odendall & Kagan, 2017; Chathuranga et al., 2021). To do this, cells have pattern recognition receptors (PRRs) for detecting and responding to specific antigens known as pathogen associated molecular patterns (Bowie & Unterholzner, 2008; Odendall & Kagan, 2017).

The first subfamily of PRRs to be discovered is the toll-like receptor (TLR) family; TLRs are located on the cell surface, as well as on endosomes, for the recognition of various microbial cell surface components (Bowie & Unterholzner, 2008; Odendall & Kagan, 2017). A few TLRs (i.e. TLR3, TLR7, TLR8 and TLR9) located on endosomes recognize viral nucleic acids (Bowie & Unterholzner, 2008; Kagan, 2012; Odendall & Kagan, 2017). Specifically, TLR3/7 recognize single-stranded RNAs like that of BoDV1 (Bowie & Unterholzner, 2008; Planz et al., 2009). Another family of PRRs are the retinoic acid-inducible gene I (RIG-I)-like receptor (RLR) proteins, which survey and detect foreign cytosolic RNA; viral RNAs are primarily recognized by the pro-inflammatory members of the RLR family [i.e. MDA5 (melanoma differentiation associated protein 5) and RIG-I] (Dixit et al., 2010; Kagan, 2012; Rehwinkel & Gack, 2020). To avoid detection by RIG-I, BoDV1 is able to trim its genome, particularly at the 3' and 5' ends (Schneider et al., 2003). Upon recognition of viral RNA, RLRs become activated and are chaperoned by the 14-3-3ε protein to MAVS (**Figure 9**). MAVS are adaptor protein complexes, containing 540 amino acids, and tail-anchored in the membranes of peroxisomes, mitochondria and ERs – they are vital supramolecular organizing centers for antiviral immune signal transduction (Dixit et al, 2010; Horner et al., 2011; Odendall & Kagan, 2017). As one of the prime targets of hepatitis C virus, its NS3/4a protein cleaves the C-terminal of MAVS, relocating it to the cytosol, hence blocking RLR signaling to escape detection (Meylan et al., 2005).

After the activation and assembly of MAVS complexes on peroxisomes and mitochondria, RLRs initiate the recruitment of downstream signaling proteins (e.g. MAPKs, E3 ubiquitin ligases, and IκB kinases), which end up activating transcription factors such as NF-κB, activator protein-1 (AP-1) and interferon regulatory factors (IRFs), which are involved in the enhancement and regulation of the overall IFN response alongside the release of pro-inflammatory cytokines (Bowie & Unterholzner, 2008; Odendall & Kagan, 2017). Cells lacking

MAVS do not provoke IFN (type I and III) or pro-inflammatory cytokine production (Seth et al., 2005; Kumar et al., 2006; Odendall et al., 2014); hence, MAVS knockout mice could not generate IFN-α- and IFN-β-mediated immune responses after Sendai virus infection (Sun et al., 2006). The activation of peroxisomal MAVS induces a type III IFN expression, characterized by a prompt, short-lived antiviral signaling, whereas that of mitochondrial MAVS results in a type I IFN expression, leading to a delayed but sustained antiviral signaling (Dixit et al., 2010; Odendall & Kagan, 2017; **Figure 9**).

Figure 9: Schematic illustration of viral RNA entry into a cell and antiviral immune signaling via MAVS

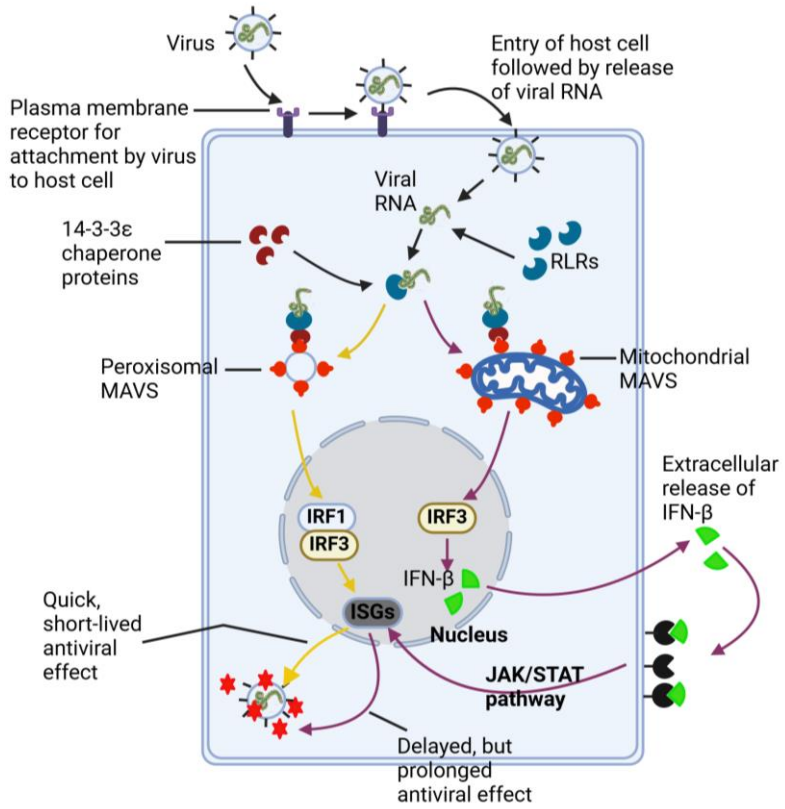

RIG-I-like receptors (RLRs) bind to viral RNA, followed by activation of MAVS proteins on peroxisomes and mitochondria to create an antiviral state within cell. Peroxisomal MAVS activation triggers interferon regulatory factors (IRFs, particularly IRF1 and IRF3), which leads to the transcription and translation of antiviral and interferon stimulating genes (ISGs) genes with rapid, short-lived antiviral effects. Mitochondrial MAVS, on the other hand, after being activated by RLRs stimulates IRF3, leading to the release of interferon (IFN)-β. IFN-β is then translocated extracellularly, binds to its receptors on the plasma membrane, and stimulates the JAK/STAT pathway. The JAK/STAT pathway subsequently induces ISGs, with a delayed, sustained antiviral effect. JAK, Janus kinase; STAT, signal transducer and activator of transcription proteins (Image created with Biorender.com, based on Dixit et al., 2010).

3. Materials and methods

3.1 Mouse lines and genotyping

Wt mice (C57BL/6JOlaHsd) were obtained from Harlan Laboratories Co. Ltd.; TNFTg mice [C57Bl/6-Tg (Grin2b-Tnf) 41.3MK]; TNFR1ko mice (B6.129-Tnfrsf1a tm1Blt/J) and TNFR2ko mice (B6.129S2-Tnfrsf1btm1Mwm/J) were kindly provided by Prof. Dr. Ulrich L.M. Eisel, Department of Molecular Neurobiology, University of Groningen, Groningen, the Netherlands. The genotype of each mouse was identified by respective quantitative polymerase chain reaction (for details see Hirz, 2017). All animals were bred and housed at the central animal laboratory of Justus Liebig University Giessen, Giessen, Germany. Mice, experimentally infected with BoDV1, were kept at the animal facility of the Biosafety Laboratory 3 of Philipps University Marburg, Marburg, Germany in accordance with animal welfare regulations under Hessen state approval [Regional Council, Giessen, file number V54-19c 2015(1) GI18/4 No. 12/2012]. For each mouse line, male and female mice were used with no special attention to equal sex distribution.

3.2 BoDV1 infection of mice, isolation and perfusion of brain regions

A BoDV1 stock (H24), originally prepared from 4-week-old Lewis rats and passaged 4 times in Balb/c mouse brains (Hallensleben et al., 1998), was injected into the brain of neonatal heterozygous TNFTg mice. Brain extracts were diluted to obtain a virus suspension of 5×10^5 ID_{50}/ml (Hirz, 2017). Out of the larger experiment being conducted, this study used two cohorts for each mouse line: (i) a non-infected cohort, where mice were not exposed to BoDV1, to serve as controls [for day 42 post infection (p.i.): 8 Wt, 5 TNFTg, 5TNFR1ko, and 8 TNFR2ko mice; see **Appendix 5**]; (ii) and an infected/experimental cohort (for day 42 p.i.: 8 Wt, 5 TNFTg, 5 TNFR1ko, 7 TNFR2ko mice; see **Appendix 5**), where mice were infected at day 0 by means of intracerebral injection with the BoDV1 suspension. The mice used for this study were euthanized at the age of 42 days and brains removed. Each brain was divided into two hemispheres, and fixed in 10% non-buffered formalin for 24 h (Hirz, 2017). Afterwards, each brain hemisphere was divided into three transverse planes according to the Bregma planes shown in **Figure 10** to obtain the hippocampus, cerebral and cerebellar cortices. Laura Brachthäuser and Dr. Manuela Hirz performed the experimental infection and brain tissue processing of all mice used in this thesis (see Brachthäuser et al., 2013; Hirz, 2017).

Figure 10: Schematic illustration of how mouse brain was cut to obtain the hippocampus, cerebral and cerebellar cortices

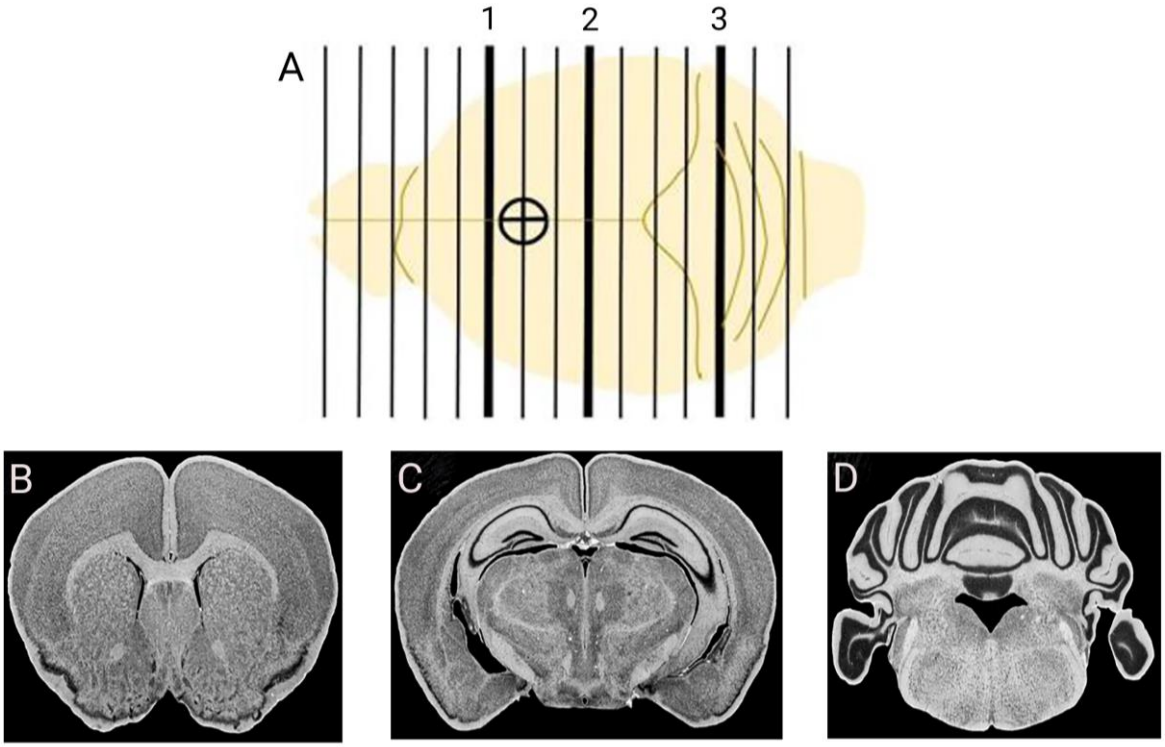

Dorsal view of an adult mouse brain (**A**), modified from atlas by T. Capra (design by AG Williams, UT Health Science Center © 1999 RW Williams; http://www.mbl.org/atlas170/atlas170_frame.html). Whole mouse brain was divided transversely (shown by thicker black lines) at levels: 1 (**B**; Bregma 1.32 mm; Interaural 5.12mm), 2 (**C**; Bregma -2.12mm; Interaural 1.68 mm) and 3 (**D**; Bregma -5.88; Interaural -2.08). Bregma (the cross inside a circle) is the point where the coronary suture and the sagittal suture intersect. Distance between bars is 1 mm. Images **B**, **C**, and **D** obtained from braininfo.rprc.washington.edu.

3.3 Indirect immunofluorescence (IF) staining

The hippocampus, cerebral and cerebellar cortices of all mice (with or without BoDV1 infection) from each mouse line were stained using the IF staining technique.

3.3.1 Antibodies

Primary antibodies used for the detection of peroxisomal and mitochondrial proteins are listed in **Table 1**. Goat anti-rabbit IgG Alexa Fluor 488 (1:300; Invitrogen of Thermo Fisher Inc., Dreieich, Germany) was used as the secondary antibody, and, DAPI (4′,6-diamidino-2-phenylindole; Sigma-Aldrich, Deisenhofen, Germany) served as the nuclear stain in all IF stainings.

Table 1: Polyclonal primary antibodies used for the IF stainings

Primary antibody	Dilution	Source (Catalogue number)
Rabbit anti-PEX14 IgG	1:10,000	Denis I. Crane, Griffith University, Brisbane, Australia
Rabbit anti-catalase IgG	1:5000	Denis I. Crane, Griffith University, Brisbane, Australia (S2SR5)
Rabbit anti-ATP5B IgG	1:2000	Sigma-Aldrich, Deisenhofen, Germany (APA 001520)
Rabbit anti-SOD2 IgG	1:1000	Abcam, Cambridge, United Kingdom (13533)

PEX14, peroxin 14; ATP5B, ATP synthase F1 subunit b; SOD2, superoxide dismutase 2; IgG, immunoglobulin G

PEX14, a peroxisomal biogenesis and membrane protein, forms a crucial part of the peroxisomal import machinery (Aubourg & Wanders, 2013; Knoblach et al., 2021); and, is an optimal marker for the identification, localization and quantification of peroxisomes in different cell types and tissues (Ahlemeyer et al., 2012; Grant et al., 2013). ATP synthase beta subunit (ATP5B), on the other hand, is a component of the mitochondrial membrane complex, playing significant roles in ATP synthesis and mitochondrial fusion/fission (Seo et al., 2016) and is used for the labelling of mitochondrial network within mammalian cells. Therefore, PEX14 and ATP5B were chosen as organelle markers for quantifying peroxisomes and mitochondria, respectively. In addition, antibodies against the main antioxidant enzymes, catalase and SOD2, of both subcellular organelles were used to investigate the antioxidant capacity of peroxisomes and mitochondria, respectively.

3.3.2 IF staining of formalin-fixed paraffin-embedded (FFPE) mouse brain tissues

Using a microtome, 2 µm-thick sections of FFPE mouse brain tissues were cut onto Superfrost® plus microscope glass slides (R. Langenbrinck Co. Ltd., Emmendingen, Germany), and fixed on a heating plate at 40°C. Slides were transferred into glass cuvettes; sections were deparaffinized with xylene (3×5 min) and rehydrated by passing through decreasing concentrations of ethanol (99%, 99%, 96%, 80%, 70% and 50%), and finally in distilled water (2×3 min). Antigen retrieval for all antibodies was performed by incubating the slides in 0.01% trypsin for 10 min on a warm plate at 37°C, followed by heating in citrate buffer (pH=6.0) 3×5 min in a standard microwave at 800 W (Microwave oven MB-392445, LG, Seoul, South Korea) with washing steps [in PBS (phosphate-buffered saline; Sigma-Aldrich, Deisenhofen, Germany) 3×5 min] in between. Slides were removed and allowed to cool down to room

temperature (RT) on the workbench. Nonspecific binding sites were blocked with 4% bovine serum albumen (BSA; Carl Roth Co. Ltd., Karlsruhe, Germany) in PBS/0.05% Tween 20 for 2 h at RT. Sections were then incubated with primary antibodies overnight. On the following day, sections were washed in PBS 3×5 min followed by incubation with the secondary antibody for 2 h at RT. Afterwards, sections were again washed in PBS 3×5 min and incubated with DAPI (1:750) to stain the nuclei, followed by washing in PBS 3×5 min. Negative controls were performed in tandem where PBS, instead of a primary antibody, was used.

3.3.3 Image acquisition using a confocal fluorescence microscope and morphometric analysis of peroxisomes and mitochondria and their main antioxidant enzymes

Using a Leica confocal laser-scanning microscope (type SPC2; 63× objective), photomicrographs were taken from: (i) the dentate gyrus (DG) and cornu ammonis (CA) band regions (mainly from CA2 and CA3, because BoDV1 spread to CA1 was rare) of the hippocampus; (ii) the cerebral cortex [Cx; laminae III (external pyramidal neurons) and V (internal pyramidal neurons)]; (iii) and the cerebellar cortex (Cb) (**Figure 11**). In the hippocampus and cerebral cortex, we further distinguished between granule and pyramidal neurons; and, in the cerebellum, granule and Purkinje cells were evaluated. Fiji Image J software (http://imagej.nih.gov/ij) was used to quantify the signals (particles) of PEX14, ATP5B, catalase and SOD2 in all photomicrographs.

Figure 11: Schematic illustration of different parts of mouse brain showing several distinct neuronal cell types

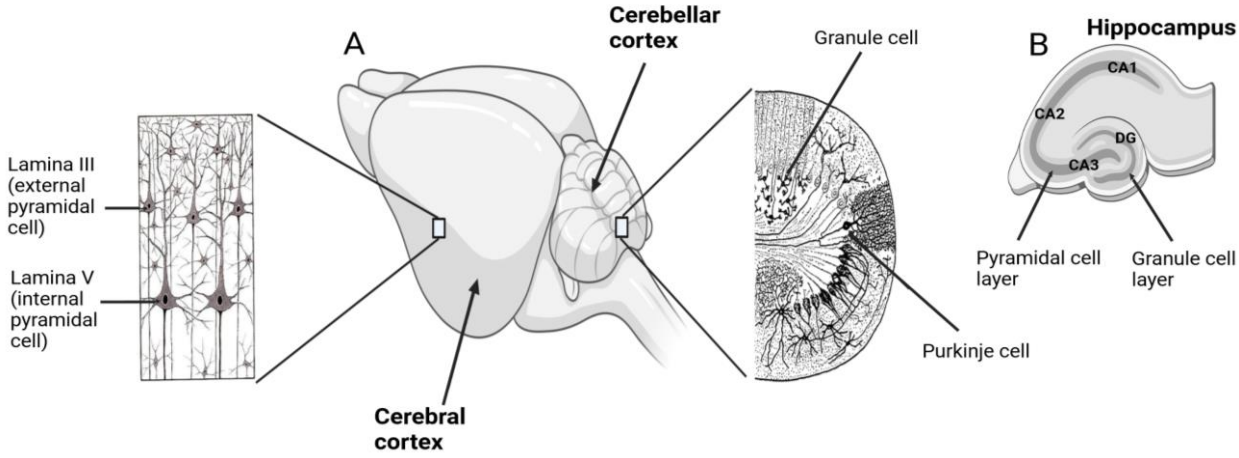

External (lamina III) and internal (lamina V) pyramidal neurons of the cerebral cortex; granule and Purkinje cells of the cerebellar cortex (**A**). Hippocampal formation showing the granule and pyramidal cell layers of the dentate gyrus (DG) and cornu ammonis (CA) band (CA1, CA2, and CA3), respectively (**B)**. Image created with BioRender.com.

Due to the particulate nature of PEX14 and catalase IF signals, their abundances were calculated as the number area density of PEX14- and catalase-positive peroxisomes, respectively. ATP5B and SOD2 IF signals appeared as a diffused network, hence, their abundances were calculated as the percentage (%) area density of ATP5B (representing all mitochondria)- and SOD2-positive mitochondria. To illustrate how the abundances of peroxisomes and mitochondria, as well their respective antioxidant enzymes, were calculated in this study, two photomicrographs of PEX14-positive and ATP5B-positive IF stainings (shown in **Figure 12**) of cortical pyramidal neurons will be used. To begin with, the photomicrographs (**Figure 12**A, C) are opened in Fiji image J software and the pyramidal cells of interest are selected using the rectangle tool, and then cropped to obtain the images as shown in **Figure 12**B, D.

Figure 12: IF staining of the cerebral cortex

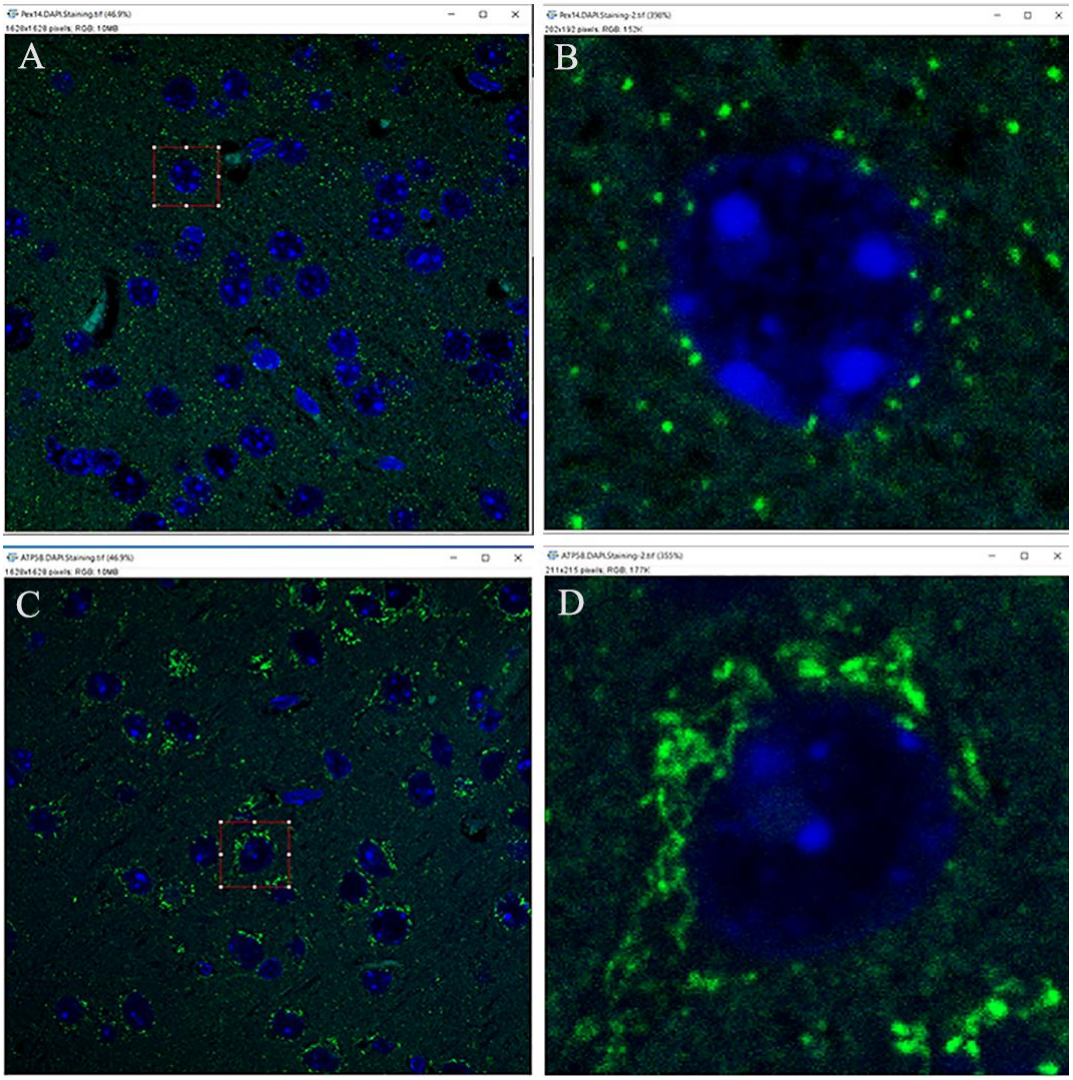

Photomicrographs showing PEX14-positive peroxisomes (**A**) and ATP5B-positive mitochondria (**C**). Cropped images of pyramidal cells from micrographs A (**B**) and C (**D**).

From the cropped images, the green and blue color channels are then split. In this Fiji Image J software, split color channels appear in white with a dark background. For the PEX14-positive peroxisomes, **Figure 13**A and **Figure 13**B show the blue DAPI stain for the nuclei and the green PEX14 stain, respectively, whilst for the ATP5B-positive mitochondria, **Figure 13**C and **Figure 13**D show DAPI and ATP5B stains, respectively – all color channels appear in white on a dark background.

Figure 13: Image J-modified photomicrographs showing split color channel images of selected pyramidal cells

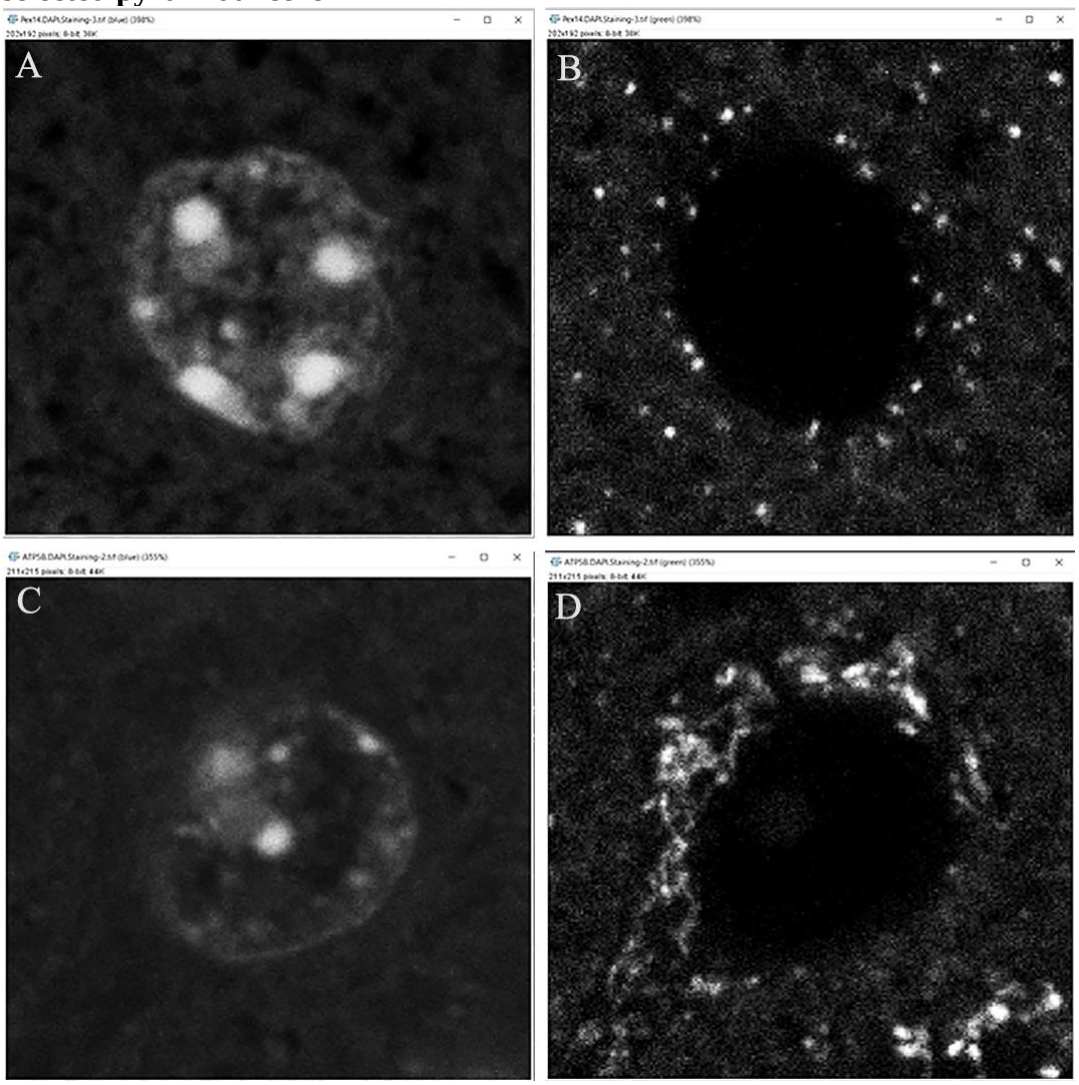

Blue channel images, (**A**) and (**C**), showing DAPI nuclear stain. Green channel images, (**B**) and (**D**), for PEX14-and ATP5B-positive signals, respectively. Immunofluorescent signals appear in white on a dark background after the color channels are split in Fiji Image J.

Using the threshold function (which highlights IF signals in red), the patterns of white signals in **Figure 13**B and **Figure 13**D are adjusted to match the green PEX14-positive signals in **Figure 12**B and the green diffused, networked ATP5B-positive signals in **Figure 12**D in order to obtain images shown in **Figure 14**A and **Figure 14**C, respectively.

Figure 14: Image thresholding of photomicrographs of pyramidal cells of the cerebral cortex

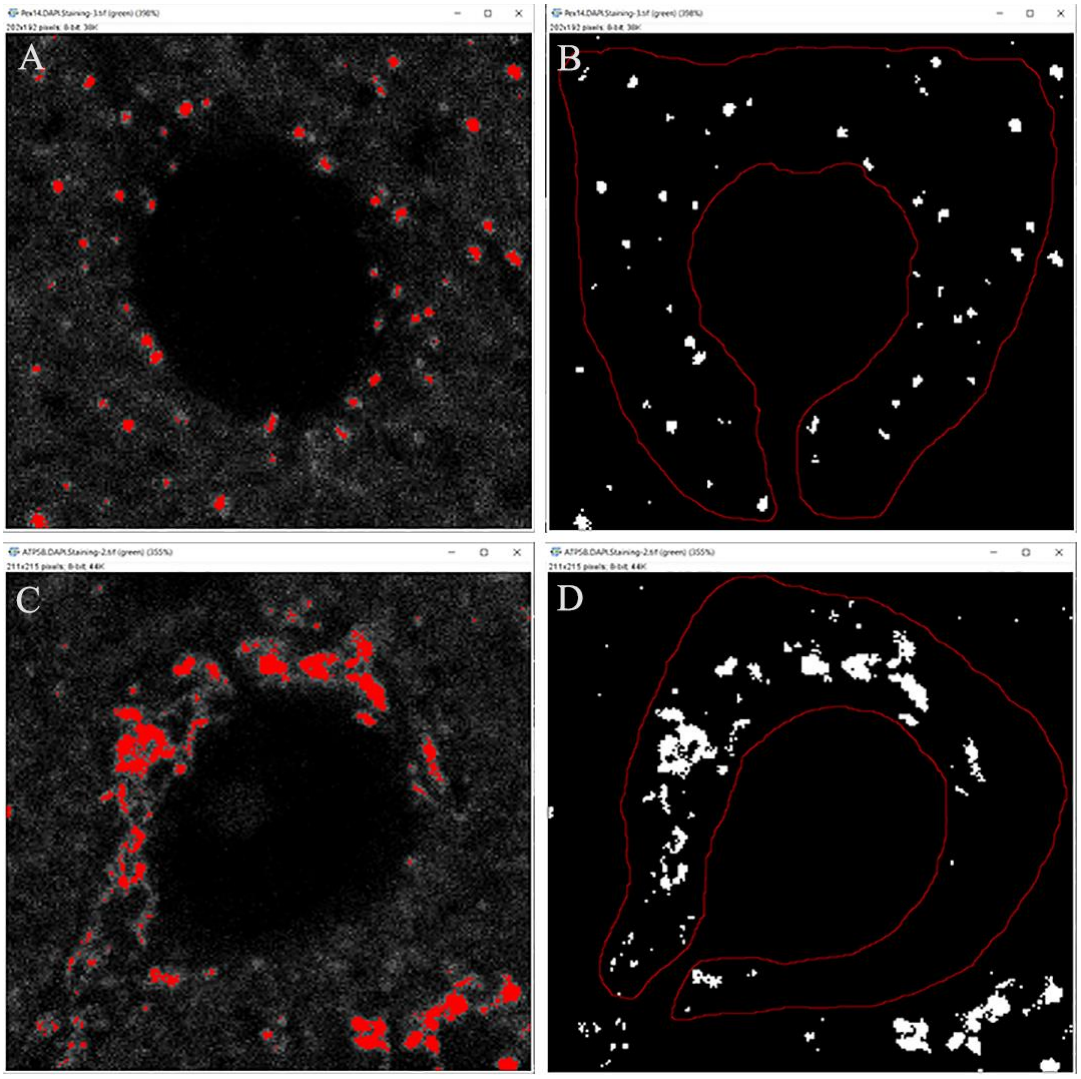

PEX14-positive peroxisome signals (**A**). ATP5-positive mitochondrion signals (**C**). Cytoplasmic area of pyramidal cell in A (**B**). Cytoplasmic area of pyramidal cell in C (**D**).

The adjusted threshold is then applied to images in **Figure 14**A **and Figure 14**C to obtain **Figure 14**B and **Figure 14**D, respectively. Using the shape of nuclei of the pyramidal cells in **Figure 12**A and **Figure 12**C as a guide, the freehand select tool was used to delineate the cytoplasmic areas in **Figure 14**B and **Figure 14**D, respectively. To calculate the abundance of peroxisomes, which represents the area number density of PEX14-positive peroxisomes in **Figure 14**B: (i) the 'analyze particles' function was used to obtain the number of PEX14-positive peroxisomes; (ii) and the corresponding cytoplasmic area was measured using the 'measure' function in Fiji Image J software.

The number of PEX14-positive peroxisomes per 100 µm² (peroxisomal abundance) was then calculated as:

$$\frac{\textit{Number of PEX14-positive peroxisomes}}{\textit{Cytoplasmic area } (px^2)}$$

where 1 pixel (px) = 0.08 µm. Similarly, catalase abundance was calculated in respective photomicrographs.

Next, to calculate the abundance of ATP5B-positive mitochondria in **Figure 14**D, which denotes the percentage (%) ATP5B area: (i) the 'analyze particles' function in Fiji image J software was also used to obtain the area of the ATP5B-positive mitochondria; (ii) and the 'measure' function for the corresponding cytoplasmic area.

The percentage area (%) of ATP5B was then calculated as:

$$\frac{\textit{Area of ATP5B-positive mitochondria } (px^2)}{\textit{Cytoplasmic area } (px^2)} \times 100$$

where 1 pixel (px) = 0.08 µm. SOD2 abundance was calculated in the exact same way in respective photomicrographs.

3.4 Statistical data analysis

FFPE brain tissue samples used for this study were from a randomly mixed population of 42-day-old male and female mice belonging to the four different mouse lines, with or without BoDV1 infection. For each neuronal cell type in a defined brain region, differences between Wt, TNFTg, TNFR1Ko and TNFR2Ko mice – with or without BoDV1 infection – were evaluated using Brown Forsythe and Welch`s one-way analysis of variance (ANOVA), followed by post-hoc Games-Howell's multiple comparisons ($\alpha = 0.05$). In case differences between non-infected and BoDV1-infected mice of the same mouse line and neuronal cell type in a defined area were to be assessed, an unpaired, non-parametric Welch`s t-test analysis ($\alpha = 0.05$) was performed. Statistical analysis was done using Graphpad Prism software (v. 8.0.2; 2019). All data are given as means +/- standard deviation of 8 Wt, 5 TNFTg, 5TNFR1Ko, and 8 TNFR2Ko mice, for the non-infected mouse group; and 8 Wt, 5 TNFTg, 5 TNFR1Ko, 7 TNFR2Ko mice for those infected with BoDV1 (see **Appendix 5**). All marked changes described in this study are of statistical significance ($P < 0.05$); no marks/labelling within the graphical figures mean there was no significant difference ($P \geq 0.05$).

4. Results

4.1 Morphometric analysis of peroxisomes, mitochondria, catalase and SOD2 in the hippocampus, cerebral and cerebellar cortices of non-infected mice

The abundances of peroxisomes, mitochondria, catalase and SOD2 were first analyzed in non-infected Wt mice to understand the distribution of peroxisomes and mitochondria as well as their main antioxidant enzymes, catalase and SOD2, respectively, within several neuronal cell types from the hippocampus, cerebral and cerebellar cortices (see section **4.1.1**). Afterwards, the same was done for non-infected TNFTg, TNFR1ko and TNFR2ko mice, and, each mouse line was compared to non-infected Wt mice (see sections **4.1.2** – **4.1.5**).

4.1.1 Morphometric analysis of peroxisomes, mitochondria, catalase and SOD2 in the hippocampus, cerebral and cerebellar cortices of non-infected Wt mice

In non-infected Wt mice, neuronal cell types in all three brain regions showed comparable peroxisomal abundances, ranging from 18/100 μm^2 in pyramidal neurons (CA band) to 21/100 μm^2 in granule neurons (DG) within the hippocampus; 14/100 μm^2 in cortical pyramidal neurons; 15/100 μm^2 and 17/100 μm^2 in cerebellar granule and Purkinje neurons, respectively (**Figure 39**A-E). Catalase abundance was 15/100 μm^2 and 16/100 μm^2 in hippocampal pyramidal (CA band) and granule (DG) neurons, respectively; 7/100 μm^2 in cortical pyramidal neurons; 10/100 μm^2 in cerebellar neurons (same amount in each of granule and Purkinje neurons) (**Figure 41**A-E). This means, 83.3% and 76.2% of peroxisomes contained detectable levels of catalase in hippocampal pyramidal and granule neurons, respectively; 50.0% in cortical pyramidal neurons; and in the cerebellar cortex, 66.7% in granule and 58.8% in Purkinje neurons of Wt mice.

On the other hand, mitochondrial abundance was 3.2% and 2.7% in hippocampal pyramidal and granule neurons, respectively; 9.2% in cortical pyramidal neurons; 3.0% in granule neurons and 17.5% in Purkinje neurons of the cerebellar cortex (**Figure 40**A-E). Thus, mitochondrial abundance was 1.9 to 6.6-fold higher in cerebellar Purkinje neurons compared to other neuronal cell types. SOD2 abundance was 0.4% and 0.2% in hippocampal pyramidal and granule neurons, respectively; 0.6% in cortical pyramidal neurons; 0.2% in granule neurons and 1.2% in Purkinje neurons of the cerebellar cortex (**Figure 42**A-E). Hence, 12.5% and 7.4% of mitochondria contained detectable SOD2 in hippocampal pyramidal and granule neurons,

respectively; 6.5% in pyramidal neurons of the cerebral cortex; 6.7% in granule neurons and 6.9% in Purkinje neurons of the cerebellar cortex of Wt mice.

4.1.2 Morphometric analysis of peroxisomes and mitochondria in the hippocampus, cerebral and cerebellar cortices of non-infected TNFTg mice in comparison to non-infected Wt mice

In TNFTg mice, TNF-α is moderately overexpressed in the forebrain regions (Probert et al., 1997; Kramer et al., 2012; Hirz, 2017). Peroxisomal abundance in non-infected TNFTg mice, was 30/100 μm^2 in pyramidal neurons (CA band) and 29/100 μm^2 in granule neurons (DG); 15/100 μm^2 in cortical pyramidal neurons; 20/100 μm^2 and 22/100 μm^2 in cerebellar granule and Purkinje neurons, respectively (**Figure 39**A-E). This shows that peroxisomal abundance was slightly higher in most neurons (except in pyramidal neurons of the cerebral cortex) of brain areas with moderate TNF-α overexpression [1.7-fold increase in pyramidal cells (CA band); 1.4-fold in granule cells (DG)] compared to respective neurons in non-infected Wt mice (**Figures 15**A-D, **16**A,B, **39**A-C).

Further, mitochondrial abundance was 28.9% in pyramidal neurons (CA band) and 16.8% in granule neurons (DG); 50.6% in cortical pyramidal neurons; 6.3% and 28.1% in cerebellar granule and Purkinje neurons, respectively (**Figure 40**A-E). This means mitochondrial abundance was higher in all neurons of TNF-α overexpressing areas of non-infected TNFTg mice [9.0-fold in pyramidal cells (CA band) band; 6.2-fold in granule cells (DG); 5.5-fold in pyramidal cells (cerebral cortex)], when compared to same neuronal cell types of Wt mice (**Figures 17**A-D, **18**A,B, **40**A-C).

Since TNF-α is overexpressed is only at low levels in the cerebellum of non-infected TNFTg mice (which served as internal control), no differences were found in the abundances of peroxisomes (**Figures 16**C,D, **39**D,E) and mitochondria (**Figures 18**C,D, **40**D,E) in cerebellar granule and Purkinje neurons compared to same cell types of non-infected Wt mice.

Figure 15: Peroxisomal abundance in pyramidal neurons (CA band) and granule neurons (DG) of non-infected Wt and TNFTg mice

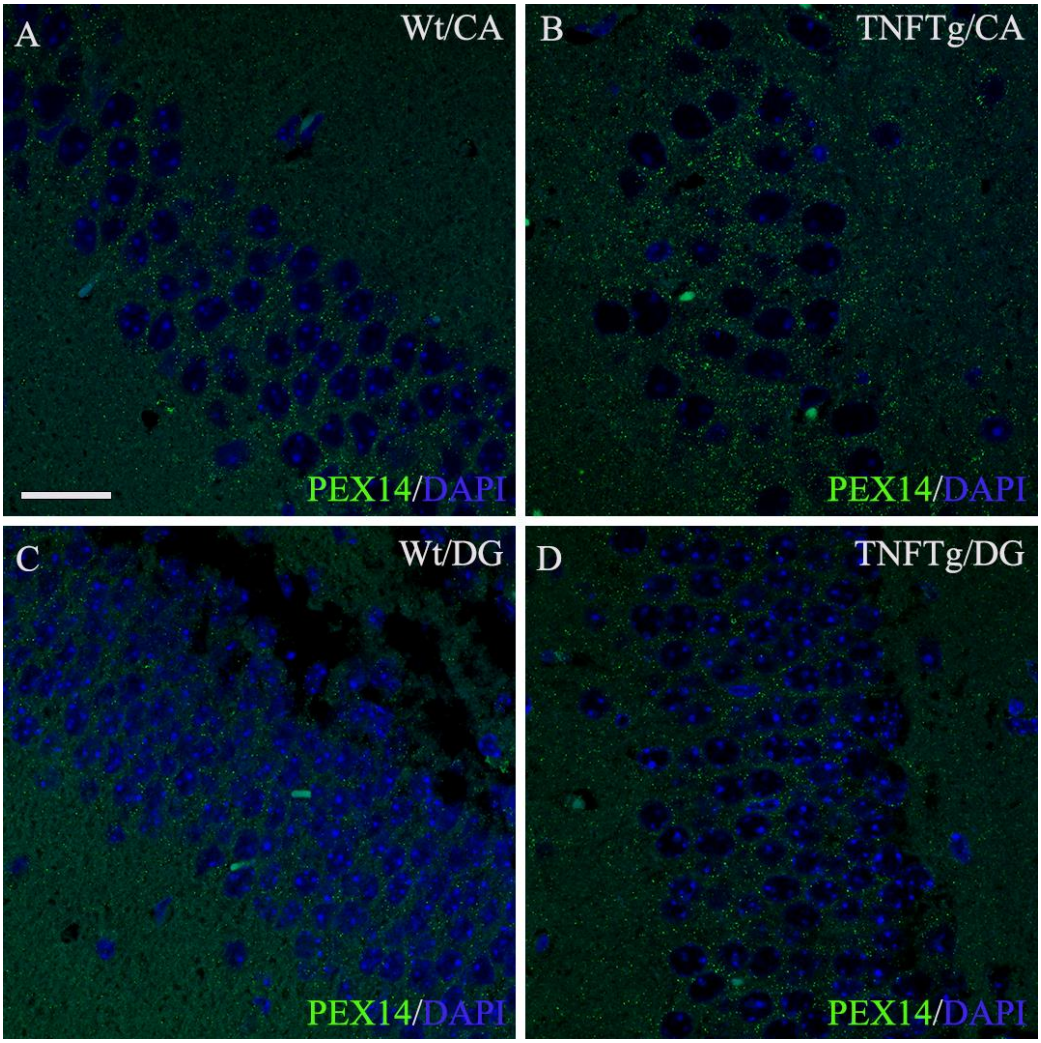

Photomicrographs of PEX14-positive peroxisomes (green) in pyramidal neurons of the cornu ammonis (CA) band [**A**, Wt; **B**, TNFTg] and granule neurons of the dentate gyrus (DG) [**C**, Wt; **D**, TNFTg]. Peroxisomal abundance increased in pyramidal and granule neurons of the CA band and DG of non-infected TNFTg mice, respectively. DAPI (blue) is the nuclear stain. ***Wt***, wild-type; ***TNFTg***; TNF transgenic. Scale bar: 20 µm for all images.

Figure 16: Peroxisomal abundance in pyramidal neurons of the cerebral cortex, and cerebellar granule and Purkinje neurons of non-infected Wt and TNFTg mice

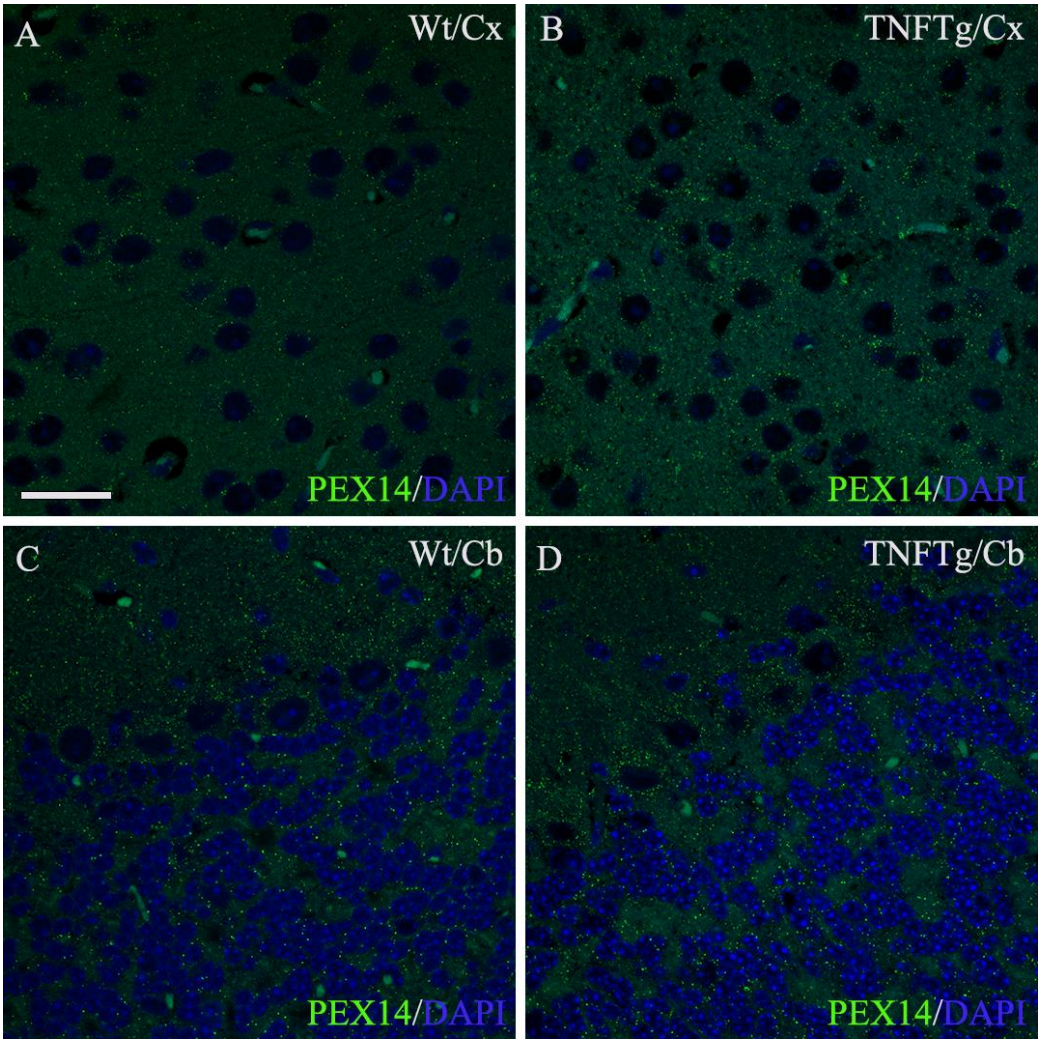

Photomicrographs of PEX14-positive peroxisomes (green) in pyramidal neurons of the cerebral cortex (Cx) [**A**, Wt; **B**, TNFTg] and cerebellar (Cb) granule and Purkinje neurons [**C**, Wt; **D**, TNFTg]. No changes in peroxisomal abundance in pyramidal neurons of the cerebral cortex, and cerebellar granule and Purkinje neurons of non-infected TNFTg mice. DAPI (blue) is the nuclear stain. ***Wt***, wild-type; ***TNFTg***; TNF transgenic. Scale bar: 20 µm for all images.

Figure 17: Mitochondrial abundance in pyramidal neurons (CA band) and granule neurons (DG) of non-infected Wt and TNFTg mice

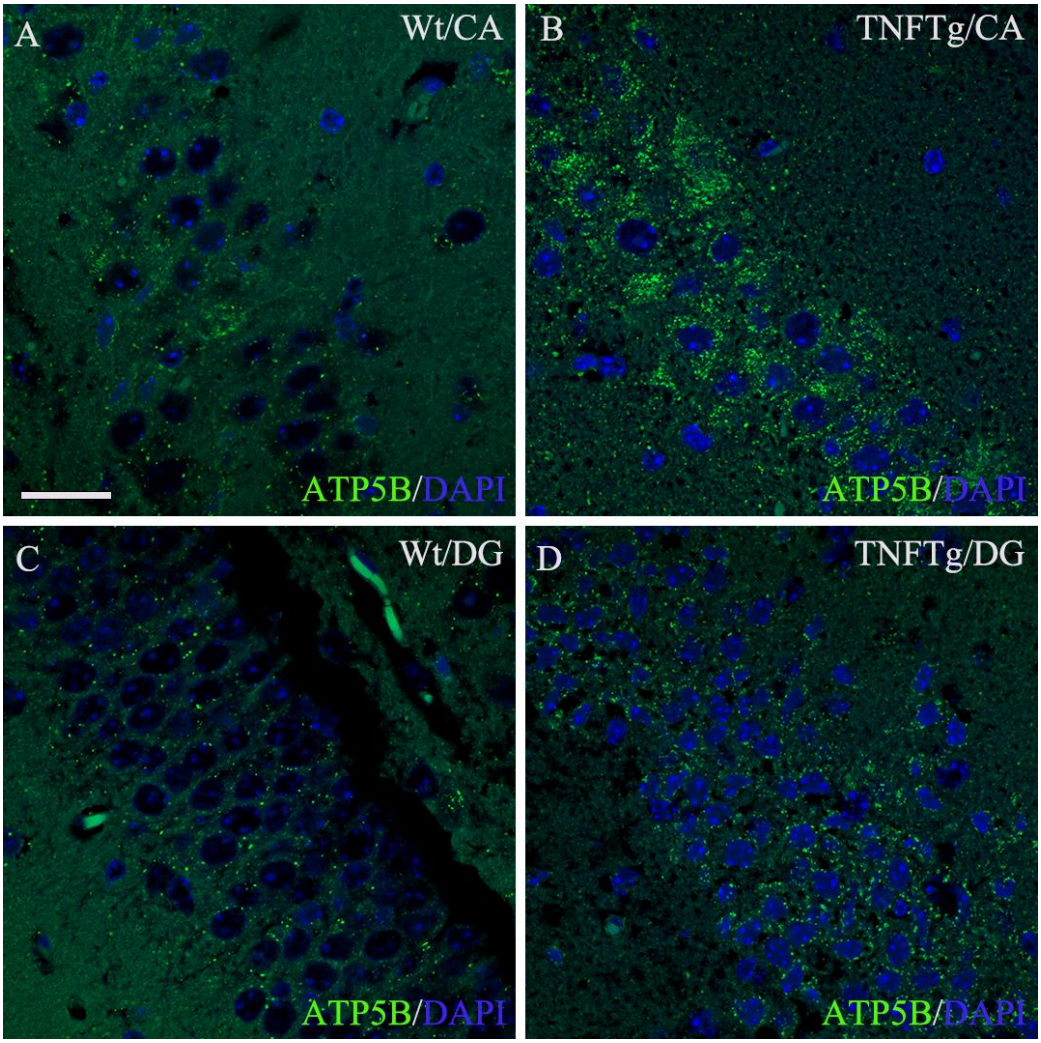

Photomicrographs of ATP5B-positive mitochondria (green) in pyramidal neurons of the cornu ammonis (CA) band [**A**, Wt; **B**, TNFTg] and granule neurons of the dentate gyrus (DG) [**C**, Wt; **D**, TNFTg]. Mitochondrial abundance increased in pyramidal and granule neurons of the CA band and DG of non-infected TNFTg mice, respectively. DAPI (blue) is the nuclear stain. ***Wt***, wild-type; ***TNFTg***; TNF transgenic. Scale bar: 20 µm for all images.

Figure 18: Mitochondrial abundance in pyramidal neurons of the cerebral cortex, and cerebellar granule and Purkinje neurons of non-infected Wt and TNFTg mice

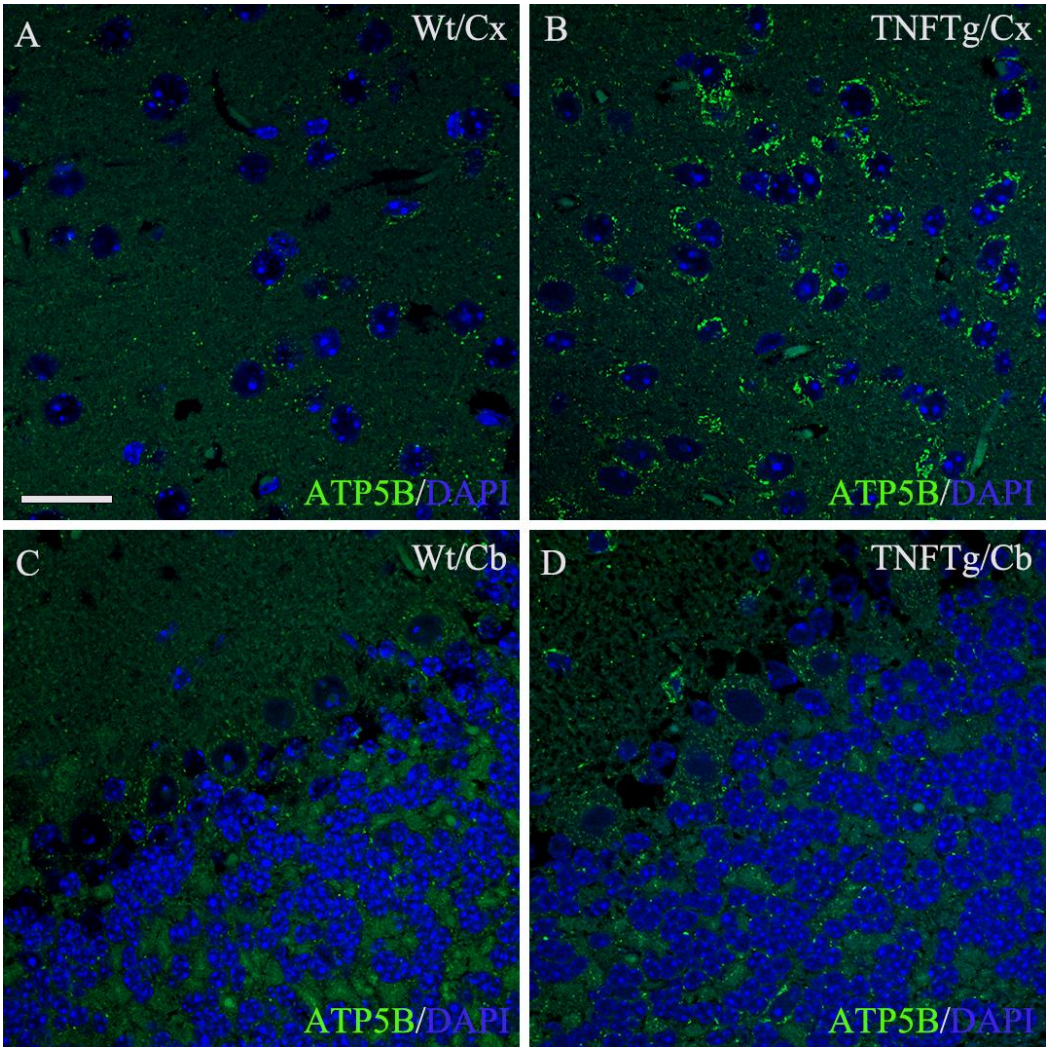

Photomicrographs of ATP5B-positive mitochondria (green) in pyramidal neurons of the cerebral cortex (Cx) [**A**, Wt; **B**, TNFTg] and cerebellar (Cb) granule and Purkinje neurons [**C**, Wt; **D**, TNFTg]. Mitochondrial abundance increased in pyramidal neurons of the cerebral cortex, but not in cerebellar granule and Purkinje neurons of non-infected TNFTg mice. DAPI (blue) is the nuclear stain. ***Wt***, wild-type; ***TNFTg***; TNF transgenic. Scale bar: 20 µm for all images.

4.1.3 Morphometric analysis of catalase and SOD2 in the hippocampus, cerebral and cerebellar cortices of non-infected TNFTg in comparison to non-infected Wt mice

In non-infected TNFTg mice, the abundance of peroxisomal catalase was 5/100 μm^2 and 6/100 μm^2 in pyramidal (CA band) and granule (DG) neurons, respectively; 3/100 μm^2 in cortical pyramidal neurons; 7/100 μm^2 in granule neurons and 6/100 μm^2 in Purkinje neurons of the cerebellar cortex (**Figure 41**A-E). Thus, catalase abundance was lower in all neuronal cell types [3.0-fold in pyramidal cells (CA band); 2.7-fold in granule cells (DG); 2.3-fold in pyramidal cells (cerebral cortex)] from TNF-α transgenic brain areas in contrast to non-infected Wt mice (**Figures 19**A-D, **20**A,B, **41**A-C).

Abundance of mitochondrial SOD2 was 4.8% in pyramidal (CA band) and 2.1% in granule (DG) neurons of the hippocampus; 6.7% in cortical pyramidal neurons; 0.3% and 0.9% in cerebellar granule and Purkinje neurons, respectively (**Figure 42**A-E). Therefore, SOD2 abundance was higher in TNF-α transgenic brain regions of non-infected TNFTg mice [12.0-fold in pyramidal neurons (CA band); 10.5-fold in granule neurons (DG); 11.2-fold in cortical pyramidal neurons] compared to those of non-infected Wt mice (**Figures 21**A-D, **22**A,B, **42**A-C).

However, there were no significant changes in peroxisomal catalase (**Figures 20**C,D, **41**D,E) and mitochondrial SOD2 (**Figures 22**C,D, **42**D,E) in cerebellar granule and Purkinje neurons compared to same cell types of Wt mice.

Figure 19: Catalase abundance in pyramidal neurons (CA band) and granule neurons (DG) of non-infected Wt and TNFTg mice

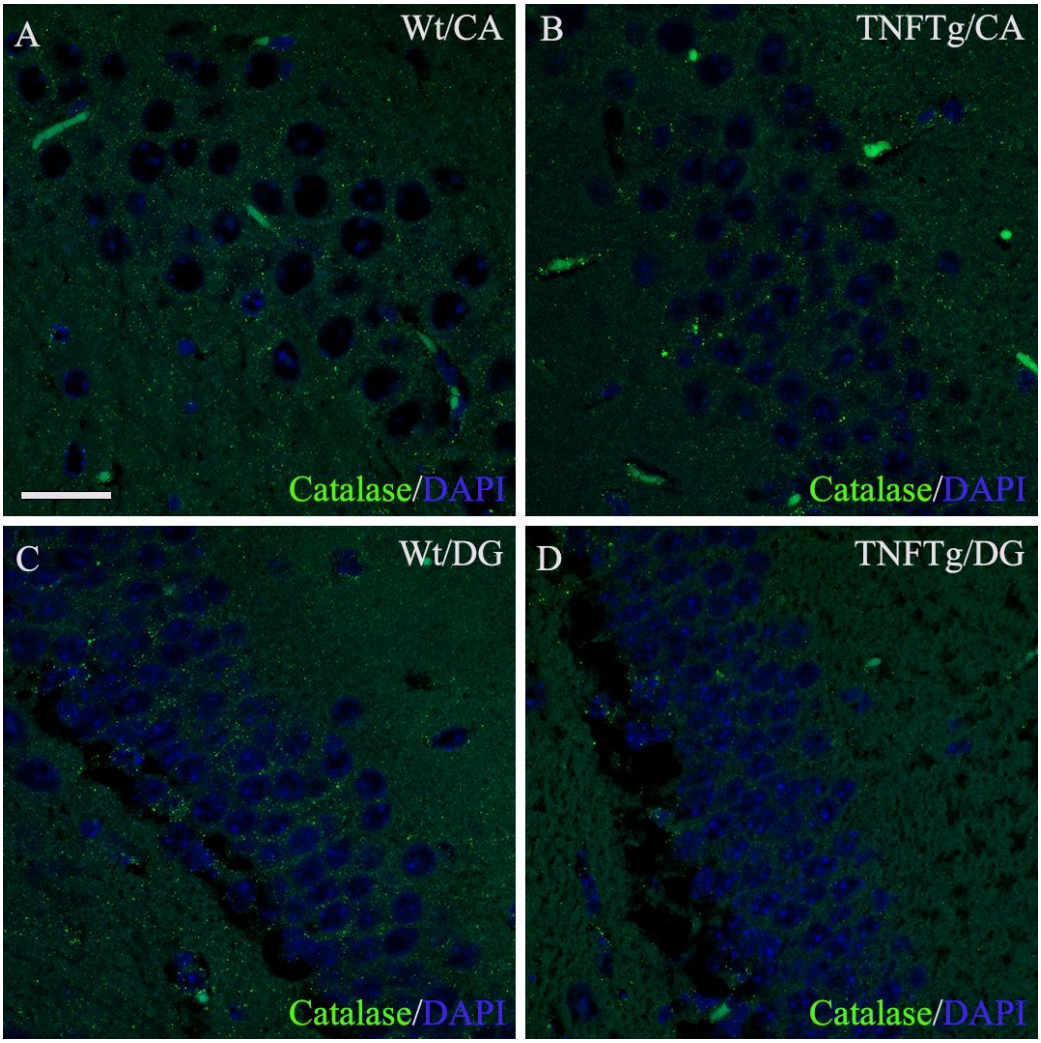

Photomicrographs of catalase-positive peroxisomes (green) in pyramidal neurons of the cornu ammonis (CA) band [**A**, Wt; **B**, TNFTg] and granule neurons of the dentate gyrus (DG) [**C**, Wt; **D**, TNFTg]. Catalase abundance decreased in pyramidal and granule neurons of the CA band and DG of non-infected TNFTg mice, respectively. DAPI (blue) is the nuclear stain. ***Wt***, wild-type; ***TNFTg***; TNF transgenic. Scale bar: 20 µm for all images.

Figure 20: Catalase abundance in pyramidal neurons of the cerebral cortex, and cerebellar granule and Purkinje neurons of non-infected Wt and TNFTg mice

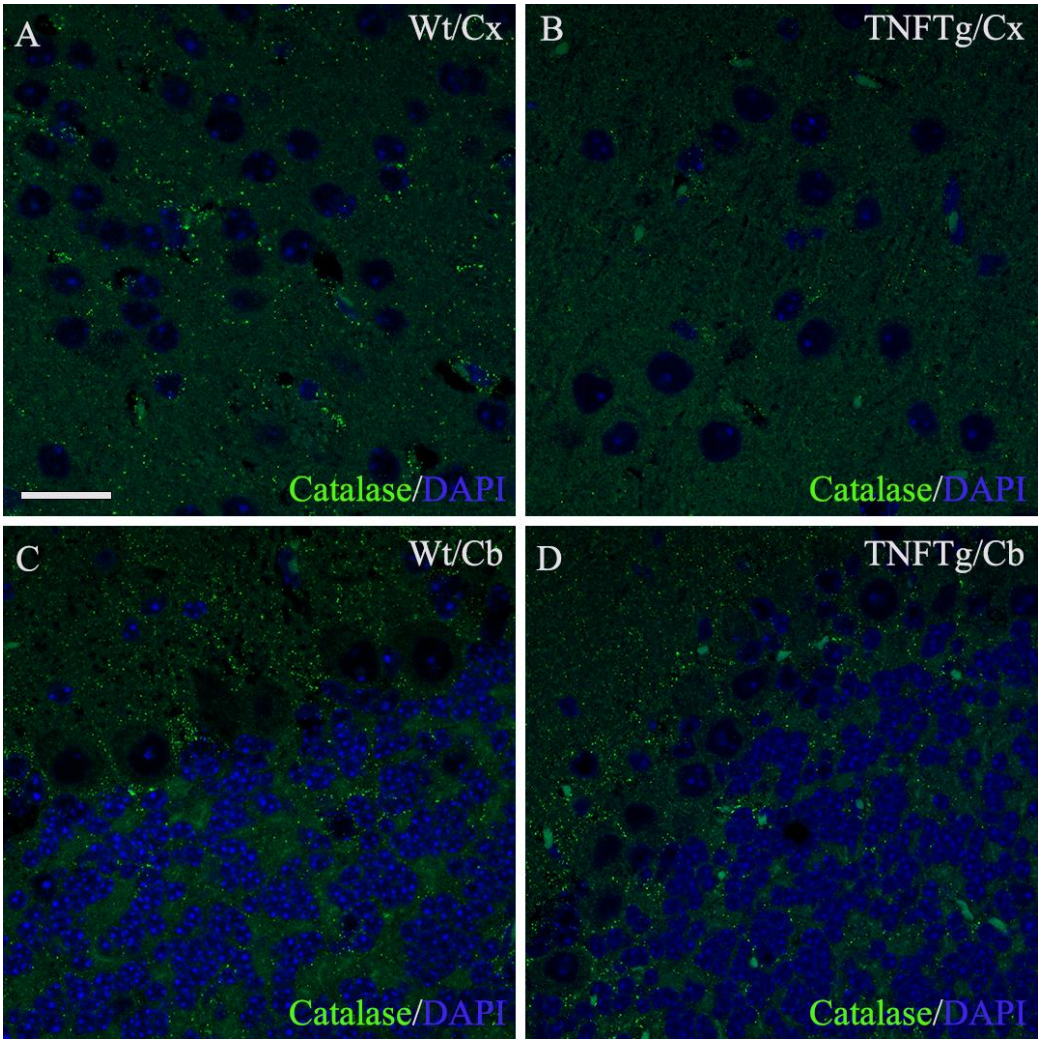

Photomicrographs of catalase-positive peroxisomes (green) in pyramidal neurons of the cerebral cortex (Cx) [**A**, Wt; **B**, TNFTg] and cerebellar (Cb) granule and Purkinje neurons [**C**, Wt; **D**, TNFTg]. Catalase abundance decreased in pyramidal neurons of the cerebral cortex, but not in cerebellar granule and Purkinje neurons of non-infected TNFTg mice. DAPI (blue) is the nuclear stain. ***Wt***, wild-type; ***TNFTg***; TNF transgenic. Scale bar: 20 μm for all images.

Figure 21: SOD2 abundance in pyramidal neurons (CA band) and granule neurons (DG) of non-infected Wt and TNFTg mice

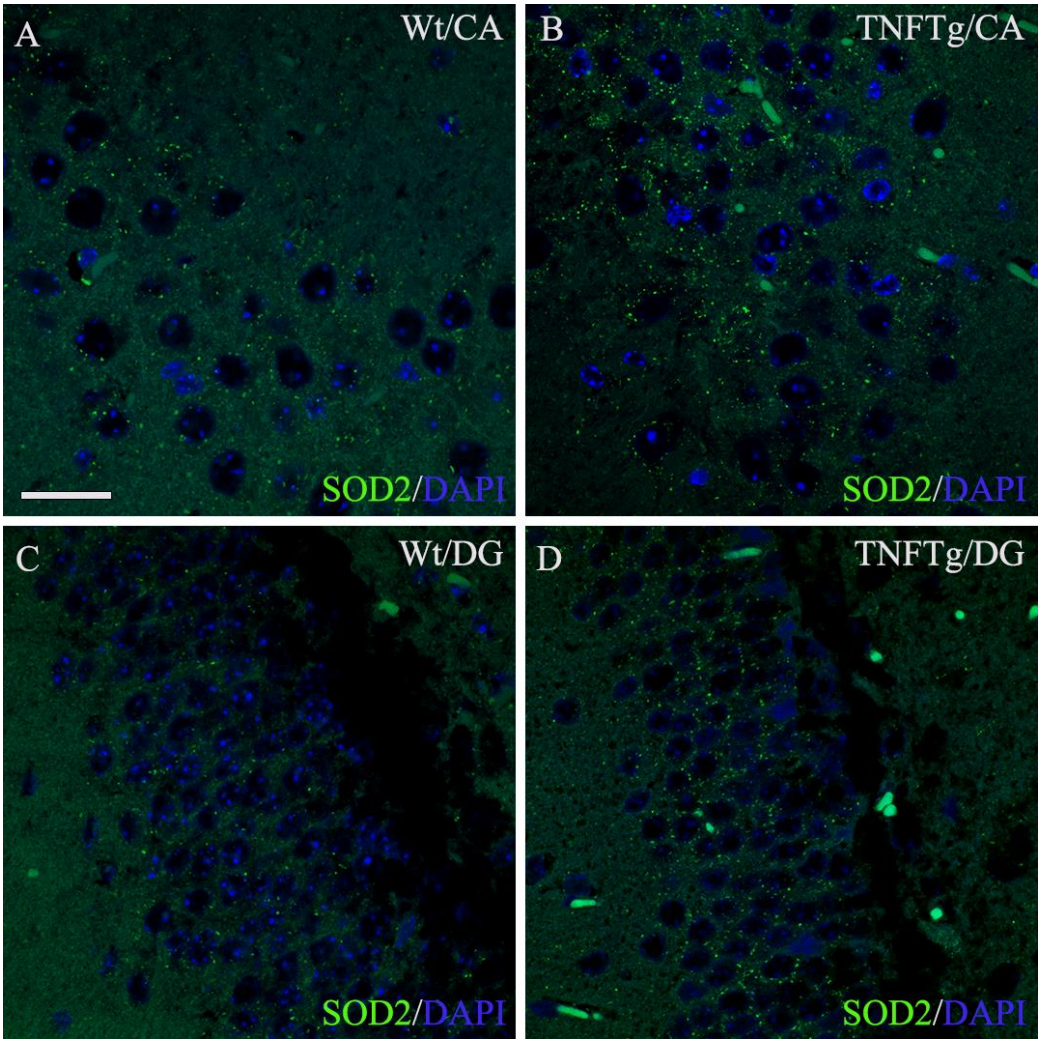

Photomicrographs of SOD2-positive mitochondria (green) in pyramidal neurons of the cornu ammonis (CA) band [**A**, Wt; **B**, TNFTg] and granule neurons of the dentate gyrus (DG) [**C**, Wt; **D**, TNFTg]. SOD2 abundance increased in pyramidal and granule neurons of the CA band and DG of non-infected TNFTg mice, respectively. DAPI (blue) is the nuclear stain. ***Wt***, wild-type; ***TNFTg***; TNF transgenic. Scale bar: 20 µm for all images.

Figure 22: SOD2 abundance in pyramidal neurons of the cerebral cortex, and cerebellar granule and Purkinje neurons of non-infected Wt and TNFTg mice

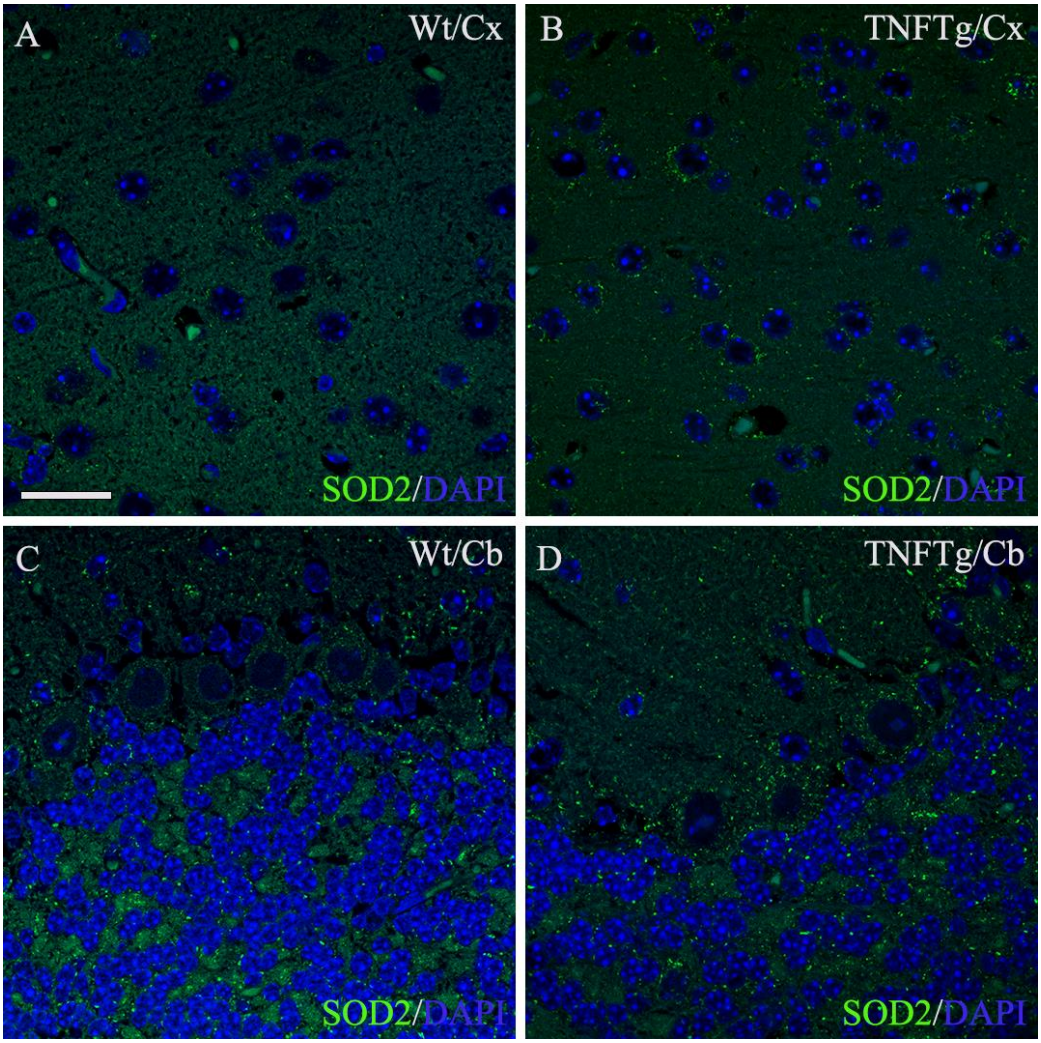

Photomicrographs of SOD2-positive mitochondria (green) in pyramidal neurons of the cerebral cortex (Cx) [**A**, Wt; **B**, TNFTg] and cerebellar (Cb) granule and Purkinje neurons [**C**, Wt; **D**, TNFTg]. No changes in SOD2 abundance in pyramidal neurons of the cerebral cortex as well as in cerebellar granule and Purkinje neurons of non-infected TNFTg mice. DAPI (blue) is the nuclear stain. ***Wt***, wild-type; ***TNFTg***; TNF transgenic. Scale bar: 20 µm for all images.

4.1.4 Morphometric analysis of peroxisomes and mitochondria in the hippocampus, cerebral and cerebellar cortices of non-infected TNFR1ko and TNFR2ko mice in comparison to non-infected Wt mice

In non-infected TNFR1ko mice, peroxisomal abundance was 29/100 µm^2 and 28/100 µm^2 in pyramidal (CA band) and granule (DG) neurons of the hippocampus, respectively; 18/100 µm^2 in cortical pyramidal neurons; 19/100 µm^2 in granule neurons and 25/100 µm^2 in Purkinje neurons of the cerebellar cortex (**Figure 39**A-E). In addition, mitochondrial abundance was 4.1% in pyramidal (CA band) and 1.7% in granule neurons of the hippocampus; 23.0% in cortical pyramidal neurons; 2.2% and 18.9% in cerebellar granule and Purkinje neurons, respectively (**Figure 40**A-E). Hence, peroxisomal (**Figures 23**A-D, **24**A-D, **39**A-E) and mitochondrial (**Figures 25**A-D, **26**A-D, **40**A-E) abundances in all neuronal cell types of non-infected TNFR1ko mice were comparable to those of non-infected Wt mice.

Furthermore, in non-infected TNFR2ko mice, peroxisomal abundance was 34/100 µm^2 and 38/100 µm^2 in pyramidal (CA band) and granule (DG) neurons of the hippocampus, respectively; 21/100 µm^2 in cortical pyramidal neurons; 26/100 µm^2 in granule neurons and 35/100 µm^2 in Purkinje neurons of the cerebellar cortex (**Figure 39**A-E). Consequently, non-infected TNFR2ko mice – unlike non-infected TNFR1ko mice – showed slightly higher peroxisomal abundance in all neuronal cell types [1.9-fold in pyramidal cells (CA band); 1.9-fold in granule cells (DG); 1.5-fold in pyramidal cells (cerebral cortex); 1.7-fold in granule cells and 2.1-fold in Purkinje cells (cerebellar cortex)] compared to same neuronal cell types of non-infected Wt mice (**Figures 27**A-D, **28**A-D, **39**A-E).

Mitochondrial abundance was 15.2% in pyramidal (CA band) and 11.7% in granule neurons of the hippocampus; 23.5% in cortical pyramidal neurons; 5.4% and 31.3% in cerebellar granule and Purkinje neurons, respectively (**Figure 40**A-E). In contrast to non-infected Wt mice, mitochondrial abundance was higher as well in most neuronal cell types of non-infected TNFR2ko mice [4.8-fold in pyramidal cells (CA band); 4.3-fold in granule cells (DG); 2.6-fold in pyramidal cells (cerebral cortex); 1.8-fold in Purkinje cells (cerebellar cortex)], except in granule cells of the cerebellar cortex (**Figures 29**A-D, **30**A-D, **40**A-E**)**.

Figure 23: Peroxisomal abundance in pyramidal neurons (CA band) and granule neurons (DG) of non-infected Wt and TNFR1ko mice

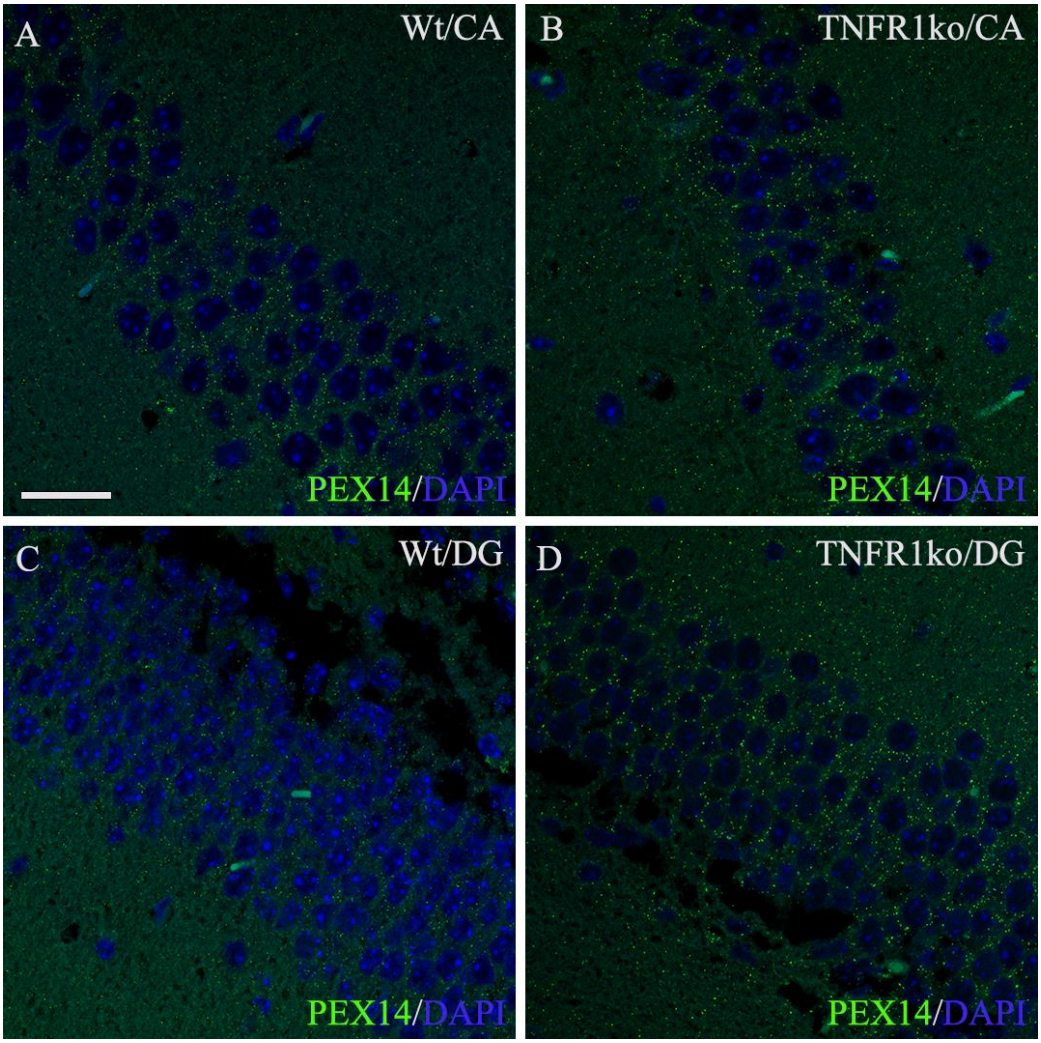

Photomicrographs of PEX14-positive peroxisomes (green) in pyramidal neurons of the cornu ammonis (CA) band [**A**, Wt; **B**, TNFR1ko] and granule neurons of the dentate gyrus (DG) [**C**, Wt; **D**, TNFR1ko]. No changes in peroxisomal abundance in pyramidal and granule neurons of the CA band and DG of non-infected TNFR1ko mice, respectively. DAPI (blue) is the nuclear stain. ***Wt***, wild-type; ***TNFR1ko***; TNF receptor 1 knockout. Scale bar: 20 µm for all images.

Figure 24: Peroxisomal abundance in pyramidal neurons of the cerebral cortex, and cerebellar granule and Purkinje neurons of non-infected Wt and TNFR1ko mice

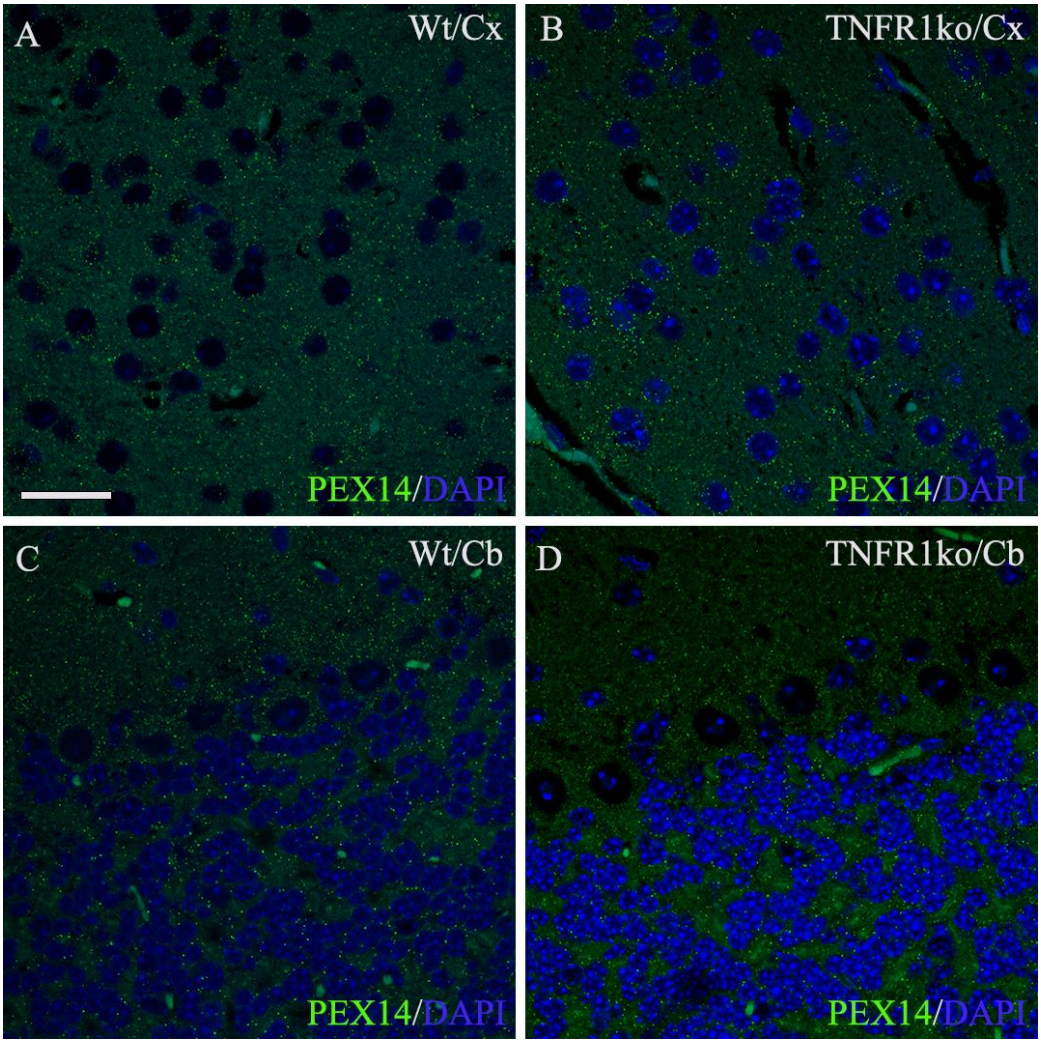

Photomicrographs of PEX14-positive peroxisomes (green) in pyramidal neurons of the cerebral cortex (Cx) [**A**, Wt; **B**, TNFR1ko] and cerebellar (Cb) granule and Purkinje neurons [**C**, Wt; **D**, TNFR1ko]. No changes in peroxisomal abundance in pyramidal neurons of the cerebral cortex, and in cerebellar granule and Purkinje neurons of non-infected TNFR1ko mice. DAPI (blue) is the nuclear stain. ***Wt***, wild-type; ***TNFR1ko***; TNF receptor 1 knockout. Scale bar: 20 µm for all images.

Figure 25: Mitochondrial abundance in pyramidal neurons (CA band) and granule neurons (DG) of non-infected Wt and TNFR1ko mice

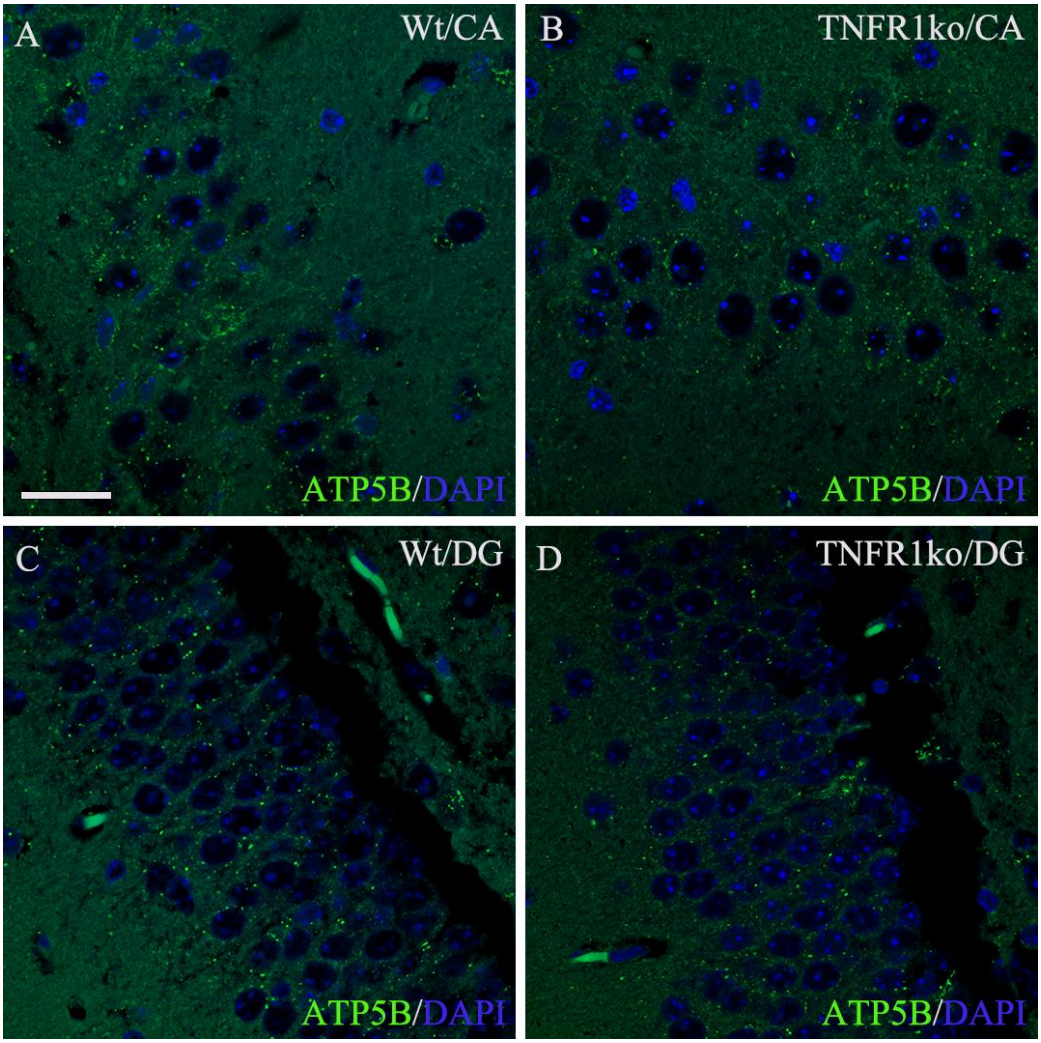

Photomicrographs of ATP5B-positive mitochondria (green) in pyramidal neurons of the cornu ammonis (CA) band [**A**, Wt; **B**, TNFR1ko] and granule neurons of the dentate gyrus (DG) [**C**, Wt; **D**, TNFR1ko]. No changes in mitochondrial abundance in pyramidal and granule neurons of the CA band and DG of non-infected TNFR1ko mice, respectively. DAPI (blue) is the nuclear stain. ***Wt***, wild-type; ***TNFR1ko***; TNF receptor 1 knockout. Scale bar: 20 µm for all images.

Figure 26: Mitochondrial abundance in pyramidal neurons of the cerebral cortex, and cerebellar granule and Purkinje neurons of non-infected Wt and TNFR1ko mice

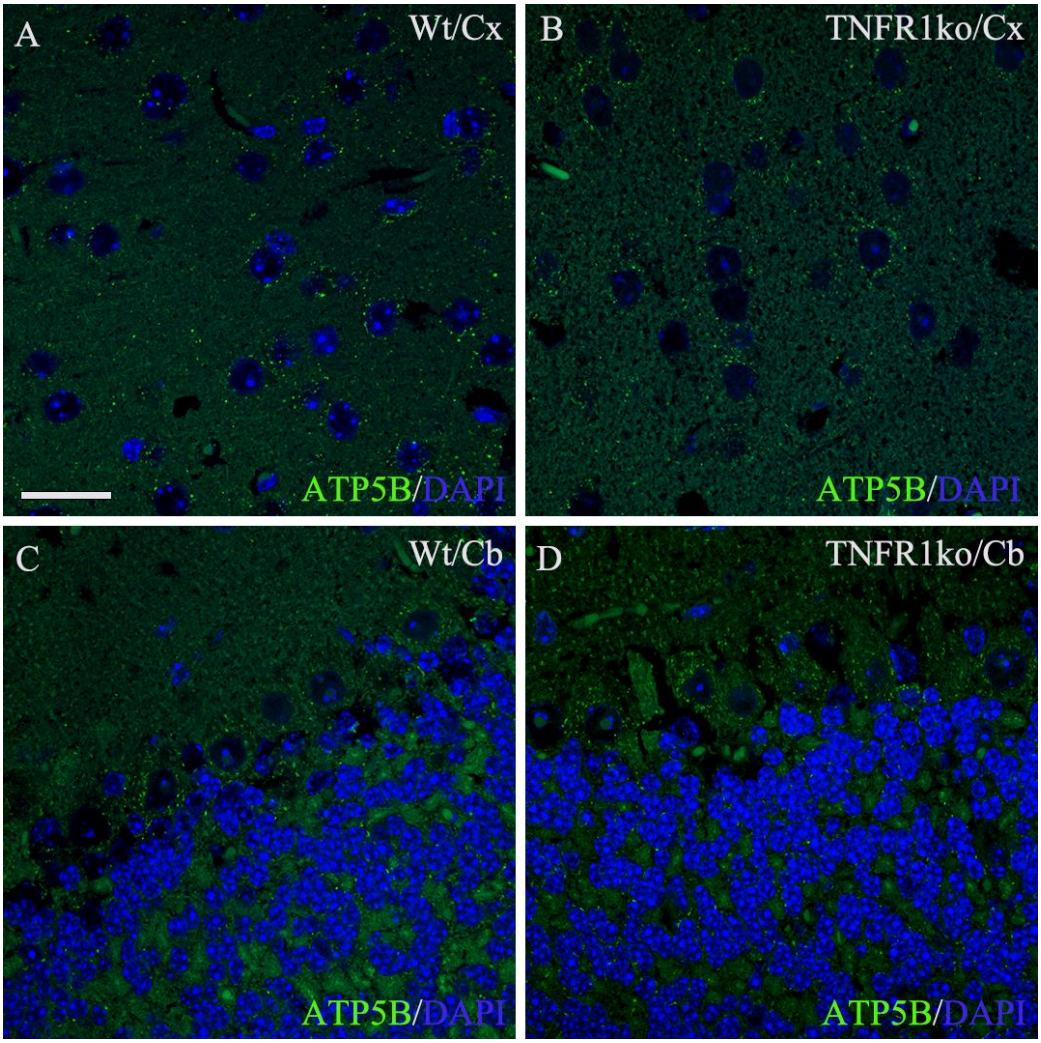

Photomicrographs of ATP5B-positive mitochondria (green) in pyramidal neurons of the cerebral cortex (Cx) [**A**, Wt; **B**, TNFR1ko] and cerebellar (Cb) granule and Purkinje neurons [**C**, Wt; **D**, TNFR1ko]. No changes in mitochondrial abundance in pyramidal neurons of the cerebral cortex as well as in cerebellar granule and Purkinje neurons of non-infected TNFR1ko mice. DAPI (blue) is the nuclear stain. ***Wt***, wild-type; ***TNFR1ko***; TNF receptor 1 knockout. Scale bar: 20 µm for all images.

Figure 27: Peroxisomal abundance in pyramidal neurons (CA band) and granule neurons (DG) of non-infected Wt and TNFR2ko mice

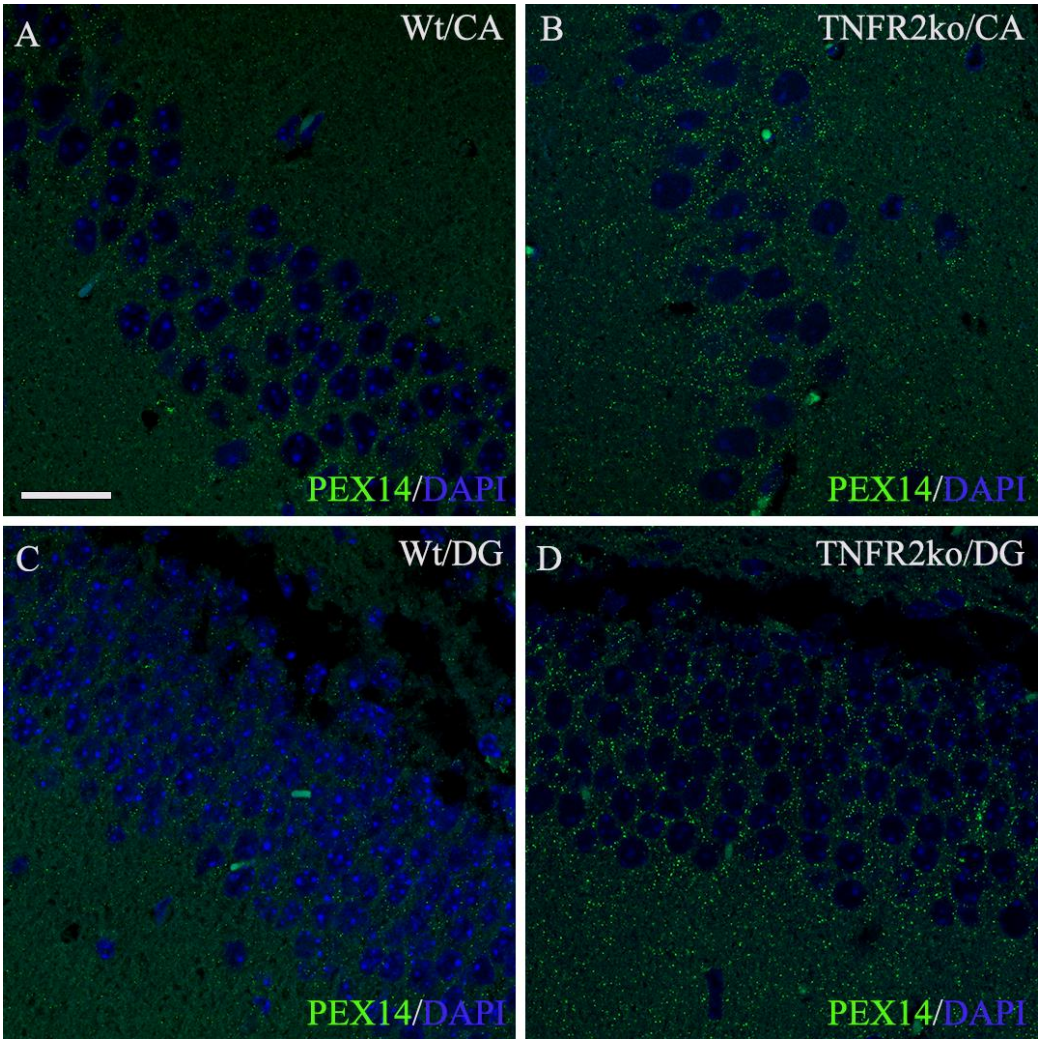

Photomicrographs of PEX14-positive peroxisomes (green) in pyramidal neurons of the cornu ammonis (CA) band [**A**, Wt; **B**, TNFR2ko] and granule neurons of the dentate gyrus (DG) [**C**, Wt; **D**, TNFR2ko]. Peroxisomal abundance increased in pyramidal and granule neurons of the CA band and DG of non-infected TNFR2ko mice, respectively. DAPI (blue) is the nuclear stain. ***Wt***, wild-type; ***TNFR2ko***; TNF receptor 2 knockout. Scale bar: 20 µm for all images.

Figure 28: Peroxisomal abundance in pyramidal neurons of the cerebral cortex, and cerebellar granule and Purkinje neurons of non-infected Wt and TNFR2ko mice

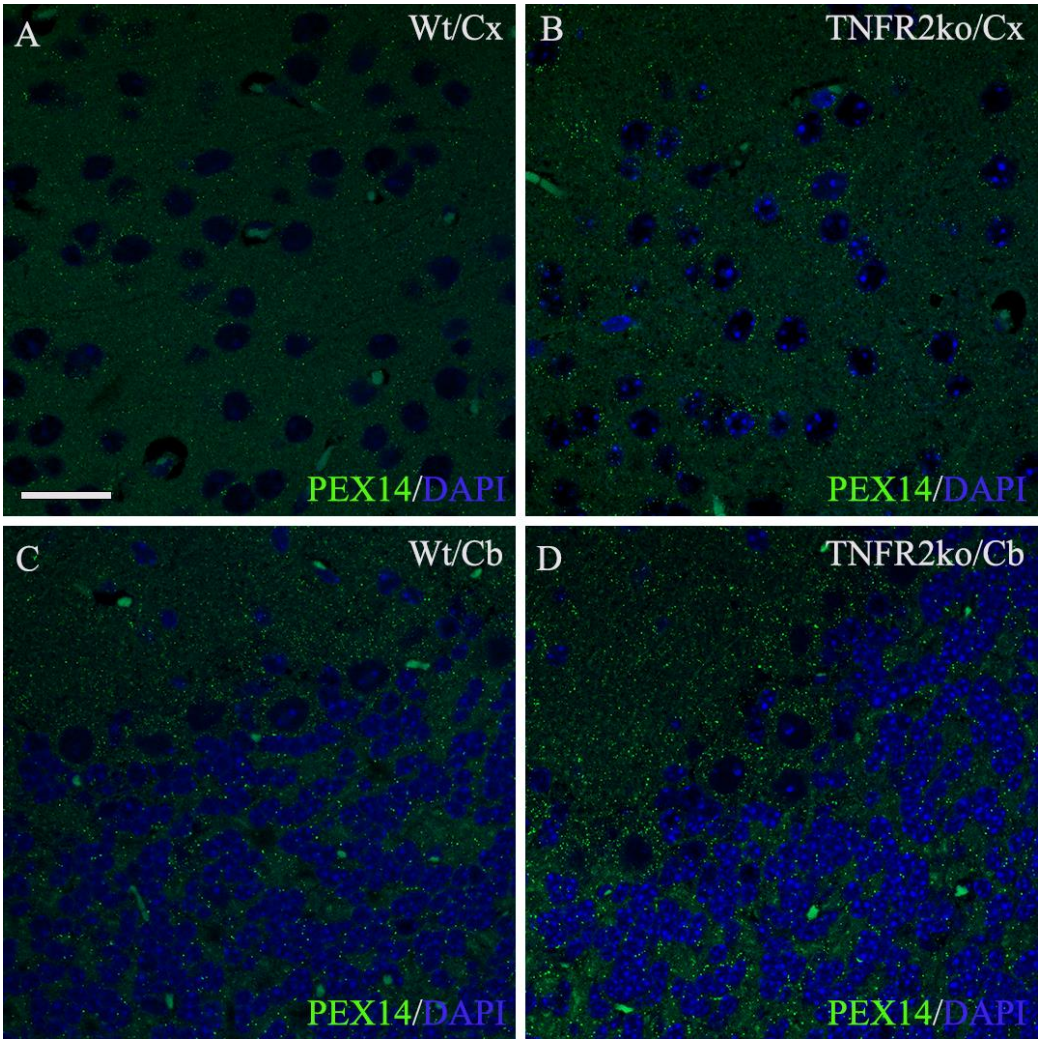

Photomicrographs of PEX14-positive peroxisomes (green) in pyramidal neurons of the cerebral cortex (Cx) [**A**, Wt; **B**, TNFR2ko] and cerebellar (Cb) granule and Purkinje neurons [**C**, Wt; **D**, TNFR2ko]. Peroxisomal abundance increased in pyramidal neurons of the cerebral cortex as well as in cerebellar granule and Purkinje neurons of non-infected TNFR2ko mice. DAPI (blue) is the nuclear stain. ***Wt***, wild-type; ***TNFR2ko***; TNF receptor 2 knockout. Scale bar: 20 µm for all images.

Figure 29: Mitochondrial abundance in pyramidal neurons (CA band) and granule neurons (DG) of non-infected Wt and TNFR2ko mice

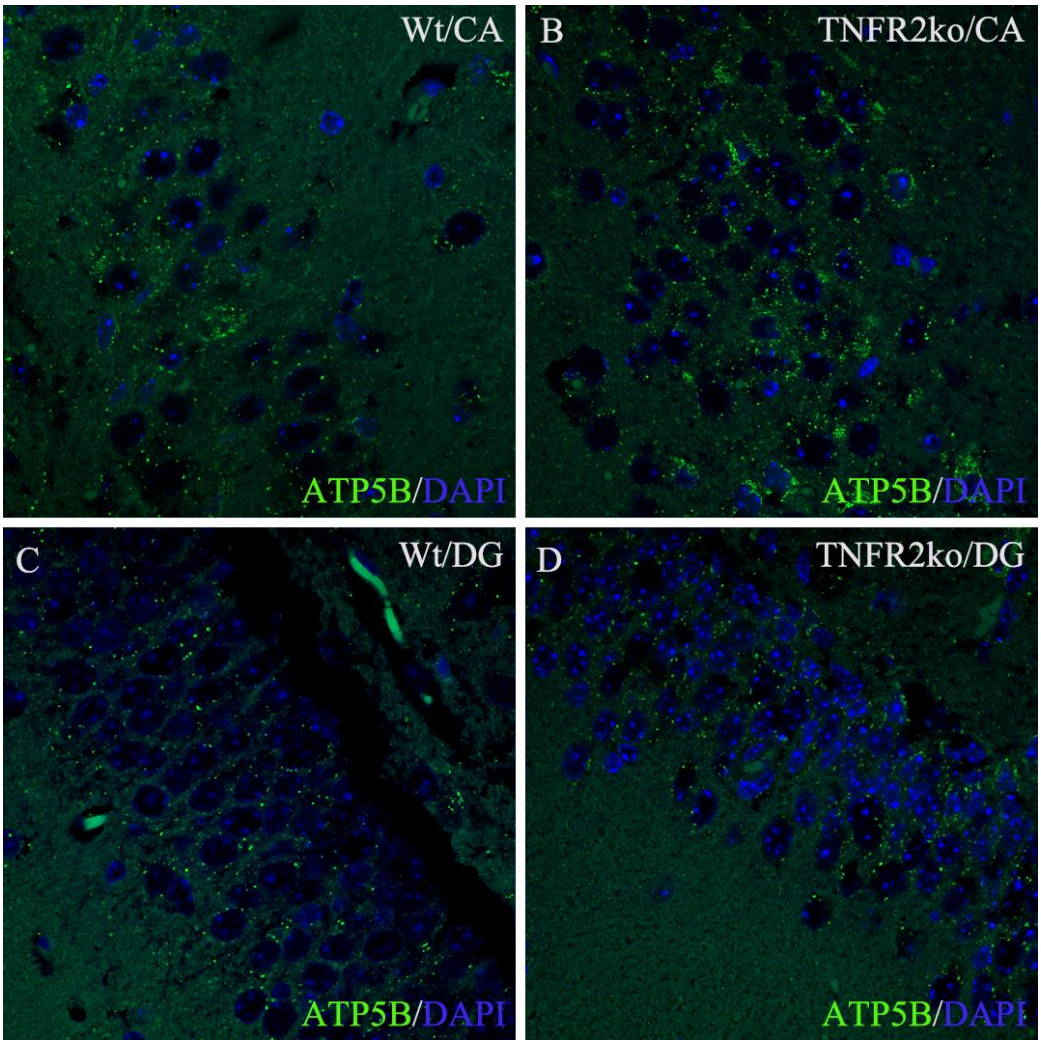

Photomicrographs of ATP5B-positive mitochondria (green) in pyramidal neurons of the cornu ammonis (CA) band [**A**, Wt; **B**, TNFR2ko] and granule neurons of the dentate gyrus (DG) [**C**, Wt; **D**, TNFR2ko]. Mitochondrial abundance increased in pyramidal and granule neurons of the CA band and DG of non-infected TNFR2ko mice, respectively. DAPI (blue) is the nuclear stain. ***Wt***, wild-type; ***TNFR2ko***; TNF receptor 2 knockout. Scale bar: 20 µm for all images.

Figure 30: Mitochondrial abundance in pyramidal neurons of the cerebral cortex, and cerebellar granule and Purkinje neurons of non-infected Wt and TNFR2ko mice

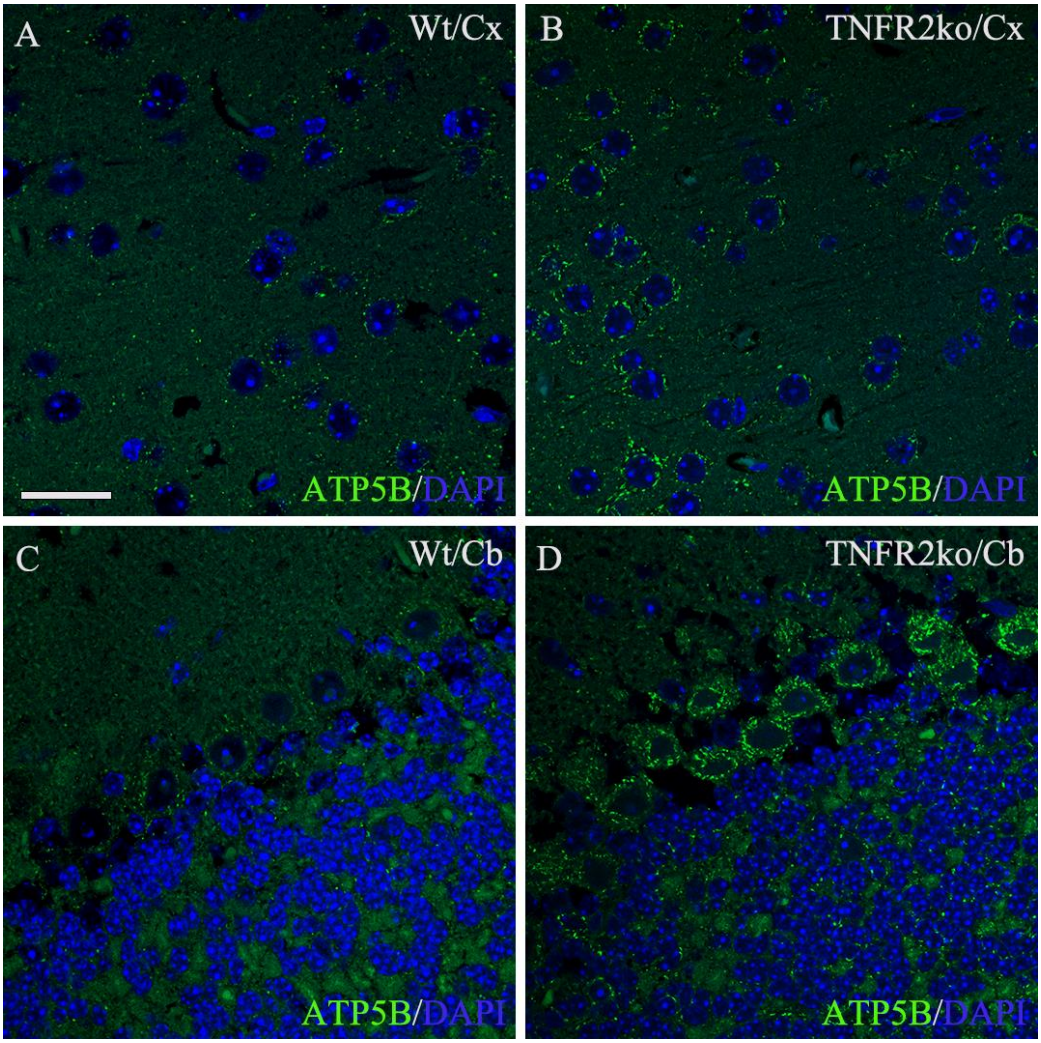

Photomicrographs of ATP5B-positive mitochondria (green) in pyramidal neurons of the cerebral cortex (Cx) [**A**, Wt; **B**, TNFR2ko] and cerebellar (Cb) granule and Purkinje neurons [**C**, Wt; **D**, TNFR2ko]. Mitochondrial abundance increased in pyramidal neurons of the cerebral cortex, and in cerebellar granule and Purkinje neurons of non-infected TNFR2ko mice. DAPI (blue) is the nuclear stain. ***Wt***, wild-type; ***TNFR2ko***; TNF receptor 2 knockout. Scale bar: 20 µm for all images.

4.1.5 Morphometric analysis of catalase and SOD2 in the hippocampus, cerebral and cerebellar cortices of non-infected TNFR1ko and TNFR2ko mice in comparison to non-infected Wt mice

In non-infected TNFR1ko mice, catalase abundance was 13/100 µm^2 and 16/100 µm^2 in pyramidal (CA band) and granule (DG) neurons of the hippocampus, respectively; 5/100 µm^2 in cortical pyramidal neurons; 7/100 µm^2 in granule neurons and 9/100 µm^2 in Purkinje neurons of the cerebellar cortex (**Figure 41**A-E). SOD2 abundance was 0.5% in pyramidal (CA band) and 0.4% in granule neurons of the hippocampus; 0.5% in cortical pyramidal neurons; 0.4% and 0.7% in cerebellar granule and Purkinje neurons, respectively (**Figure 42**A-E). Similar to the organelle abundances, catalase (**Figures 31**A-D, **32**A-D, **41**A-E) and SOD2 (**Figures 33**A-D, **34**A-D, **42**A-E) abundances in all neuronal cell types of non-infected TNFR1ko mice were comparable to those of non-infected Wt mice.

Concerning catalase abundance in non-infected TNFR2ko mice, 15/100 µm^2 was found in pyramidal neurons (CA band) and 18/100 µm^2 in granule neurons (DG) of the hippocampus; 6/100 µm^2 in cortical pyramidal neurons; 10/100 µm^2 and 12/100 µm^2 in cerebellar granule and Purkinje neurons, respectively (**Figure 41**A-E). SOD2 abundance was 1.0% in pyramidal (CA band) and 0.4% in granule neurons of the hippocampus; 0.6% in cortical pyramidal neurons; 0.3% and 0.9% in cerebellar granule and Purkinje neurons, respectively (**Figure 42**A-E). Despite the higher peroxisomal and mitochondrial abundances in non-infected TNFR2ko mice, there were no significant changes in catalase (**Figures 35**A-D, **36**A-D, **41**A-E) and SOD2 (**Figures 37**A-D, **38**A-D, **42**A-E) abundances in contrast to non-infected Wt mice.

Figure 31: Catalase abundance in pyramidal neurons (CA band) and granule neurons (DG) of non-infected Wt and TNFR1ko mice

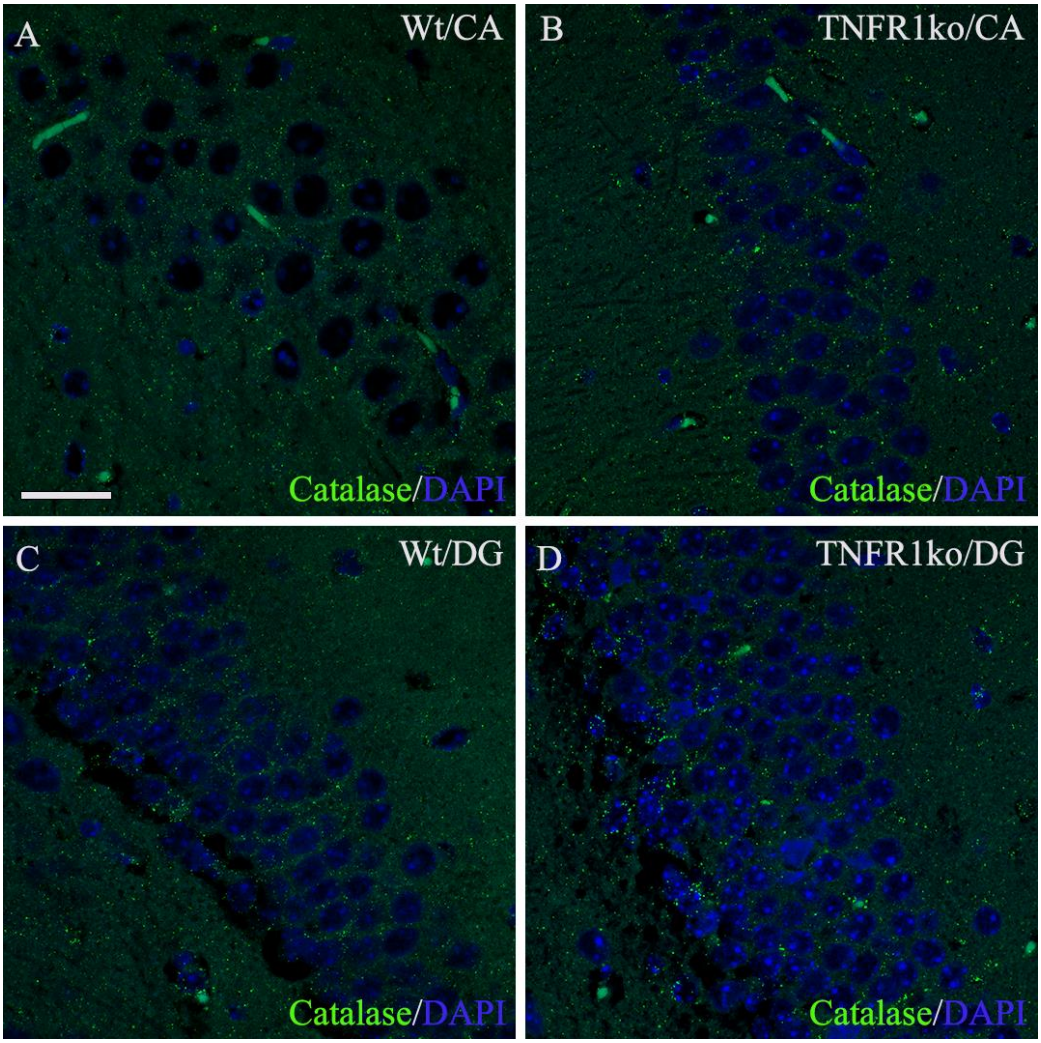

Photomicrographs of catalase-positive peroxisomes (green) in pyramidal neurons of the cornu ammonis (CA) band [**A**, Wt; **B**, TNFR1ko] and granule neurons of the dentate gyrus (DG) [**C**, Wt; **D**, TNFR1ko]. No changes in catalase abundance in pyramidal and granule neurons of the CA band and DG of non-infected TNFR1ko mice, respectively. DAPI (blue) is the nuclear stain. ***Wt***, wild-type; ***TNFR1ko***; TNF receptor 1 knockout. Scale bar: 20 µm for all images.

Figure 32: Catalase abundance in pyramidal neurons of the cerebral cortex, and cerebellar granule and Purkinje neurons of non-infected Wt and TNFR1ko mice

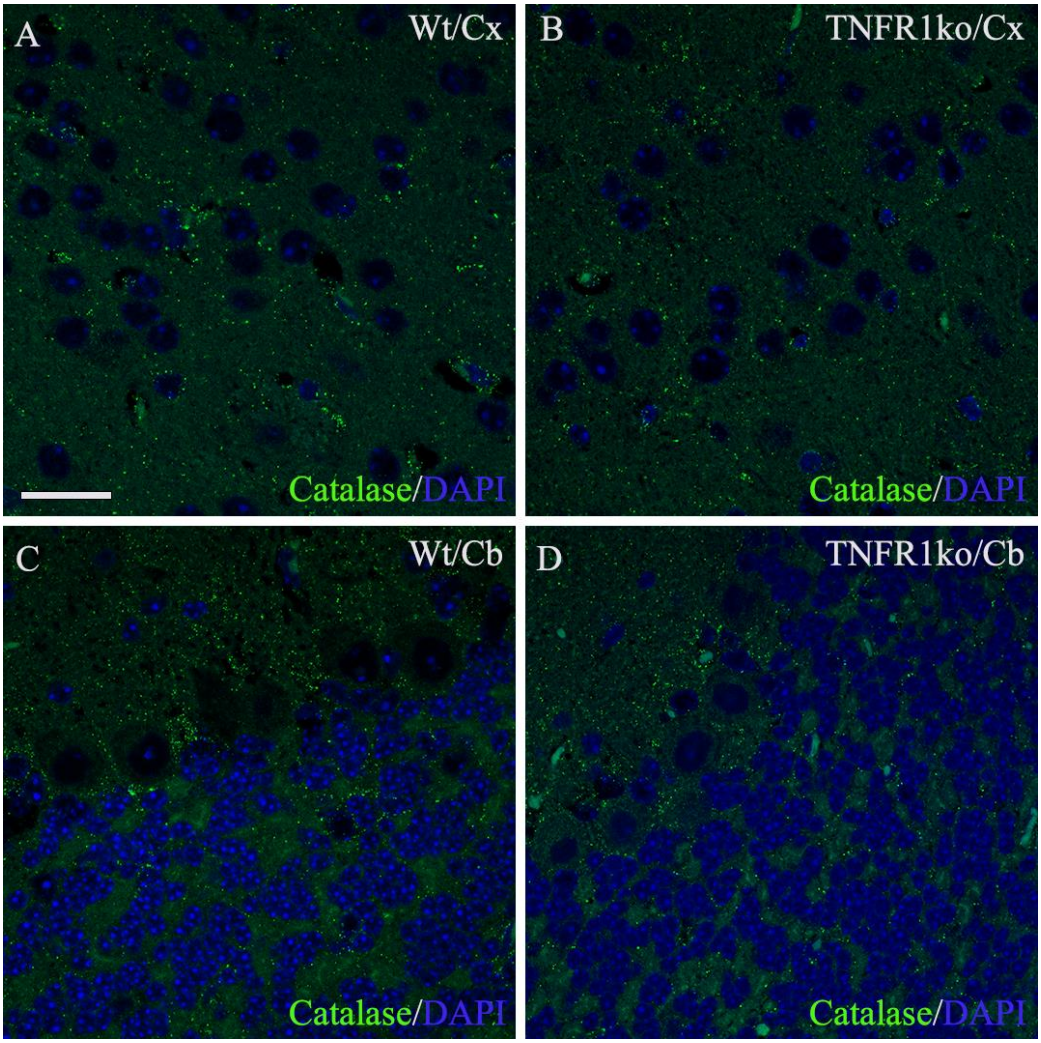

Photomicrographs of catalase-positive peroxisomes (green) in pyramidal neurons of the cerebral cortex (Cx) [**A**, Wt; **B**, TNFR1ko] and cerebellar (Cb) granule and Purkinje neurons [**C**, Wt; **D**, TNFR1ko]. No changes in catalase abundance in pyramidal neurons of the cerebral cortex, and in cerebellar granule and Purkinje neurons of non-infected TNFR1ko mice. DAPI (blue) is the nuclear stain. ***Wt***, wild-type; ***TNFR1ko***; TNF receptor 1 knockout. Scale bar: 20 µm for all images.

Figure 33: SOD2 abundance in pyramidal neurons (CA band) and granule neurons (DG) of non-infected Wt and TNFR1ko mice

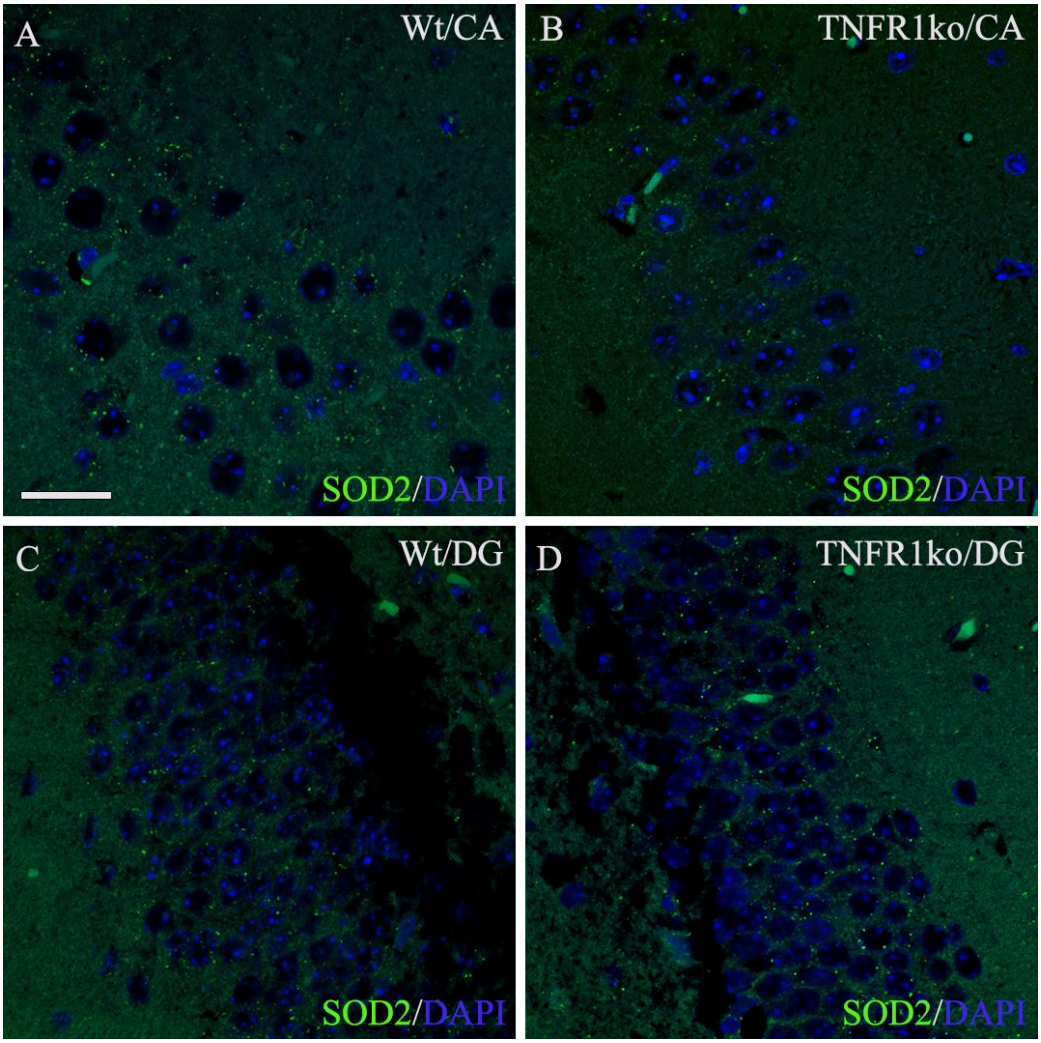

Photomicrographs of SOD2-positive mitochondria (green) in pyramidal neurons of the cornu ammonis (CA) band [**A**, Wt; **B**, TNFR1ko] and granule neurons of the dentate gyrus (DG) [**C**, Wt; **D**, TNFR1ko]. No changes in SOD2 abundance in pyramidal and granule neurons of the CA band and DG of non-infected TNFR1ko mice, respectively. DAPI (blue) is the nuclear stain. ***Wt***, wild-type; ***TNFR1ko***; TNF receptor 1 knockout. Scale bar: 20 µm for all images.

Figure 34: SOD2 abundance in pyramidal neurons of the cerebral cortex, and cerebellar granule and Purkinje neurons of non-infected Wt and TNFR1ko mice

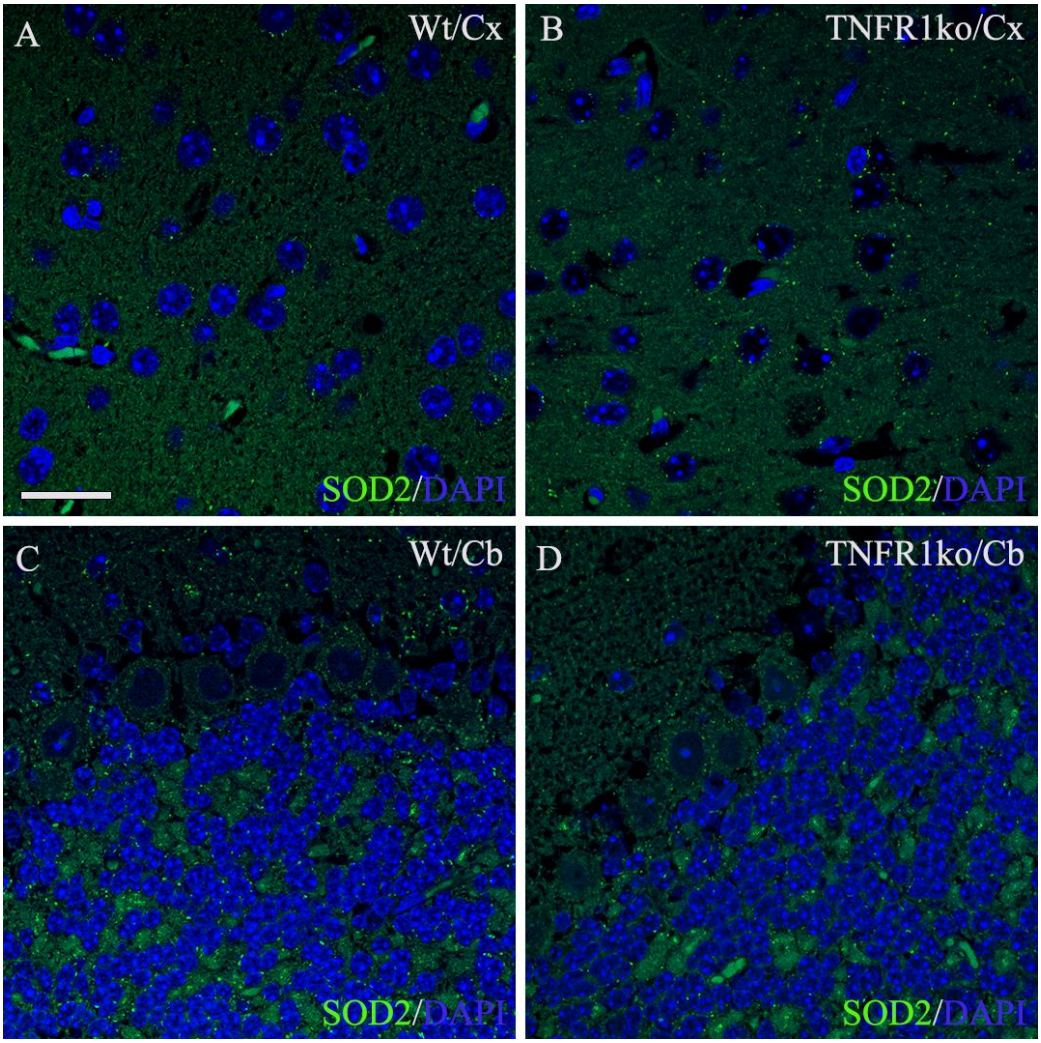

Photomicrographs of SOD2-positive mitochondria (green) in pyramidal neurons of the cerebral cortex (Cx) [**A**, Wt; **B**, TNFR1ko] and cerebellar (Cb) granule and Purkinje neurons [**C**, Wt; **D**, TNFR1ko]. No changes in SOD2 abundance in pyramidal neurons of the cerebral cortex as well as in cerebellar granule and Purkinje neurons of non-infected TNFR1ko mice. DAPI (blue) is the nuclear stain. ***Wt***, wild-type; ***TNFR1ko***; TNF receptor 1 knockout. Scale bar: 20 µm for all images.

Figure 35: Catalase abundance in pyramidal neurons (CA band) and granule neurons (DG) of non-infected Wt and TNFR2ko mice

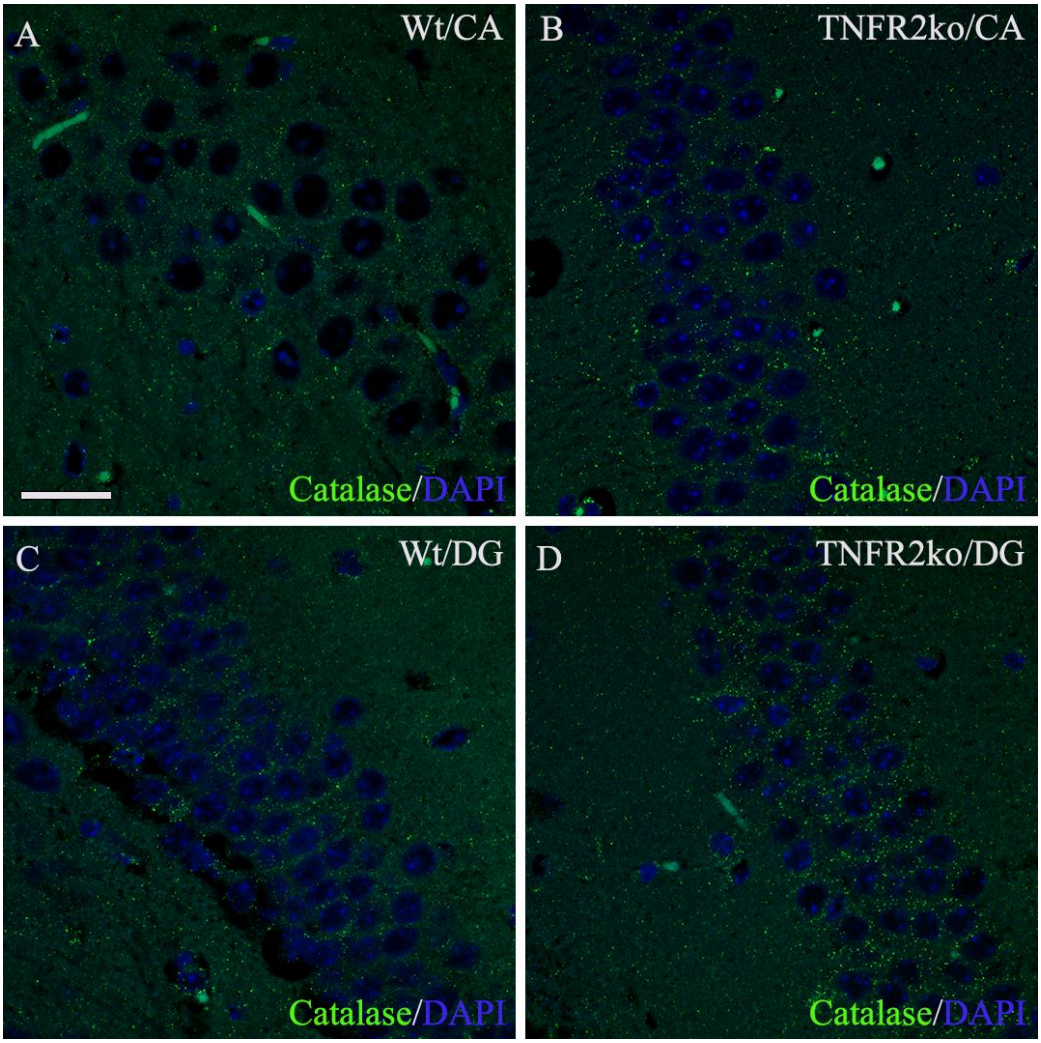

Photomicrographs of catalase-positive peroxisomes (green) in pyramidal neurons of the cornu ammonis (CA) band [**A**, Wt; **B**, TNFR2ko] and granule neurons of the dentate gyrus (DG) [**C**, Wt; **D**, TNFR2ko]. No changes in catalase abundance in pyramidal and granule neurons of the CA band and DG of non-infected TNFR2ko mice, respectively. DAPI (blue) is the nuclear stain. ***Wt***, wild-type; ***TNFR2ko***; TNF receptor 2 knockout. Scale bar: 20 µm for all images.

Figure 36: Catalase abundance in pyramidal neurons of the cerebral cortex, and cerebellar granule and Purkinje neurons of non-infected Wt and TNFR2ko mice

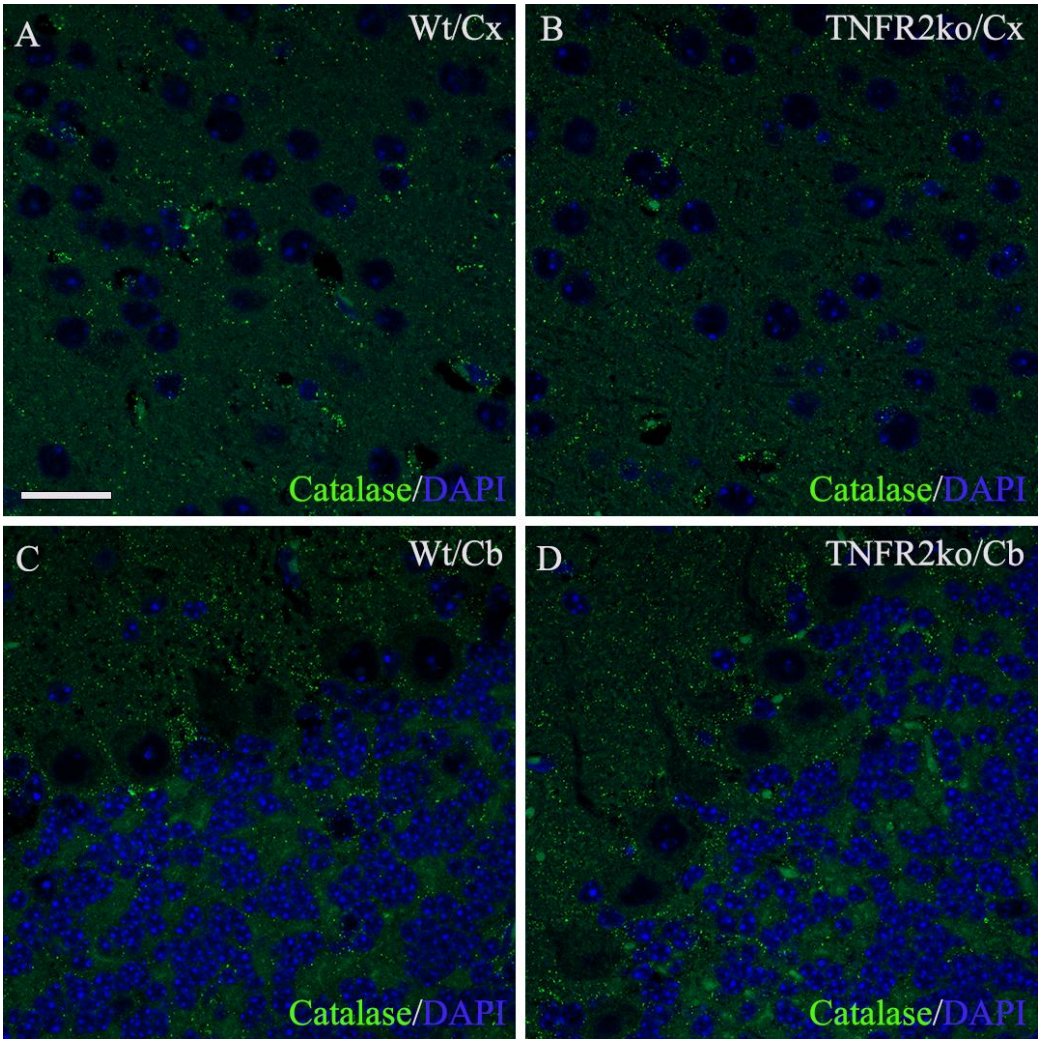

Photomicrographs of catalase-positive peroxisomes (green) in pyramidal neurons of the cerebral cortex (Cx) [**A**, Wt; **B**, TNFR2ko] and cerebellar (Cb) granule and Purkinje neurons [**C**, Wt; **D**, TNFR2ko]. No changes in catalase abundance in pyramidal neurons of the cerebral cortex, and in cerebellar granule and Purkinje neurons of non-infected TNFR2ko mice. DAPI (blue) is the nuclear stain. ***Wt***, wild-type; ***TNFR2ko***; TNF receptor 2 knockout. Scale bar: 20 µm for all images.

Figure 37: SOD2 abundance in pyramidal neurons (CA band) and granule neurons (DG) of non-infected Wt and TNFR2ko mice

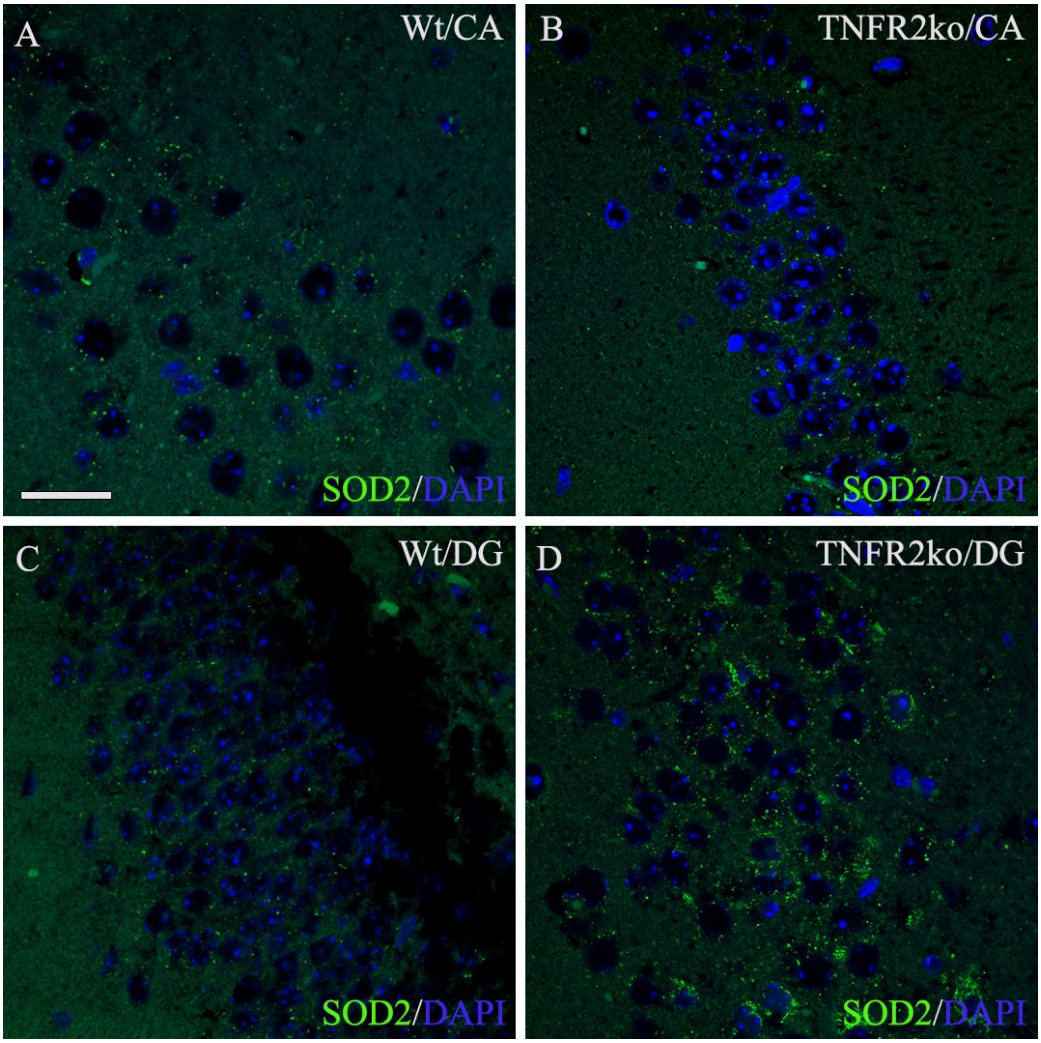

Photomicrographs of SOD2-positive mitochondria (green) in pyramidal neurons of the cornu ammonis (CA) band [**A**, Wt; **B**, TNFR2ko] and granule neurons of the dentate gyrus (DG) [**C**, Wt; **D**, TNFR2ko]. No changes in SOD2 abundance in pyramidal and granule neurons of the CA band and DG of non-infected TNFR2ko mice, respectively. DAPI (blue) is the nuclear stain. ***Wt***, wild-type; ***TNFR2ko***; TNF receptor 2 knockout. Scale bar: 20 µm for all images.

Figure 38: SOD2 abundance in pyramidal neurons of the cerebral cortex, and cerebellar granule and Purkinje neurons of non-infected Wt and TNFR2ko mice

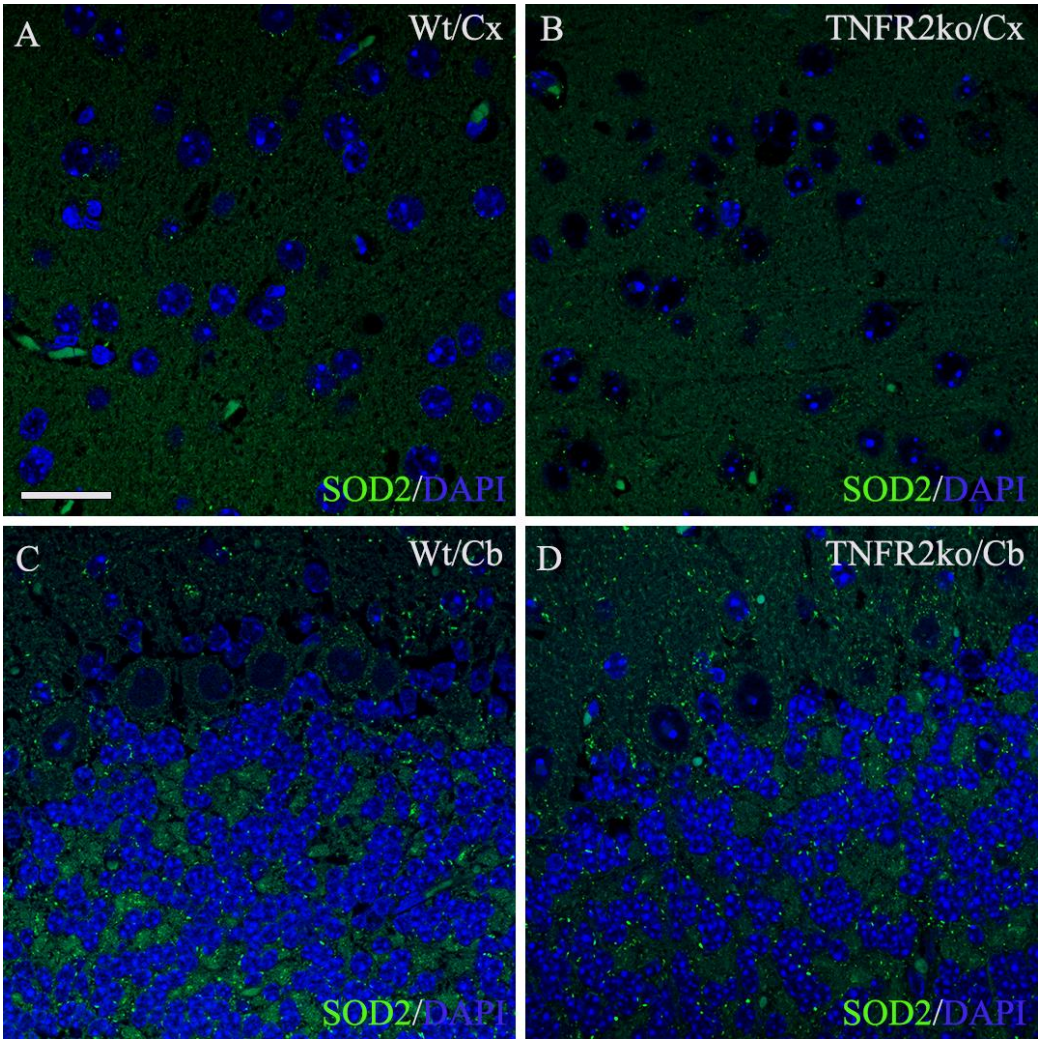

Photomicrographs of SOD2-positive mitochondria (green) in pyramidal neurons of the cerebral cortex (Cx) [**A**, Wt; **B**, TNFR2ko] and cerebellar (Cb) granule and Purkinje neurons [**C**, Wt; **D**, TNFR2ko]. No changes in SOD2 abundance in pyramidal neurons of the cerebral cortex as well as in cerebellar granule and Purkinje neurons of non-infected TNFR2ko mice. DAPI (blue) is the nuclear stain. ***Wt***, wild-type; ***TNFR2ko***; TNF receptor 2 knockout. Scale bar: 20 µm for all images.

Figure 39: One-way ANOVA comparison of peroxisomal abundances in different brain regions of non-infected mice

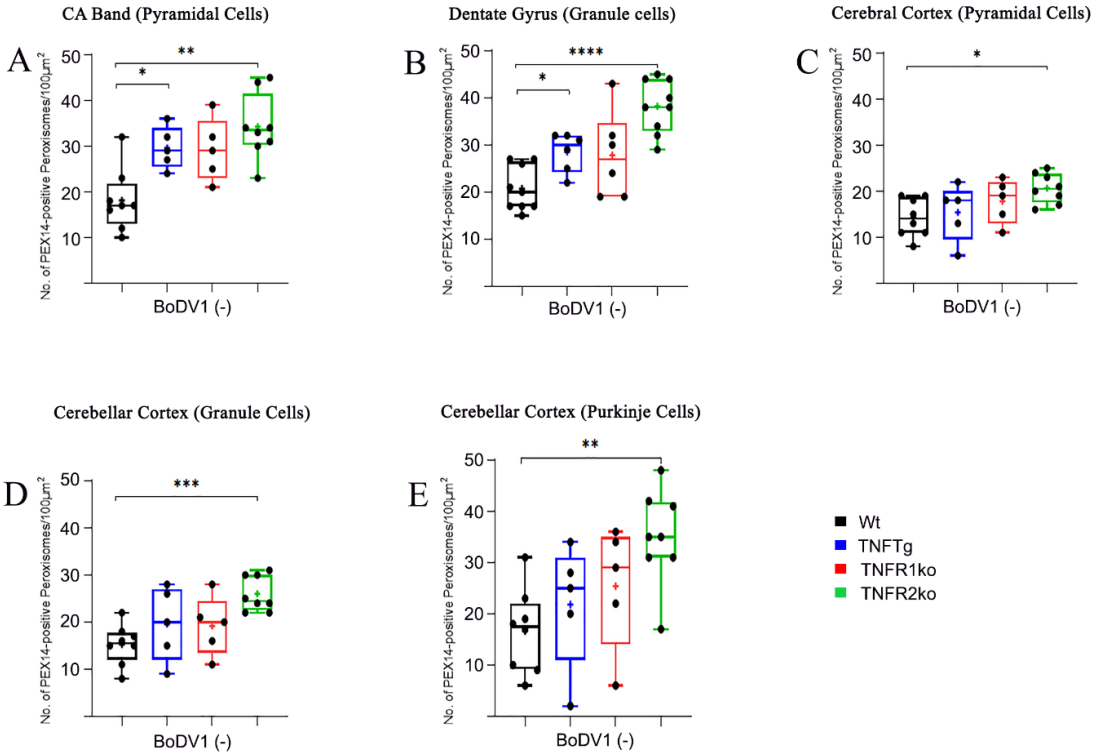

PEX14-positive peroxisomes in the hippocampus, cerebral and cerebellar cortices of non-infected mice of each mouse line [i.e. Wt (black), TNFTg (blue), TNFR1ko (red) and TNFR2ko (green) mice] (**A**-**E**). Peroxisomal abundance increased in most TNF-α transgenic brain areas of non-infected TNFTg mice, and in all brain areas of non-infected TNFR2ko mice. ***Wt***, wild-type; ***TNFTg***, TNF transgenic; ***TNFR1ko***, TNF receptor 1 knockout; ***TNFR2ko***, TNF receptor 2 knockout; ***BoDV1(-)***, without BoDV1 infection. P-values: 0.01–0.05 (*); 0.001–0.01 (**); 0.0001–0.001 (***); < 0.0001 (****).

Figure 40: One-way ANOVA comparison of mitochondrial abundances in different brain regions of non-infected mice

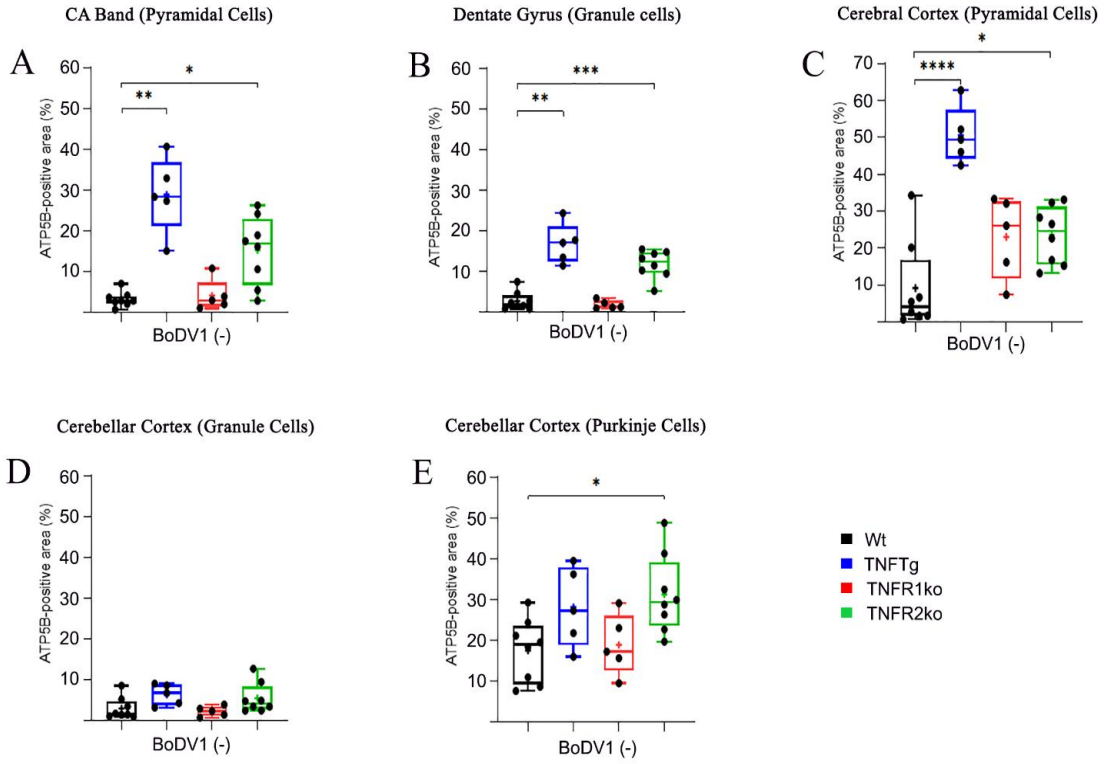

ATP5B-positive mitochondria in the hippocampus, cerebral and cerebellar cortices of non-infected mice of each mouse line [i.e. Wt (black), TNFTg (blue), TNFR1ko (red) and TNFR2ko (green) mice] (**A**-**E**). Mitochondrial abundance increased in all TNF-α transgenic brain areas of non-infected TNFTg mice, and in all brain areas of non-infected TNFR2ko mice. ***Wt***, wild-type; ***TNFTg***, TNF transgenic; ***TNFR1ko***, TNF receptor 1 knockout; ***TNFR2ko***, TNF receptor 2 knockout; ***BoDV1(-)***, without BoDV1 infection. P-values: 0.01–0.05 (*); 0.001–0.01 (**); 0.0001–0.001 (***); < 0.0001 (****).

Figure 41: One-way ANOVA comparison of catalase abundances in different brain regions of non-infected mice

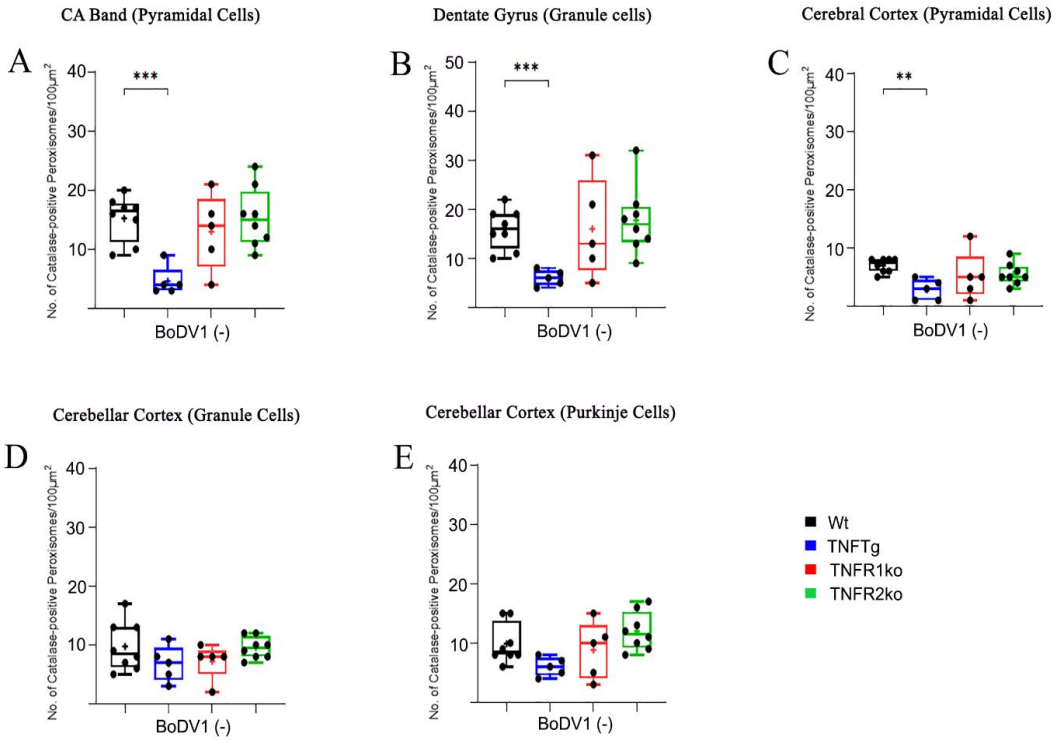

Catalase-positive peroxisomes in the hippocampus, cerebral and cerebellar cortices of non-infected mice of each mouse line [i.e. Wt (black), TNFTg (blue), TNFR1ko (red) and TNFR2ko (green) mice] (**A**-**E**). Catalase abundance decreased in all TNF-α transgenic brain areas (not in the cerebellum) of non-infected TNFTg mice, but no changes in non-infected TNFR2ko mice. ***Wt***, wild-type; ***TNFTg***, TNF transgenic; ***TNFR1ko***, TNF receptor 1 knockout; ***TNFR2ko***, TNF receptor 2 knockout; ***BoDV1(-)***, without BoDV1 infection. P-values: 0.001–0.01 (**); 0.0001–0.001 (***).

Figure 42: One-way ANOVA comparison of SOD2 abundances in different brain regions of non-infected mice

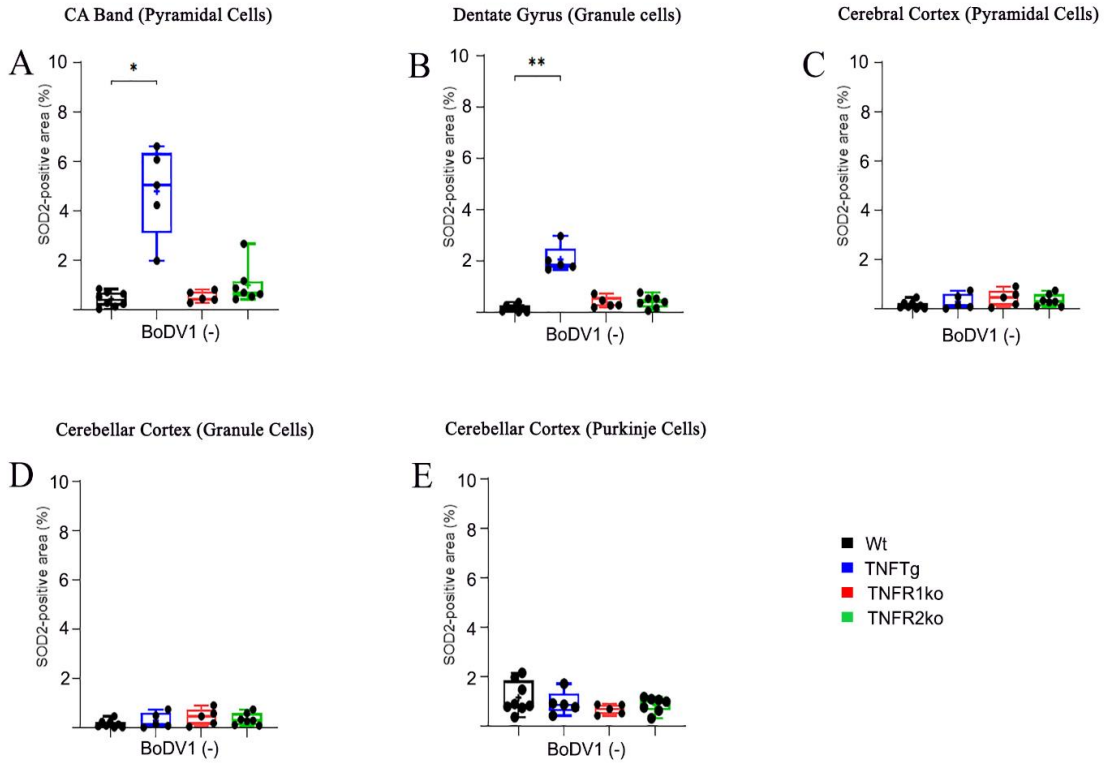

SOD2-positive mitochondria in the hippocampus, cerebral and cerebellar cortices of non-infected mice of each mouse line [i.e. Wt (black), TNFTg (blue), TNFR1ko (red) and TNFR2ko (green) mice] (**A**-**E**). SOD2 abundance increased mainly in the hippocampus of non-infected TNFTg mice, but no changes in non-infected TNFR2ko mice. ***Wt***, wild-type; ***TNFTg***, TNF transgenic; ***TNFR1ko***, TNF receptor 1 knockout; ***TNFR2ko***, TNF receptor 2 knockout; ***BoDV1(-)***, without BoDV1 infection. P-values: 0.01–0.05 (*); 0.001–0.01 (**).

4.2 Morphometric analysis of peroxisomes, mitochondria, catalase and SOD2 in the hippocampus, cerebral and cerebellar cortices of BoDV1-infected mice

Using Welch's t-test, the abundances of peroxisomes, mitochondria, catalase and SOD2 in several neuronal cell types of non-infected mice of each mouse line (which served as controls) were compared to same cell types of BoDV1-infected mice belonging to the same mouse line (**Table 2**). Moreover, using one-way ANOVA, the differences in abundances between the BoDV1-infected mouse lines analyzed (see **Appendices 1**-**4**).

4.2.1 Morphometric analysis of peroxisomes and mitochondria in the hippocampus, cerebral and cerebellar cortices of BoDV1-infected Wt mice

Following BoDV1 infection of Wt mice, peroxisomal abundance was 26/100 µm^2 in pyramidal (CA band) neurons and 27/100 µm^2 in granule neurons (DG) of the hippocampus; 22/100 µm^2 in cortical pyramidal neurons; 22/100 µm^2 and 26/100 µm^2 in cerebellar granule and Purkinje neurons, respectively (see **Appendix 1**A-E). This shows that peroxisomal abundance increased slightly in all neuronal cell types [1.4-fold in pyramidal cells (CA band); 1.3-fold in granule cells (DG); 1.6-fold in pyramidal cells (cerebral cortex); 1.5-fold in granule and 1.5-fold in Purkinje cells (cerebellar cortex)] after BoDV1 infection (**Figures 43**A,B, **44**A,B, **45**A,B, **46**A,B; **Table 2**). Furthermore, mitochondrial abundance in BoDV1-infected Wt mice was 1.5% in pyramidal (CA band) neurons and 1.0% in granule neurons (DG) of the hippocampus; 3.6% in cortical pyramidal neurons; 0.7% and 4.6% in cerebellar granule and Purkinje neurons, respectively (see **Appendix 2**A-E). Here, mitochondrial abundance decreased significantly in most neuronal cell types [2.1-fold in pyramidal cells (CA band); 4.3-fold in granule cells and 3.8-fold in Purkinje cells (cerebellar cortex)] but not in granule cells of the DG and pyramidal cells of the cerebral cortex after BoDV1 infection of Wt mice (**Figures 43**C,D, **44**C,D, **45**C,D, **46**C,D; **Table 2**).

Figure 43: Peroxisomal and mitochondrial abundances in pyramidal neurons (CA band) of non- and BoDV1-infected Wt mice

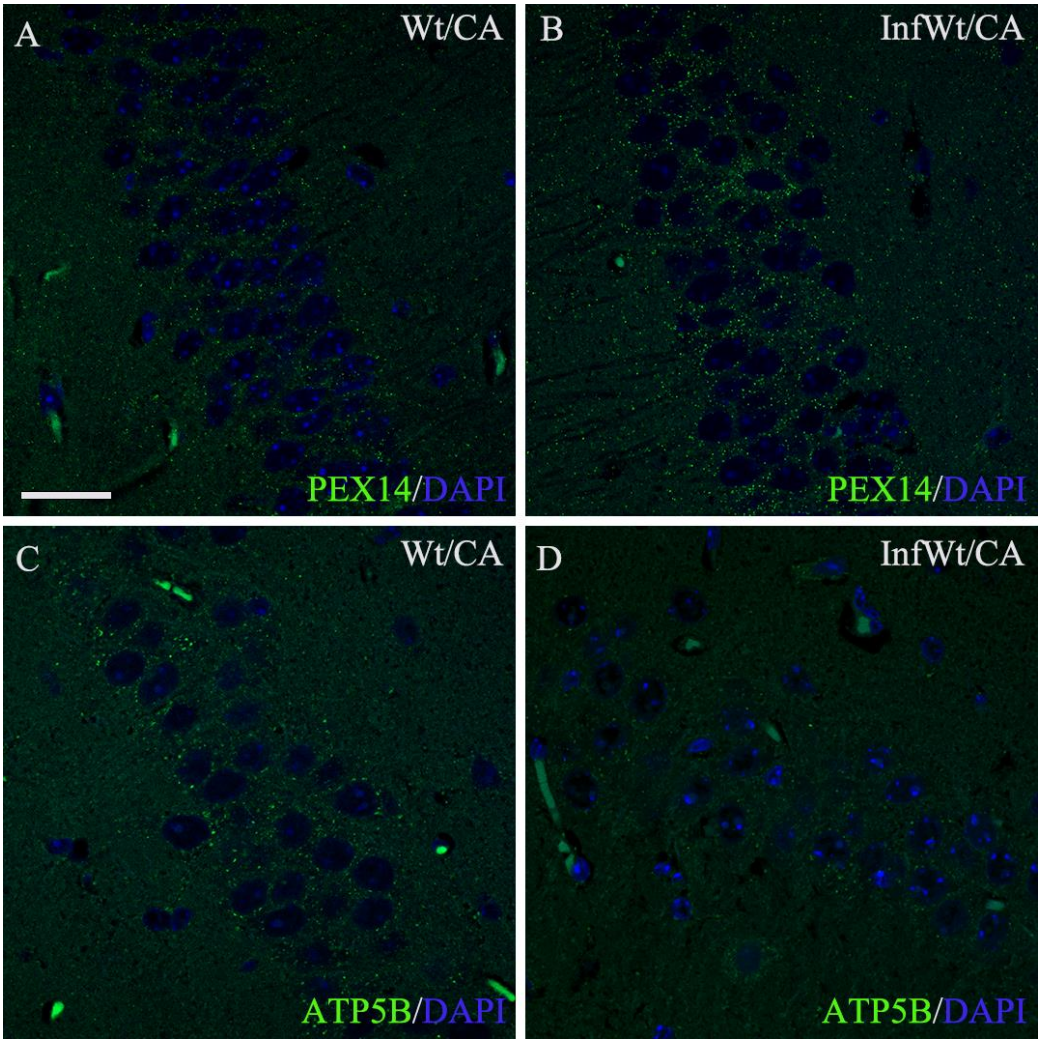

Photomicrographs of PEX14-positive peroxisomes (green) in pyramidal neurons of the cornu ammonis (CA) band of non-infected (**A**) and BoDV1-infected (**B**) Wt mice, and ATP5B-positive mitochondria (green) in pyramidal neurons (CA band) of non-infected (**C**) and BoDV1-infected (**D**) Wt mice. Peroxisomal abundance increased but that of mitochondria decreased in pyramidal neurons of the CA band of Wt mice after BoDV1 infection. DAPI (blue) is the nuclear stain. ***Wt***, wild-type; ***InfWt***, BoDV1-infected Wt. Scale bar: 20 µm for all images.

Figure 44: Peroxisomal and mitochondrial abundances in granule neurons (DG) of non- and BoDV1-infected Wt mice

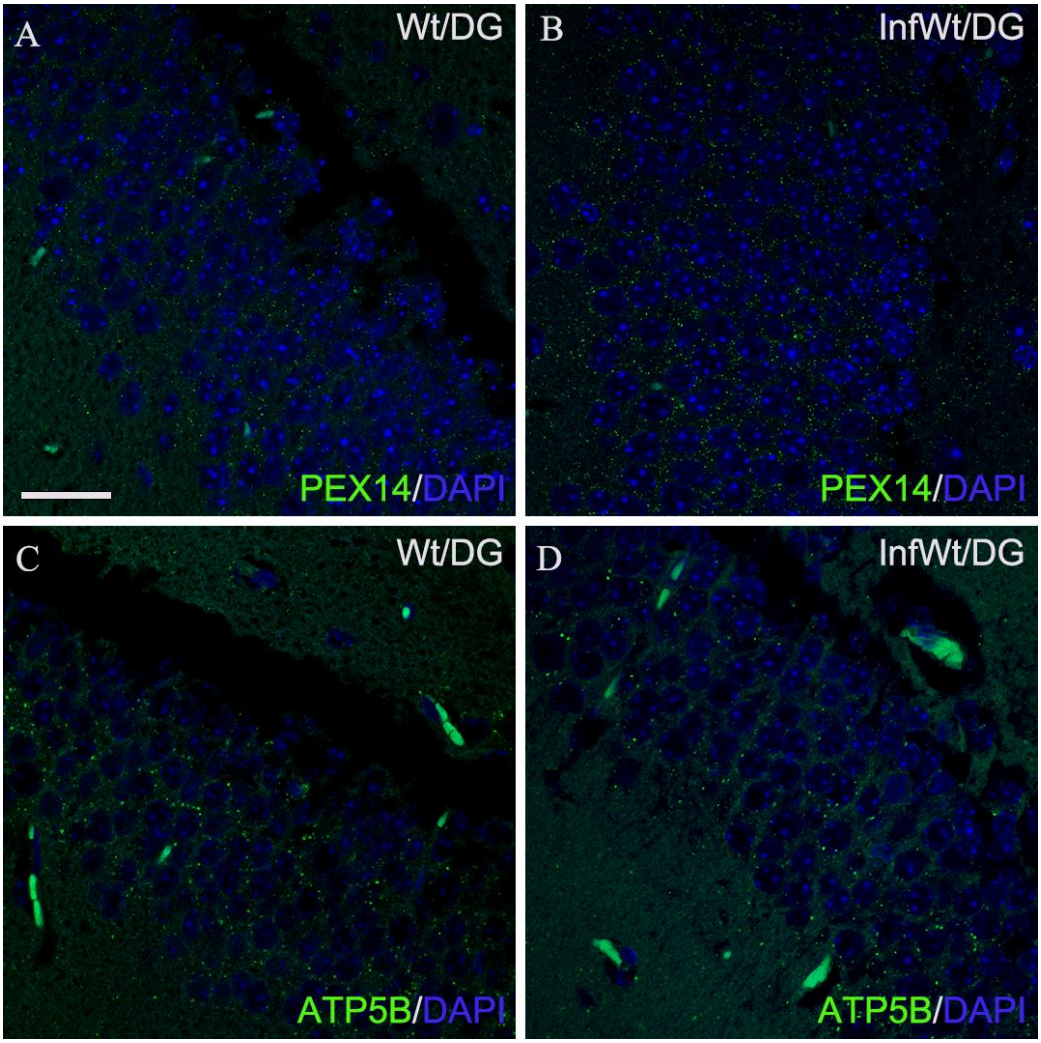

Photomicrographs of PEX14-positive peroxisomes (green) in granule neurons of the dentate gyrus (DG) of non-infected (**A**) and BoDV1-infected (**B**) Wt mice, and ATP5B-positive mitochondria (green) in granule neurons (DG) of non-infected (**C**) and BoDV1-infected (**D**) Wt mice. Peroxisomal abundance increased but that of mitochondria did not change in granule cells of the dentate gyrus of Wt mice after BoDV1 infection. DAPI (blue) is the nuclear stain. ***Wt***, wild-type; ***InfWt***, BoDV1-infected Wt. Scale bar: 20 µm for all images.

Figure 45: Peroxisomal and mitochondrial abundances in pyramidal neurons of the cerebral cortex of non- and BoDV1-infected Wt mice

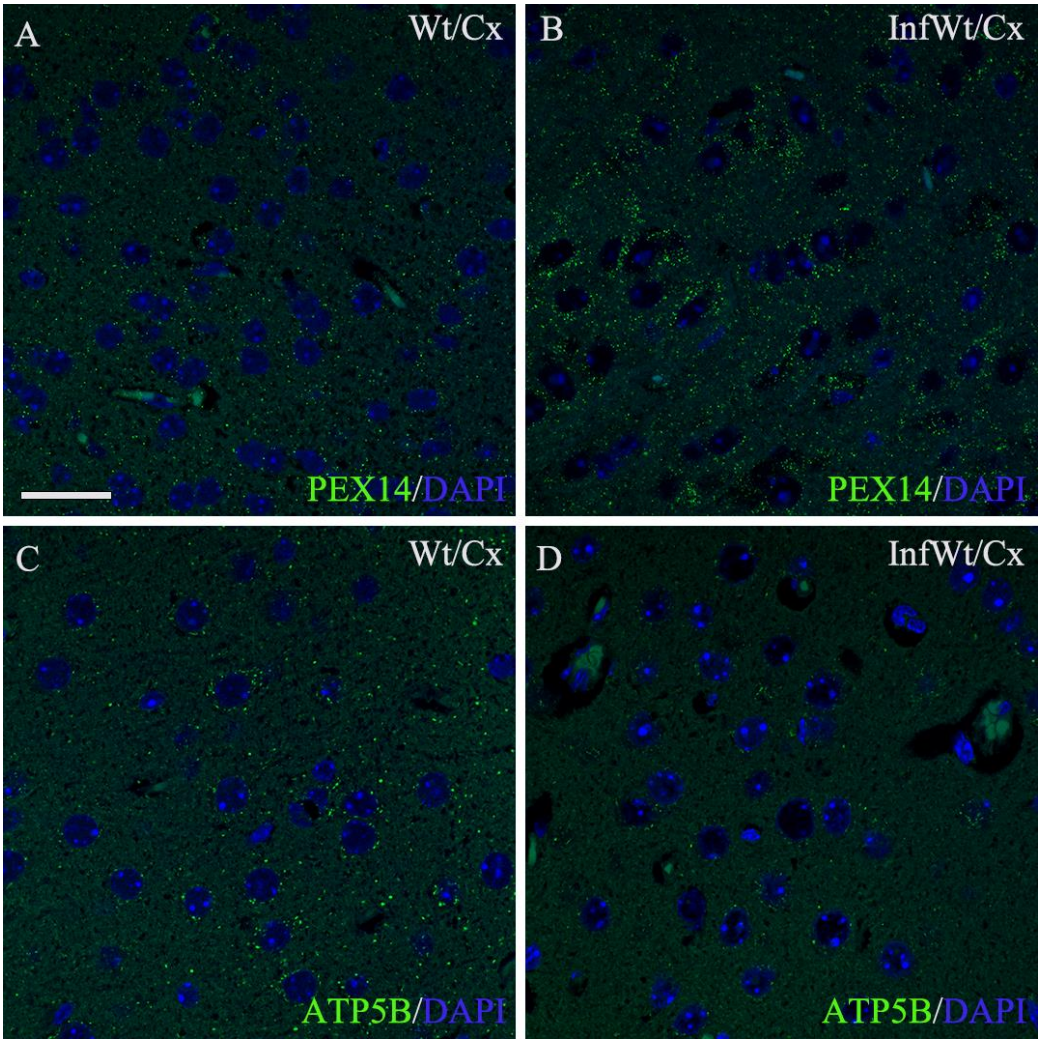

Photomicrographs of PEX14-positive peroxisomes (green) in pyramidal neurons of the cerebral cortex (Cx) of non-infected (**A**) and BoDV1-infected (**B**) Wt mice, and ATP5B-positive mitochondria (green) in pyramidal neurons (Cx) of non-infected (**C**) and BoDV1-infected (**D**) Wt mice. Peroxisomal abundance increased but that of mitochondria decreased in pyramidal neurons of the cerebral cortex of Wt mice after BoDV1 infection. DAPI (blue) is the nuclear stain. ***Wt***, wild-type; ***InfWt***, BoDV1-infected Wt. Scale bar: 20 µm for all images.

Figure 46: Peroxisomal and mitochondrial abundances in cerebellar granule and Purkinje neurons of non- and BoDV1-infected Wt mice

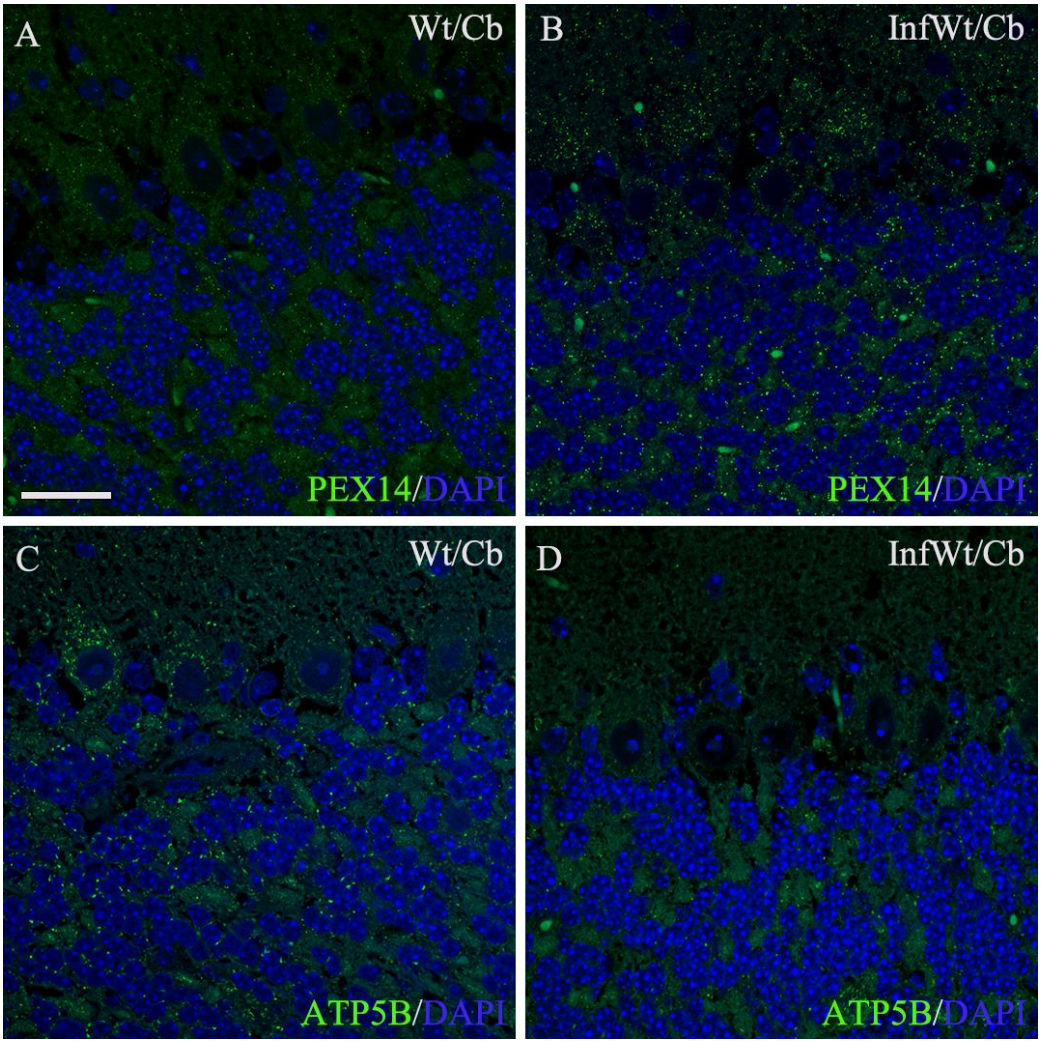

Photomicrographs of PEX14-positive peroxisomes (green) in cerebellar (Cb) granule and Purkinje neurons of non-infected (**A**) and BoDV1-infected (**B**) Wt mice, and ATP5B-positive mitochondria (green) in cerebellar granule and Purkinje neurons of non-infected (**C**) and BoDV1-infected (**D**) Wt mice. Peroxisomal abundance increased but that of mitochondria decreased in both granule and Purkinje neurons of the cerebellar cortex of Wt mice after BoDV1 infection. DAPI (blue) is the nuclear stain. ***Wt***, wild-type; ***InfWt***, BoDV1-infected Wt. Scale bar: 20 µm for all images.

4.2.2 Morphometric analysis of catalase and SOD2 in the hippocampus, cerebral and cerebellar cortices of BoDV1-infected Wt mice

In BoDV1-infected Wt mice, catalase abundance was 5/100 µm^2 in pyramidal neurons (CA band) and 5/100 µm^2 in granule neurons (DG) of the hippocampus; 2/100 µm^2 in cortical pyramidal neurons; 3/100 µm^2 and 2/100 µm^2 in cerebellar granule and Purkinje neurons, respectively (see **Appendix 3**A-E). This depicts a dramatic decrease in catalase abundance in all neuronal cell types of Wt mice [3.0-fold in pyramidal cells (CA band); 3.2-fold in granule cells (DG); 3.5-fold in pyramidal cells (cerebral cortex); 3.3-fold in granule cells and 5.0-fold in Purkinje cells (cerebellar cortex)] after BoDV1 infection (**Figures 47**A,B, **48**A,B, **49**A,B, **50**A,B; **Table 2**).

Besides, SOD2 abundance was 0.2% in pyramidal neurons (CA band) and 0.02% in granule neurons (DG) of the hippocampus; 0.08% in cortical pyramidal neurons; 0.1% and 0.4% in cerebellar granule and Purkinje neurons, respectively (see **Appendix 4**A-E). This means, SOD2 abundance decreased in all but granule neurons of the DG [2.7-fold in pyramidal cells (CA band); 7.5-fold in pyramidal cells (cerebral cortex); 10.0-fold in granule cells and 3.3-fold in Purkinje cells (cerebellar cortex)] after BoDV1 infection of Wt mice (**Figures 47**C,D, **48**C,D, **49**C,D, **50**C,D; **Table 2**).

Figure 47: Catalase and SOD2 abundances in pyramidal neurons (CA band) of non- and BoDV1-infected Wt mice

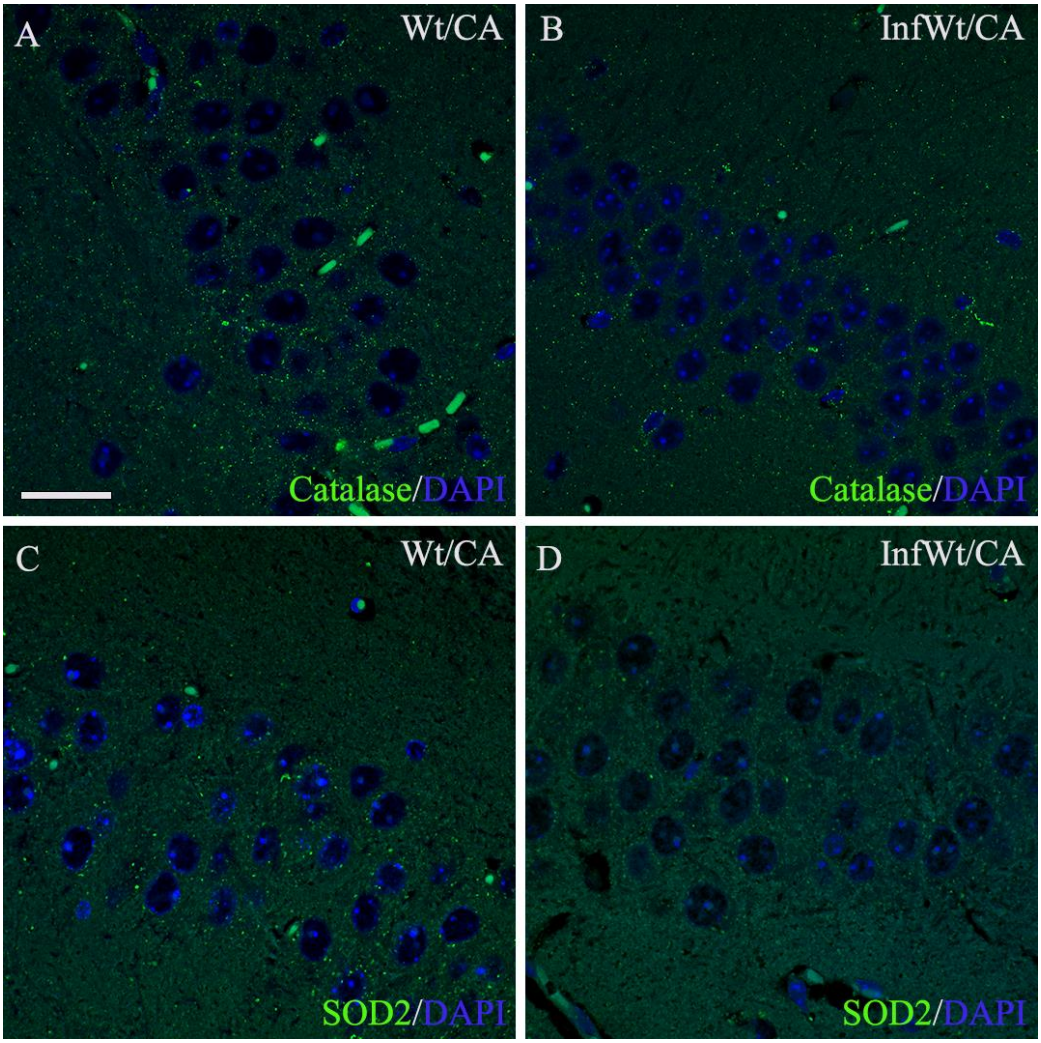

Photomicrographs of catalase-positive peroxisomes (green) in pyramidal neurons of the cornu ammonis (CA) band of non-infected (**A**) and BoDV1-infected (**B**) Wt mice, SOD2-positive mitochondria (green) in pyramidal neurons (CA band) of non-infected (**C**) and BoDV1-infected (**D**) Wt mice. Both catalase and SOD2 abundances decreased in pyramidal neurons of the CA band of Wt mice after BoDV1 infection. DAPI (blue) is the nuclear stain. ***Wt***, wild-type; ***InfWt***, BoDV1-infected Wt. Scale bar: 20 µm for all images.

Figure 48: Catalase and SOD2 abundances in granule neurons (DG) of non- and BoDV1-infected Wt mice

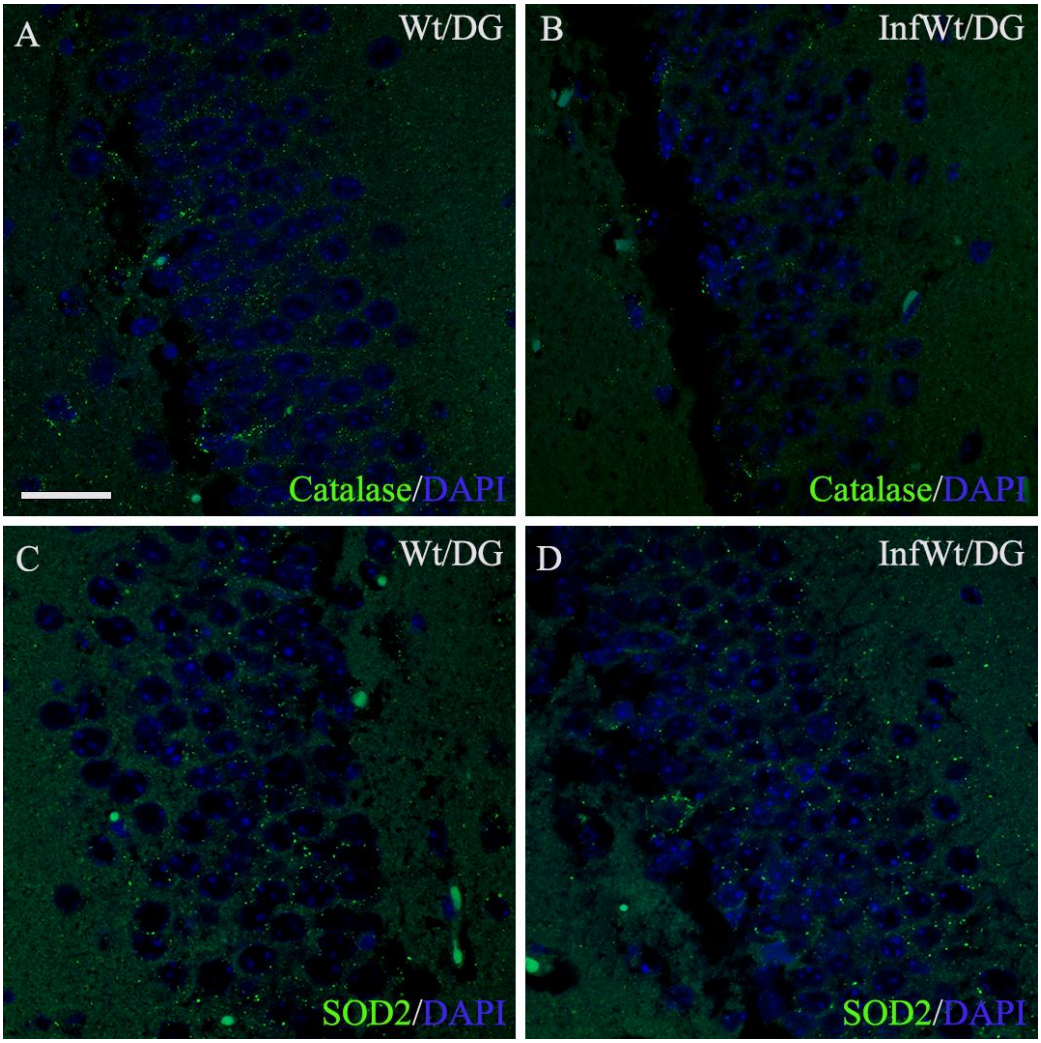

Photomicrographs of catalase-positive peroxisomes (green) in granule neurons of the dentate gyrus (DG) of non-infected (**A**) and BoDV1-infected (**B**) Wt mice, and SOD2-positive mitochondria (green) in granule neurons (DG) of non-infected (**C**) and BoDV1-infected (**D**) Wt mice. Catalase abundance decreased but that of SOD2 did not change in granule neurons of the dentate gyrus of Wt mice after BoDV1 infection. DAPI (blue) is the nuclear stain. ***Wt***, wild-type; ***InfWt***, BoDV1-infected Wt. Scale bar: 20 µm for all images.

Figure 49: Catalase and SOD2 abundances in pyramidal neurons of the cerebral cortex of non- and BoDV1-infected Wt mice

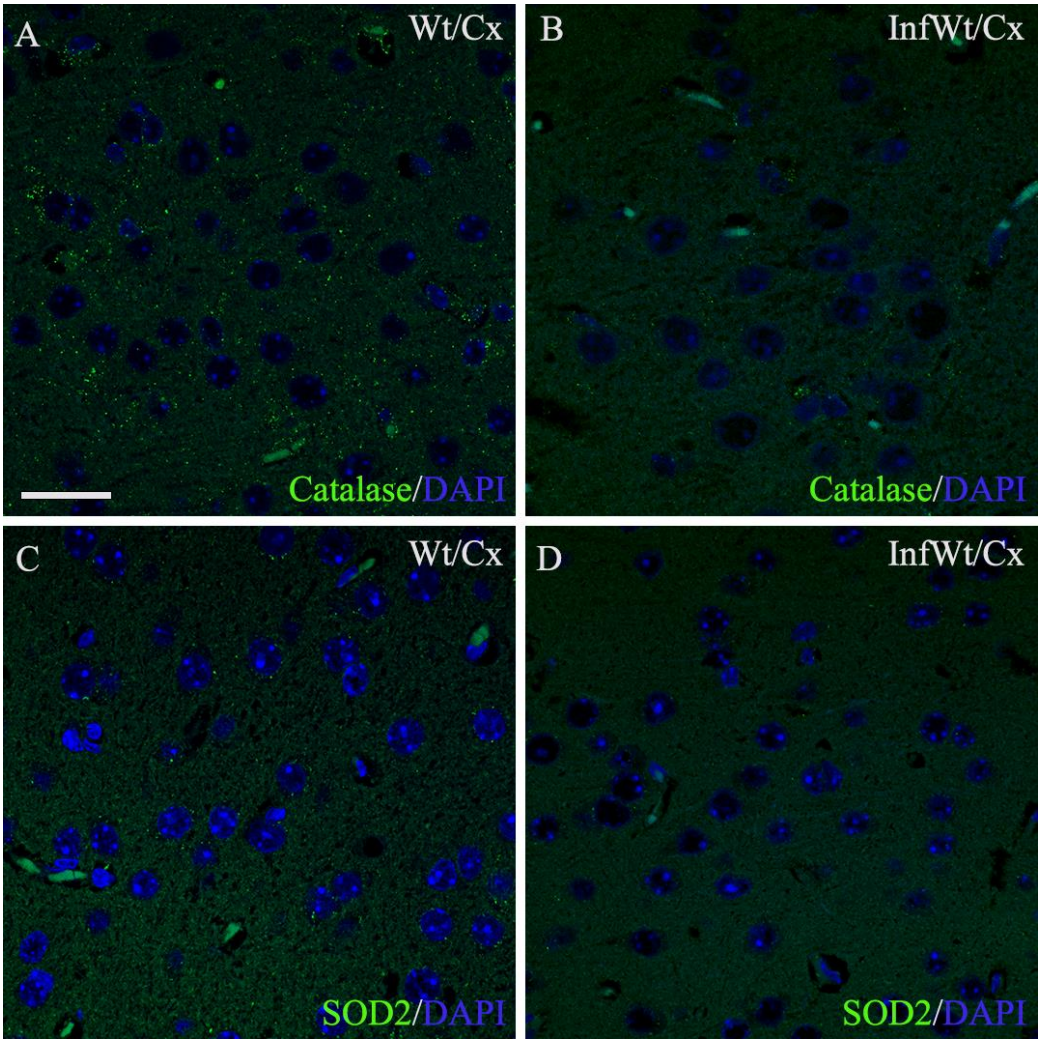

Photomicrographs of catalase-positive peroxisomes (green) in pyramidal neurons of the cerebral cortex (Cx) of non-infected (**A**) and BoDV1-infected (**B**) Wt mice, and SOD2-positive mitochondria (green) in pyramidal neurons (Cx) of non-infected (**C**) and BoDV1-infected (**D**) Wt mice. Both catalase and SOD2 abundances decreased in pyramidal neurons of the cerebral cortex of Wt mice after BoDV1 infection. DAPI (blue) is the nuclear stain. ***Wt***, wild-type; ***InfWt***, BoDV1-infected Wt. Scale bar: 20 µm for all images.

Figure 50: Catalase and SOD2 abundances in cerebellar granule and Purkinje neurons of non- and BoDV1-infected Wt mice

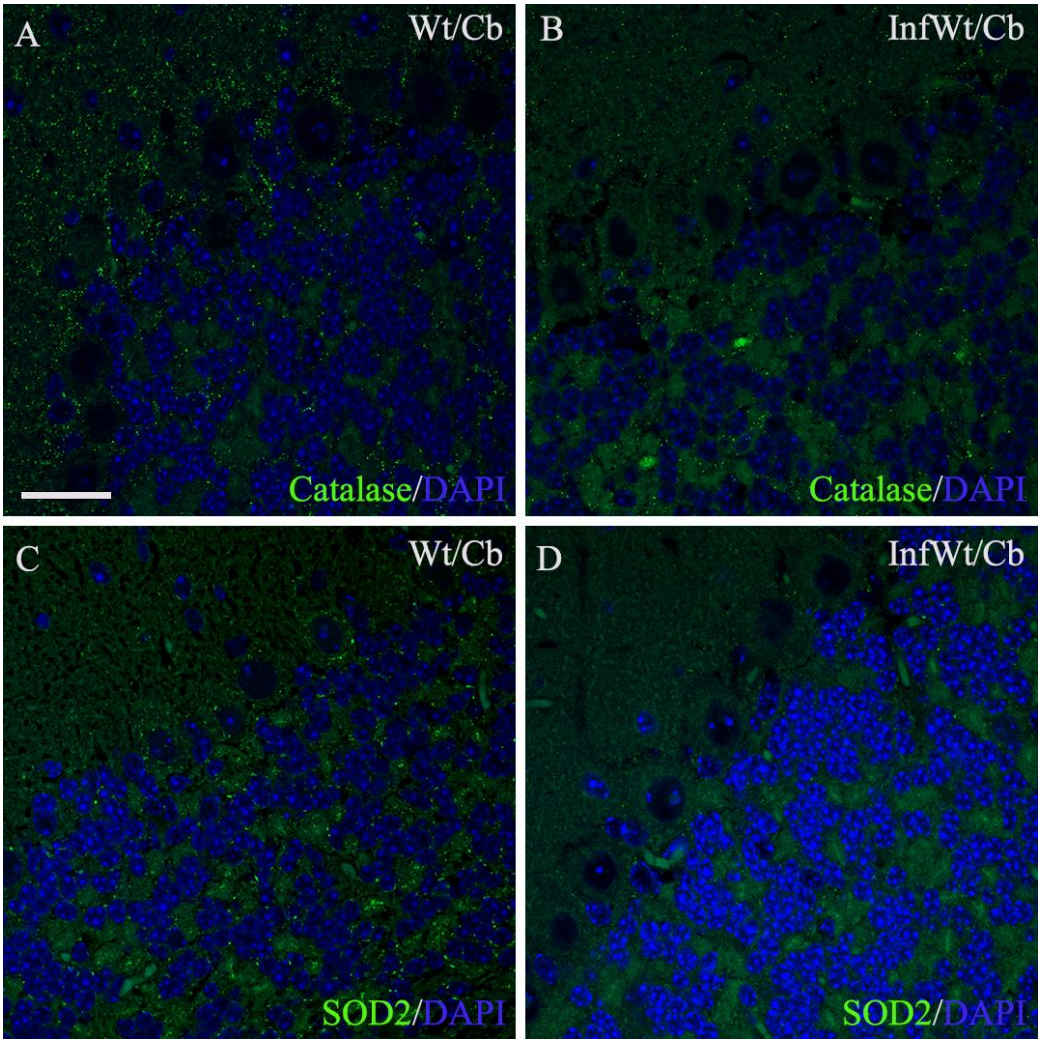

Photomicrographs of catalase-positive peroxisomes (green) in cerebellar (Cb) granule and Purkinje neurons of non-infected (**A**) and BoDV1-infected (**B**) Wt mice, and SOD2-positive mitochondria (green) in cerebellar granule and Purkinje neurons of non-infected (**C**) and BoDV1-infected (**D**) Wt mice. Both catalase and SOD2 abundances decreased in granule and Purkinje neurons of the cerebellar cortex of Wt mice after BoDV1 infection. DAPI (blue) is the nuclear stain. ***Wt***, wild-type; ***InfWt***, BoDV1-infected Wt. Scale bar: 20 µm for all images.

4.2.3 Morphometric analysis of peroxisomes and mitochondria in the hippocampus, cerebral and cerebellar cortices of BoDV1-infected TNFTg mice

After the analysis of peroxisomal and mitochondrial abundances in BoDV1-infected TNFTg mice, we compared to those of respective non-infected mice and BoDV1-infected Wt mice. Following BoDV1 infection of TNFTg mice, peroxisomal abundance was 26/100 μm^2 in pyramidal neurons (CA band) and 26/100 μm^2 in granule neurons (DG) of the hippocampus; 18/100 μm^2 in cortical pyramidal neurons; 22/100 μm^2 and 29/100 μm^2 in cerebellar granule and Purkinje neurons, respectively (see **Appendix 1**A-E). This demonstrates that peroxisomal abundance did not change in all neuronal cell types from TNF-α transgenic brain areas after BoDV1 infection (**Figures 51**A,B, **52**A,B, **53**A,B; **Table 2**). Further, the abundance of mitochondria was found to be 16.0% in pyramidal neurons (CA band) and 6.5% in granule neurons (DG) of the hippocampus; 27.9% in cortical pyramidal neurons; 5.1% and 19.8% in cerebellar granule and Purkinje neurons, respectively (see **Appendix 2**A-E). Here, mitochondrial abundance decreased in all TNF-α transgenic brain areas [1.8-fold in pyramidal cells (CA band); 2.6-fold in granule cells (DG); and 1.8-fold in pyramidal cells (cerebral cortex)] (**Figures 51**C,D, **52**C,D, **5**C,D; **Table 2**) after BoDV1 infection.

Despite the decrease in mitochondrial abundance after BoDV1 infection of TNFTg mice, all TNF-α overexpressing neuronal cell types showed significantly higher mitochondrial abundance compared to BoDV1-infected Wt mice [10.7-fold in pyramidal cells (CA band); 6.5-fold in granule cells (DG); and 7.8-fold in pyramidal cells (cerebral cortex)] (see **Appendix 2**A-C). Interestingly, in the non-transgenic cerebellar cortex, peroxisomal and mitochondrial abundances did not change in both granule and Purkinje neurons after BoDV1 infection (**Figure 54**A-D; **Table 2**), different from what was seen in the cerebellar neurons of Wt mice after BoDV1 infection. However, Purkinje neurons of the non-transgenic cerebellar cortex of BoDV1-infected TNFTg mice had 4.3-fold higher mitochondrial abundance compared to same cell type of BoDV1-infected Wt mice (see **Appendix 2**D,E).

Figure 51: Peroxisomal and mitochondrial abundances in pyramidal neurons (CA band) of non- and BoDV1-infected TNFTg mice

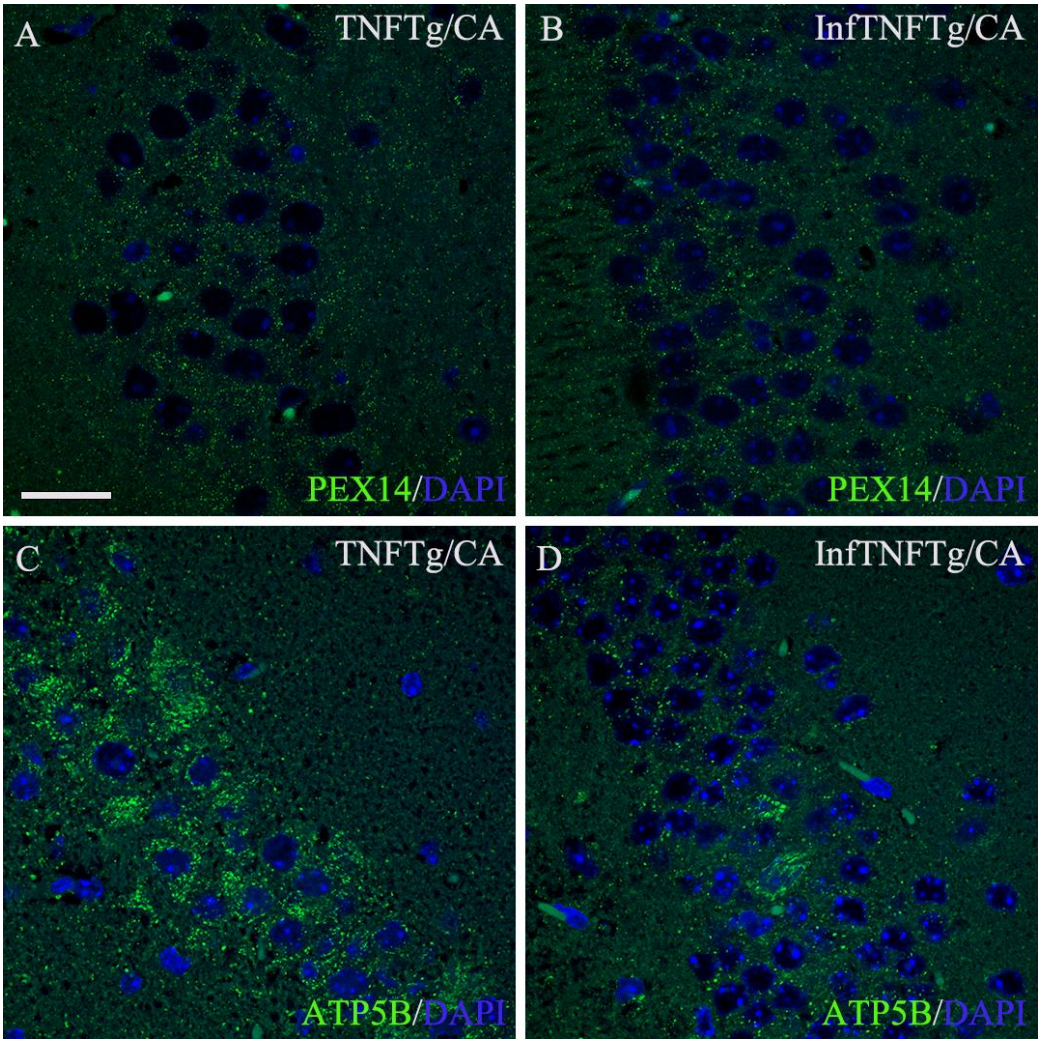

Photomicrographs of PEX14-positive peroxisomes (green) in pyramidal neurons of the cornu ammonis (CA) band of non-infected (**A**) and BoDV1-infected (**B**) TNFTg mice, ATP5B-positive mitochondria (green) in pyramidal neurons (CA band) of non-infected (**C**) and BoDV1-infected (**D**) TNFTg mice. Mitochondrial abundance decreased but that of peroxisomes did not change in pyramidal neurons of the CA band of TNFTg mice after BoDV1 infection. DAPI (blue) is the nuclear stain. ***TNFTg***, TNF-α transgenic; ***InfTNFTg***, BoDV1-infected TNFTg. Scale bar: 20 µm for all images.

Figure 52: Peroxisomal and mitochondrial abundances in granule neurons (DG) of non- and BoDV1-infected TNFTg mice

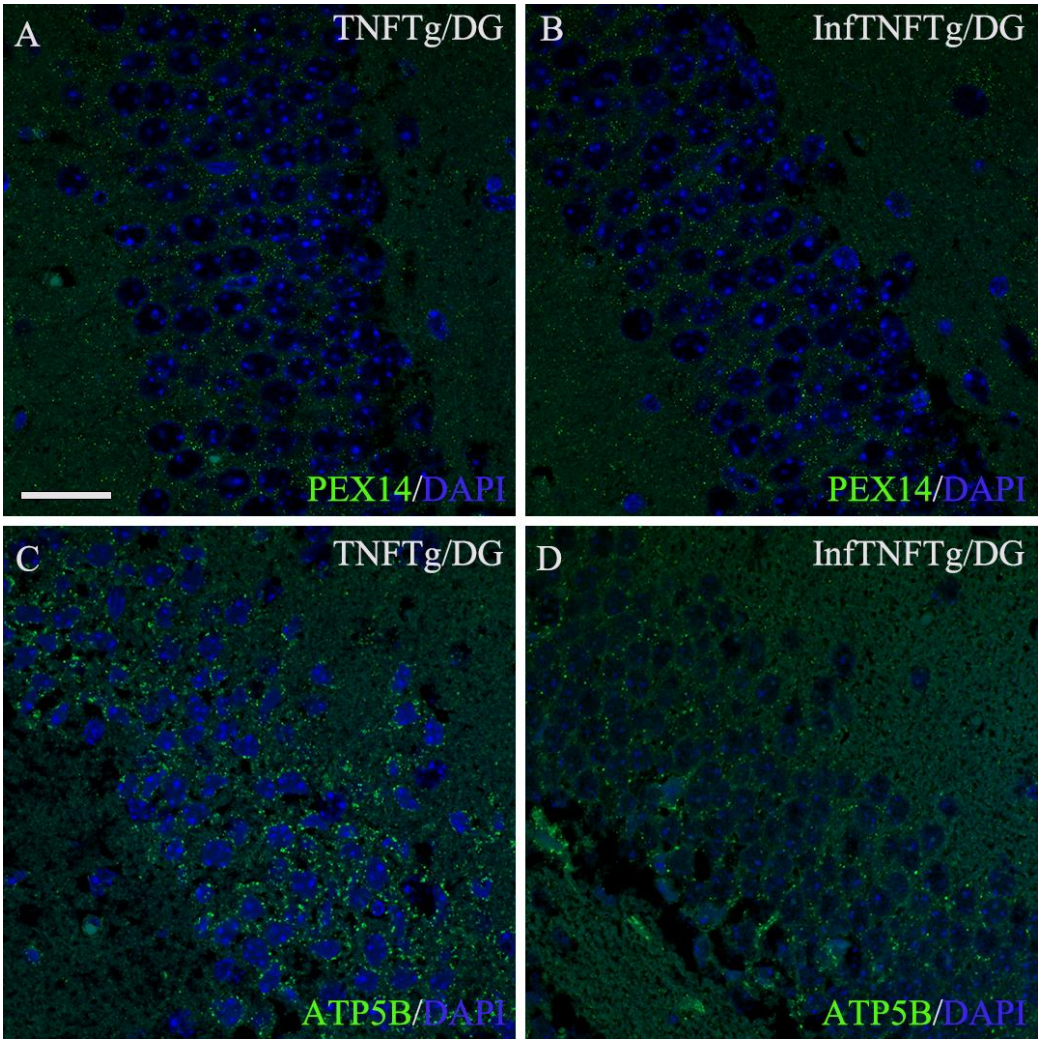

Photomicrographs of PEX14-positive peroxisomes (green) in granule neurons of the dentate gyrus (DG) of non-infected (**A**) and BoDV1-infected (**B**) TNFTg mice, and ATP5B-positive mitochondria (green) in granule neurons (DG) of non-infected (**C**) and BoDV1-infected (**D**) TNFTg mice. Mitochondrial abundance decreased but that of peroxisomes did not change in granule neurons of the dentate gyrus of TNFTg mice after BoDV1 infection. DAPI (blue) is the nuclear stain. ***TNFTg***, TNF-α transgenic; ***InfTNFTg***, BoDV1-infected TNFTg. Scale bar: 20 µm for all images.

Figure 53: Peroxisomal and mitochondrial abundances in pyramidal neurons of the cerebral cortex of non- and BoDV1-infected TNFTg mice

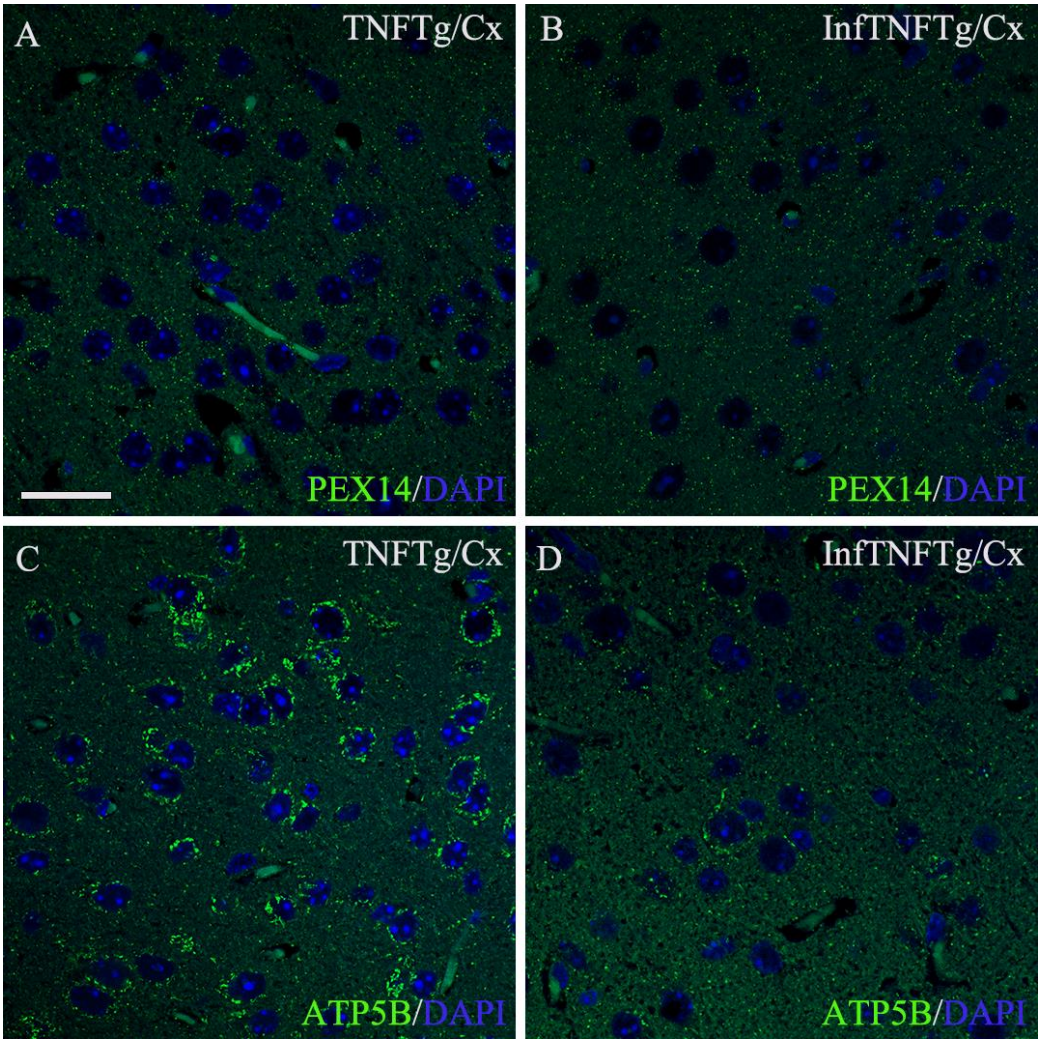

Photomicrographs of PEX14-positive peroxisomes (green) in pyramidal neurons of the cerebral cortex (Cx) of non-infected (**A**) and BoDV1-infected (**B**) TNFTg mice, and ATP5B-positive mitochondria (green) in pyramidal neurons (Cx) of non-infected (**C**) and BoDV1-infected (**D**) TNFTg mice. Mitochondrial abundance decreased but that of peroxisomes did not change in pyramidal neurons of the cerebral cortex of TNFTg mice after BoDV1 infection. DAPI (blue) is the nuclear stain. ***TNFTg***, TNF-α transgenic; ***InfTNFTg***, BoDV1-infected TNFTg. Scale bar: 20 µm for all images.

Figure 54: Peroxisomal and mitochondrial abundances in cerebellar granule and Purkinje neurons of non- and BoDV1-infected TNFTg

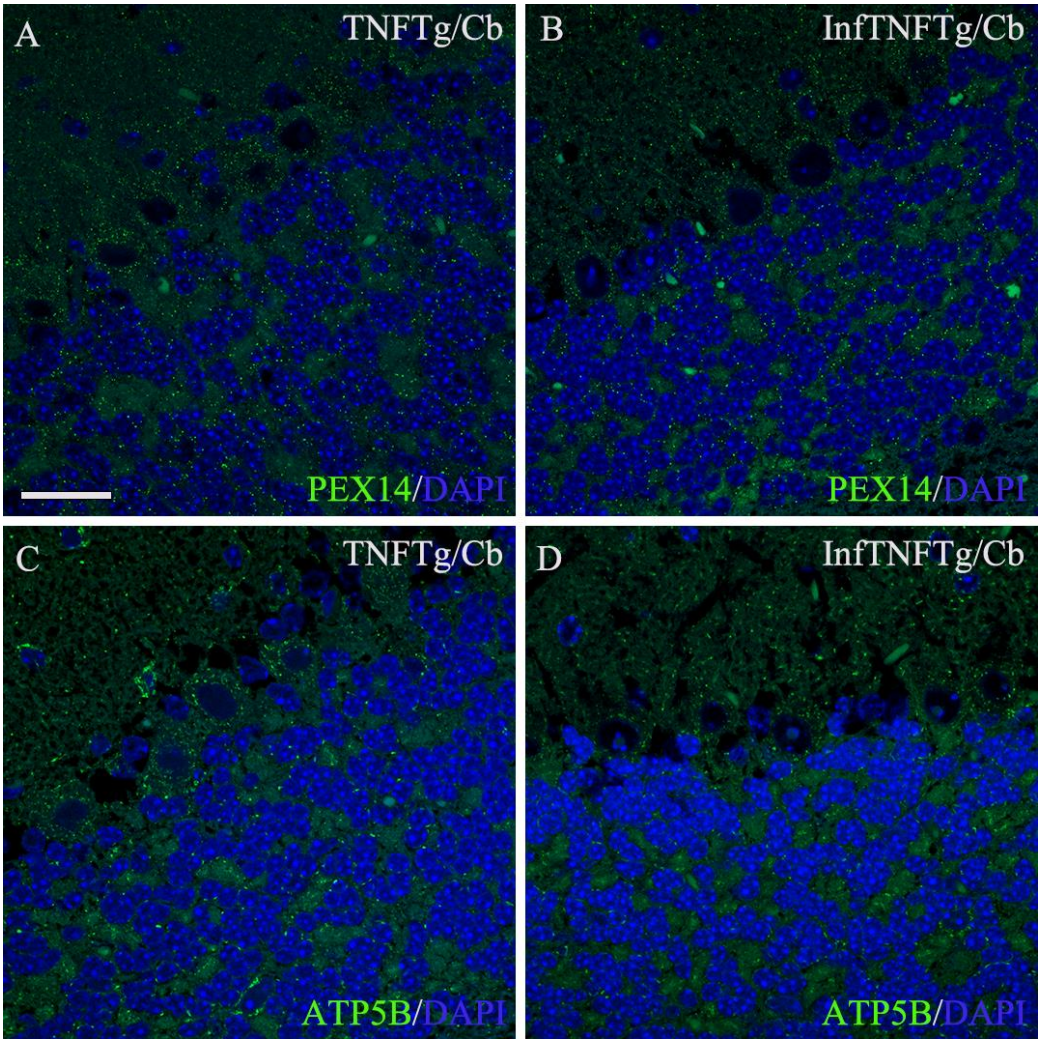

Photomicrographs of PEX14-positive peroxisomes (green) in cerebellar (Cb) granule and Purkinje neurons of non-infected (**A**) and BoDV1-infected (**B**) TNFTg mice, and ATP5B-positive mitochondria (green) in cerebellar granule and Purkinje neurons of non-infected (**C**) and BoDV1-infected (**D**) TNFTg mice. No changes in peroxisomal or mitochondrial abundance in both granule and Purkinje neurons of the cerebellar cortex after BoDV1 infection. DAPI (blue) is the nuclear stain. ***TNFTg***, TNF-α transgenic; ***InfTNFTg***, BoDV1-infected TNFTg. Scale bar: 20 µm for all images.

4.2.4 Morphometric analysis of catalase and SOD2 in the hippocampus, cerebral and cerebellar cortices of BoDV1-infected TNFTg mice

Here, catalase and SOD2 abundances in BoDV1-infected TNFTg mice were compared to those of respective non-infected mice and BoDV1-infected mice. Catalase abundance was 6/100 μm^2 in pyramidal neurons (CA band) and 4/100 μm^2 in granule neurons (DG) of the hippocampus; 2/100 μm^2 in cortical pyramidal neurons; 2/100 μm^2 and 2/100 μm^2 in cerebellar granule and Purkinje neurons, respectively, after BoDV1 infection of TNFTg mice (see **Appendix 3**A-E). That of SOD2 was 0.3% in pyramidal neurons (CA band) and 1.6% in granule neurons (DG) of the hippocampus; 1.7% in cortical pyramidal neurons; 0.4% and 2.5% in cerebellar granule and Purkinje neurons, respectively (see **Appendix 4**A-E). Concerning the antioxidant enzymes, no further decrease in catalase abundance was seen in neuronal cell types from TNF-α transgenic brain areas after BoDV1 infection of TNFTg mice (**Figures 55**A,B, **56**A,B, **57**A,B; **Table 2**). However, SOD2 abundance decreased [7.0-fold in granule cells (DG); 3.0-fold in pyramidal cells (CA band); 3.9-fold in pyramidal cells (cerebral cortex)] (**Figures 55**C,D, **56**C,D, **57**C,D; **Table 2**).

Regardless of the overall decrease, SOD2 abundance was significantly higher in pyramidal neurons of the CA band (8.0-fold) and in cortical pyramidal neurons (17.0-fold) compared to same cell types of BoDV1-infected Wt mice (see **Appendix 4**A-C). In the non-transgenic cerebellar cortex, catalase abundance decreased [3.5- and 3.0-fold in granule and Purkinje neurons, respectively], whereas SOD2 abundance increased 2.8-fold in Purkinje neurons only in BoDV1-infected TNFTg mice, contrary to what was seen in the cerebellar cortex of BoDV1-infected Wt mice (**Figure 58**A-D; **Table 2**). In addition, SOD2 abundance was 6.9-fold higher in Purkinje neurons of BoDV1-infected TNFTg mice than in BoDV1-infected Wt mice (see **Appendix** 4E).

Figure 55: Catalase and SOD2 abundances in pyramidal neurons (CA band) of non- and BoDV1-infected TNFTg mice

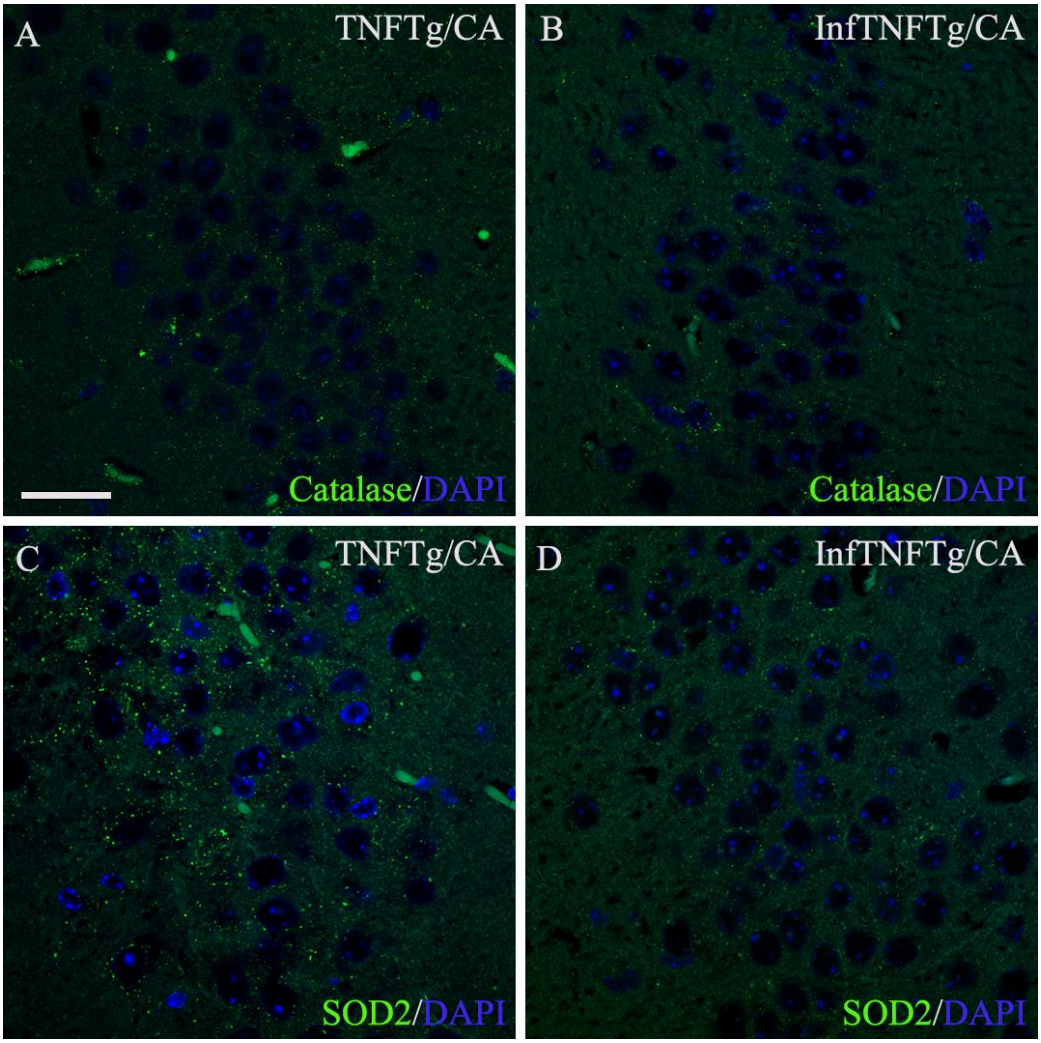

Photomicrographs of catalase-positive peroxisomes (green) in pyramidal neurons of the cornu ammonis (CA) band of non-infected (**A**) and BoDV1-infected (**B**) TNFTg mice, SOD2-positive mitochondria (green) in pyramidal neurons (CA band) of non-infected (**C**) and BoDV1-infected (**D**) TNFTg mice. SOD2 abundance decreased but that of catalase did not change in pyramidal neurons of the CA band of TNFTg mice after BoDV1 infection. DAPI (blue) is the nuclear stain. ***TNFTg***, TNF-α transgenic; ***InfTNFTg***, BoDV1-infected TNFTg. Scale bar: 20 µm for all images.

Figure 56: Catalase and SOD2 abundances in granule neurons (DG) of non- and BoDV1-infected TNFTg mice

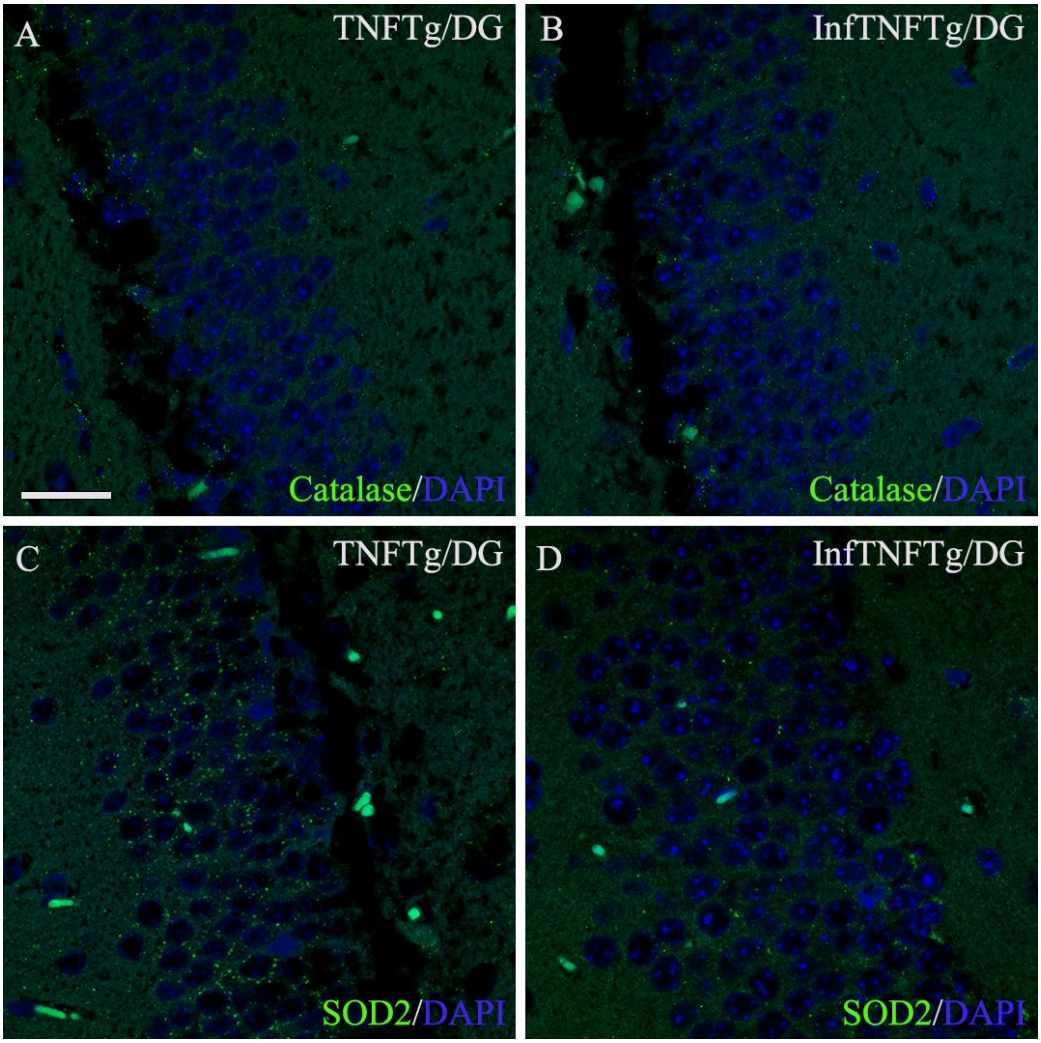

Photomicrographs of catalase-positive peroxisomes (green) in granule neurons of the dentate gyrus (DG) of non-infected (**A**) and BoDV1-infected (**B**) TNFTg mice, and SOD2-positive mitochondria (green) in granule neurons (DG) of non-infected (**C**) and BoDV1-infected (**D**) TNFTg mice. SOD2 abundance decreased but that of catalase did not change in granule neurons of the dentate gyrus of TNFTg mice after BoDV1 infection. DAPI (blue) is the nuclear stain. ***TNFTg***, TNF-α transgenic; ***InfTNFTg***, BoDV1-infected TNFTg. Scale bar: 20 µm for all images.

Figure 57: Catalase and SOD2 abundances in pyramidal neurons of the cerebral cortex of non- and BoDV1-infected TNFTg mice

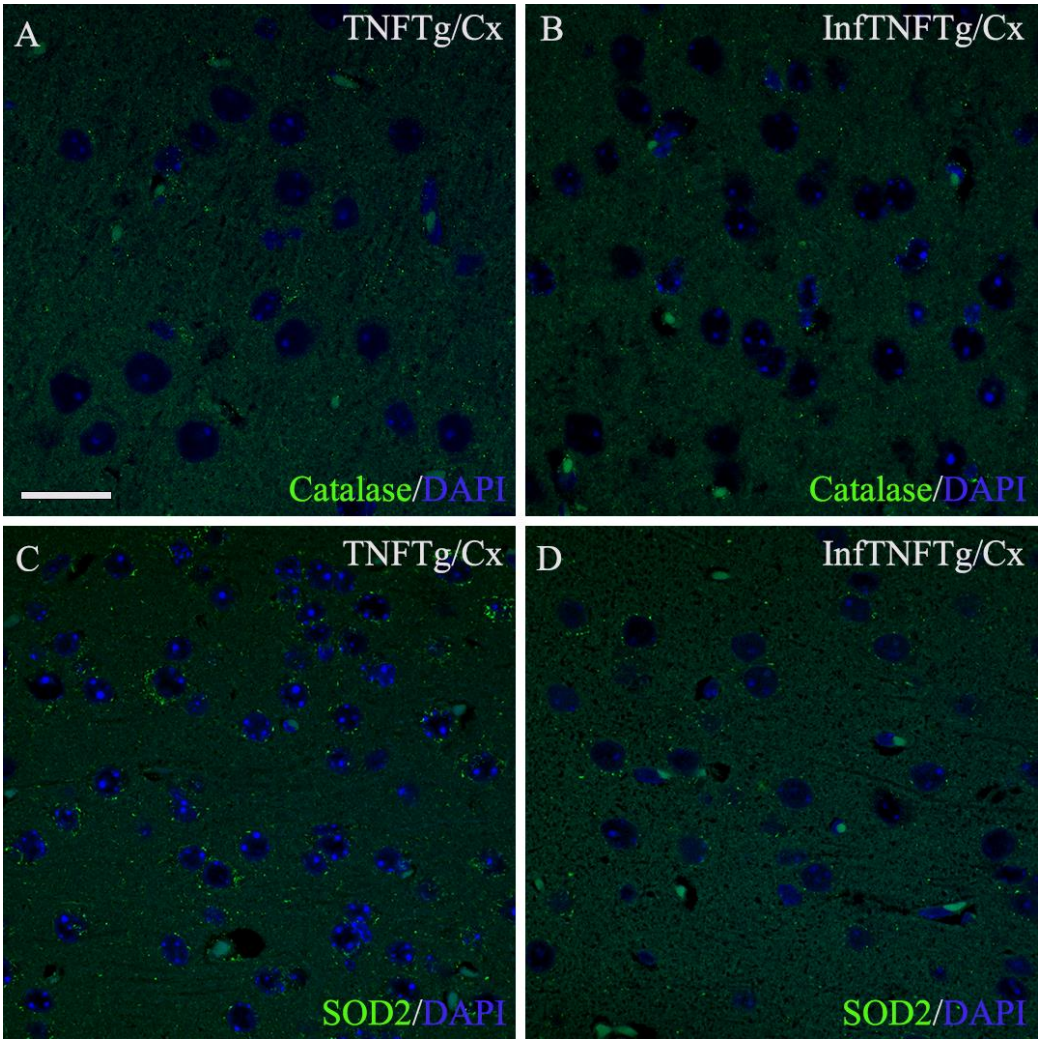

Photomicrographs of catalase-positive peroxisomes (green) in pyramidal neurons of the cerebral cortex (Cx) of non-infected (**A**) and BoDV1-infected (**B**) TNFTg mice, and SOD2-positive mitochondria (green) in pyramidal neurons (Cx) of non-infected (**C**) and BoDV1-infected (**D**) TNFTg mice. SOD2 abundance decreased but that of catalase did not change in pyramidal neurons of the cerebral cortex of TNFTg mice after BoDV1 infection. DAPI (blue) is the nuclear stain. ***TNFTg***, TNF-α transgenic; ***InfTNFTg***, BoDV1-infected TNFTg. Scale bar: 20 µm for all images.

Figure 58: Catalase and SOD2 abundances in cerebellar granule and Purkinje neurons of non- and BoDV1-infected TNFTg

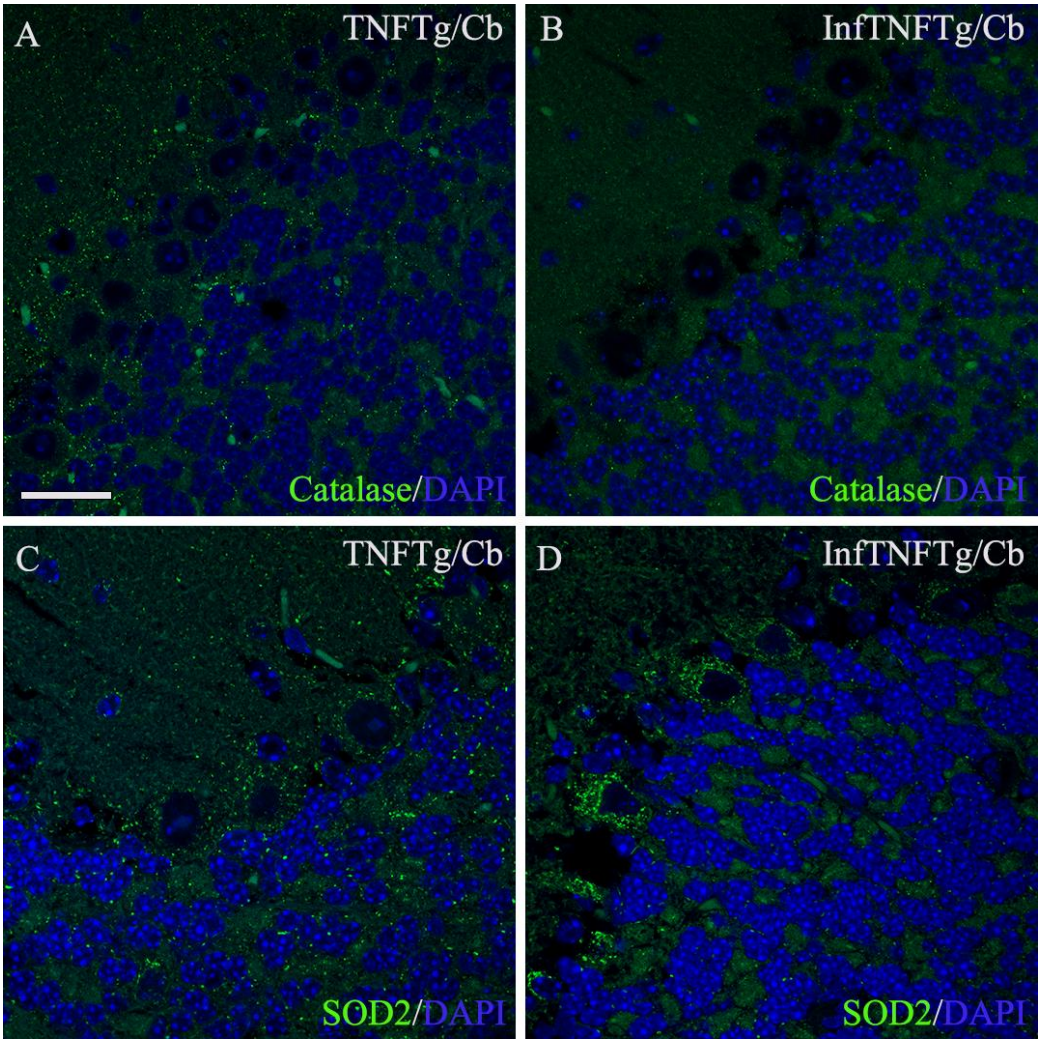

Photomicrographs of catalase-positive peroxisomes (green) in cerebellar (Cb) granule and Purkinje neurons of non-infected (**A**) and BoDV1-infected (**B**) TNFTg mice, and SOD2-positive mitochondria (green) in cerebellar granule and Purkinje neurons of non-infected (**C**) and BoDV1-infected (**D**) TNFTg mice. Catalase abundance decreased in both granule and Purkinje neurons but that of SOD2 was comparable in granule neurons and increased in Purkinje neurons of TNFTg mice after BoDV1 infection. DAPI (blue) is the nuclear stain. ***TNFTg***, TNF-α transgenic; ***InfTNFTg***, BoDV1-infected TNFTg. Scale bar: 20 µm for all images.

4.2.5 Morphometric analysis of peroxisomes and mitochondria in the hippocampus, cerebral and cerebellar cortices of BoDV1-infected TNFR1ko mice

After BoDV1 infection, peroxisomal and mitochondrial abundances in TNFR1ko mice were compared to those of respective non-infected mice and BoDV1-infected Wt mice. Peroxisomal abundance in TNFR1ko mice was 27/100 µm^2 in pyramidal neurons (CA band) and 27/100 µm^2 in granule neurons (DG) of the hippocampus; 20/100 µm^2 in cortical pyramidal neurons; 20/100 µm^2 and 30/100 µm^2 in cerebellar granule and Purkinje neurons, respectively (see **Appendix 1**A-E). Mitochondrial abundance was 2.4% in pyramidal neurons (CA band) and 1.2% in granule neurons (DG) of the hippocampus; 3.4% in cortical pyramidal neurons; 2.4% and 5.1% in cerebellar granule and Purkinje neurons, respectively (see **Appendix 2**A-E). Thus, peroxisomal abundance remained comparable in all neuronal cell types after BoDV1 infection of TNFR1ko mice when compared to respective non-infected mice (**Figures 59**A,B, **60**A,B, **61**A,B**, 62**A,B; **Table 2**). Mitochondrial abundance did not change as well in most neuronal cell types, except in cortical pyramidal neurons and cerebellar Purkinje neurons, where there was 6.8- and 3.7-fold significant decrease, respectively when compared to the non-infected TNFR1ko mice (**Figures 59**C,D, **60**C,D, **61**C,D, **62**C,D; **Table 2**).

Figure 59: Peroxisomal and mitochondrial abundances in pyramidal neurons (CA band) of non- and BoDV1-infected TNFR1ko mice

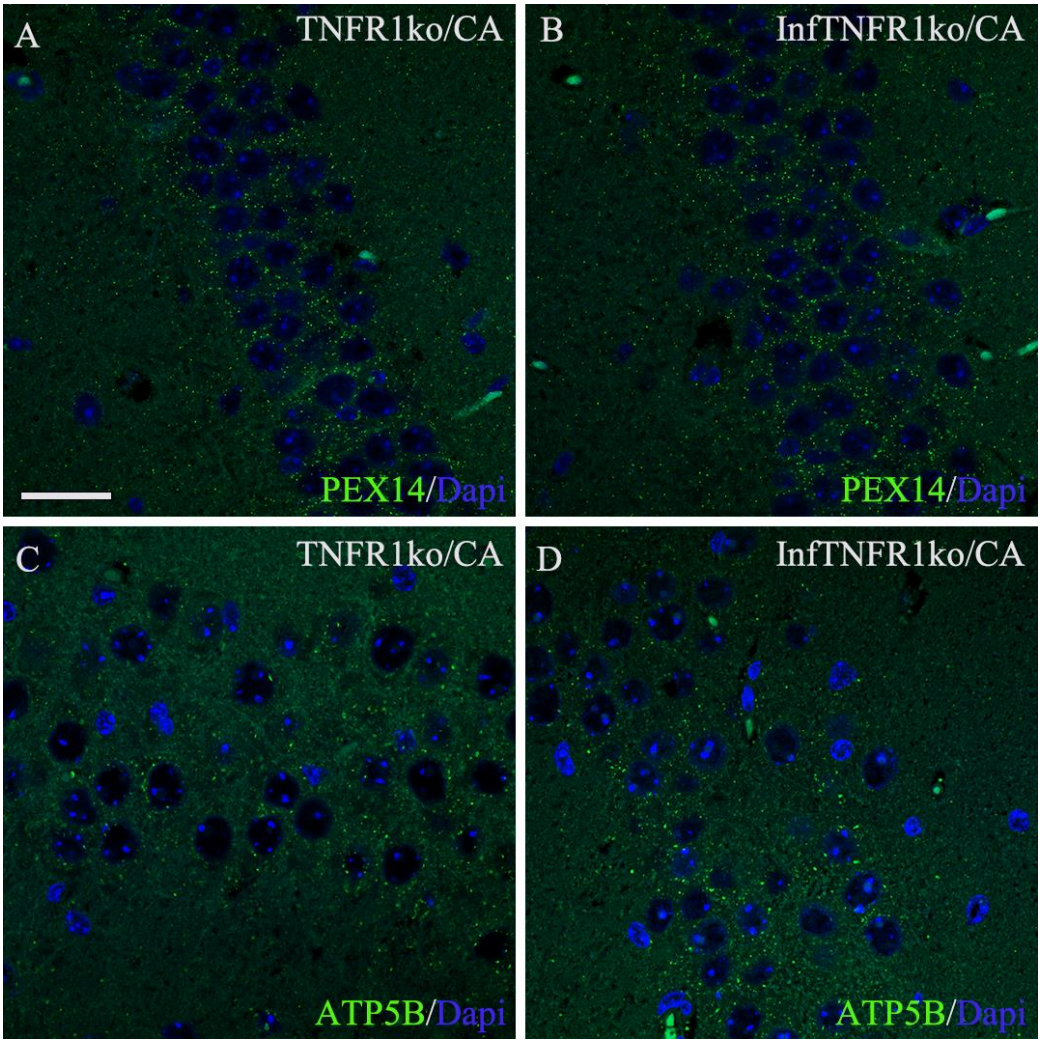

Photomicrographs of PEX14-positive peroxisomes (green) in pyramidal neurons of the cornu ammonis (CA) band of non-infected (**A**) and BoDV1-infected (**B**) TNFR1ko mice, ATP5B-positive mitochondria (green) in pyramidal neurons (CA band) of non-infected (**C**) and BoDV1-infected (**D**) TNFR1ko mice. No changes in peroxisomal and mitochondrial abundances in pyramidal neurons of the CA band of TNR1ko mice after BoDV1 infection. DAPI (blue) is the nuclear stain. ***TNFR1ko***, TNF receptor 1 knockout; ***InfTNFR1ko***, BoDV1-infected TNFR1ko. Scale bar: 20 µm for all images.

Figure 60: Peroxisomal and mitochondrial abundances in granule neurons (DG) of non- and BoDV1-infected TNFR1ko mice

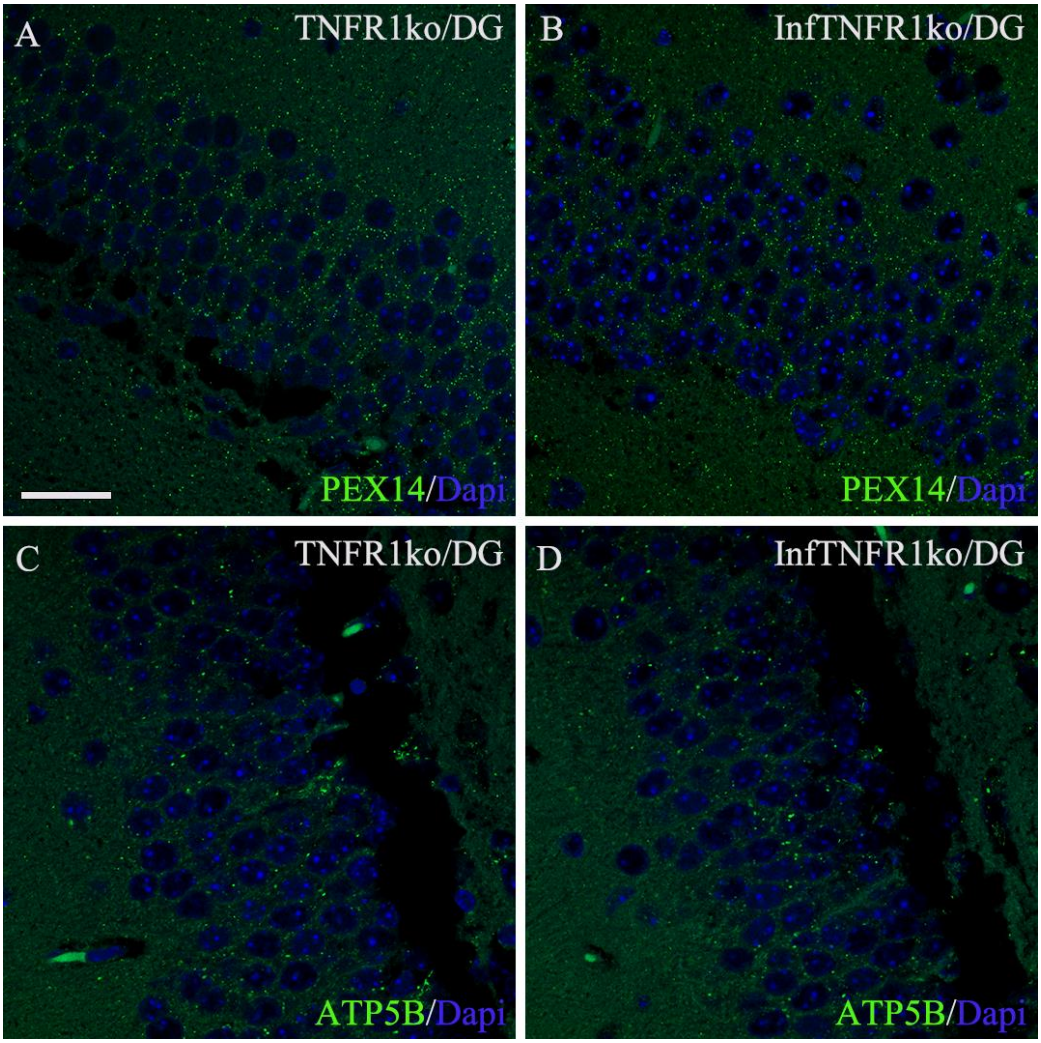

Photomicrographs of PEX14-positive peroxisomes (green) in granule neurons of the dentate gyrus (DG) of non-infected (**A**) and BoDV1-infected (**B**) TNFR1ko mice, and ATP5B-positive mitochondria (green) in granule neurons (DG) of non-infected (**C**) and BoDV1-infected (**D**) TNFR1ko mice. No changes in peroxisomal and mitochondrial abundances in granule neurons of the dentate gyrus of TNR1ko mice after BoDV1 infection. DAPI (blue) is the nuclear stain. ***TNFR1ko***, TNF receptor 1 knockout; ***InfTNFR1ko***, BoDV1-infected TNFR1ko. Scale bar: 20 µm for all images.

Figure 61: Peroxisomal and mitochondrial abundances in pyramidal neurons of the cerebral cortex of non- and BoDV1-infected TNFR1ko mice

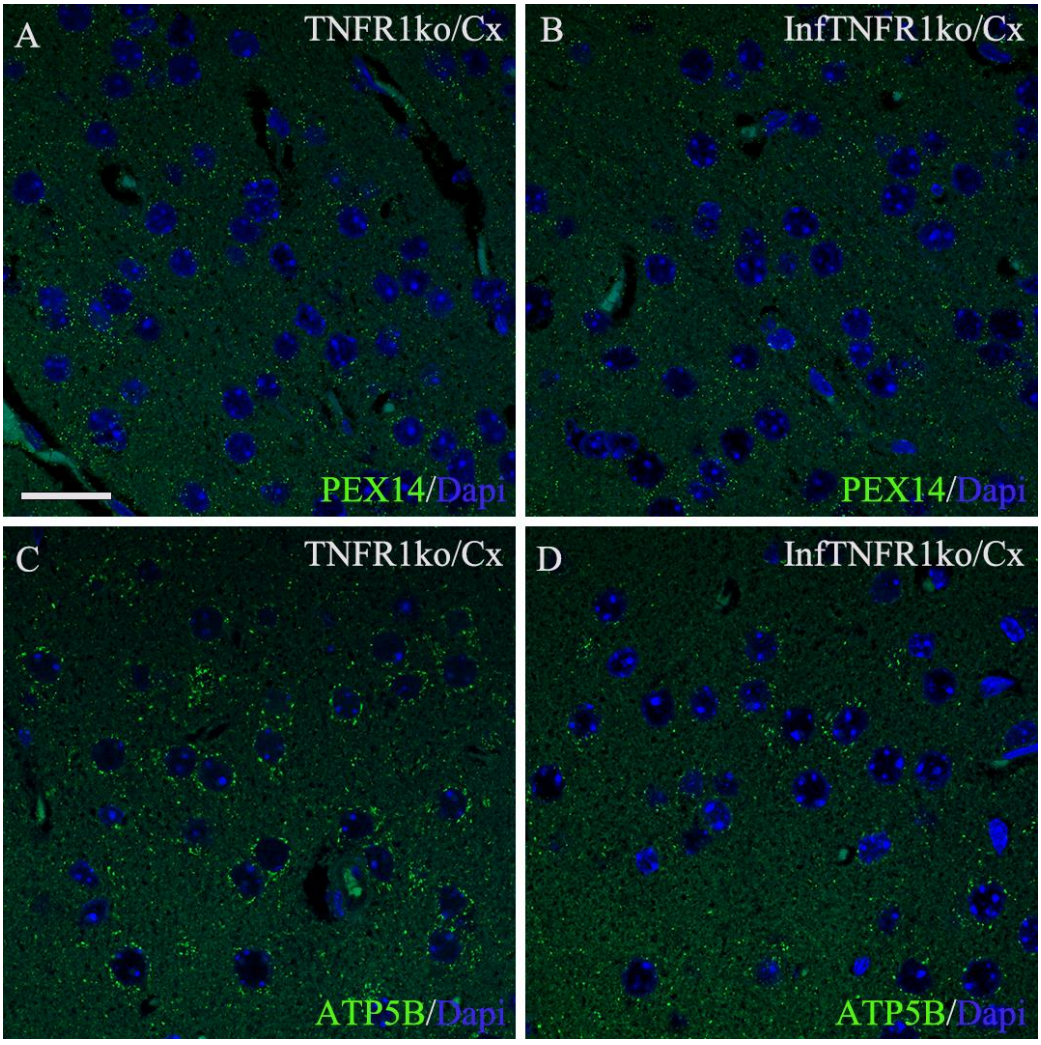

Photomicrographs of PEX14-positive peroxisomes (green) in pyramidal neurons of the cerebral cortex (Cx) of non-infected (**A**) and BoDV1-infected (**B**) TNFR1ko mice, and ATP5B-positive mitochondria (green) in pyramidal neurons (Cx) of non-infected (**C**) and BoDV1-infected (**D**) TNFR1ko mice. Mitochondrial abundance decreased but that of peroxisomes did not change in pyramidal neurons of the cerebral cortex of TNFR1ko mice after BoDV1 infection. DAPI (blue) is the nuclear stain. ***TNFR1ko***, TNF receptor 1 knockout; ***InfTNFR1ko***, BoDV1-infected TNFR1ko. Scale bar: 20 µm for all images.

Figure 62: Peroxisomal and mitochondrial abundances in cerebellar granule and Purkinje neurons of non- and BoDV1-infected TNFR1ko

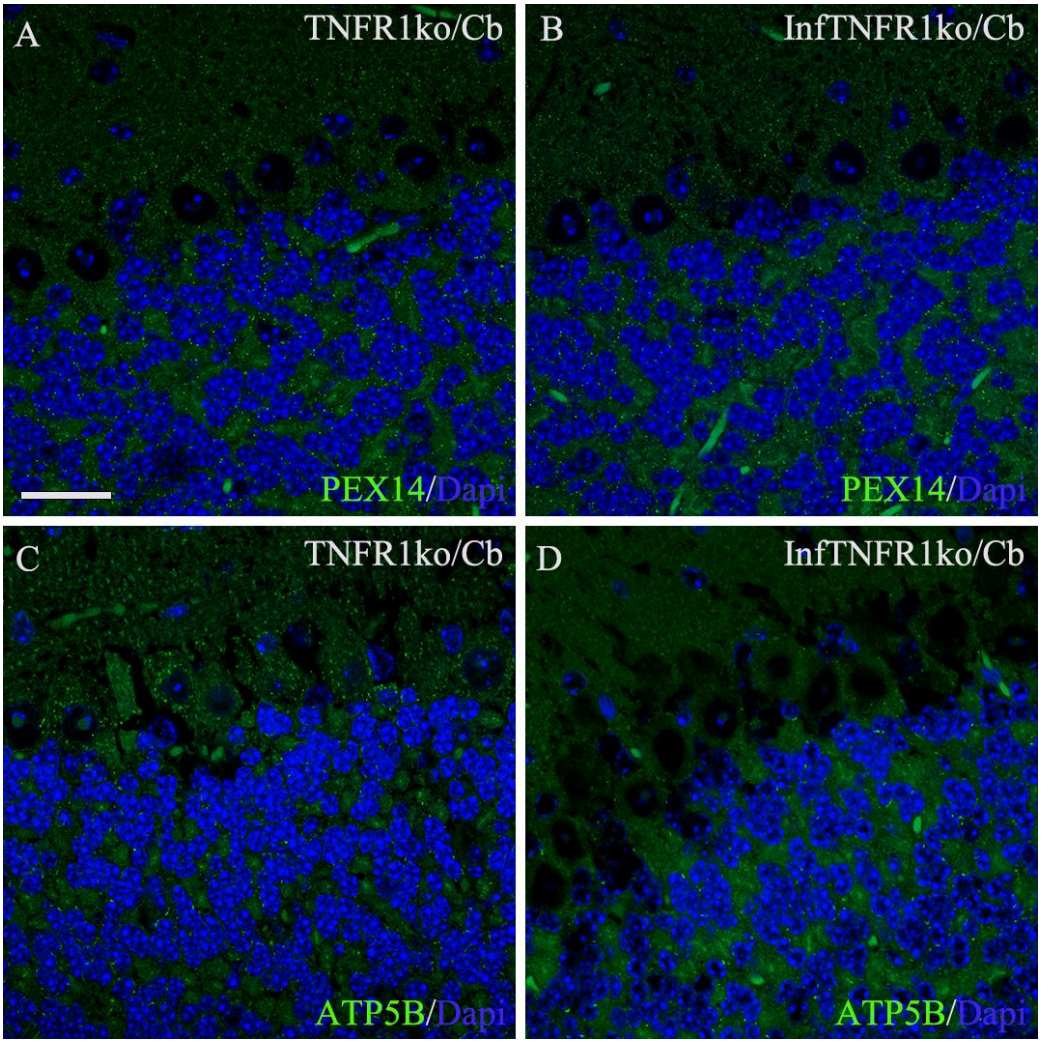

Photomicrographs of PEX14-positive peroxisomes (green) in cerebellar (Cb) granule and Purkinje neurons of non-infected (**A**) and BoDV1-infected (**B**) TNFR1ko mice, and ATP5B-positive mitochondria (green) in cerebellar granule and Purkinje neurons of non-infected (**C**) and BoDV1-infected (**D**) TNFR1ko mice. Peroxisomal abundance did not change in both granule and Purkinje neurons but that of mitochondria decreased in Purkinje neurons only and remained comparable in granule neurons of TNFR1ko mice after BoDV1 infection. DAPI (blue) is the nuclear stain. ***TNFR1ko***, TNF receptor 1 knockout; ***InfTNFR1ko***, BoDV1-infected TNFR1ko. Scale bar: 20 µm for all images.

4.2.6 Morphometric analysis of catalase and SOD2 in the hippocampus, cerebral and cerebellar cortices of BoDV1-infected TNFR1ko mice

The abundances of catalase and SOD2 in BoDV1-infected TNFR1ko were analyzed and compared to respective non-infected mice and BoDV1-infected Wt mice. Catalase abundance in BoDV1-infected TNFR1ko mice was 16/100 µm^2 in pyramidal neurons (CA band) and 17/100 µm^2 in granule neurons (DG) of the hippocampus; 1/100 µm^2 in cortical pyramidal neurons; 1/100 µm^2 and 6/100 µm^2 in cerebellar granule and Purkinje neurons, respectively (see **Appendix 3**A-E). Additionally, SOD2 abundance was 0.4% in pyramidal neurons (CA band) and 0.4% in granule neurons (DG) of the hippocampus; 0.7% in cortical pyramidal neurons; 0.4% and 0.8% in cerebellar granule and Purkinje neurons, respectively (see **Appendix 4**A-E). This shows that in all but cerebellar granule neurons (where there was a 7.0-fold decrease in catalase), no significant changes in catalase or SOD2 abundances occurred after BoDV1 infection of TNFR1ko mice (**Figures 63**A-D, **64**A-D, **65**A-D, **66**A-D; **Table 2**). However, BoDV1-infected TNFR1ko mice had higher catalase but not SOD2 abundance in most neuronal cell types [3.2-fold in pyramidal cells (CA band); 3.4-fold in granule cells (DG); and 3.0-fold in Purkinje cells (cerebellar cortex)] compared to BoDV1-infected Wt mice (**Appendices 3**A-E, **4**A-E**)**.

Figure 63: Catalase and SOD2 abundances in pyramidal neurons (CA band) of non- and BoDV1-infected TNFR1ko mice

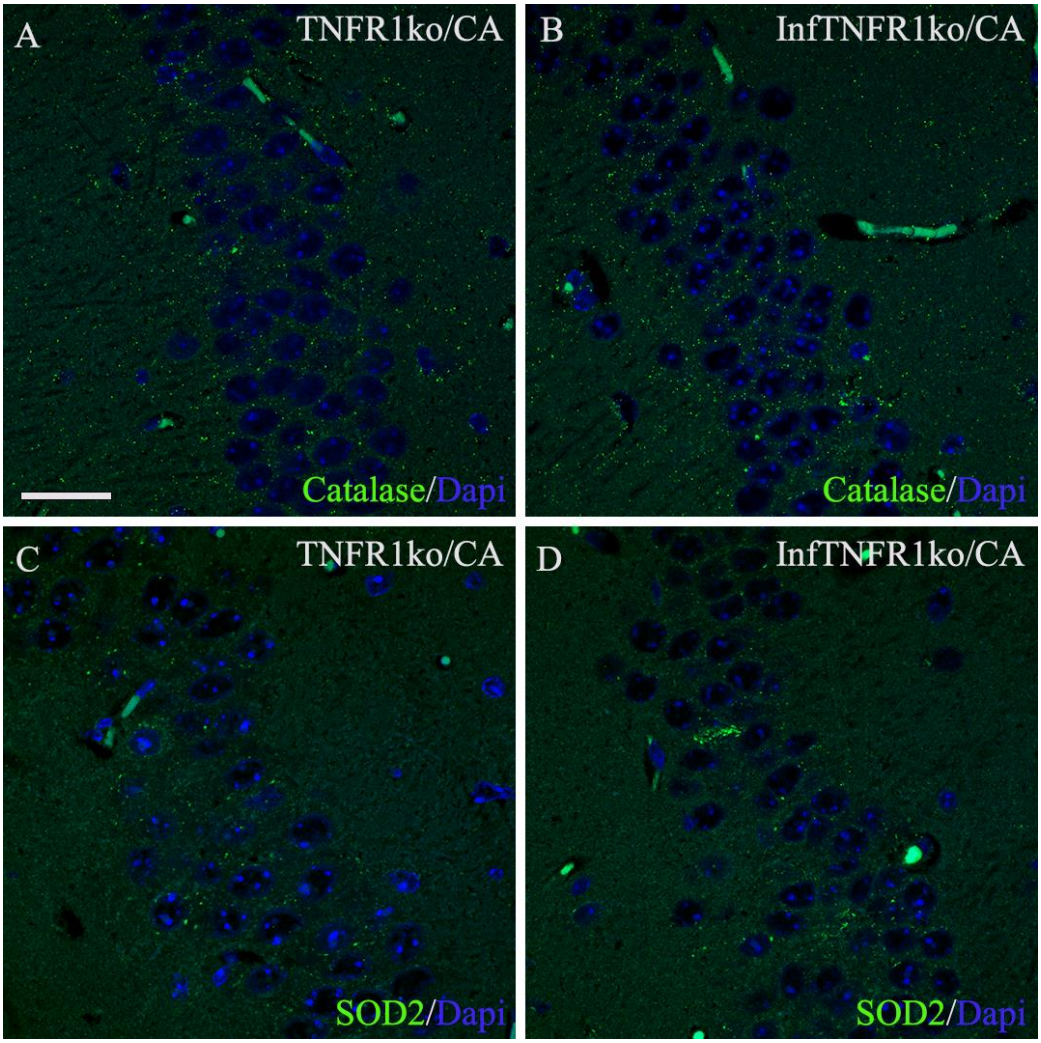

Photomicrographs of catalase-positive peroxisomes (green) in pyramidal neurons of the cornu ammonis (CA) band of non-infected (**A**) and BoDV1-infected (**B**) TNFR1ko mice, SOD2-positive mitochondria (green) in pyramidal neurons (CA band) of non-infected (**C**) and BoDV1-infected (**D**) TNFR1ko mice. No changes in catalase and SOD2 abundances in pyramidal neurons of the CA band of TNFR1ko mice after BoDV1 infection. DAPI (blue) is the nuclear stain. ***TNFR1ko***, TNF receptor 1 knockout; ***InfTNFR1ko***, BoDV1-infected TNFR1ko. Scale bar: 20 µm for all images.

Figure 64: Catalase and SOD2 abundances in granule neurons (DG) of non- and BoDV1-infected TNFR1ko mice

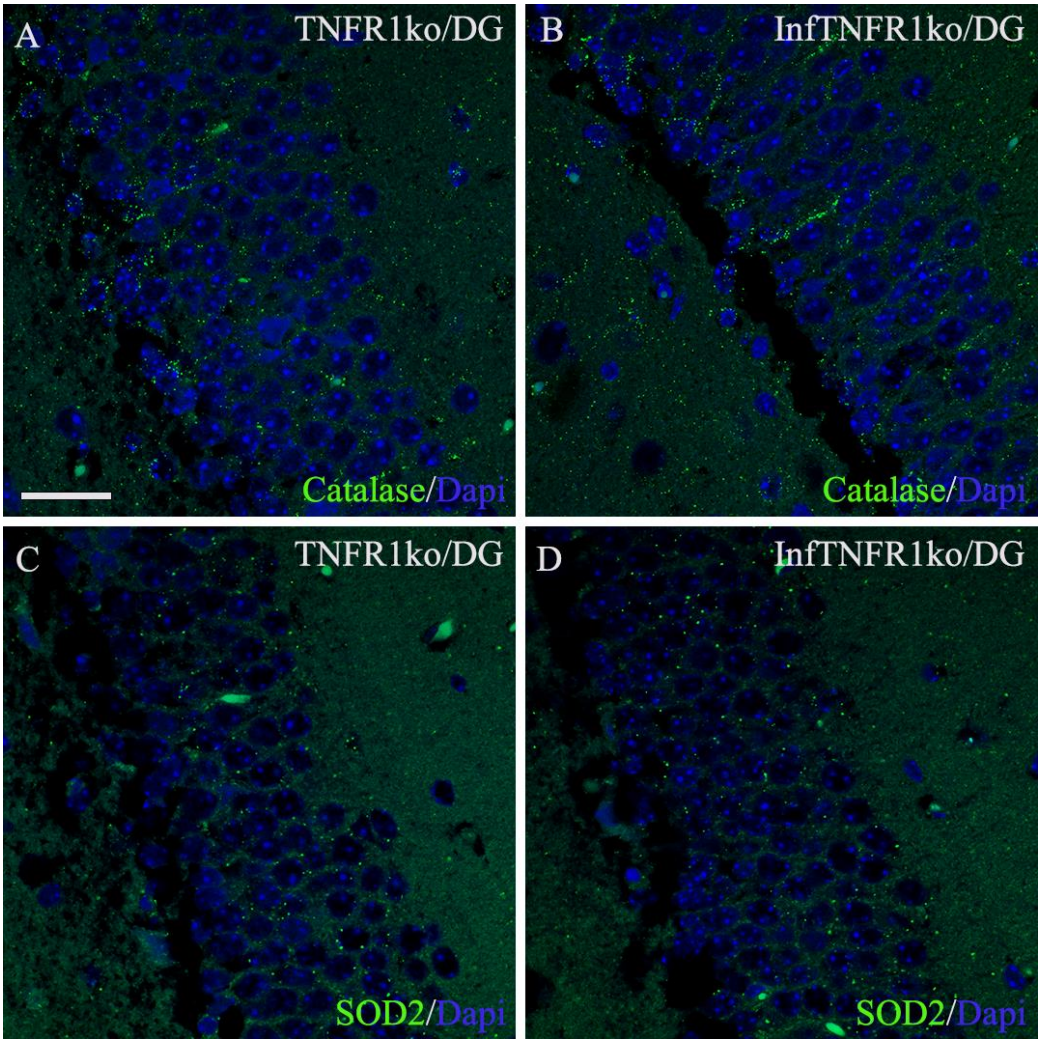

Photomicrographs of catalase-positive peroxisomes (green) in granule neurons of the dentate gyrus (DG) of non-infected (**A**) and BoDV1-infected (**B**) TNFR1ko mice, and SOD2-positive mitochondria (green) in granule neurons (DG) of non-infected (**C**) and BoDV1-infected (**D**) TNFR1ko mice. No changes in catalase and SOD2 abundances in granule neurons of the dentate gyrus of TNFR1ko mice after BoDV1 infection. DAPI (blue) is the nuclear stain. ***TNFR1ko***, TNF receptor 1 knockout; ***InfTNFR1ko***, BoDV1-infected TNFR1ko. Scale bar: 20 µm for all images.

Figure 65: Catalase and SOD2 abundances in pyramidal neurons of the cerebral cortex of non- and BoDV1-infected TNFR1ko mice

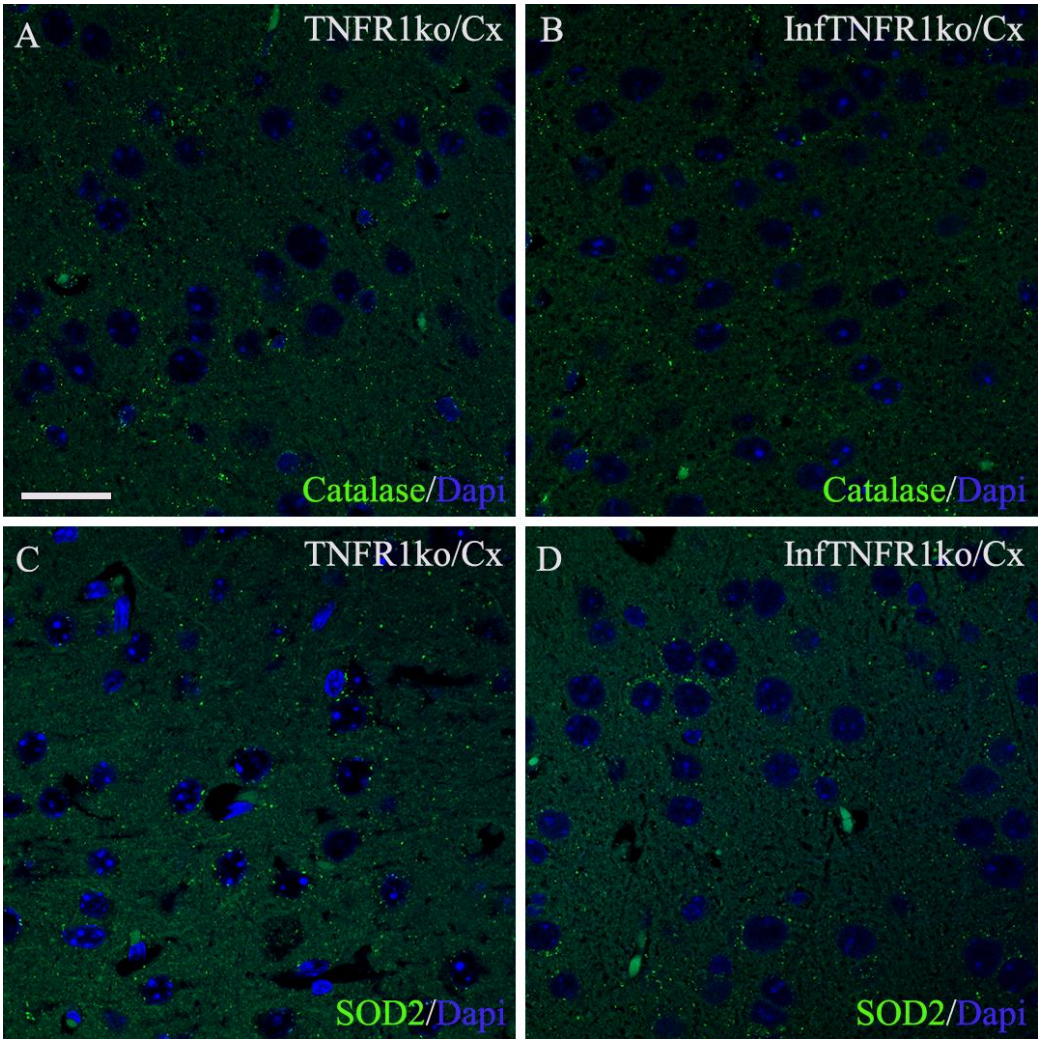

Photomicrographs of catalase-positive peroxisomes (green) in pyramidal neurons of the cerebral cortex (Cx) of non-infected (**A**) and BoDV1-infected (**B**) TNFR1ko mice, and SOD2-positive mitochondria (green) in pyramidal neurons (Cx) of non-infected (**C**) and BoDV1-infected (**D**) TNFR1ko mice. No changes in catalase and SOD2 abundances in pyramidal neurons of the cerebral cortex of TNFR1ko mice after BoDV1 infection. DAPI (blue) is the nuclear stain. ***TNFR1ko***, TNF receptor 1 knockout; ***InfTNFR1ko***, BoDV1-infected TNFR1ko. Scale bar: 20 µm for all images.

Figure 66: Catalase and SOD2 abundances in cerebellar granule and Purkinje neurons of non- and BoDV1-infected TNFR1ko

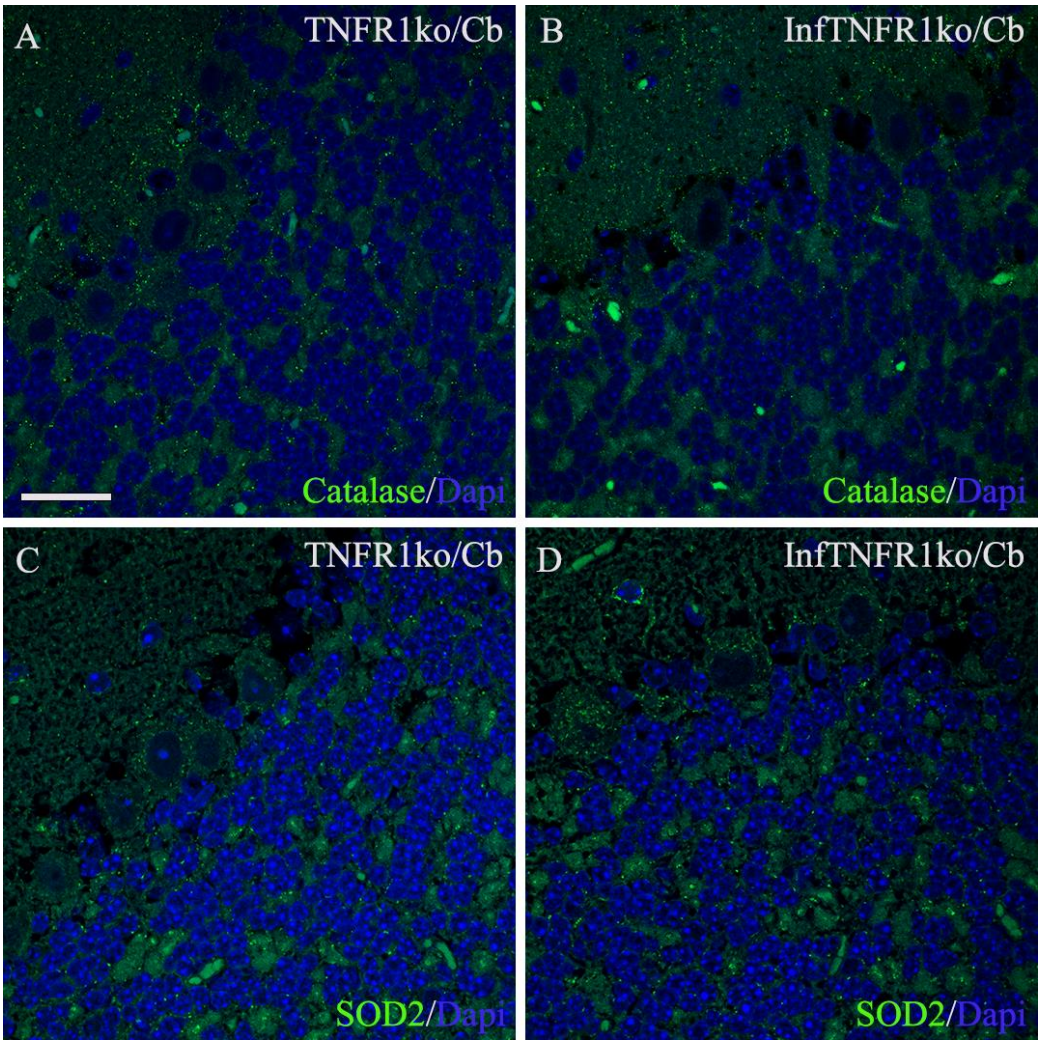

Photomicrographs of catalase-positive peroxisomes (green) in cerebellar (Cb) granule and Purkinje neurons of non-infected (**A**) and BoDV1-infected (**B**) TNFR1ko mice, and SOD2-positive mitochondria (green) in cerebellar granule and Purkinje neurons of non-infected (**C**) and BoDV1-infected (**D**) TNFR1ko mice. SOD2 abundance did not change in both granule and Purkinje neurons but catalase abundance decreased in granule neurons only of TNFR1ko mice after BoDV1 infection. DAPI (blue) is the nuclear stain. ***TNFR1ko***, TNF receptor 1 knockout; ***InfTNFR1ko***, BoDV1-infected TNFR1ko. Scale bar: 20 µm for all images.

4.2.7 Morphometric analysis of peroxisomes and mitochondria in the hippocampus, cerebral and cerebellar cortices of BoDV1-infected TNFR2ko mice

Peroxisomal and mitochondrial abundances were analyzed in BoDV1-infected TNFR2ko mice. Afterwards, the abundances were compared to those of respective non-infected mice, and BoDV1-infected TNFR1ko and Wt mice. Following BoDV1 infection of TNFR2ko mice, peroxisomal abundance was 42/100 μm^2 in pyramidal neurons (CA band) and 38/100 μm^2 in granule neurons (DG) of the hippocampus; 32/100 μm^2 in cortical pyramidal neurons; 27/100 μm^2 and 40/100 μm^2 in cerebellar granule and Purkinje neurons, respectively (see **Appendix 1**A-E). Mitochondrial abundance was 3.8% in pyramidal neurons (CA band) and 1.8% in granule neurons (DG) of the hippocampus; 6.2% in cortical pyramidal neurons; 1.6% and 6.1% in cerebellar granule and Purkinje neurons, respectively (see **Appendix 2**A-E). This indicates that after BoDV1 infection of TNFR2ko mice, peroxisomal abundance increased further in most neurons [1.2-fold in pyramidal cells (CA band); 1.5-fold in pyramidal cells (cerebral cortex); 1.2-fold in Purkinje cells (cerebellar cortex)], except in granule neurons of both DG and cerebellar cortex (**Figures 67**A,B, **68**A,B, **69**A,B, **70**A,B; **Table 2**). Conversely, the abundance of mitochondria decreased in all neuronal cell types [4.0-fold in pyramidal cells (CA band); 6.5-fold in granule cells (DG); 3.8-fold in pyramidal cells (cerebral cortex); 3.4-fold in granule cells and 5.1-fold in Purkinje cells (cerebellar cortex)] of BoDV1-infected TNFR2ko mice (**Figures 67**C,D, **68**C,D, **69**C,D, **70**C,D; **Table 2**).

The increase in peroxisomal abundance in BoDV1-infected TNFR2ko was more than that seen in BoDV1-infected Wt mice. Hence, BoDV1-infected TNFR2ko mice, in comparison to BoDV1-infected Wt mice, showed slightly higher peroxisomal abundance in most neuronal cell types [1.6-fold in pyramidal neurons (CA band); 1.4-fold in granule neurons (DG); and 1.5-fold in Purkinje neurons (cerebellar cortex], except in cortical pyramidal neurons and cerebellar granule neurons (see **Appendix 1**A-E).

BoDV1-infected TNFR2ko mice also showed slightly higher peroxisomal abundance compared to BoDV1-infected TNFR1ko [1.6-fold in pyramidal cells (CA band); 1.4-fold in granule cells (DG); 1.6-fold in pyramidal cells (cerebral cortex); and 1.3-fold in Purkinje cells (cerebellar cortex)] (see **Appendix 1**A-C,E). In addition, BoDV1-infected TNFR2ko mice had 2.5-fold higher mitochondrial abundance in pyramidal cells (CA band) compared to BoDV1-infected Wt mice (see **Appendix 2**A).

Figure 67: Peroxisomal and mitochondrial abundances in pyramidal neurons (CA band) of non- and BoDV1-infected TNFR2ko mice

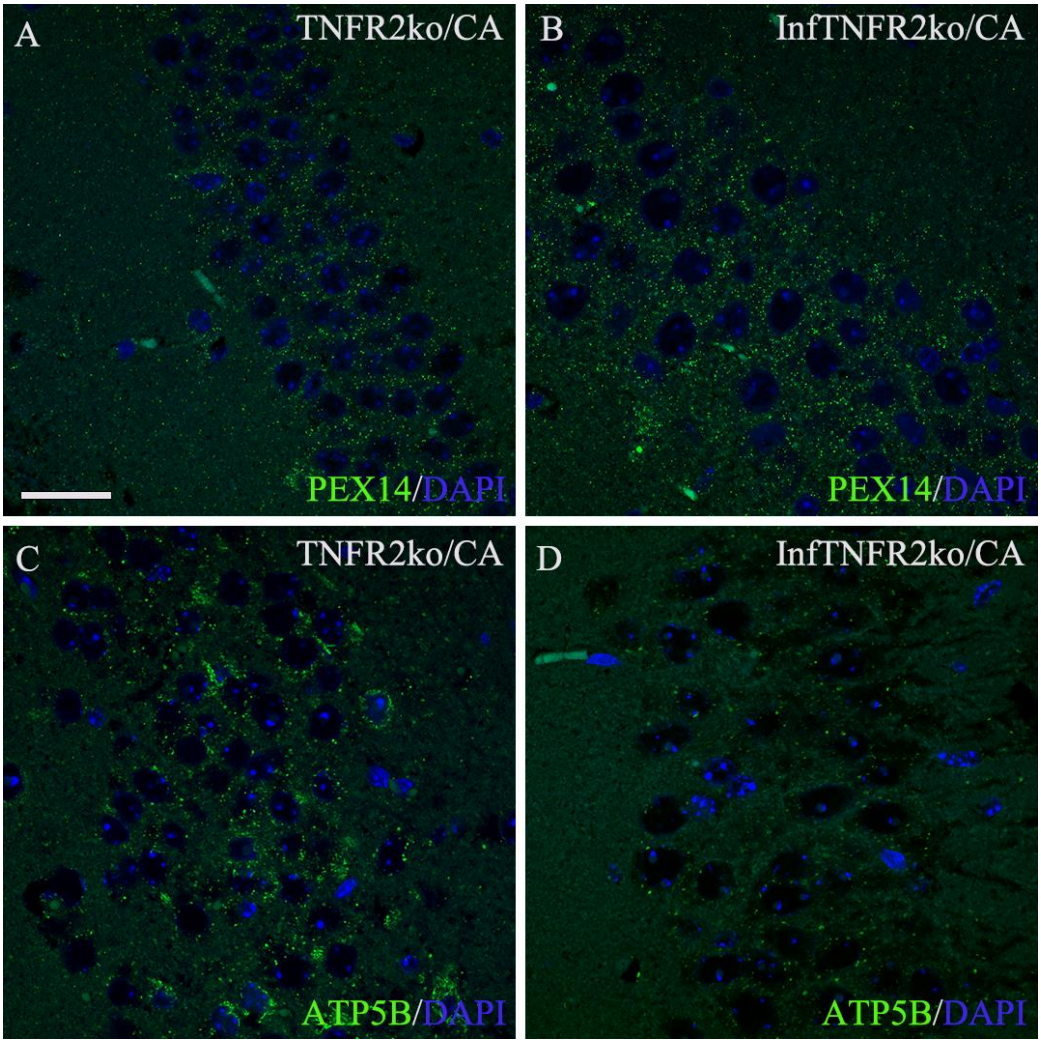

Photomicrographs of PEX14-positive peroxisomes (green) in pyramidal neurons of the cornu ammonis (CA) band of non-infected (**A**) and BoDV1-infected (**B**) TNFR2ko mice, ATP5B-positive mitochondria (green) in pyramidal neurons (CA band) of non-infected (**C**) and BoDV1-infected (**D**) TNFR2ko mice. Peroxisomal abundance increased but that of mitochondria decreased in pyramidal neurons of the CA band of TNFR2ko mice after BoDV1 infection. DAPI (blue) is the nuclear stain. ***TNFR2ko***, TNF receptor 2 knockout; ***InfTNFR2ko***, BoDV1-infected TNFR2ko. Scale bar: 20 µm for all images.

Figure 68: Peroxisomal and mitochondrial abundances in granule neurons (DG) of non- and BoDV1-infected TNFR2ko mice

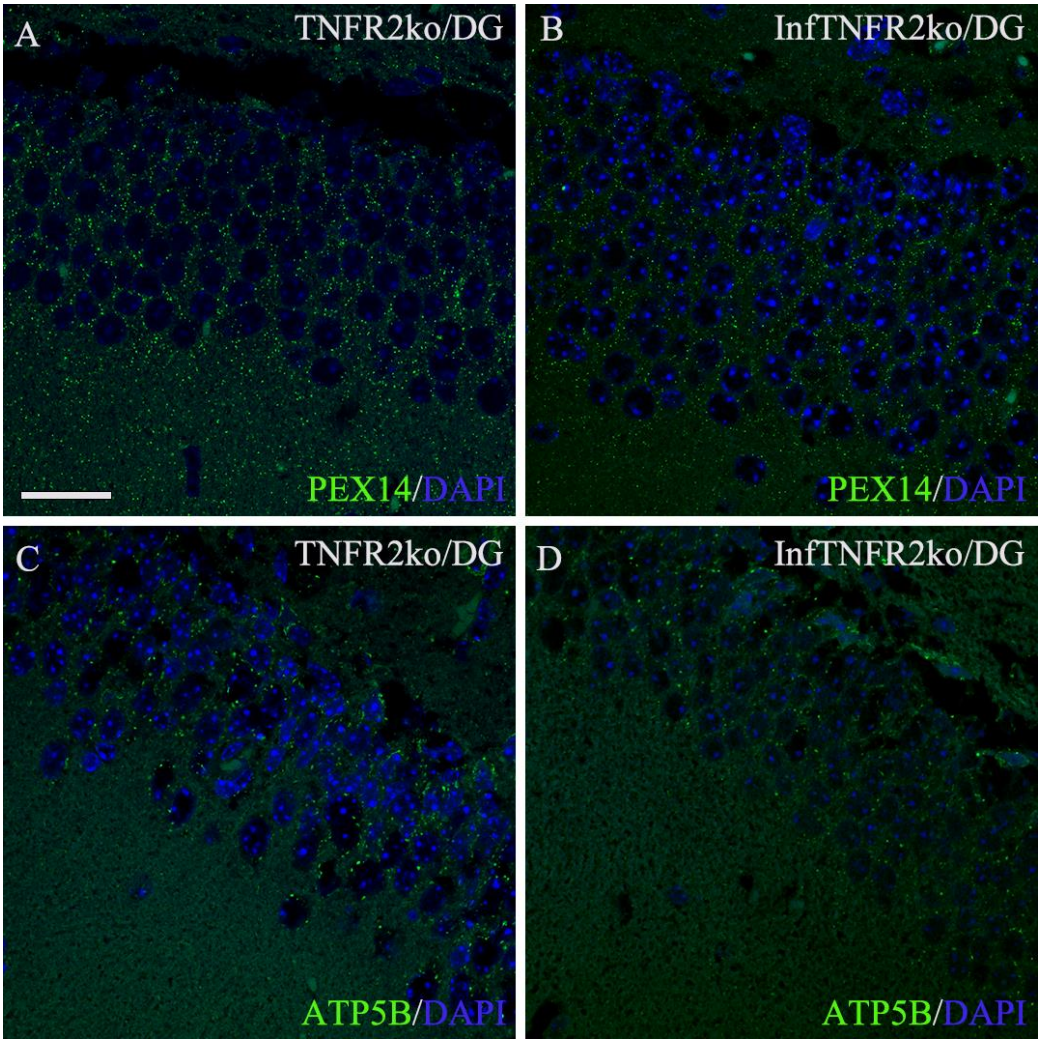

Photomicrographs of PEX14-positive peroxisomes (green) in granule neurons of the dentate gyrus (DG) of non-infected (**A**) and BoDV1-infected (**B**) TNFR2ko mice, and ATP5B-positive mitochondria (green) in granule neurons (DG) of non-infected (**C**) and BoDV1-infected (**D**) TNFR2ko mice. Peroxisomal abundance did not change but that of mitochondria decreased in granule neurons of the dentate gyrus of TNFR2ko mice after BoDV1 infection. DAPI (blue) is the nuclear stain. ***TNFR2ko***, TNF receptor 2 knockout; ***InfTNFR2ko***, BoDV1-infected TNFR2ko. Scale bar: 20 µm for all images.

Figure 69: Peroxisomal and mitochondrial abundances in pyramidal neurons of the cerebral cortex of non- and BoDV1-infected TNFR2ko mice

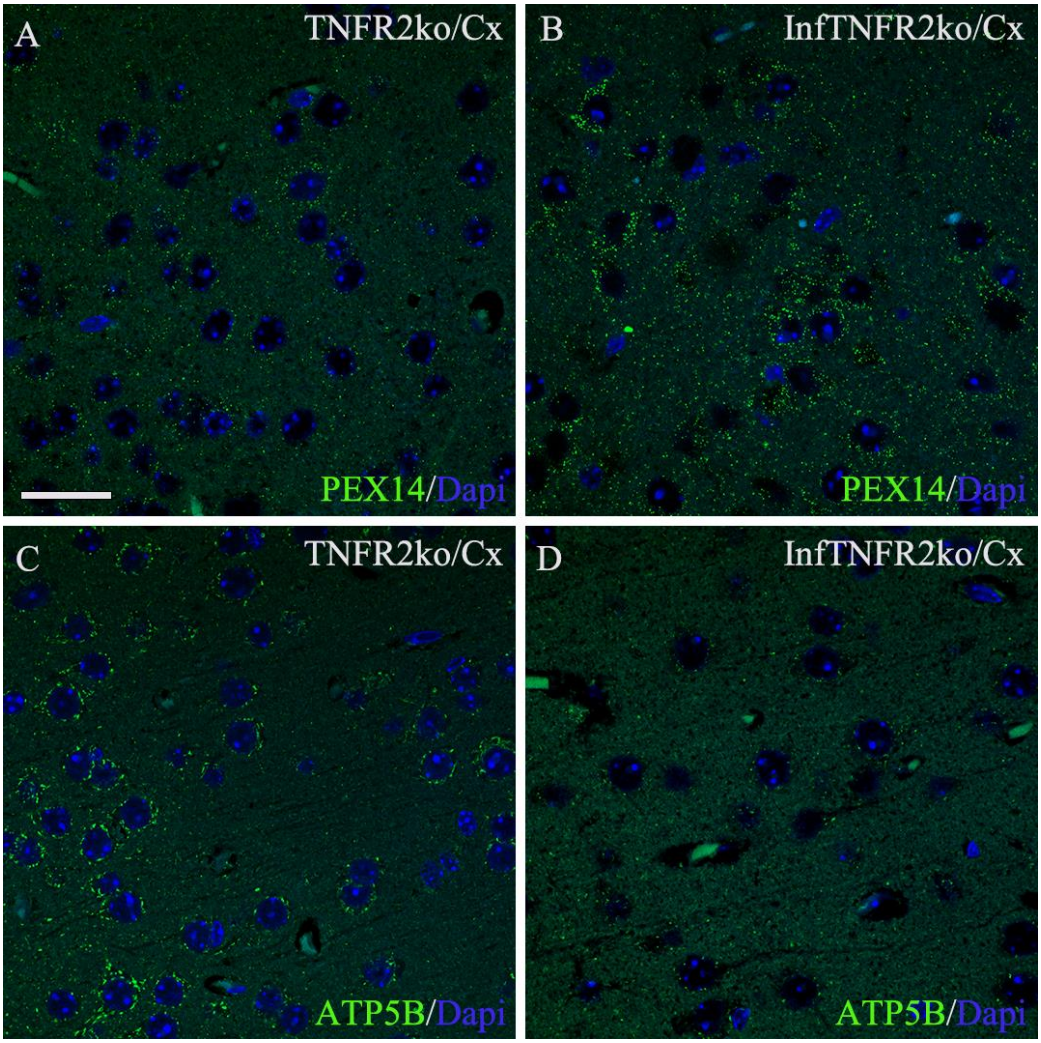

Photomicrographs of PEX14-positive peroxisomes (green) in pyramidal neurons of the cerebral cortex (Cx) of non-infected (**A**) and BoDV1-infected (**B**) TNFR2ko mice, and ATP5B-positive mitochondria (green) in pyramidal neurons (Cx) of non-infected (**C**) and BoDV1-infected (**D**) TNFR2ko mice. Peroxisomal abundance increased but that of mitochondria decreased in pyramidal neurons of the cerebral cortex of TNFR2ko mice after BoDV1 infection. DAPI (blue) is the nuclear stain. ***TNFR2ko***, TNF receptor 2 knockout; ***InfTNFR2ko***, BoDV1-infected TNFR2ko. Scale bar: 20 µm for all images.

Figure 70: Peroxisomal and mitochondrial abundances in cerebellar granule and Purkinje neurons of non- and BoDV1-infected TNFR2ko

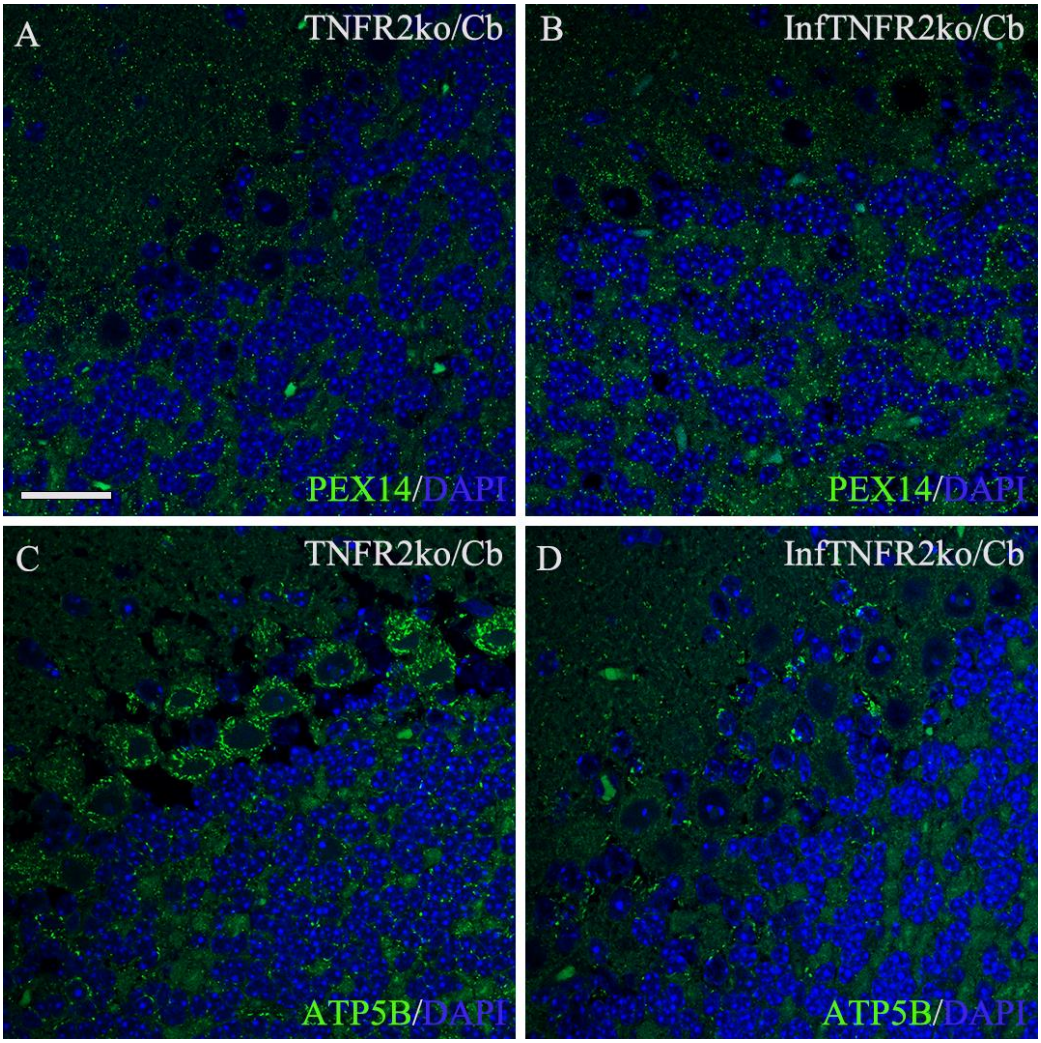

Photomicrographs of PEX14-positive peroxisomes (green) in cerebellar (Cb) granule and Purkinje neurons of non-infected (**A**) and BoDV1-infected (**B**) TNFR2ko mice, and ATP5B-positive mitochondria (green) in cerebellar granule and Purkinje neurons of non-infected (**C**) and BoDV1-infected (**D**) TNFR2ko mice. Peroxisomal abundance increased in Purkinje neurons only but that of mitochondria decreased in both granule and Purkinje neurons of the cerebellar cortex of TNFR2ko mice after BoDV1 infection. DAPI (blue) is the nuclear stain. ***TNFR2ko***, TNF receptor 2 knockout; ***InfTNFR2ko***, BoDV1-infected TNFR2ko. Scale bar: 20 µm for all images.

4.2.8 Morphometric analysis of catalase and SOD2 in the hippocampus, cerebral and cerebellar cortices of BoDV1-infected TNFR2ko mice

In BoDV1-infected TNFR2ko mice, catalase abundance was 4/100 µm^2 in pyramidal neurons (CA band) and 7/100 µm^2 in granule neurons (DG) of the hippocampus; 2/100 µm^2 in cortical pyramidal neurons; 2/100 µm^2 and 1/100 µm^2 in cerebellar granule and Purkinje neurons, respectively (see **Appendix 3**A-E). At the same time, SOD2 abundance was 0.2% in pyramidal neurons (CA band) and 0.05% in granule neurons (DG) of the hippocampus; 0.2% in cortical pyramidal neurons; 0.09% in each of cerebellar granule and Purkinje neurons (see **Appendix 4**A-E). This implies that in BoDV1-infected TNFR2ko, catalase abundance decreased in all neuronal cell types [3.8-fold in pyramidal cells (CA band); 2.6-fold in granule cells (DG); 3.0-fold in pyramidal cells (cerebral cortex); 5.0-fold in granule cells and 12.0-fold in Purkinje cells (cerebellar cortex)] (**Figures 71**A,B, **72**A,B, **73**A,B, **74**A,B; **Table 2**). SOD2 abundance decreased as well [5-fold in pyramidal cells (CA band); 8.0-fold in granule cells (DG); 3.0-fold in pyramidal cells (cerebral cortex); 3.3-fold in granule cells and 10.0-fold in Purkinje cells (cerebellar cortex)] when compared to respective non-infected mice (**Figures 71**C,D, **72**C,D, **73**C,D, **74**C,D; **Table 2**).

As a result, some neuronal cell types of BoDV1-infected TNFR2ko mice showed lower catalase abundance [4.0-fold in pyramidal cells (CA band) and 6.0-fold in Purkinje cells (cerebellar cortex)] and SOD2 abundance [8.7-fold in Purkinje cells (cerebellar cortex)] compared to BoDV1-infected TNFR1ko mice (see **Appendices 3**A,E, **4**E).

Figure 71: Catalase and SOD2 abundances in pyramidal neurons (CA band) of non- and BoDV1-infected TNFR2ko mice

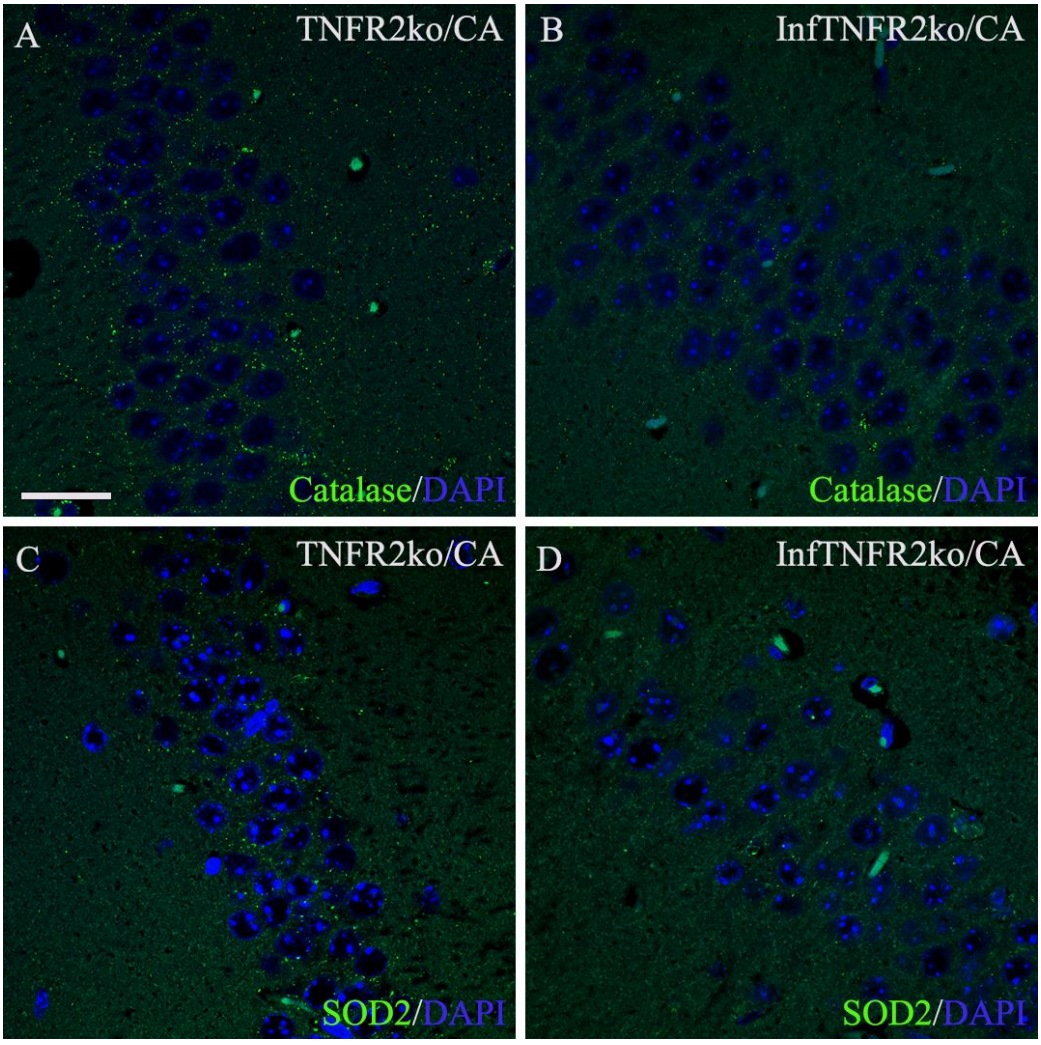

Photomicrographs of catalase-positive peroxisomes (green) in pyramidal neurons of the cornu ammonis (CA) band of non-infected (**A**) and BoDV1-infected (**B**) TNFR2ko mice, SOD2-positive mitochondria (green) in pyramidal neurons (CA band) of non-infected (**C**) and BoDV1-infected (**D**) TNFR2ko mice. Catalase and SOD2 abundances decreased in pyramidal neurons of the CA band of TNFR2ko mice after BoDV1 infection. DAPI (blue) is the nuclear stain. ***TNFR2ko***, TNF receptor 2 knockout; ***InfTNFR2ko***, BoDV1-infected TNFR2ko. Scale bar: 20 µm for all images.

Figure 72: Catalase and SOD2 abundances in granule neurons (DG) of non- and BoDV1-infected TNFR2ko mice

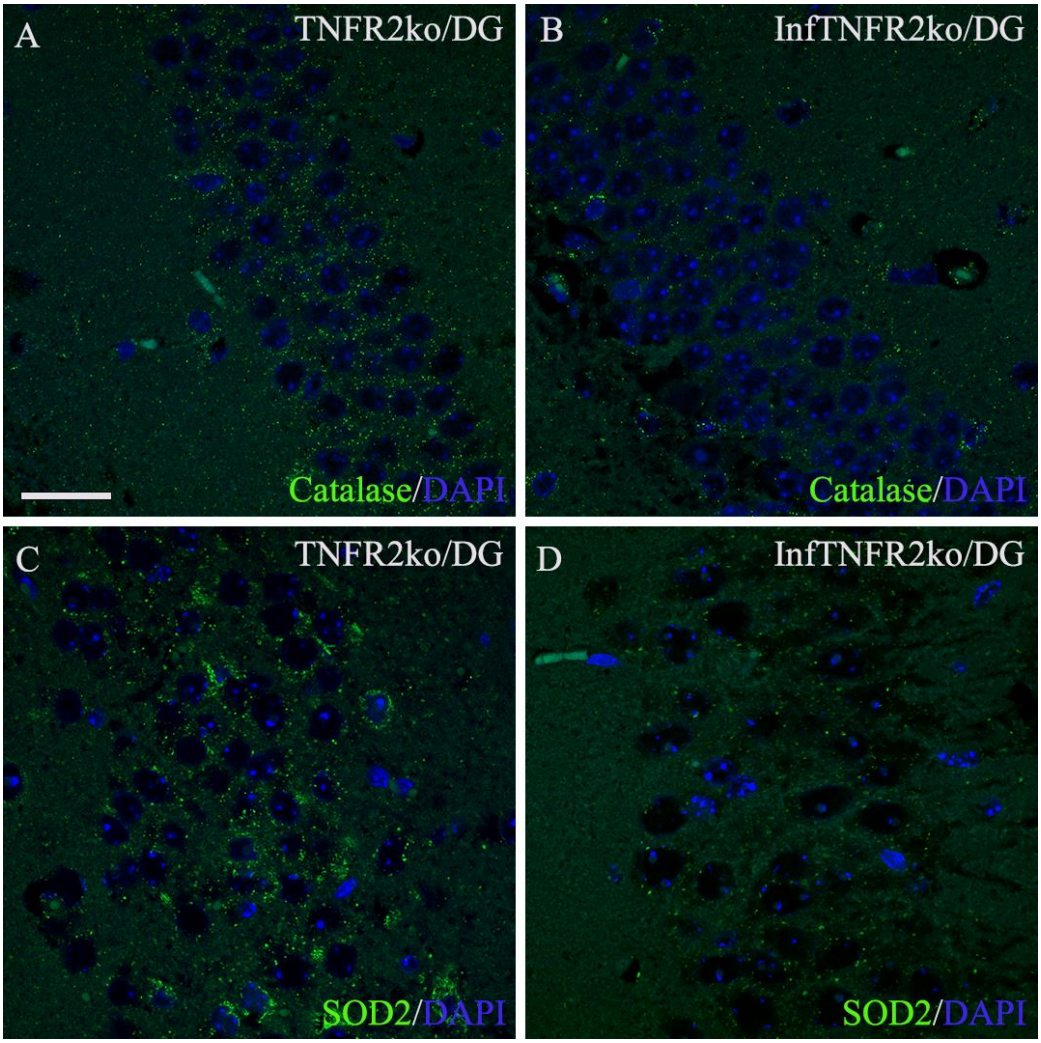

Photomicrographs of catalase-positive peroxisomes (green) in granule neurons of the dentate gyrus (DG) of non-infected (**A**) and BoDV1-infected (**B**) TNFR2ko mice, and SOD2-positive mitochondria (green) in granule neurons (DG) of non-infected (**C**) and BoDV1-infected (**D**) TNFR2ko mice. Catalase and SOD2 abundances decreased in granule neurons of the dentate gyrus of TNFR2ko mice after BoDV1 infection. DAPI (blue) is the nuclear stain. ***TNFR2ko***, TNF receptor 2 knockout; ***InfTNFR2ko***, BoDV1-infected TNFR2ko. Scale bar: 20 µm for all images.

Figure 73: Catalase and SOD2 abundances in pyramidal neurons of the cerebral cortex of non- and BoDV1-infected TNFR2ko mice

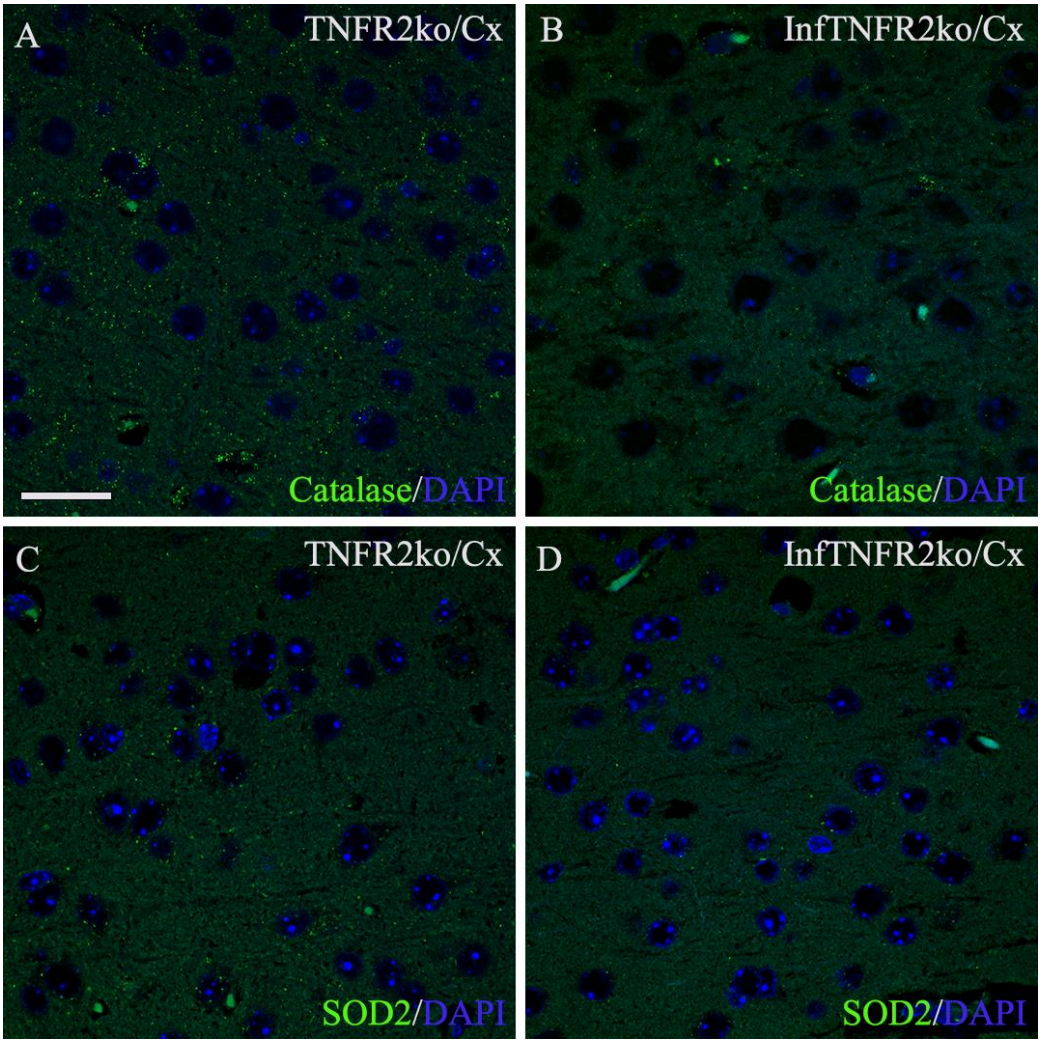

Photomicrographs of catalase-positive peroxisomes (green) in pyramidal neurons of the cerebral cortex (Cx) of non-infected (**A**) and BoDV1-infected (**B**) TNFR2ko mice, and SOD2-positive mitochondria (green) in pyramidal neurons (Cx) of non-infected (**C**) and BoDV1-infected (**D**) TNFR2ko mice. Catalase and SOD2 abundances decreased in pyramidal neurons of the cerebral cortex of TNFR2ko mice after BoDV1 infection. DAPI (blue) is the nuclear stain. ***TNFR2ko***, TNF receptor 2 knockout; ***InfTNFR2ko***, BoDV1-infected TNFR2ko. Scale bar: 20 µm for all images.

Figure 74: Catalase and SOD2 abundances in cerebellar granule and Purkinje neurons of non- and BoDV1-infected TNFR2ko

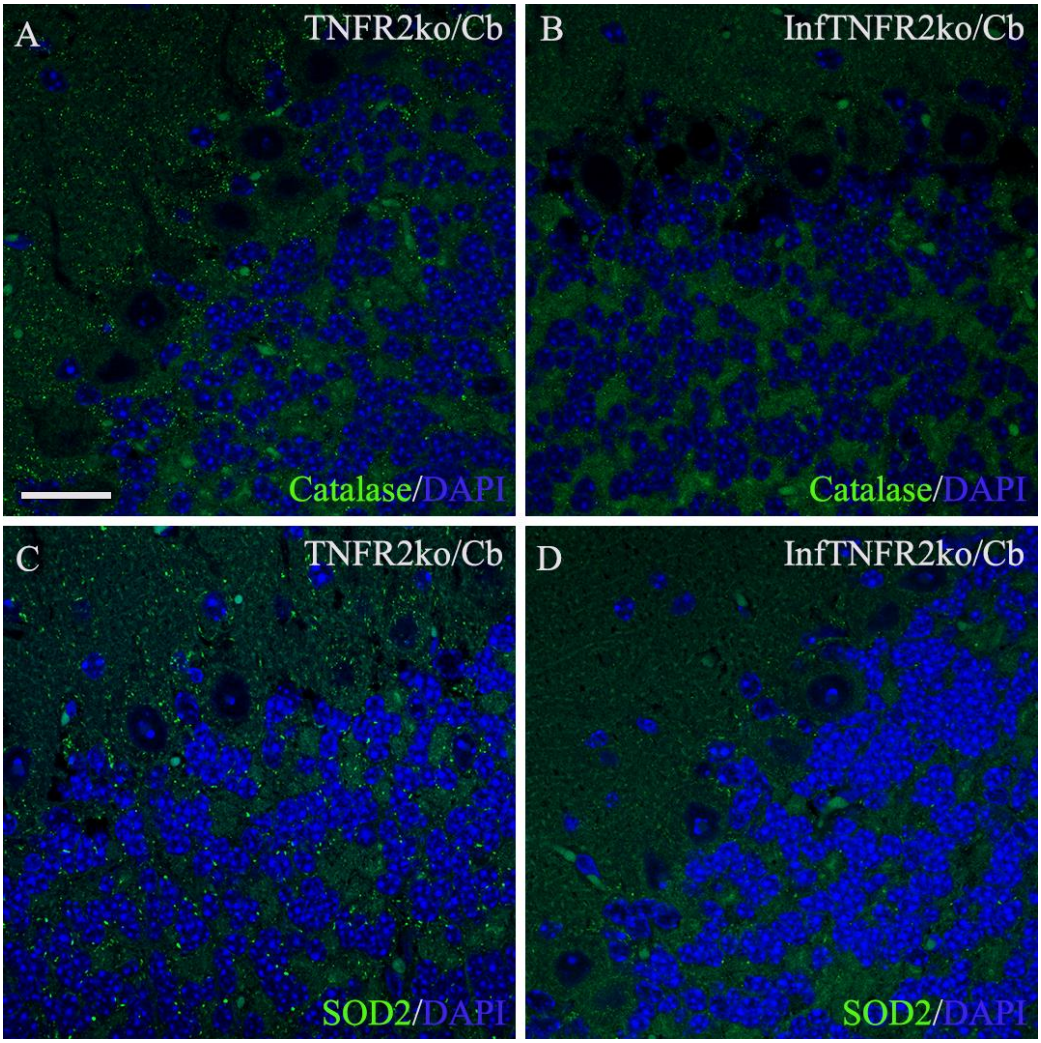

Photomicrographs of catalase-positive peroxisomes (green) in cerebellar (Cb) granule and Purkinje neurons of non-infected (**A**) and BoDV1-infected (**B**) TNFR2ko mice, and SOD2-positive mitochondria (green) in cerebellar granule and Purkinje neurons of non-infected (**C**) and BoDV1-infected (**D**) TNFR2ko mice. Catalase and SOD2 abundances decreased in both granule and Purkinje neurons of the cerebellar cortex of TNFR2ko mice after BoDV1 infection. DAPI (blue) is the nuclear stain. ***TNFR2ko***, TNF receptor 2 knockout; ***InfTNFR2ko***, BoDV1-infected TNFR2ko. Scale bar: 20 µm for all images.

Table 2: **Welch's t-test comparison of peroxisomal, mitochondrial, catalase and SOD2 abundances from the same brain region between non- and BoDV1-infected mice of the same mouse line**

	Mouse lines			
	Wt vs. InfWt	TNFTg vs. InfTNFTg	TNFR1ko vs. InfTNFR1ko	TNFR2ko vs. InfTNFR2ko
PEX14				
GrDG	*	n.s.	n.s.	n.s.
PyCA	*	n.s.	n.s.	*
PyCx	*	n.s.	n.s.	*
GrCb	**	n.s.	n.s.	n.s.
PuCb	*	n.s.	n.s.	*
ATP5B				
GrDG	n.s.	**	n.s.	****
PyCA	*	*	n.s.	**
PyCx	n.s.	***	*	***
GrCb	*	n.s.	n.s.	*
PuCb	**	*	n.s.	***
Catalase				
GrDG	****	n.s.	n.s.	**
PyCA	****	n.s.	n.s.	****
PyCx	****	n.s.	n.s.	***
GrCb	**	*	**	****
PuCb	***	**	n.s.	****
SOD2				
GrDG	n.s.	***	n.s.	**
PyCA	*	*	n.s.	*
PyCx	*	**	n.s.	**
GrCb	*	n.s.	n.s.	*
PuCb	*	*	n.s.	***

GrDG, granule neurons of dentate gyrus; **PyCA**, pyramidal neurons of cornu ammonis band; **PyCx**, pyramidal neurons of cerebral cortex; **GrCb**, granule neurons of cerebellar cortex; **PuCb**, Purkinje neurons of cerebellar cortex. ***Wt***, wild-type; ***TNFTg***, TNF-α transgenic; ***TNFR1ko***, TNF receptor 1 knockout; ***TNFR2ko***, TNF receptor 2 knockout; ***InfWt***, BoDV1-infected Wt; ***InfTNFTg***, BoDV1-infected TNFTg; ***InfTNFR1ko***, BoDV1-infected TNFR1ko; ***InfTNFR2ko***, BoDV1-infected TNFR2ko. P-values: ≥ 0.05 (n.s., non-significant); 0.01–0.05 (*); 0.001–0.01 (**); 0.0001–0.001(***); < 0.0001(****).

4.3 Summary of results

Overall, the findings of this study are summarized in the graphical abstract shown below (**Figure 75**).

Figure 75: Graphical summary of results demonstrating alterations in peroxisomal and mitochondrial dynamics, and their respective main antioxidant enzymes, before and after BoDV1 infection in different mouse lines

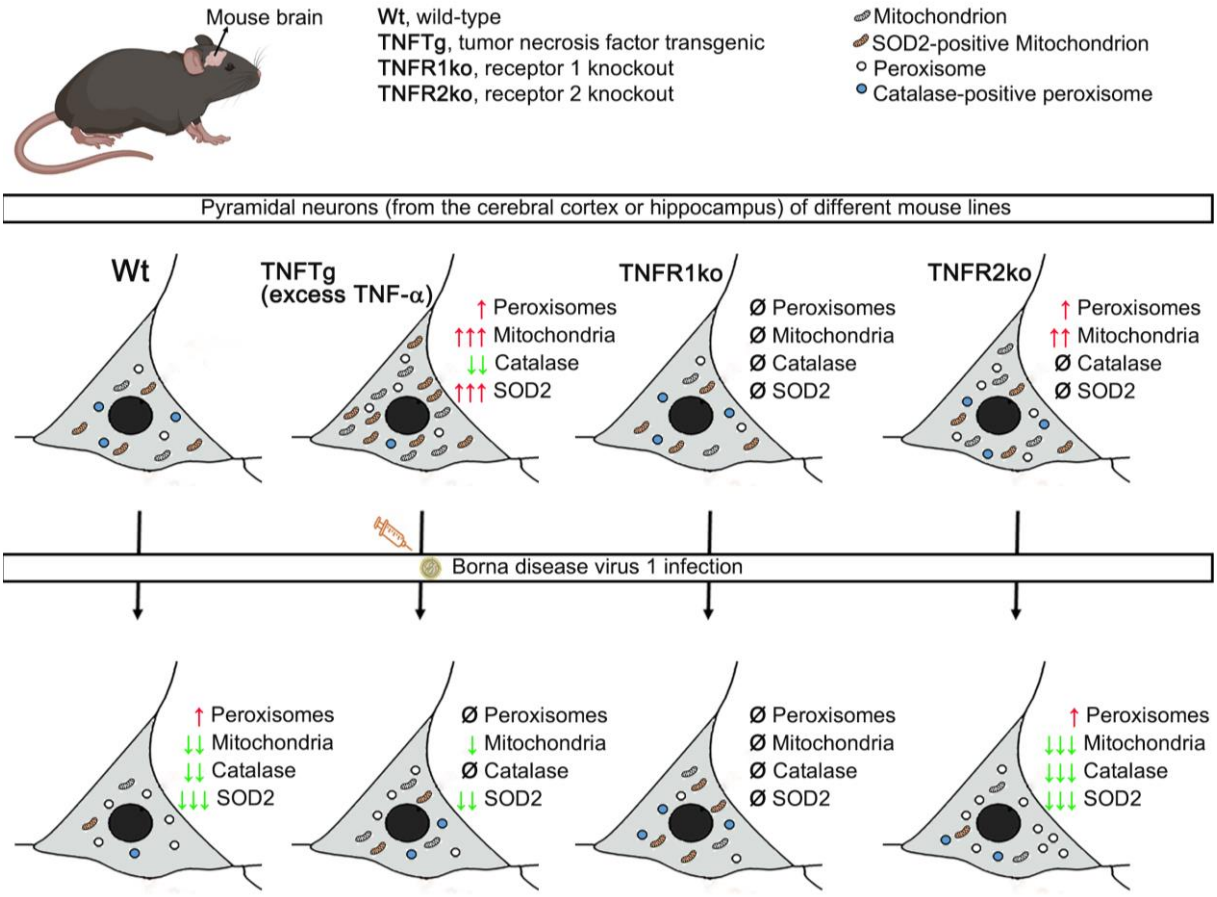

TNF-α overexpression in TNFTg mice increased peroxisomal, mitochondrial and SOD2 abundances but that of catalase decreased. Physiological, endogenous levels of TNF-α increased the abundances of both subcellular organelles and not their main antioxidant enzymes in TNFR2ko mice. BoDV1 infection decreased mitochondrial, catalase and SOD2 abundances but that of peroxisomes increased, particularly in Wt and TNFR2ko mice – no changes in TNFR1ko mice. TNF-α overexpression in TNFTg mice counteracted BoDV1-driven changes in peroxisomal and catalase abundances. Red arrow (↑), increase; green arrow (↓), decrease; Ø, no significant change (created with Biorender.com).

5. Discussion

The usage of animals in infection studies over the years has proven invaluable in understanding the pathomechanims of several diseases, including that caused by BoDV1. Moreover, the development and availability of TNF transgenic and TNF-α receptor knockout mice have advanced researches aimed at understanding the role TNF-α and its receptors. TNF-α is one main mediator of BoDV1-induced activation of the immune system (Marchetti et al., 2004; Kramer et al., 2012). Peroxisomes and mitochondria are among the major sources of ROS within eukaryotic cells, including neurons (Fransen et al. 2012); and, both organelles play critical roles in the intracellular innate antiviral immune signaling (Fransen et al., 2017; Jean et al., 2018; Elesela & Lukacs, 2021). Hence, using our mouse models with an altered TNF system, we investigated the likely changes in peroxisomal, mitochondrial, catalase, and SOD2 abundances, before and after BoDV1 infection. In this section, we discuss the: (i) role(s) of TNF-α/TNFR1/TNFR2 as regards the abundances of both subcellular compartments and their main antioxidant enzymes, catalase and SOD2, respectively, under physiological conditions; (ii) probable mechanisms underlying the BoDV1-driven changes in both organelles, catalase, and SOD2 of Wt, TNFTg, TNFR1ko, and TNFR2ko mice, with special focus on the role(s) of TNFR1 and TNFR2.

5.1 Effect of endogenous TNF-α and its overexpression on peroxisomal and mitochondrial dynamics and their main antioxidant enzymes

Comparing organelle abundances in different neuronal cell types of non-infected Wt mice, mitochondrial abundances varied markedly with only minor changes in peroxisomes. The highest abundances of mitochondria were in cerebellar Purkinje cells and cortical pyramidal neurons, probably because projection neurons need a sustainable mitochondrial energy support for saltatory conduction and transport of organelles and neurotransmitters along the axon (Hyder et al. 2013). Moreover, distinct neuronal cell types of non-infected Wt mice had different catalase and SOD2 abundances in peroxisomes and mitochondria, respectively, which might be a reflection of their respective metabolic states or functions (Hyder et al. 2013).

In non-infected TNFTg mice, chronic exposure of granule and pyramidal neurons in forebrain regions to TNF-α increased the abundance of peroxisomes – even to a higher extent the one of mitochondria – compared to non-infected Wt mice. TNF-α signaling can generate ROS, causing oxidative stress (Zelová & Hošek, 2013; Raziyeva et al., 2021), which directly inhibits

peroxisomal β-oxidation (Beier et al., 1997; Vijayan et al., 2017), leading to the accumulation of VLCFAs and activation of PPAR-α (Christofides et al., 2021). Increased levels of both ROS (Schrader & Fahimi, 2006) and VLCFAs (Lu et al., 2022) can induce peroxisomal proliferation, which might explain the increase in peroxisomes in non-infected TNFTg mice. Mitochondrial fragmentation and biogenesis can be triggered in both acute (Maeda & Fadeel et al., 2014; Delmotte et al., 2021) and chronic (Davizon-Castillo et al., 2019) exposures of neurons to TNF-α, due to TNF-α-induced increases in ROS, ER stress and activation of PGC-1α (Kastl et al., 2014; Fransen et al., 2017). Moreover, PPAR-α acts synergistically with PGC-1α to regulate the abundances and metabolic activities of peroxisomes and mitochondria (Fransen et al., 2017), hence could explain the increase in the abundances of both subcellular organelles. In acute TNF-α treatment conditions, mitochondrial fission and biogenesis occurred in murine (Brown et al., 2019) and human (Yang et al., 2022) primary neurons; human smooth muscle cells (Delmotte et al., 2021): and, in human T lymphocyte and fibroblast cell lines (Maeda & Fadeel, 2014). There is scant data on the chronic effects of TNF-α treatment on subcellular compartments such as mitochondria within different cell types (e.g. neurons). Davizon-Castillo et al. showed that elevated TNF-α in old mice, as well as the daily injection of young mice with TNF-α for 20 days, led to increased mitochondrial mass within platelets (Davizon-Castillo et al., 2019).

An important redox-based relationship exists between peroxisomes and mitochondria. Peroxisomes have the ability to integrate signals from other subcellular compartments and change their own metabolism as well as that of other organelles such as mitochondria (Titorenko et al., 2011). Several studies posit that altering peroxisomal ROS metabolism stimulates oxidative stress in mitochondria with consequent production of ROS, lowered membrane potential, and disrupted ATP generation (Koepke et al., 2007; Ivaschenko et al., 2011). In the present study, although the abundance of peroxisomes was slightly elevated in TNF-α transgenic brain areas of non-infected TNFTg mice, catalase decreased. Potential mechanisms underpinning the decrease in catalase in TNF-α transgenic brain areas include the (i) depletion of this enzyme by TNF-α-induced rising levels of ROS, (ii) inhibition of PPARγ functions by TNF-α (Cawthorn & Sethi, 2008; Lencel et al., 2011), (iii) and a defective import of catalase into peroxisomes due to rising levels of ROS (Legakis et al., 2002). Thus, in further studies, ROS, and PPARγ levels and function can be analyzed in detail to unravel the underlying mechanism(s). Similar to our findings, TNF-α treatment of microglial cells in vitro and excess TNF-α within brain tissues of multiple sclerosis patients or respective mouse models were

found to reduce catalase levels, resulting in oxidative stress (Roczkowsky et al., 2022). The acute TNF-α treatment of rat hepatocytes did not only suppress peroxisomal β-oxidation – which is a trigger of peroxisomal biogenesis – but also downregulated the expression of messenger RNAs (mRNAs) for proteins such as catalase (Beier et al., 1992; Beier et al., 1997).

The current study demonstrates that the number of mitochondria with detectable levels of SOD2 increased in the same proportion in all neuronal cell types from TNF-α overexpressing brain areas. Elsewhere, the pretreatment of cultured neurons or astrocytes with TNF-α augmented SOD2 activity (Bruce-Keller et al. 1999). SOD2 gene expression is regulated mainly by the transcription factors NRF-2, AP-1 and NF-κB (Kim et al., 2017). The binding of TNF-α to TNFR1 and TNFR2 serves as one of the main triggers of AP-1 and NF-κB (Yang et al., 2018), which might explain the increase in SOD2 in TNF-α transgenic brain areas. Peroxisomes generate more ROS than mitochondria in rat liver (Fransen et al., 2012). Assuming that is the case in neurons, the reactionary increase in mitochondrial abundance – more than that of peroxisomes – along with SOD2 could be a compensatory response to the decrease in peroxisomal catalase to help detoxify excess ROS, which further emphasizes the crosstalk between both organelles in maintaining intracellular redox homeostasis (Fransen et al., 2017). Moreover, in order to ascertain if changes in peroxisomal, mitochondrial, catalase and SOD2 abundances were due to excess TNF-α, granule and Purkinje cells of the non-transgenic cerebellar cortex of TNFTg mice were analyzed to serve as an internal control. No significant changes in either peroxisomal, mitochondrial, catalase or SOD2 abundances occurred, incriminating the prolonged TNF-α overexpression as the cause.

The data on TNFR1- and TNFR2ko mice revealed that endogenous, physiological levels of TNF-α increased peroxisomal and mitochondrial abundances via TNFR1 signaling in the absence of TNFR2, but did not affect the abundances of catalase and SOD2. Thus, physiological levels of TNF-α appear to be involved in the biogenesis of both organelles, where TNFR1 signaling upregulates whereas that of TNFR2 downregulates the abundances of both peroxisomes and mitochondria. This observation underscores the overall process by which TNF-α induces cell proliferation and differentiation, especially in progenitor cells (You et al., 2015). Moreover, since the abundances of both subcellular organelles increased but not their main antioxidant enzymes in non-infected TNFR2ko mice, it could be possible that a fraction of these organelles may (i) be immature, (ii) have defective import machineries, (iii) or effete. Nonetheless, the probable mechanism(s) underpinning the increased abundances of

peroxisomes and mitochondria in non-infected TNFR2ko mice at physiological levels of TNF-α necessitate further investigations.

5.2 Effect of BoDV1 infection on peroxisomal and mitochondrial dynamics and their main antioxidant enzymes

Viruses depend entirely on host cell machinery for their replication and proliferation; they usurp host cell metabolism and transform physiological functions (Bowie & Unterholzner, 2008; Dixit et al., 2010; Odendall & Kagan, 2017). Certain enveloped viruses exploit peroxisomal metabolism to biosynthesize lipids such as plasmalogens for their viral membrane syntheses during replication (Lazarow, 2011; Jean et al., 2018; Cook et al., 2019). In BoDV1-infected mice (especially in Wt and TNFR2ko), peroxisomal abundance increased compared to non-infected mice. Although BoDV1 replicates in the nucleus, this increase may reflect the need of peroxisomes by BoDV1 for viral membrane assembly and replication as shown in the case of influenza viruses, where an increase in peroxisomal abundance and ether phospholipid production occurred simultaneously (Tanner et al., 2014). Moreover, primary skin fibroblasts from Zellweger patients – which completely lack peroxisomes – were resistant to infection by enveloped herpesviruses (Jean et al., 2018; Cook et al., 2019). In the present study, BoDV1 distribution and persistence were comparable in all mouse lines, even in TNFR1ko where no changes in peroxisomes occurred (Kramer et al., 2012; Hirz, 2017). Overall, although peroxisomal abundance remained unchanged in the hippocampus, cerebral and cerebellar cortices of BoDV1-infected TNFR1ko mice, BoDV1 still replicated and spread to all brain regions. Hence, to suggest that peroxisomes are needed by this enveloped virus for replication may be farfetched.

Contrary to the findings of our study, some enveloped viruses decreased peroxisome numbers after infection of target cells, which was due to direct interactions between viral proteins and PEX proteins. For example, the open reading frame (ORF)-14 of SARS-CoV2 was shown to interact with human PEX14 (Knoblach et al., 2021); the capsid proteins of West Nile and Dengue viruses targeted PEX19 (You et al., 2015); and the NS2A protein of Zika virus bound to PEX3 and PEX19 (Coyaud et al., 2018), all leading to an inhibition of peroxisomal biogenesis. In addition, HIV infection caused an upregulation of micro RNAs in the brain of patients as well as in transfected macrophages, leading to loss of peroxisomes – these micro RNAs targeted mRNAs encoding peroxisomal biogenesis proteins like PEX2, PEX7, PEX11β and PEX13 (Xu et al., 2017).

Further, BoDV1 infection decreased mitochondrial abundance in all mouse lines except TNFR1ko mice – the pattern of decrease was similar in Wt and TNFR2ko mice. Generally, enveloped viruses hinder mitochondrial biogenesis and/or stimulate mitophagy due to organelle injury (Refolo et al., 2020; Burtscher et al., 2020; Elesela & Lukacs, 2021). This promotes viral escape of the innate antiviral immune system and replication (You et al., 2015; Jean et al., 2018; Ferreira et al., 2019; Elesela & Lukacs, 2021). After the entry of a virus into a host cell, viral nucleic acids – whether single- or double stranded RNA or DNA – and proteins are recognized by PRRs in the cytosol or on endosomes (Bowie & Unterholzner, 2008; Hennessy & McKernan, 2021; Elesela & Lukacs, 2021). One particular PRR, the RLRs, interact with MAVS situated on both peroxisomes and mitochondria. The X protein of BoDV1 can interact with MAVS on mitochondria, curtailing both the antiviral response engineered by this organelle and the apoptosis of BoDV1-infected neurons, which promotes the perpetual infection of brain cells (Poenisch et al., 2009; Li et al., 2013; Ferré et al., 2016). Szelechowski et al. showed that the X protein induced mitochondrial filamentation (Szelechowski et al., 2014); however, our study demonstrates that BoDV1 infection caused mitochondrial loss in neurons. Our investigation used the whole compliment of a mouse-adapted strain of BoDV1, and not just the X protein as used by Szelechowski et al., which may account for the differences in mitochondrial dynamics. Nevertheless, precisely how mitochondrial abundance decreased requires further investigations. Mitochondrial loss hinders MAVS aggregation, resulting in a dampened downstream innate antiviral signaling, consequently enhancing viral persistence in the CNS (Bowie & Unterholzner, 2008; Odendall & Kagan, 2017; Chathuranga et al., 2021). In other studies, Hepatitis B (Kim et al., 2013; Hossain et al., 2020) and C viruses (Kim et al., 2013, Kim et al., 2014; Javed et al., 2018) shifted mitochondrial dynamics toward fission and mitophagy, which attenuated virus-induced apoptosis of host cells and reduced ROS generation from mitochondria, resulting in a dampened immune response (Elesela & Lukacs, 2021). The mitochondrion-localized inhibitor of apoptosis of human cytomegalovirus virus also induced mitochondrial fragmentation and loss, stifling downstream innate immune signaling (Castanier et al., 2010).

As part of attempts by neurons to eliminate microbes, ROS may be generated, followed by an increase in antioxidant enzymes (Elesela & Lukacs, 2021). Depending on the degree or duration of inflammation, neurons lose their capacities to detoxify rising levels of ROS, thereby, oxidative stress sets in with deleterious damage to subcellular organelles and their functions (Terlecky et al., 2012; Muhammad, 2020; Elesela & Lukacs, 2021). Hence, the decrease in catalase and SOD2 in different brain regions after BoDV1 infection, particularly in Wt and

TNFR2ko mice, very likely destabilized intracellular redox homeostasis, leading to oxidative stress, mitochondrial damage and loss. The decrease in catalase and SOD2 implies that BoDV1 infection of the CNS generated H_2O_2 and $O_2^{\cdot -}$. After experimental exposure to BoDV1, neonatal mice may develop BD (TNFTg mice develop seizures), typified by a non-purulent meningoencephalitis with microglial activation and unusual astrogliosis (Kramer et al., 2012; Hirz, 2017). Therefore, reduced levels of catalase and SOD2 and potentially increased ROS may be part of the mechanisms by which BoDV1 causes changes in glial morphology or metabolism and neuronal metabolism.

Unlike peroxisomes, where there was an increase in abundance, mitochondrial abundance along with SOD2 and catalase abundances decreased in several distinct neuronal cell types following BoDV1 infection. This was the case for Wt and TNFR2ko mice but not in TNFR1ko mice, incriminating TNFR1 signaling as a major role-player in the observed BoDV1-driven changes of the peroxisomal and mitochondrial compartments. Generally, TNFR1- and TNFR2-signaling have opposite effects on neurons (Bruce-Keller et al. 1999; Muhammad, 2020). Even though TNFR1ko and TNFR2ko mice showed comparable inflammatory and astrocytic changes in the brain after BoDV1 infection (Hirz, 2017), peroxisomal and mitochondrial dynamics as well as their antioxidant capacities were markedly altered in neurons of TNFR2ko mice than in TNFR1ko mice. Since the loss of mitochondria, SOD2 and catalase can be detrimental to cells, these findings buttress the generally accepted, overall protective and pro-survival roles of TNFR2 (McCoy & Tansey, 2008; Kramer et al., 2012; Muhammad, 2020). In other studies, mTNF-α/TNFR2 signaling (in the absence of TNFR1) truncated the ischemic destruction of retinal tissue (Fontaine et al, 2002) and autoimmune encephalomyelitis (Suvannavejh et al., 2000). Additionally, Wt and TNFR1ko mice pre-sensitized with TNF-α or agonistic TNFR2-specific antibodies were tolerant to excitotoxicity, whereas neurons from TNFR2ko died after glutamate and/or TNF-α treatments (Marchetti et al, 2004). In another mouse model – where mice were infected with *Listeria monocytogenes* –,TNFR2 enhanced the survival and clonal expansion of CD4+ and CD8+ T cells by inhibiting apoptosis (Kim et al., 2006). In a non-inflammatory physiological environment, the deletion of TNFR2 in mouse brain impaired motor functions, novel object and spatial memory recognition and increased anxiety-like behavior, whereas the deletion of TNFR1 conferred insusceptibility to age-mediated anxiety-like behavior (Naudé et al., 2014).

After BoDV1 infection of TNFTg mice, peroxisomal and catalase abundances did not change in neuronal cell types from transgenic brain areas; however, mitochondrial and SOD2

abundances decreased, although still at a higher level than found in BoDV1-infected Wt mice. Suggestively, subjecting TNF-α-primed neurons to a second insult (i.e. BoDV1) counteracted, to some extent, the BoDV1-driven modifications of the peroxisomal compartment. Marchetti et al. demonstrated that TNF-α overexpression in mice substantially protects primary cortical neurons from glutamate-induced apoptosis (Marchetti et al., 2004). In the cerebellar cortex of TNFTg mice, where TNF-α overexpression is much lower compared to forebrain regions, catalase abundance decreased in both Purkinje and granule neurons whilst SOD2 abundance increased in Purkinje neurons but remained unchanged in granule neurons. Noteworthy, there seems to be a counteractive response by the mitochondrial compartment to the decreased antioxidant capacity of peroxisomes in the non-transgenic cerebellar cortex after BoDV1 infection, which reinforces the popular notion about the redox-based crosstalk between peroxisomes and mitochondria (Koepke et al., 2007; Ivaschenko et al., 2011).

5.3 Outlook

The findings of this study emphasizes the relevance of transgene and knockout technologies in animal infection studies. Using IF staining technique, the quantitative, morphometric analyses of the peroxisomal and mitochondrial compartments in three different brain areas (i.e. hippocampus, cerebral and cerebellar cortices) of Wt, TNFTg, TNFR1ko and TNFR2ko mice, with and without BoDV1 infection, were carried out. We discovered that moderately overexpressed TNF-α, as well endogenous TNF-α in the absence of TNFR2, could lead to changes in the peroxisomal and mitochondrial abundance in several distinct neuronal cell types – in the case of overexpression, modifications of their main antioxidant enzymes also occurred. Nonetheless, in addition to the IF stainings performed in the present study, electron microscopy could have been done to observe the structures of peroxisomes and mitochondria, which may reveal any possible changes in the sizes and shapes of these subcellular organelles in neurons, particularly after BoDV1 infection of mice. Further, molecular biology and biochemical methods (e.g. enzyme or by-product assays) may help find out if the BoDV1-mediated increase in peroxisomes occurred via the disruption of β-oxidation of VLCFAs or the interactions of peroxisomes with certain viral proteins promoted lipid synthesis for BoDV1 membrane assembly. Additional investigations into mitochondrial respiratory functions, membrane potential, and the mitophagic process may also help identify any BoDV1-driven functional derangements in the mitochondrial compartments, which possibly led to mitochondrial loss in several neuronal cell types after BoDV1 infection of mice.

Moreover, our study shows that BoDV1 infection altered the antioxidant capacity of peroxisomes and mitochondria, which provides a lead for future studies to determine the levels of ROS (including H_2O_2, $O_2^{\cdot -}$ etc.) in the hippocampus, cerebral and cerebellar cortices. This could confirm if changes in ROS levels occurred alongside the alterations in abundances of both organelles and their antioxidant enzymes. Additionally, semi-quantitative protein analysis (e.g. western blot) could be done in tandem to the IF stainings to verify the fluorescent antibody detection patterns of peroxisomal PEX14 and catalase, as well as that of mitochondrial ATP5B and SOD2 analyzed in this study. Drugs or chemicals blocking specific proteins or enzymes at different stages along TNFR1/2 signaling may also help unravel the mechanism(s) behind how TNFR1 signaling mediated the BoDV1-induced changes in both subcellular organelles and their main antioxidant enzymes. Although peroxisomes are prime targets for enveloped viruses for their viral membrane components, morphometric and quantitative analyses of the endoplasmic reticulum (main site for lipid synthesis) could be performed in future studies to better understand the versatility of BoDV1 in interacting with all sites of lipid synthesis in neurons during BoDV1 infection.

In the natural setting, BoDV1 infection progresses to BD mainly in horses and sheep, and sometimes in humans. In order to shed more light on the differences in susceptibility of different species of animals (e.g. horses, sheep, and humans) to natural BoDV1 infections, the abundances of peroxisomes and mitochondria and their main antioxidant enzymes can be analyzed using brain samples of dead hosts.

6. Summary

Borna disease virus 1 (BoDV1) causes persistent infection in the mammalian brain, characterized by glial activation and T cell-mediated immunopathological neuroinflammation in susceptible end hosts. Peroxisomes and mitochondria play essential roles in cellular antiviral immune response, but the effect of BoDV1 infection on peroxisomal and mitochondrial dynamics and their main antioxidant enzymes was still not clear. This study used different mouse lines – i.e. tumor necrosis factor-α transgenic (TNFTg), TNF receptor-1 knockout (TNFR1ko), and TNFR2ko mice in comparison to wild-type (Wt) mice – in a model where 42-day-old non-infected mice were compared to respective BoDV1-infected mice and the other mouse lines. In the TNFTg mouse line, moderate overexpression of TNF-α in the forebrain regions creates a proinflammatory state, mimicking chronic inflammation. Focusing on the hippocampus, cerebral and cerebellar cortices, the abundances of peroxisomes and mitochondria alongside their main antioxidant enzymes, catalase and superoxide dismutase 2 (SOD2), respectively, were analyzed in several distinct neuronal cell types of each mouse line, with or without BoDV1 infection. In non-infected Wt mice, mitochondrial but not peroxisomal abundances were highest in cerebral pyramidal neurons and cerebellar Purkinje neurons. In non-infected TNFTg mice, a strong increase in mitochondrial (6.9-fold) and SOD2 (12.1-fold) abundances was detected; peroxisomal abundance increased slightly (1.5-fold), but that of catalase decreased (2.9-fold). Unlike in non-infected TNFR1ko (where no changes occurred), the abundances of both subcellular organelles, but not of their antioxidant enzymes, increased in non-infected TNFR2ko mice. Following BoDV1 infection, a strong decrease in mitochondrial (2.1–6.5-fold), SOD2 (2.7–9.1-fold), and catalase (2.7–10.3-fold) abundances, but a slight increase in peroxisomes (1.3–1.6-fold) were seen in Wt and TNFR2ko mice. Little or no changes occurred in BoDV1-infected TNFR1ko mice. Chronic TNF-α overexpression in TNFTg mice hampered changes in peroxisome and catalase abundances after BoDV1 infection, but not that of mitochondria and SOD2. The findings of this study suggest that the TNF system is involved in the biogenesis of peroxisomes and mitochondria. Moreover, TNFR1 signaling mediated the BoDV1-induced alterations of both organelles and the availability of their main antioxidant enzymes, highlighting new mechanisms by which BoDV1 could evade the innate immune system and achieve viral persistence.

7. Zusammenfassung

Das Borna Disease Virus 1 (BoDV1) verursacht eine anhaltende Infektion im Gehirn von Säugetieren, die durch Glia-Aktivierung und T-Zell-vermittelte immunopathologische Neuroinflammation bei empfänglichen Endwirten gekennzeichnet ist. Peroxisomen und Mitochondrien spielen eine entscheidende Rolle bei der zellulären antiviralen Immunantwort, aber die Auswirkung einer BoDV1-Infektion auf die peroxisomale und mitochondriale Dynamik und ihre jeweiligen antioxidativen Kapazitäten, Catalase und SOD2, war noch nicht klar. Diese Studie verwendete verschiedene Mauslinien – d. h. Tumor-Nekrose-Faktor-α-transgene (TNFTg), TNF-Rezeptor-1-Knockout- (TNFR1ko) und TNFR2ko-Mäuse im Vergleich zu Wildtyp-Mäusen (Wt) – in 42 Tage alten, nicht infizierten und BoDV1-infizierten Mäusen. In der TNFTg-Mauslinie führte eine mäßige Überexpression von TNF-α in den Vorderhirnregionen zu einem proinflammatorischen Zustand, der einer chronischen Entzündung entspricht. Es wurde der Hippocampus, die Großhirn- und die Kleinhirnrinde mit jeweils unterschiedlichen neuronalen Zelltypen analysiert. Bei nicht infizierten Wt-Mäusen waren die mitochondrialen, aber nicht die peroxisomalen Häufigkeiten in den Pyramidenneuronen der Hirnrinde und den Purkinje-Neuronen des Kleinhirns am höchsten. Bei nicht infizierten TNFTg-Mäusen wurde ein starker Anstieg der mitochondrialen (6,9-fach) und SOD2-Häufigkeit (12,1-fach) festgestellt; Die peroxisomale Häufigkeit nahm leicht zu (1,5-fach), die von Katalase nahm jedoch ab (2,9-fach). Anders als bei nicht infizierten TNFR1ko-Mäusen (wo keine Veränderungen auftraten) nahm bei nicht infizierten TNFR2ko-Mäusen die Häufigkeit beider Organellen zu, nicht jedoch die ihrer antioxidativen Enzyme. Nach einer BoDV1-Infektion kam es zu einem starken Rückgang der Häufigkeit von Mitochondrien (2,1–6,5-fach), SOD2 (2,7–9,1-fach) und Katalase (2,7–10,3-fach). Ein leichter Anstieg der Peroxisomen (1,3–1,6-fach) wurden bei Wt- und TNFR2ko-Mäusen beobachtet, wohingegen bei TNFR1ko-Mäusen keine Veränderungen auftraten. Die chronische Überexpression von TNF-α bei TNFTg-Mäusen beeinträchtigte Veränderungen der Peroxisomen- und Katalasehäufigkeit nach einer BoDV1-Infektion, nicht jedoch die von Mitochondrien und SOD2. Die Ergebnisse dieser Studie legen nahe, dass das TNF-System an der Biogenese von Peroxisomen und Mitochondrien beteiligt ist. Darüber hinaus vermittelte die TNFR1-Signalübertragung die BoDV1-induzierten Veränderungen beider Organellen und die Verfügbarkeit ihrer wichtigsten antioxidativen Enzyme, was neue Mechanismen aufzeigt, durch die BoDV1 das angeborene Immunsystem umgehen und somit eine Persistenz erreichen könnte.

8. References

Ahlemeyer, B., Gottwald, M., & Baumgart-Vogt, E. (2012). Deletion of a single allele of the Pex11β gene is sufficient to cause oxidative stress, delayed differentiation and neuronal death in mouse brain. *Disease models & mechanisms*, *5*(1), 125–140. https://doi.org/10.1242/dmm.007708

Ahlemeyer, B., Neubert, I., Kovacs, W. J., & Baumgart-Vogt, E. (2007). Differential expression of peroxisomal matrix and membrane proteins during postnatal development of mouse brain. *The Journal of comparative neurology*, *505*(1), 1–17. https://doi.org/10.1002/cne.21448

Amarasinghe, G. K., Ayllón, M. A., Bào, Y., Basler, C. F., Bavari, S., Blasdell, K. R., Briese, T., Brown, P. A., Bukreyev, A., Balkema-Buschmann, A., Buchholz, U. J., Chabi-Jesus, C., Chandran, K., Chiapponi, C., Crozier, I., de Swart, R. L., Dietzgen, R. G., Dolnik, O., Drexler, J. F., Dürrwald, R., … Kuhn, J. H. (2019). Taxonomy of the order Mononegavirales: update 2019. *Archives of virology*, *164*(7), 1967–1980. https://doi.org/10.1007/s00705-019-04247-4

Anand, S. K., & Tikoo, S. K. (2013). Viruses as modulators of mitochondrial functions. *Advances in virology*, *2013*, 738794. https://doi.org/10.1155/2013/738794

Andrade-Navarro, M. A., Sanchez-Pulido, L., & McBride, H. M. (2009). Mitochondrial vesicles: an ancient process providing new links to peroxisomes. *Current opinion in cell biology*, *21*(4), 560–567. https://doi.org/10.1016/j.ceb.2009.04.005

Annesley, S. J., & Fisher, P. R. (2019). Mitochondria in Health and Disease. *Cells*, *8*(7), 680. https://doi.org/10.3390/cells8070680

Aubourg, P. & Wanders, R. (2013). Peroxisomal disorders. *Handbook of Clinical Neurology*, 113, 1593-1609. https://doi.org/10.1016/B978-0-444-59565-2.00028-9

Baillie, J., Sahlender, D. A., & Sinclair, J. H. (2003). Human cytomegalovirus infection inhibits tumor necrosis factor alpha (TNF-alpha) signaling by targeting the 55-kilodalton TNF-alpha receptor. *Journal of virology*, *77*(12), 7007–7016. https://doi.org/10.1128/jvi.77.12.7007-7016.2003

Bajramovic, J. J., Münter, S., Syan, S., Nehrbass, U., Brahic, M., & Gonzalez-Dunia, D. (2003). Borna disease virus glycoprotein is required for viral dissemination in neurons. *Journal of virology*, *77*(22), 12222–12231. https://doi.org/10.1128/jvi.77.22.12222-12231.2003

References

Baumgart, E., Vanhorebeek, I., Grabenbauer, M., Borgers, M., Declercq, P. E., Fahimi, H. D., & Baes, M. (2001). Mitochondrial alterations caused by defective peroxisomal biogenesis in a mouse model for Zellweger syndrome (PEX5 knockout mouse). *The American journal of pathology*, *159*(4), 1477–1494. https://doi.org/10.1016/S0002-9440(10)62534-5

Beattie, M. S., Ferguson, A. R., & Bresnahan, J. C. (2010). AMPA-receptor trafficking and injury-induced cell death. *The European journal of neuroscience*, *32*(2), 290–297. https://doi.org/10.1111/j.1460-9568.2010.07343.x

Beier, K., Völkl, A., & Fahimi, H. D. (1992). Suppression of peroxisomal lipid beta-oxidation enzymes of TNF-alpha. *FEBS letters*, *310*(3), 273–276. https://doi.org/10.1016/0014-5793(92)81347-o

Beier, K., Völkl, A., & Fahimi, H. D. (1997). TNF-alpha downregulates the peroxisome proliferator activated receptor-alpha and the mRNAs encoding peroxisomal proteins in rat liver. *FEBS letters*, *412*(2), 385–387. https://doi.org/10.1016/s0014-5793(97)00805-3

Berger, J., Dorninger, F., Forss-Petter, S., & Kunze, M. (2016). Peroxisomes in brain development and function. *Biochimica et biophysica acta*, *1863*(5), 934–955. https://doi.org/10.1016/j.bbamcr.2015.12.005

Bienert, G. P., & Chaumont, F. (2014). Aquaporin-facilitated transmembrane diffusion of hydrogen peroxide. *Biochimica et biophysica acta*, *1840*(5), 1596–1604. https://doi.org/10.1016/j.bbagen.2013.09.017

Bouchez, C., & Devin, A. (2019). Mitochondrial Biogenesis and Mitochondrial Reactive Oxygen Species (ROS): A Complex Relationship Regulated by the cAMP/PKA Signaling Pathway. *Cells*, *8*(4), 287. https://doi.org/10.3390/cells8040287

Bourg, M., Herzog, S., Encarnação, J. A., Nobach, D., Lange-Herbst, H., Eickmann, M., & Herden, C. (2013). Bicolored white-toothed shrews as reservoir for borna disease virus, Bavaria, Germany. *Emerging infectious diseases*, *19*(12), 2064–2066. https://doi.org/10.3201/eid1912.131076

Boveris, A., Oshino, N., & Chance, B. (1972). The cellular production of hydrogen peroxide. *The Biochemical journal*, *128*(3), 617–630. https://doi.org/10.1042/bj1280617

Bowie, A. G., & Unterholzner, L. (2008). Viral evasion and subversion of pattern-recognition receptor signalling. *Nature reviews. Immunology*, *8*(12), 911–922. https://doi.org/10.1038/nri2436

References

Brachthäuser, L., Eisel, U. L., & Herden, C. (2013). Borna disease virus infection of TNF-transgenic neurons: in vitro model for dysregulation of the anticonvulsive dynorphin system. Clin Neuropathol, 32, 417-418.

Braverman, N. E., & Moser, A. B. (2012). Functions of plasmalogen lipids in health and disease. *Biochimica et biophysica acta*, *1822*(9), 1442–1452. https://doi.org/10.1016/j.bbadis.2012.05.008

Brown, A. D., Fogarty, M. J., Mantilla, C. B., & Sieck, G. C. (2019). The Effect of TNF-α on Mitochondrial Morphology in Model (NSC-34) Motor Neurons. Experimental Biology 2019 Meeting Abstracts, 542.17-542.17.

Bruce-Keller, A. J., Geddes, J. W., Knapp, P. E., McFall, R. W., Keller, J. N., Holtsberg, F. W., Parthasarathy, S., Steiner, S. M., & Mattson, M. P. (1999). Anti-death properties of TNF against metabolic poisoning: mitochondrial stabilization by MnSOD. *Journal of neuroimmunology*, *93*(1-2), 53–71. https://doi.org/10.1016/s0165-5728(98)00190-8

Burtscher, J., Cappellano, G., Omori, A., Koshiba, T., & Millet, G. P. (2020). Mitochondria: In the Cross Fire of SARS-CoV-2 and Immunity. *iScience*, *23*(10), 101631. https://doi.org/10.1016/j.isci.2020.101631

Cabal-Hierro, L., & Lazo, P. S. (2012). Signal transduction by tumor necrosis factor receptors. *Cellular signalling*, *24*(6), 1297–1305. https://doi.org/10.1016/j.cellsig.2012.02.006

Carbone, K. M., Rubin, S. A., Sierra-Honigmann, A. M., & Lederman, H. M. (1993). Characterization of a glial cell line persistently infected with borna disease virus (BDV): influence of neurotrophic factors on BDV protein and RNA expression. *Journal of virology*, *67*(3), 1453–1460. https://doi.org/10.1128/JVI.67.3.1453-1460.1993

Cassereau, J., Chevrollier, A., Bonneau, D., Verny, C., Procaccio, V., Reynier, P., & Ferré, M. (2011). A locus-specific database for mutations in GDAP1 allows analysis of genotype-phenotype correlations in Charcot-Marie-Tooth diseases type 4A and 2K. *Orphanet journal of rare diseases*, *6*, 87. https://doi.org/10.1186/1750-1172-6-87

Castanier, C., Garcin, D., Vazquez, A., & Arnoult, D. (2010). Mitochondrial dynamics regulate the RIG-I-like receptor antiviral pathway. *EMBO reports*, *11*(2), 133–138. https://doi.org/10.1038/embor.2009.258

Cawthorn, W. P., & Sethi, J. K. (2008). TNF-alpha and adipocyte biology. *FEBS letters*, *582*(1), 117–131. https://doi.org/10.1016/j.febslet.2007.11.051

References

Chao, Y. H., Robak, L. A., Xia, F., Koenig, M. K., Adesina, A., Bacino, C. A., Scaglia, F., Bellen, H. J., & Wangler, M. F. (2016). Missense variants in the middle domain of DNM1L in cases of infantile encephalopathy alter peroxisomes and mitochondria when assayed in Drosophila. *Human molecular genetics*, *25*(9), 1846–1856. https://doi.org/10.1093/hmg/ddw059

Chathuranga, K., Weerawardhana, A., Dodantenna, N., & Lee, J. S. (2021). Regulation of antiviral innate immune signaling and viral evasion following viral genome sensing. *Experimental & molecular medicine*, *53*(11), 1647–1668. https://doi.org/10.1038/s12276-021-00691-y

Christofides, A., Konstantinidou, E., Jani, C., & Boussiotis, V. A. (2021). The role of peroxisome proliferator-activated receptors (PPAR) in immune responses. *Metabolism: clinical and experimental*, *114*, 154338. https://doi.org/10.1016/j.metabol.2020.154338

Cipolla, C. M., & Lodhi, I. J. (2017). Peroxisomal Dysfunction in Age-Related Diseases. *Trends in endocrinology and metabolism: TEM*, *28*(4), 297–308. https://doi.org/10.1016/j.tem.2016.12.003

Cook, K. C., Moreno, J. A., Jean Beltran, P. M., & Cristea, I. M. (2019). Peroxisome Plasticity at the Virus-Host Interface. *Trends in microbiology*, *27*(11), 906–914. https://doi.org/10.1016/j.tim.2019.06.006

Cook, W. S., Yeldandi, A. V., Rao, M. S., Hashimoto, T., & Reddy, J. K. (2000). Less extrahepatic induction of fatty acid beta-oxidation enzymes by PPAR alpha. *Biochemical and biophysical research communications*, *278*(1), 250–257. https://doi.org/10.1006/bbrc.2000.3739

Corona, J. C., de Souza, S. C., & Duchen, M. R. (2014). PPARγ activation rescues mitochondrial function from inhibition of complex I and loss of PINK1. *Experimental neurology*, *253*, 16–27. https://doi.org/10.1016/j.expneurol.2013.12.012

Coyaud, E., Ranadheera, C., Cheng, D., Gonçalves, J., Dyakov, B. J. A., Laurent, E. M. N., St-Germain, J., Pelletier, L., Gingras, A. C., Brumell, J. H., Kim, P. K., Safronetz, D., & Raught, B. (2018). Global Interactomics Uncovers Extensive Organellar Targeting by Zika Virus. *Molecular & cellular proteomics: MCP*, *17*(11), 2242–2255. https://doi.org/10.1074/mcp.TIR118.000800

References

Davizon-Castillo, P., McMahon, B., Aguila, S., Bark, D., Ashworth, K., Allawzi, A., Campbell, R. A., Montenont, E., Nemkov, T., D'Alessandro, A., Clendenen, N., Shih, L., Sanders, N. A., Higa, K., Cox, A., Padilla-Romo, Z., Hernandez, G., Wartchow, E., Trahan, G. D., Nozik-Grayck, E., … Di Paola, J. (2019). TNF-α-driven inflammation and mitochondrial dysfunction define the platelet hyperreactivity of aging. *Blood*, *134*(9), 727–740. https://doi.org/10.1182/blood.2019000200

Delmotte, P., Marin Mathieu, N., & Sieck, G. C. (2021). TNFα induces mitochondrial fragmentation and biogenesis in human airway smooth muscle. *American journal of physiology. Lung cellular and molecular physiology*, *320*(1), L137–L151. https://doi.org/10.1152/ajplung.00305.2020

Del Río L. A. (2011). Peroxisomes as a cellular source of reactive nitrogen species signal molecules. *Archives of biochemistry and biophysics*, *506*(1), 1–11. https://doi.org/10.1016/j.abb.2010.10.022

Diebold, L., & Chandel, N. S. (2016). Mitochondrial ROS regulation of proliferating cells. *Free radical biology & medicine*, *100*, 86–93. https://doi.org/10.1016/j.freeradbiomed.2016.04.198

Dixit, E., Boulant, S., Zhang, Y., Lee, A. S., Odendall, C., Shum, B., Hacohen, N., Chen, Z. J., Whelan, S. P., Fransen, M., Nibert, M. L., Superti-Furga, G., & Kagan, J. C. (2010). Peroxisomes are signaling platforms for antiviral innate immunity. *Cell*, *141*(4), 668–681. https://doi.org/10.1016/j.cell.2010.04.018

Dong, Y., Dekens, D. W., De Deyn, P. P, Naudé, P. J. W., & Eisel, U. L. M. (2015). Targeting of tumor necrosis factor alpha receptors as a therapeutic strategy for neurode-generative disorders. *Antibodies.* 4:369–408. doi:10.3390/antib4040369

Dürrwald, R., Kolodziejek, J., Weissenböck, H., & Nowotny, N. (2014). The bicolored white-toothed shrew Crocidura leucodon (HERMANN 1780) is an indigenous host of mammalian Borna disease virus. *PloS one*, *9*(4), e93659. https://doi.org/10.1371/journal.pone.0093659

Elesela, S., & Lukacs, N. W. (2021). Role of Mitochondria in Viral Infections. *Life (Basel, Switzerland)*, *11*(3), 232. https://doi.org/10.3390/life11030232

Everett, H., Barry, M., Sun, X., Lee, S. F., Frantz, C., Berthiaume, L. G., McFadden, G., & Bleackley, R. C. (2002). The myxoma poxvirus protein, M11L, prevents apoptosis by direct interaction with the mitochondrial permeability transition pore. *The Journal of experimental medicine*, *196*(9), 1127–1139. https://doi.org/10.1084/jem.20011247

References

Ferré, C. A., Davezac, N., Thouard, A., Peyrin, J. M., Belenguer, P., Miquel, M. C., Gonzalez-Dunia, D., & Szelechowski, M. (2016). Manipulation of the N-terminal sequence of the Borna disease virus X protein improves its mitochondrial targeting and neuroprotective potential. *FASEB journal: official publication of the Federation of American Societies for Experimental Biology*, *30*(4), 1523–1533. https://doi.org/10.1096/fj.15-279620

Ferreira, A. R., Marques, M., & Ribeiro, D. (2019). Peroxisomes and Innate Immunity: Antiviral Response and Beyond. *International journal of molecular sciences*, *20*(15), 3795. https://doi.org/10.3390/ijms20153795

Figiel I. (2008). Pro-inflammatory cytokine TNF-alpha as a neuroprotective agent in the brain. *Acta neurobiologiae experimentalis*, *68*(4), 526–534.

Fontaine, V., Mohand-Said, S., Hanoteau, N., Fuchs, C., Pfizenmaier, K., & Eisel, U. (2002). Neurodegenerative and neuroprotective effects of tumor Necrosis factor (TNF) in retinal ischemia: opposite roles of TNF receptor 1 and TNF receptor 2. *The Journal of neuroscience: the official journal of the Society for Neuroscience*, *22*(7), RC216. https://doi.org/10.1523/JNEUROSCI.22-07-j0001.2002

Fourcade, S., Ferrer, I., & Pujol, A. (2015). Oxidative stress, mitochondrial and proteostasis malfunction in adrenoleukodystrophy: A paradigm for axonal degeneration. *Free radical biology & medicine*, *88*(Pt A), 18–29. https://doi.org/10.1016/j.freeradbiomed.2015.05.041

Frankola, K. A., Greig, N. H., Luo, W., & Tweedie, D. (2011). Targeting TNF-α to elucidate and ameliorate neuroinflammation in neurodegenerative diseases. *CNS & neurological disorders drug targets*, *10*(3), 391–403. https://doi.org/10.2174/187152711794653751

Fransen, M., Lismont, C., & Walton, P. (2017). The Peroxisome-Mitochondria Connection: How and Why?. *International journal of molecular sciences*, *18*(6), 1126. https://doi.org/10.3390/ijms18061126

Fransen, M., Nordgren, M., Wang, B., & Apanasets, O. (2012). Role of peroxisomes in ROS/RNS-metabolism: implications for human disease. *Biochimica et biophysica acta*, *1822*(9), 1363–1373. https://doi.org/10.1016/j.bbadis.2011.12.001

Fujita, M., Ouchi, H., Ikegame, S., Harada, E., Matsumoto, T., Uchino, J., Nakanishi, Y., & Watanabe, K. (2016). Critical role of tumor necrosis factor receptor 1 in the pathogenesis of pulmonary emphysema in mice. *International journal of chronic obstructive pulmonary disease*, *11*, 1705–1712. https://doi.org/10.2147/COPD.S108919

References

Gandre-Babbe, S., & van der Bliek, A. M. (2008). The novel tail-anchored membrane protein Mff controls mitochondrial and peroxisomal fission in mammalian cells. *Molecular biology of the cell*, *19*(6), 2402–2412. https://doi.org/10.1091/mbc.e07-12-1287

Gogolla, N., Galimberti, I., DePaola, V., & Caroni, P. (2006). Preparation of organotypic hippocampal slice cultures for long-term live imaging. *Nature protocols*, *1*(3), 1165–1171. https://doi.org/10.1038/nprot.2006.168

Gottlieb, R. A., & Stotland, A. (2015). MitoTimer: a novel protein for monitoring mitochondrial turnover in the heart. *Journal of molecular medicine (Berlin, Germany)*, *93*(3), 271–278. https://doi.org/10.1007/s00109-014-1230-6

Gough, P., & Myles, I. A. (2020). Tumor Necrosis Factor Receptors: Pleiotropic Signaling Complexes and Their Differential Effects. *Frontiers in immunology*, *11*, 585880. https://doi.org/10.3389/fimmu.2020.585880

Grant, P., Ahlemeyer, B., Karnati, S., Berg, T., Stelzig, I., Nenicu, A., Kuchelmeister, K., Crane, D. I., & Baumgart-Vogt, E. (2013). The biogenesis protein PEX14 is an optimal marker for the identification and localization of peroxisomes in different cell types, tissues, and species in morphological studies. *Histochemistry and cell biology*, *140*(4), 423–442. https://doi.org/10.1007/s00418-013-1133-6

Hallensleben, W., Schwemmle, M., Hausmann, J., Stitz, L., Volk, B., Pagenstecher, A., & Staeheli, P. (1998). Borna disease virus-induced neurological disorder in mice: infection of neonates results in immunopathology. *Journal of virology*, *72*(5), 4379–4386. https://doi.org/10.1128/JVI.72.5.4379-4386.1998

Hennessy, C., & McKernan, D. P. (2021). Anti-Viral Pattern Recognition Receptors as Therapeutic Targets. *Cells*, *10*(9), 2258. https://doi.org/10.3390/cells10092258

Herden, C., Briese, T., Lipkin, W. I., & Richt, J. A. (2013). Bornaviridae. In D. M. Knipe & P. M. Howley (Eds.), Fields Virology (6th ed., pp. 1124–1150). Lippincott Williams & Wilkins.

Hilbe, M., Herrsche, R., Kolodziejek, J., Nowotny, N., Zlinszky, K., & Ehrensperger, F. (2006). Shrews as reservoir hosts of borna disease virus. *Emerging infectious diseases*, *12*(4), 675–677. https://doi.org/10.3201/eid1204.051418

Hirz, M. (2017).Pathogeneses of epileptiform convulsions in TNF-transgenic mice after Borna disease virus infection: role of astroglia. Institute for Veterinary Pathology, Justus-Liebig University, Gießen. *PhD Thesis*.

References

Hofer, M., Hausmann, J., Staeheli, P., & Pagenstecher, A. (2004). Cerebral expression of interleukin-12 induces neurological disease via differential pathways and recruits antigen-specific T cells in virus-infected mice. *The American journal of pathology*, *165*(3), 949–958. https://doi.org/10.1016/S0002-9440(10)63356-1

Hoffmann, B., Tappe, D., Höper, D., Herden, C., Boldt, A., Mawrin, C., Niederstraßer, O., Müller, T., Jenckel, M., van der Grinten, E., Lutter, C., Abendroth, B., Teifke, J. P., Cadar, D., Schmidt-Chanasit, J., Ulrich, R. G., & Beer, M. (2015). A Variegated Squirrel Bornavirus Associated with Fatal Human Encephalitis. *The New England journal of medicine*, *373*(2), 154–162. https://doi.org/10.1056/NEJMoa1415627

Hoivik, D. J., Qualls, C. W., Jr, Mirabile, R. C., Cariello, N. F., Kimbrough, C. L., Colton, H. M., Anderson, S. P., Santostefano, M. J., Morgan, R. J., Dahl, R. R., Brown, A. R., Zhao, Z., Mudd, P. N., Jr, Oliver, W. B., Jr, Brown, H. R., & Miller, R. T. (2004). Fibrates induce hepatic peroxisome and mitochondrial proliferation without overt evidence of cellular proliferation and oxidative stress in cynomolgus monkeys. *Carcinogenesis*, *25*(9), 1757–1769. https://doi.org/10.1093/carcin/bgh182

Honda, T., & Tomonaga, K. (2013). Nucleocytoplasmic shuttling of viral proteins in borna disease virus infection. *Viruses*, *5*(8), 1978–1990. https://doi.org/10.3390/v5081978

Horner, S. M., Liu, H. M., Park, H. S., Briley, J., & Gale, M., Jr (2011). Mitochondrial-associated endoplasmic reticulum membranes (MAM) form innate immune synapses and are targeted by hepatitis C virus. *Proceedings of the National Academy of Sciences of the United States of America*, *108*(35), 14590–14595. https://doi.org/10.1073/pnas.1110133108

Hossain, M. G., Akter, S., Ohsaki, E., & Ueda, K. (2020). Impact of the Interaction of Hepatitis B Virus with Mitochondria and Associated Proteins. *Viruses*, *12*(2), 175. https://doi.org/10.3390/v12020175

Huber, N., Guimaraes, S., Schrader, M., Suter, U., & Niemann, A. (2013). Charcot-Marie-Tooth disease-associated mutants of GDAP1 dissociate its roles in peroxisomal and mitochondrial fission. *EMBO reports*, *14*(6), 545–552. https://doi.org/10.1038/embor.2013.56

Huybrechts, S. J., Van Veldhoven, P. P., Brees, C., Mannaerts, G. P., Los, G. V., & Fransen, M. (2009). Peroxisome dynamics in cultured mammalian cells. *Traffic (Copenhagen, Denmark)*, *10*(11), 1722–1733. https://doi.org/10.1111/j.1600-0854.2009.00970.x

References

Hwang, I., Lee, J., Huh, J. Y., Park, J., Lee, H. B., Ho, Y. S., & Ha, H. (2012). Catalase deficiency accelerates diabetic renal injury through peroxisomal dysfunction. *Diabetes*, *61*(3), 728–738. https://doi.org/10.2337/db11-0584

Hyder, F., Rothman, D. L., & Bennett, M. R. (2013). Cortical energy demands of signaling and nonsignaling components in brain are conserved across mammalian species and activity levels. *Proceedings of the National Academy of Sciences of the United States of America*, *110*(9), 3549–3554. https://doi.org/10.1073/pnas.1214912110

Islinger, M., Voelkl, A., Fahimi, H. D., & Schrader, M. (2018). The peroxisome: an update on mysteries 2.0. *Histochemistry and cell biology*, *150*(5), 443–471. https://doi.org/10.1007/s00418-018-1722-5

Ivashchenko, O., Van Veldhoven, P. P., Brees, C., Ho, Y. S., Terlecky, S. R., & Fransen, M. (2011). Intraperoxisomal redox balance in mammalian cells: oxidative stress and interorganellar cross-talk. *Molecular biology of the cell*, *22*(9), 1440–1451. https://doi.org/10.1091/mbc.E10-11-0919

Javed, F., & Manzoor, S. (2018). HCV non-structural NS4A protein of genotype 3a induces mitochondria mediated death by activating Bax and the caspase cascade. *Microbial pathogenesis*, *124*, 346–355. https://doi.org/10.1016/j.micpath.2018.08.065

Jean Beltran, P. M., Cook, K. C., Hashimoto, Y., Galitzine, C., Murray, L. A., Vitek, O., & Cristea, I. M. (2018). Infection-Induced Peroxisome Biogenesis Is a Metabolic Strategy for Herpesvirus Replication. *Cell host & microbe*, *24*(4), 526–541.e7. https://doi.org/10.1016/j.chom.2018.09.002

Kagan J. C. (2012). Signaling organelles of the innate immune system. *Cell*, *151*(6), 1168–1178. https://doi.org/10.1016/j.cell.2012.11.011

Kalinina, E. V., Chernov, N. N., & Saprin, A. N. (2008). Involvement of thio-, peroxi-, and glutaredoxins in cellular redox-dependent processes. *Biochemistry. Biokhimiia*, *73*(13), 1493–1510. https://doi.org/10.1134/s0006297908130099

Kastl, L., Sauer, S. W., Ruppert, T., Beissbarth, T., Becker, M. S., Süss, D., Krammer, P. H., & Gülow, K. (2014). TNF-α mediates mitochondrial uncoupling and enhances ROS-dependent cell migration via NF-κB activation in liver cells. *FEBS letters*, *588*(1), 175–183. https://doi.org/10.1016/j.febslet.2013.11.033

References

Kausar, S., Wang, F., & Cui, H. (2018). The Role of Mitochondria in Reactive Oxygen Species Generation and Its Implications for Neurodegenerative Diseases. *Cells*, *7*(12), 274. https://doi.org/10.3390/cells7120274

Kim, E. Y., Priatel, J. J., Teh, S. J., & Teh, H. S. (2006). TNF receptor type 2 (p75) functions as a costimulator for antigen-driven T cell responses in vivo. *Journal of immunology (Baltimore, Md.: 1950)*, *176*(2), 1026–1035. https://doi.org/10.4049/jimmunol.176.2.1026

Kim, S. J., Khan, M., Quan, J., Till, A., Subramani, S., & Siddiqui, A. (2013). Hepatitis B virus disrupts mitochondrial dynamics: induces fission and mitophagy to attenuate apoptosis. *PLoS pathogens*, *9*(12), e1003722. https://doi.org/10.1371/journal.ppat.1003722

Kim, S. J., Syed, G. H., & Siddiqui, A. (2013). Hepatitis C virus induces the mitochondrial translocation of Parkin and subsequent mitophagy. *PLoS pathogens*, *9*(3), e1003285. https://doi.org/10.1371/journal.ppat.1003285

Kim, S. J., Syed, G. H., Khan, M., Chiu, W. W., Sohail, M. A., Gish, R. G., & Siddiqui, A. (2014). Hepatitis C virus triggers mitochondrial fission and attenuates apoptosis to promote viral persistence. *Proceedings of the National Academy of Sciences of the United States of America*, *111*(17), 6413–6418. https://doi.org/10.1073/pnas.1321114111

Kim, Y. S., Gupta Vallur, P., Phaëton, R., Mythreye, K., & Hempel, N. (2017). Insights into the Dichotomous Regulation of SOD2 in Cancer. *Antioxidants (Basel, Switzerland)*, *6*(4), 86. https://doi.org/10.3390/antiox6040086

Kirkman, H. N., & Gaetani, G. F. (2007). Mammalian catalase: a venerable enzyme with new mysteries. *Trends in biochemical sciences*, *32*(1), 44–50. https://doi.org/10.1016/j.tibs.2006.11.003

Knoblach, B., Ishida, R., Hobman, T. C., & Rachubinski, R. A. (2021). Peroxisomes exhibit compromised structure and matrix protein content in SARS-CoV-2-infected cells. *Molecular biology of the cell*, *32*(14), 1273–1282. https://doi.org/10.1091/mbc.E21-02-0074

Koch, A., Yoon, Y., Bonekamp, N. A., McNiven, M. A., & Schrader, M. (2005). A role for Fis1 in both mitochondrial and peroxisomal fission in mammalian cells. *Molecular biology of the cell*, *16*(11), 5077–5086. https://doi.org/10.1091/mbc.e05-02-0159

Koch, J., Feichtinger, R. G., Freisinger, P., Pies, M., Schrödl, F., Iuso, A., Sperl, W., Mayr, J. A., Prokisch, H., & Haack, T. B. (2016). Disturbed mitochondrial and peroxisomal dynamics

due to loss of MFF causes Leigh-like encephalopathy, optic atrophy and peripheral neuropathy. *Journal of medical genetics*, *53*(4), 270–278. https://doi.org/10.1136/jmedgenet-2015-103500

Koepke, J. I., Nakrieko, K. A., Wood, C. S., Boucher, K. K., Terlecky, L. J., Walton, P. A., & Terlecky, S. R. (2007). Restoration of peroxisomal catalase import in a model of human cellular aging. *Traffic (Copenhagen, Denmark)*, *8*(11), 1590–1600. https://doi.org/10.1111/j.1600-0854.2007.00633.x

Koepke, J. I., Wood, C. S., Terlecky, L. J., Walton, P. A., & Terlecky, S. R. (2008). Progeric effects of catalase inactivation in human cells. *Toxicology and applied pharmacology*, *232*(1), 99–108. https://doi.org/10.1016/j.taap.2008.06.004

Koniaris, L. G., Wand, G., & Wright, T. M. (2001). TNF mediates a murine model of Addison's crisis. *Shock (Augusta, Ga.)*, *15*(1), 29–34. https://doi.org/10.1097/00024382-200115010-00005

Korn, K., Coras, R., Bobinger, T., Herzog, S. M., Lücking, H., Stöhr, R., Huttner, H. B., Hartmann, A., & Ensser, A. (2018). Fatal Encephalitis Associated with Borna Disease Virus 1. *The New England journal of medicine*, *379*(14), 1375–1377. https://doi.org/10.1056/NEJMc1800724

Koshiba, T., Yasukawa, K., Yanagi, Y., & Kawabata, S. (2011). Mitochondrial membrane potential is required for MAVS-mediated antiviral signaling. *Science signaling*, *4*(158), ra7. https://doi.org/10.1126/scisignal.2001147

Kramer, K., Schaudien, D., Eisel, U. L., Herzog, S., Richt, J. A., Baumgärtner, W., & Herden, C. (2012). TNF-overexpression in Borna disease virus-infected mouse brains triggers inflammatory reaction and epileptic seizures. *PloS one*, *7*(7), e41476. https://doi.org/10.1371/journal.pone.0041476

Kuhn, J. H., Dürrwald, R., Bào, Y., Briese, T., Carbone, K., Clawson, A. N., deRisi, J. L., Garten, W., Jahrling, P. B., Kolodziejek, J., Rubbenstroth, D., Schwemmle, M., Stenglein, M., Tomonaga, K., Weissenböck, H., & Nowotny, N. (2015). Taxonomic reorganization of the family Bornaviridae. *Archives of virology*, *160*(2), 621–632. https://doi.org/10.1007/s00705-014-2276-z

Kumar, H., Kawai, T., Kato, H., Sato, S., Takahashi, K., Coban, C., Yamamoto, M., Uematsu, S., Ishii, K. J., Takeuchi, O., & Akira, S. (2006). Essential role of IPS-1 in innate immune

responses against RNA viruses. *The Journal of experimental medicine*, *203*(7), 1795–1803. https://doi.org/10.1084/jem.20060792

Kupke, A., Becker, S., Wewetzer, K., Ahlemeyer, B., Eickmann, M., & Herden, C. (2019). Intranasal Borna Disease Virus (BoDV1) Infection: Insights into Initial Steps and Potential Contagiosity. International Journal of Molecular Sciences, 20(6), 1318. https://doi.org/10.3390/ijms20061318

Lauer, C., Völkl, A., Riedl, S., Fahimi, H. D., & Beier, K. (1999). Impairment of peroxisomal biogenesis in human colon carcinoma. *Carcinogenesis*, *20*(6), 985–989. https://doi.org/10.1093/carcin/20.6.985

Lazarow P. B. (2011). Viruses exploiting peroxisomes. *Current opinion in microbiology*, *14*(4), 458–469. https://doi.org/10.1016/j.mib.2011.07.009

Legakis, J. E., Koepke, J. I., Jedeszko, C., Barlaskar, F., Terlecky, L. J., Edwards, H. J., Walton, P. A., & Terlecky, S. R. (2002). Peroxisome senescence in human fibroblasts. *Molecular biology of the cell*, *13*(12), 4243–4255. https://doi.org/10.1091/mbc.e02-06-0322

Lencel, P., Delplace, S., Hardouin, P., & Magne, D. (2011). TNF-α stimulates alkaline phosphatase and mineralization through PPARγ inhibition in human osteoblasts. *Bone*, *48*(2), 242–249. https://doi.org/10.1016/j.bone.2010.09.001

Li, J. Q., Xue, H., Zhou, L., Dong, L. H., Wei, D. P., & Li, H. (2014). Mechanism of fatty acid synthase in drug tolerance related to epithelial-mesenchymal transition of breast cancer. *Asian Pacific journal of cancer prevention: APJCP*, *15*(18), 7617–7623. https://doi.org/10.7314/apjcp.2014.15.18.7617

Li, J., & Wang, W. (2021). Mechanisms and Functions of Pexophagy in Mammalian Cells. *Cells*, *10*(5), 1094. https://doi.org/10.3390/cells10051094

Li, X., & Gould, S. J. (2003). The dynamin-like GTPase DLP1 is essential for peroxisome division and is recruited to peroxisomes in part by PEX11. *The Journal of biological chemistry*, *278*(19), 17012–17020. https://doi.org/10.1074/jbc.M212031200

Liesche, F., Ruf, V., Zoubaa, S., Kaletka, G., Rosati, M., Rubbenstroth, D., Herden, C., Goehring, L., Wunderlich, S., Wachter, M. F., Rieder, G., Lichtmannegger, I., Permanetter, W., Heckmann, J. G., Angstwurm, K., Neumann, B., Märkl, B., Haschka, S., Niller, H.-H., … Schlegel, J. (2019). The neuropathology of fatal encephalomyelitis in human Borna virus

infection. Acta Neuropathologica, 138(4), 653–665. https://doi.org/10.1007/s00401-019-02047-3

Lipkin, W. I., Herden C, Richt, J. A. & Briese, T. (2023). Bornaviridae. In D. M. Knipe & P. M. Howley (Eds.), Fields Virology (7th ed., pp. 131–160). Lippincott Williams & Wilkins.

Lismont, C., Nordgren, M., Van Veldhoven, P. P., & Fransen, M. (2015). Redox interplay between mitochondria and peroxisomes. *Frontiers in cell and developmental biology*, *3*, 35. https://doi.org/10.3389/fcell.2015.00035

Litwin, J. A., Beier, K., Völkl, A., Hofmann, W. J., & Fahimi, H. D. (1999). Immunocytochemical investigation of catalase and peroxisomal lipid beta-oxidation enzymes in human hepatocellular tumors and liver cirrhosis. *Virchows Archiv : an international journal of pathology*, *435*(5), 486–495. https://doi.org/10.1007/s004280050432

Lodhi, I. J., & Semenkovich, C. F. (2014). Peroxisomes: a nexus for lipid metabolism and cellular signaling. *Cell metabolism*, *19*(3), 380–392. https://doi.org/10.1016/j.cmet.2014.01.002

López-Erauskin, J., Galino, J., Ruiz, M., Cuezva, J. M., Fabregat, I., Cacabelos, D., Boada, J., Martínez, J., Ferrer, I., Pamplona, R., Villarroya, F., Portero-Otín, M., Fourcade, S., & Pujol, A. (2013). Impaired mitochondrial oxidative phosphorylation in the peroxisomal disease X-linked adrenoleukodystrophy. *Human molecular genetics*, *22*(16), 3296–3305. https://doi.org/10.1093/hmg/ddt186

Lu, Q., Zong, W., Zhang, M., Chen, Z., & Yang, Z. (2022). The Overlooked Transformation Mechanisms of VLCFAs: Peroxisomal β-Oxidation. *Agriculture*, *12*, 947. https://doi.org/10.3390/agriculture12070947

MacLachlan, N J, & Dubovi, E. J. (2011). Fenner's Veterinary Virology (N James MacLachlan & E. J. Dubovi (eds.); Fourth). Elsevier.

Maeda, A., & Fadeel, B. (2014). Mitochondria released by cells undergoing TNF-α-induced necroptosis act as danger signals. *Cell death & disease*, *5*(7), e1312. https://doi.org/10.1038/cddis.2014.277

Makino, A., Fujino, K., Parrish, N. F., Honda, T., & Tomonaga, K. (2015). Borna disease virus possesses an NF-κB inhibitory sequence in the nucleoprotein gene. *Scientific reports*, *5*, 8696. https://doi.org/10.1038/srep08696

References

Marchetti, L., Klein, M., Schlett, K., Pfizenmaier, K., & Eisel, U. L. (2004). Tumor necrosis factor (TNF)-mediated neuroprotection against glutamate-induced excitotoxicity is enhanced by N-methyl-D-aspartate receptor activation. Essential role of a TNF receptor 2-mediated phosphatidylinositol 3-kinase-dependent NF-kappa B pathway. *The Journal of biological chemistry*, *279*(31), 32869–32881. https://doi.org/10.1074/jbc.M311766200

McCoy, M. K., & Tansey, M. G. (2008). TNF signaling inhibition in the CNS: implications for normal brain function and neurodegenerative disease. *Journal of neuroinflammation*, *5*, 45. https://doi.org/10.1186/1742-2094-5-45

Meyer, J. N., Leuthner, T. C., & Luz, A. L. (2017). Mitochondrial fusion, fission, and mitochondrial toxicity. *Toxicology*, *391*, 42–53. https://doi.org/10.1016/j.tox.2017.07.019

Meylan, E., Curran, J., Hofmann, K., Moradpour, D., Binder, M., Bartenschlager, R., & Tschopp, J. (2005). Cardif is an adaptor protein in the RIG-I antiviral pathway and is targeted by hepatitis C virus. *Nature*, *437*(7062), 1167–1172. https://doi.org/10.1038/nature04193

Morales, J. A., Herzog, S., Kompter, C., Frese, K., & Rott, R. (1988). Axonal transport of Borna disease virus along olfactory pathways in spontaneously and experimentally infected rats. *Medical microbiology and immunology*, *177*(2), 51–68. https://doi.org/10.1007/BF00189527

Muhammad, M. (2020). Tumor Necrosis Factor Alpha: A Major Cytokine of Brain Neuroinflammation. IntechOpen. doi: 10.5772/intechopen.85476

Nakai, K. & Imai, K. (2019). Prediction of Protein Localization. *Encyclopedia of Bioinformatics and Computational Biology*, 2, 53-59. https://doi.org/10.1016/B978-0-12-809633-8.20270-7

Narayan, O., Herzog, S., Frese, K., Scheefers, H., & Rott, R. (1983). Behavioral disease in rats caused by immunopathological responses to persistent borna virus in the brain. *Science (New York, N.Y.)*, *220*(4604), 1401–1403. https://doi.org/10.1126/science.6602380

Naudé, P. J., den Boer, J. A., Luiten, P. G., & Eisel, U. L. (2011). Tumor necrosis factor receptor cross-talk. *The FEBS journal*, *278*(6), 888–898. https://doi.org/10.1111/j.1742-4658.2011.08017.x

Naudé, P. J., Dobos, N., van der Meer, D., Mulder, C., Pawironadi, K. G., den Boer, J. A., van der Zee, E. A., Luiten, P. G., & Eisel, U. L. (2014). Analysis of cognition, motor performance and anxiety in young and aged tumor necrosis factor alpha receptor 1 and 2 deficient mice. *Behavioural brain research*, *258*, 43–51. https://doi.org/10.1016/j.bbr.2013.10.006

References

Neuspiel, M., Schauss, A. C., Braschi, E., Zunino, R., Rippstein, P., Rachubinski, R. A., Andrade-Navarro, M. A., & McBride, H. M. (2008). Cargo-selected transport from the mitochondria to peroxisomes is mediated by vesicular carriers. *Current biology : CB*, *18*(2), 102–108. https://doi.org/10.1016/j.cub.2007.12.038

Neznanov, N., Kondratova, A., Chumakov, K. M., Angres, B., Zhumabayeva, B., Agol, V. I., & Gudkov, A. V. (2001). Poliovirus protein 3A inhibits tumor necrosis factor (TNF)-induced apoptosis by eliminating the TNF receptor from the cell surface. *Journal of virology*, *75*(21), 10409–10420. https://doi.org/10.1128/JVI.75.21.10409-10420.2001

Niller, H. H., Angstwurm, K., Rubbenstroth, D., Schlottau, K., Ebinger, A., Giese, S., Wunderlich, S., Banas, B., Forth, L. F., Hoffmann, D., Höper, D., Schwemmle, M., Tappe, D., Schmidt-Chanasit, J., Nobach, D., Herden, C., Brochhausen, C., Velez-Char, N., Mamilos, A., … Schmidt, B. (2020). Zoonotic spillover infections with Borna disease virus 1 leading to fatal human encephalitis, 1999–2019: an epidemiological investigation. The Lancet Infectious Diseases. https://doi.org/10.1016/S1473-3099(19)30546-8

Nobach, D., Bourg, M., Herzog, S., Lange-Herbst, H., Encarnação, J. A., Eickmann, M., & Herden, C. (2015). Shedding of Infectious Borna Disease Virus-1 in Living Bicolored White-Toothed Shrews. *PloS one*, *10*(8), e0137018. https://doi.org/10.1371/journal.pone.0137018

Nobach, D., Müller, J., Tappe, D., & Herden, C. (2020). Update on immunopathology of bornavirus infections in humans and animals. *Advances in virus research*, *107*, 159–222. https://doi.org/10.1016/bs.aivir.2020.06.004

Odendall, C., & Kagan, J. C. (2017). Activation and pathogenic manipulation of the sensors of the innate immune system. *Microbes and infection*, *19*(4-5), 229–237. https://doi.org/10.1016/j.micinf.2017.01.003

Odendall, C., Dixit, E., Stavru, F., Bierne, H., Franz, K. M., Durbin, A. F., Boulant, S., Gehrke, L., Cossart, P., & Kagan, J. C. (2014). Diverse intracellular pathogens activate type III interferon expression from peroxisomes. *Nature immunology*, *15*(8), 717–726. https://doi.org/10.1038/ni.2915

Okamoto, H., Kimura, M., Watanabe, N., & Ogihara, M. (2009). Tumor necrosis factor (TNF) receptor-2-mediated DNA synthesis and proliferation in primary cultures of adult rat hepatocytes: The involvement of endogenous transforming growth factor-alpha. *European journal of pharmacology*, *604*(1-3), 12–19. https://doi.org/10.1016/j.ejphar.2008.12.004

References

Opitz-Araya, X., & Barria, A. (2011). Organotypic hippocampal slice cultures. *Journal of visualized experiments : JoVE*, (48), 2462. https://doi.org/10.3791/2462

Oyler-Yaniv, J., Oyler-Yaniv, A., Maltz, E., & Wollman, R. (2021). TNF controls a speed-accuracy tradeoff in the cell death decision to restrict viral spread. *Nature communications*, *12*(1), 2992. https://doi.org/10.1038/s41467-021-23195-9

Peeters, A., Shinde, A. B., Dirkx, R., Smet, J., De Bock, K., Espeel, M., Vanhorebeek, I., Vanlander, A., Van Coster, R., Carmeliet, P., Fransen, M., Van Veldhoven, P. P., & Baes, M. (2015). Mitochondria in peroxisome-deficient hepatocytes exhibit impaired respiration, depleted DNA, and PGC-1α independent proliferation. *Biochimica et biophysica acta*, *1853*(2), 285–298. https://doi.org/10.1016/j.bbamcr.2014.11.017

Pegoretti, V., Baron, W., Laman, J. D., & Eisel, U. L. M. (2018). Selective Modulation of TNF-TNFRs Signaling: Insights for Multiple Sclerosis Treatment. *Frontiers in immunology*, *9*, 925. https://doi.org/10.3389/fimmu.2018.00925

Petriv, O. I., & Rachubinski, R. A. (2004). Lack of peroxisomal catalase causes a progeric phenotype in Caenorhabditis elegans. *The Journal of biological chemistry*, *279*(19), 19996–20001. https://doi.org/10.1074/jbc.M400207200

Planz, O., Pleschka, S., & Wolff, T. (2009). Borna disease virus: a unique pathogen and its interaction with intracellular signalling pathways. *Cellular microbiology*, *11*(6), 872–879. https://doi.org/10.1111/j.1462-5822.2009.01310.x

Poenisch, M., Burger, N., Staeheli, P., Bauer, G., & Schneider, U. (2009). Protein X of Borna disease virus inhibits apoptosis and promotes viral persistence in the central nervous systems of newborn-infected rats. *Journal of virology*, *83*(9), 4297–4307. https://doi.org/10.1128/JVI.02321-08

Probert, L., Akassoglou, K., Kassiotis, G., Pasparakis, M., Alexopoulou, L., & Kollias, G. (1997). TNF-alpha transgenic and knockout models of CNS inflammation and degeneration. *Journal of neuroimmunology*, *72*(2), 137–141. https://doi.org/10.1016/s0165-5728(96)00184-1

Rahman, M. M., & McFadden, G. (2006). Modulation of tumor necrosis factor by microbial pathogens. *PLoS pathogens*, *2*(2), e4. https://doi.org/10.1371/journal.ppat.0020004

Rauf, A., Badoni, H., Abu-Izneid, T., Olatunde, A., Rahman, M. M., Painuli, S., Semwal, P., Wilairatana, P., & Mubarak, M. S. (2022). Neuroinflammatory Markers: Key Indicators in the

References

Pathology of Neurodegenerative Diseases. *Molecules (Basel, Switzerland)*, *27*(10), 3194. https://doi.org/10.3390/molecules27103194

Raziyeva, K., Kim, Y., Zharkinbekov, Z., Kassymbek, K., Jimi, S., & Saparov, A. (2021). Immunology of Acute and Chronic Wound Healing. *Biomolecules*, *11*(5), 700. https://doi.org/10.3390/biom11050700

Refolo, G., Vescovo, T., Piacentini, M., Fimia, G. M., & Ciccosanti, F. (2020). Mitochondrial Interactome: A Focus on Antiviral Signaling Pathways. *Frontiers in cell and developmental biology*, *8*, 8. https://doi.org/10.3389/fcell.2020.00008

Rehwinkel, J., & Gack, M. U. (2020). RIG-I-like receptors: their regulation and roles in RA sensing. *Nature reviews. Immunology*, *20*(9), 537–551. https://doi.org/10.1038/s41577-020-0288-3

Richt, J. A., Grabner, A., & Herzog, S. (2000). Borna disease in horses. *The Veterinary clinics of North America. Equine practice*, *16*(3), 579–xi. https://doi.org/10.1016/s0749-0739(17)30097-4

Richt, J. A., Pfeuffer, I., Christ, M., Frese, K., Bechter, K., & Herzog, S. (1997). Borna disease virus infection in animals and humans. *Emerging infectious diseases*, *3*(3), 343–352. https://doi.org/10.3201/eid0303.970311

Roczkowsky, A., Doan, M. A. L., Hlavay, B., Mamik, M. K., Branton, W. G., McKenzie, B. A., Saito, L. B., Schmitt, L., Eitzen, G., Di Cara, F., Wuest, M., Wuest, F., Rachubinski, R., & Power, C. (2022). Peroxisome injury in multiple sclerosis: protective effects of 4-phenylbutyrate in CNS-associated macrophages. *The Journal of neuroscience : the official journal of the Society for Neuroscience*, *42*(37), 7152–7165. Advance online publication. https://doi.org/10.1523/JNEUROSCI.0312-22.2022

Rubbenstroth, D., Briese, T., Dürrwald, R., Horie 堀江真行, M., Hyndman, T. H., Kuhn, J. H., Nowotny, N., Payne, S., Stenglein, M. D., Tomonaga 朝長啓造, K., & Ictv Report Consortium (2021). ICTV Virus Taxonomy Profile: *Bornaviridae*. *The Journal of general virology*, *102*(7), 001613. https://doi.org/10.1099/jgv.0.001613

Rubin, S. A., Waltrip, R. W., 2nd, Bautista, J. R., & Carbone, K. M. (1993). Borna disease virus in mice: host-specific differences in disease expression. *Journal of virology*, *67*(1), 548–552. https://doi.org/10.1128/JVI.67.1.548-552.1993

References

Salpietro, V., Phadke, R., Saggar, A., Hargreaves, I. P., Yates, R., Fokoloros, C., Mankad, K., Hertecant, J., Ruggieri, M., McCormick, D., & Kinali, M. (2015). Zellweger syndrome and secondary mitochondrial myopathy. *European journal of pediatrics*, *174*(4), 557–563. https://doi.org/10.1007/s00431-014-2431-2

Schlottau, K., Forth, L., Angstwurm, K., Höper, D., Zecher, D., Liesche, F., Hoffmann, B., Kegel, V., Seehofer, D., Platen, S., Salzberger, B., Liebert, U. G., Niller, H. H., Schmidt, B., Matiasek, K., Riemenschneider, M. J., Brochhausen, C., Banas, B., Renders, L., Moog, P., … Beer, M. (2018). Fatal Encephalitic Borna Disease Virus 1 in Solid-Organ Transplant Recipients. *The New England journal of medicine*, *379*(14), 1377–1379. https://doi.org/10.1056/NEJMc1803115

Schneider, U., Naegele, M., Staeheli, P., & Schwemmle, M. (2003). Active borna disease virus polymerase complex requires a distinct nucleoprotein-to-phosphoprotein ratio but no viral X protein. *Journal of virology*, *77*(21), 11781–11789. https://doi.org/10.1128/jvi.77.21.11781-11789.2003

Schrader, M., & Fahimi, H. D. (2006). Peroxisomes and oxidative stress. *Biochimica et biophysica acta*, *1763*(12), 1755–1766. https://doi.org/10.1016/j.bbamcr.2006.09.006

Schrader, M., Thiemann, M., & Fahimi, H. D. (2003). Peroxisomal motility and interaction with microtubules. *Microscopy research and technique*, *61*(2), 171–178. https://doi.org/10.1002/jemt.10326

Schriner, S. E., Linford, N. J., Martin, G. M., Treuting, P., Ogburn, C. E., Emond, M., Coskun, P. E., Ladiges, W., Wolf, N., Van Remmen, H., Wallace, D. C., & Rabinovitch, P. S. (2005). Extension of murine life span by overexpression of catalase targeted to mitochondria. *Science (New York, N.Y.)*, *308*(5730), 1909–1911. https://doi.org/10.1126/science.1106653

Schulze, V., Große, R., Fürstenau, J., Forth, L. F., Ebinger, A., Richter, M. T., Tappe, D., Mertsch, T., Klose, K., Schlottau, K., Hoffmann, B., Höper, D., Mundhenk, L., Ulrich, R. G., Beer, M., Müller, K. E., & Rubbenstroth, D. (2020). Borna disease outbreak with high mortality in an alpaca herd in a previously unreported endemic area in Germany. *Transboundary and emerging diseases*, *67*(5), 2093–2107. https://doi.org/10.1111/tbed.13556

Schwemmle, M., Salvatore, M., Shi, L., Richt, J., Lee, C. H., & Lipkin, W. I. (1998). Interactions of the borna disease virus P, N, and X proteins and their functional implications.

The Journal of biological chemistry, *273*(15), 9007–9012. https://doi.org/10.1074/jbc.273.15.9007

Seo, H., Lee, I., Chung, H. S., Bae, G. U., Chang, M., Song, E., & Kim, M. J. (2016). ATP5B regulates mitochondrial fission and fusion in mammalian cells, Animal Cells and Systems, 20:3, 157-164, DOI: 10.1080/19768354.2016.1188855

Seth, R. B., Sun, L., Ea, C. K., & Chen, Z. J. (2005). Identification and characterization of MAVS, a mitochondrial antiviral signaling protein that activates NF-kappaB and IRF 3. *Cell*, *122*(5), 669–682. https://doi.org/10.1016/j.cell.2005.08.012

Shamseldin, H. E., Alshammari, M., Al-Sheddi, T., Salih, M. A., Alkhalidi, H., Kentab, A., Repetto, G. M., Hashem, M., & Alkuraya, F. S. (2012). Genomic analysis of mitochondrial diseases in a consanguineous population reveals novel candidate disease genes. *Journal of medical genetics*, *49*(4), 234–241. https://doi.org/10.1136/jmedgenet-2012-100836

Sharma, I. & Ahmad, P. (2014). Oxidative damage to plants. *Antioxidant Networks and Signaling*, 131-148. https://doi.org/10.1016/B978-0-12-799963-0.00004-6

Singh, I., & Pujol, A. (2010). Pathomechanisms underlying X-adrenoleukodystrophy: a three-hit hypothesis. *Brain pathology (Zurich, Switzerland)*, *20*(4), 838–844. https://doi.org/10.1111/j.1750-3639.2010.00392.x

Staeheli, P., Sauder, C., Hausmann, J., Ehrensperger, F., & Schwemmle, M. (2000). Epidemiology of Borna disease virus. *The Journal of general virology*, *81*(Pt 9), 2123–2135. https://doi.org/10.1099/0022-1317-81-9-2123

Staeheli, P., Sentandreu, M., Pagenstecher, A., & Hausmann, J. (2001). Alpha/beta interferon promotes transcription and inhibits replication of borna disease virus in persistently infected cells. *Journal of virology*, *75*(17), 8216–8223. https://doi.org/10.1128/jvi.75.17.8216-8223.2001

Stitz, L., Bilzer, T., & Planz, O. (2002). The immunopathogenesis of Borna disease virus infection. *Frontiers in bioscience: a journal and virtual library*, *7*, d541–d555. https://doi.org/10.2741/A793

Sugiura, A., Mattie, S., Prudent, J., & McBride, H. M. (2017). Newly born peroxisomes are a hybrid of mitochondrial and ER-derived pre-peroxisomes. *Nature*, *542*(7640), 251–254. https://doi.org/10.1038/nature21375

Sun, Q., Sun, L., Liu, H. H., Chen, X., Seth, R. B., Forman, J., & Chen, Z. J. (2006). The specific and essential role of MAVS in antiviral innate immune responses. *Immunity*, *24*(5), 633–642. https://doi.org/10.1016/j.immuni.2006.04.004

Suvannavejh, G. C., Lee, H. O., Padilla, J., Dal Canto, M. C., Barrett, T. A., & Miller, S. D. (2000). Divergent roles for p55 and p75 tumor necrosis factor receptors in the pathogenesis of MOG(35-55)-induced experimental autoimmune encephalomyelitis. *Cellular immunology*, *205*(1), 24–33. https://doi.org/10.1006/cimm.2000.1706

Szelechowski, M., Bétourné, A., Monnet, Y., Ferré, C. A., Thouard, A., Foret, C., Peyrin, J. M., Hunot, S., & Gonzalez-Dunia, D. (2014). A viral peptide that targets mitochondria protects against neuronal degeneration in models of Parkinson's disease. *Nature communications*, *5*, 5181. https://doi.org/10.1038/ncomms6181

Tanner, L. B., Chng, C., Guan, X. L., Lei, Z., Rozen, S. G., & Wenk, M. R. (2014). Lipidomics identifies a requirement for peroxisomal function during influenza virus replication. *Journal of lipid research*, *55*(7), 1357–1365. https://doi.org/10.1194/jlr.M049148

Tappe, D., Frank, C., Offergeld, R., Wagner-Wiening, C., Stark, K., Rubbenstroth, D., Giese, S., Lattwein, E., Schwemmle, M., Beer, M., Schmidt-Chanasit, J., & Wilking, H. (2019). Low prevalence of Borna disease virus 1 (BoDV-1) IgG antibodies in humans from areas endemic for animal Borna disease of Southern Germany. *Scientific reports*, *9*(1), 20154. https://doi.org/10.1038/s41598-019-56839-4

Tappe, D., Pörtner, K., Frank, C., Wilking, H., Ebinger, A., Herden, C., Schulze, C., Muntau, B., Eggert, P., Allartz, P., Schuldt, G., Schmidt-Chanasit, J., Beer, M., & Rubbenstroth, D. (2021). Investigation of fatal human Borna disease virus 1 encephalitis outside the previously known area for human cases, Brandenburg, Germany - a case report. *BMC infectious diseases*, *21*(1), 787. https://doi.org/10.1186/s12879-021-06439-3

Terlecky, S. R., Koepke, J. I., & Walton, P. A. (2006). Peroxisomes and aging. *Biochimica et biophysica acta*, *1763*(12), 1749–1754. https://doi.org/10.1016/j.bbamcr.2006.08.017

Terlecky, S. R., Terlecky, L. J., & Giordano, C. R. (2012). Peroxisomes, oxidative stress, and inflammation. *World journal of biological chemistry*, *3*(5), 93–97. https://doi.org/10.4331/wjbc.v3.i5.93

Titorenko, V. I., & Terlecky, S. R. (2011). Peroxisome metabolism and cellular aging. *Traffic (Copenhagen, Denmark)*, *12*(3), 252–259. https://doi.org/10.1111/j.1600-0854.2010.01144.x

References

Tizard, I., Ball, J., Stoica, G., & Payne, S. (2016). The pathogenesis of bornaviral diseases in mammals. *Animal health research reviews*, *17*(2), 92–109. https://doi.org/10.1017/S1466252316000062

Trompier, D., Vejux, A., Zarrouk, A., Gondcaille, C., Geillon, F., Nury, T., Savary, S., & Lizard, G. (2014). Brain peroxisomes. *Biochimie*, *98*, 102–110. https://doi.org/10.1016/j.biochi.2013.09.009

Unterstab, G., Ludwig, S., Anton, A., Planz, O., Dauber, B., Krappmann, D., Heins, G., Ehrhardt, C., & Wolff, T. (2005). Viral targeting of the interferon-{beta}-inducing Traf family member-associated NF-{kappa}B activator (TANK)-binding kinase-1. *Proceedings of the National Academy of Sciences of the United States of America*, *102*(38), 13640–13645. https://doi.org/10.1073/pnas.0502883102

Van Herreweghe, F., Festjens, N., Declercq, W., & Vandenabeele, P. (2010). Tumor necrosis factor-mediated cell death: to break or to burst, that's the question. *Cellular and molecular life sciences : CMLS*, *67*(10), 1567–1579. https://doi.org/10.1007/s00018-010-0283-0

Vanstone, J. R., Smith, A. M., McBride, S., Naas, T., Holcik, M., Antoun, G., Harper, M. E., Michaud, J., Sell, E., Chakraborty, P., Tetreault, M., Care4Rare Consortium, Majewski, J., Baird, S., Boycott, K. M., Dyment, D. A., MacKenzie, A., & Lines, M. A. (2016). DNM1L-related mitochondrial fission defect presenting as refractory epilepsy. *European journal of human genetics : EJHG*, *24*(7), 1084–1088. https://doi.org/10.1038/ejhg.2015.243

Vijayan, V., Srinu, T., Karnati, S., Garikapati, V., Linke, M., Kamalyan, L., Mali, S. R., Sudan, K., Kollas, A., Schmid, T., Schulz, S., Spengler, B., Weichhart, T., Immenschuh, S., & Baumgart-Vogt, E. (2017). A New Immunomodulatory Role for Peroxisomes in Macrophages Activated by the TLR4 Ligand Lipopolysaccharide. *Journal of immunology (Baltimore, Md. : 1950)*, *198*(6), 2414–2425. https://doi.org/10.4049/jimmunol.1601596

Walton, P. A., & Pizzitelli, M. (2012). Effects of peroxisomal catalase inhibition on mitochondrial function. *Frontiers in physiology*, *3*, 108. https://doi.org/10.3389/fphys.2012.00108

Wanders, R. J., & Waterham, H. R. (2006). Biochemistry of mammalian peroxisomes revisited. *Annual review of biochemistry*, *75*, 295–332. https://doi.org/10.1146/annurev.biochem.74.082803.133329

References

Wanders, R. J., Waterham, H. R., & Ferdinandusse, S. (2016). Metabolic Interplay between Peroxisomes and Other Subcellular Organelles Including Mitochondria and the Endoplasmic Reticulum. *Frontiers in cell and developmental biology*, *3*, 83. https://doi.org/10.3389/fcell.2015.00083

Wang, Y. X., Lee, C. H., Tiep, S., Yu, R. T., Ham, J., Kang, H., & Evans, R. M. (2003). Peroxisome-proliferator-activated receptor delta activates fat metabolism to prevent obesity. *Cell*, *113*(2), 159–170. https://doi.org/10.1016/s0092-8674(03)00269-1

Wang, Y., Branicky, R., Noë, A., & Hekimi, S. (2018). Superoxide dismutases: Dual roles in controlling ROS damage and regulating ROS signaling. *The Journal of cell biology*, *217*(6), 1915–1928. https://doi.org/10.1083/jcb.201708007

Waterham, H. R., & Ebberink, M. S. (2012). Genetics and molecular basis of human peroxisome biogenesis disorders. *Biochimica et biophysica acta*, *1822*(9), 1430–1441. https://doi.org/10.1016/j.bbadis.2012.04.006

Waterham, H. R., Ferdinandusse, S., & Wanders, R. J. (2016). Human disorders of peroxisome metabolism and biogenesis. *Biochimica et biophysica acta*, *1863*(5), 922–933. https://doi.org/10.1016/j.bbamcr.2015.11.015

Waterham, H. R., Koster, J., van Roermund, C. W., Mooyer, P. A., Wanders, R. J., & Leonard, J. V. (2007). A lethal defect of mitochondrial and peroxisomal fission. *The New England journal of medicine*, *356*(17), 1736–1741. https://doi.org/10.1056/NEJMoa064436

Werner-Keiss, N., Garten, W., Richt, J. A., Porombka, D., Algermissen, D., Herzog, S., Baumgärtner, W., & Herden, C. (2008). Restricted expression of Borna disease virus glycoprotein in brains of experimentally infected Lewis rats. *Neuropathology and applied neurobiology*, *34*(6), 590–602. https://doi.org/10.1111/j.1365-2990.2008.00940.x

Wiese, S., Gronemeyer, T., Ofman, R., Kunze, M., Grou, C. P., Almeida, J. A., Eisenacher, M., Stephan, C., Hayen, H., Schollenberger, L., Korosec, T., Waterham, H. R., Schliebs, W., Erdmann, R., Berger, J., Meyer, H. E., Just, W., Azevedo, J. E., Wanders, R. J., & Warscheid, B. (2007). Proteomics characterization of mouse kidney peroxisomes by tandem mass spectrometry and protein correlation profiling. *Molecular & cellular proteomics : MCP*, *6*(12), 2045–2057. https://doi.org/10.1074/mcp.M700169-MCP200

Xu, Z., Asahchop, E. L., Branton, W. G., Gelman, B. B., Power, C., & Hobman, T. C. (2017). MicroRNAs upregulated during HIV infection target peroxisome biogenesis factors:

References

Implications for virus biology, disease mechanisms and neuropathology. *PLoS pathogens*, *13*(6), e1006360. https://doi.org/10.1371/journal.ppat.1006360

Yang, S., Wang, J., Brand, D. D., & Zheng, S. G. (2018). Role of TNF-TNF Receptor 2 Signal in Regulatory T Cells and Its Therapeutic Implications. *Frontiers in immunology*, *9*, 784. https://doi.org/10.3389/fimmu.2018.00784

Yang, Y., Liu, Y., Zhu, J., Song, S., Huang, Y., Zhang, W., Sun, Y., Hao, J., Yang, X., Gao, Q., Ma, Z., Zhang, J., & Gu, X. (2022). Neuroinflammation-mediated mitochondrial dysregulation involved in postoperative cognitive dysfunction. *Free radical biology & medicine*, *178*, 134–146. https://doi.org/10.1016/j.freeradbiomed.2021.12.004

Yoo, S. M., & Jung, Y. K. (2018). A Molecular Approach to Mitophagy and Mitochondrial Dynamics. *Molecules and cells*, *41*(1), 18–26. https://doi.org/10.14348/molcells.2018.2277

You, J., Hou, S., Malik-Soni, N., Xu, Z., Kumar, A., Rachubinski, R. A., Frappier, L., & Hobman, T. C. (2015). Flavivirus Infection Impairs Peroxisome Biogenesis and Early Antiviral Signaling. *Journal of virology*, *89*(24), 12349–12361. https://doi.org/10.1128/JVI.01365-15

Young, C. N., Koepke, J. I., Terlecky, L. J., Borkin, M. S., Boyd, S. L., & Terlecky, S. R. (2008). Reactive oxygen species in tumor necrosis factor-alpha-activated primary human keratinocytes: implications for psoriasis and inflammatory skin disease. *The Journal of investigative dermatology*, *128*(11), 2606–2614. https://doi.org/10.1038/jid.2008.122

Yuan, H., Fu, F., Zhuo, J., Wang, W., Nishitani, J., An, D. S., Chen, I. S., & Liu, X. (2005). Human papillomavirus type 16 E6 and E7 oncoproteins upregulate c-IAP2 gene expression and confer resistance to apoptosis. *Oncogene*, *24*(32), 5069–5078. https://doi.org/10.1038/sj.onc.1208691

Zelová, H., & Hošek, J. (2013). TNF-α signalling and inflammation: interactions between old acquaintances. *Inflammation research: official journal of the European Histamine Research Society ... [et al.]*, *62*(7), 641–651. https://doi.org/10.1007/s00011-013-0633-0

Zhang, L., Berta, T., Xu, Z. Z., Liu, T., Park, J. Y., & Ji, R. R. (2011). TNF-α contributes to spinal cord synaptic plasticity and inflammatory pain: distinct role of TNF receptor subtypes 1 and 2. *Pain*, *152*(2), 419–427. https://doi.org/10.1016/j.pain.2010.11.014

9.0 Appendix

9.1 Results

Appendix 1: One-way ANOVA comparison of peroxisomal abundances in different brain regions of BoDV1-infected mice

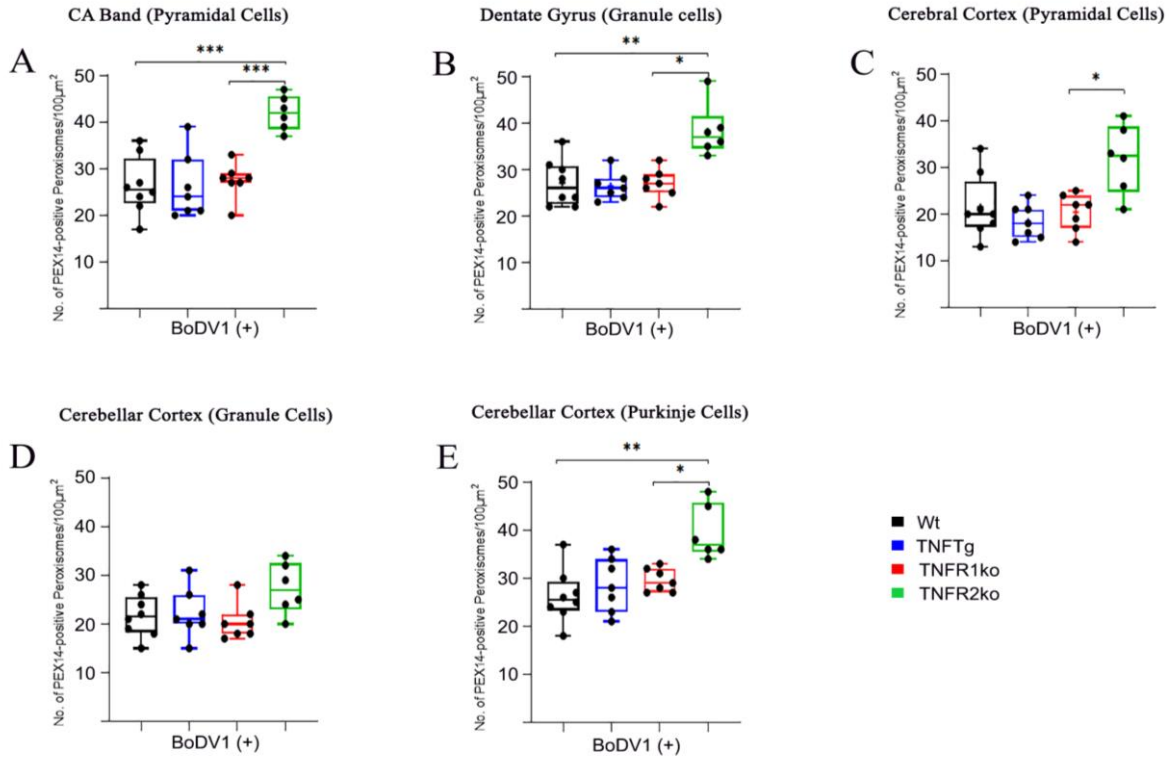

PEX14-positive peroxisomes in the hippocampus, cerebral and cerebellar cortices of each mouse line [Wt (black), TNFTg (blue), TNFR1ko (red) and TNFR2ko (green) mice] after BoDV1 infection (**A**-**E**). Peroxisomal abundance was higher in TNFR2ko mice than in Wt and TNFR1ko after BoDV1 infection. ***Wt***, wild-type; ***TNFTg***, TNF transgenic; ***TNFR1ko***, TNF receptor 1 knockout; ***TNFR2ko***, TNF receptor 2 knockout; ***BoDV1(+)***, with BoDV1 infection. P-values: 0.01–0.05 (*); 0.001–0.01 (**); 0.0001–0.001 (***).

Appendix 2: One-way ANOVA comparison of mitochondrial abundances in different brain regions of BoDV1-infected mice

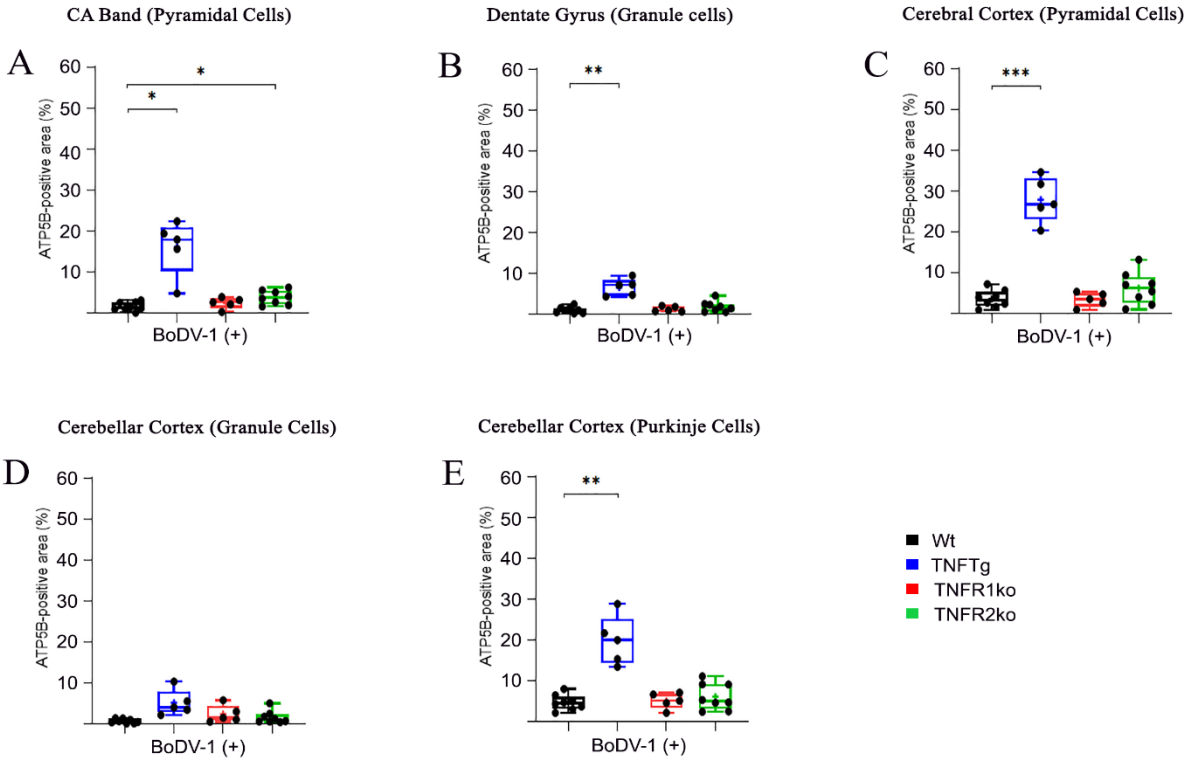

ATP5-positive mitochondria in the hippocampus, cerebral and cerebellar cortices of each mouse line [Wt (black), TNFTg (blue), TNFR1ko (red) and TNFR2ko (green) mice] after BoDV1 infection (**A**-**E**). There was an overall decrease in mitochondrial abundance in all but TNFR1ko mice. Despite this decrease, mitochondrial abundance was higher in most brain regions in TNFTg mice compared to Wt mice after BoDV1 infection. ***Wt***, wild-type; ***TNFTg***, TNF transgenic; ***TNFR1ko***, TNF receptor 1 knockout; ***TNFR2ko***, TNF receptor 2 knockout; ***BoDV1(+)***, with BoDV1 infection. P-values: 0.01–0.05 (*); 0.001–0.01 (**); 0.0001–0.001 (***).

Appendix 3: One-way ANOVA comparison of catalase abundances in different brain regions of BoDV1-infected mice

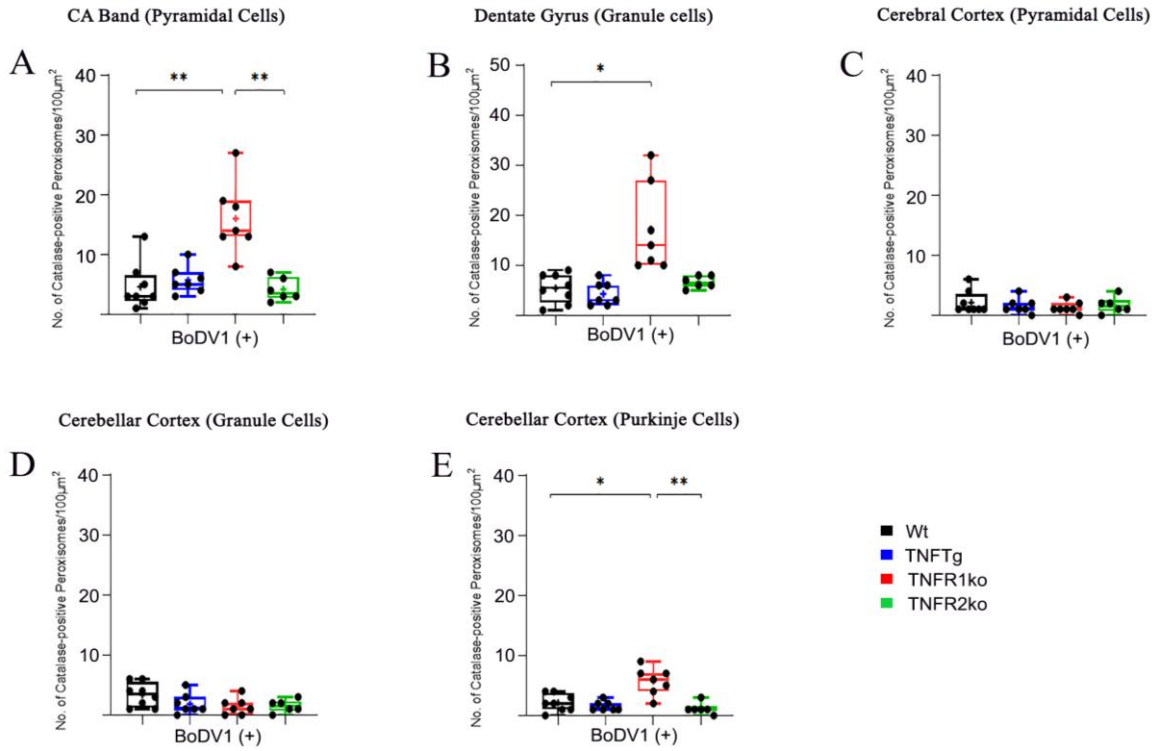

Catalase-positive peroxisomes in the hippocampus, cerebral and cerebellar cortices of each mouse line [Wt (black), TNFTg (blue), TNFR1ko (red) and TNFR2ko (green) mice] after BoDV1 infection (**A**-**E**). Regardless of the overall decrease in catalase abundances in different mouse lines, no changes were seen in most brain regions of TNFR1ko mice after BoDV1 infection. Thus, BoDV1-infected TNFR1ko mice had higher catalase abundance in most brain regions compared to BoDV1-infected Wt mice. ***Wt***, wild-type; ***TNFTg***, TNF transgenic; ***TNFR1ko***, TNF receptor 1 knockout; ***TNFR2ko***, TNF receptor 2 knockout; ***BoDV1(+)***, with BoDV1 infection. P-values: 0.01–0.05 (*); 0.001–0.01 (**).

Appendix 4: One-way ANOVA comparison of SOD2 abundances in different brain regions of BoDV1-infected mice

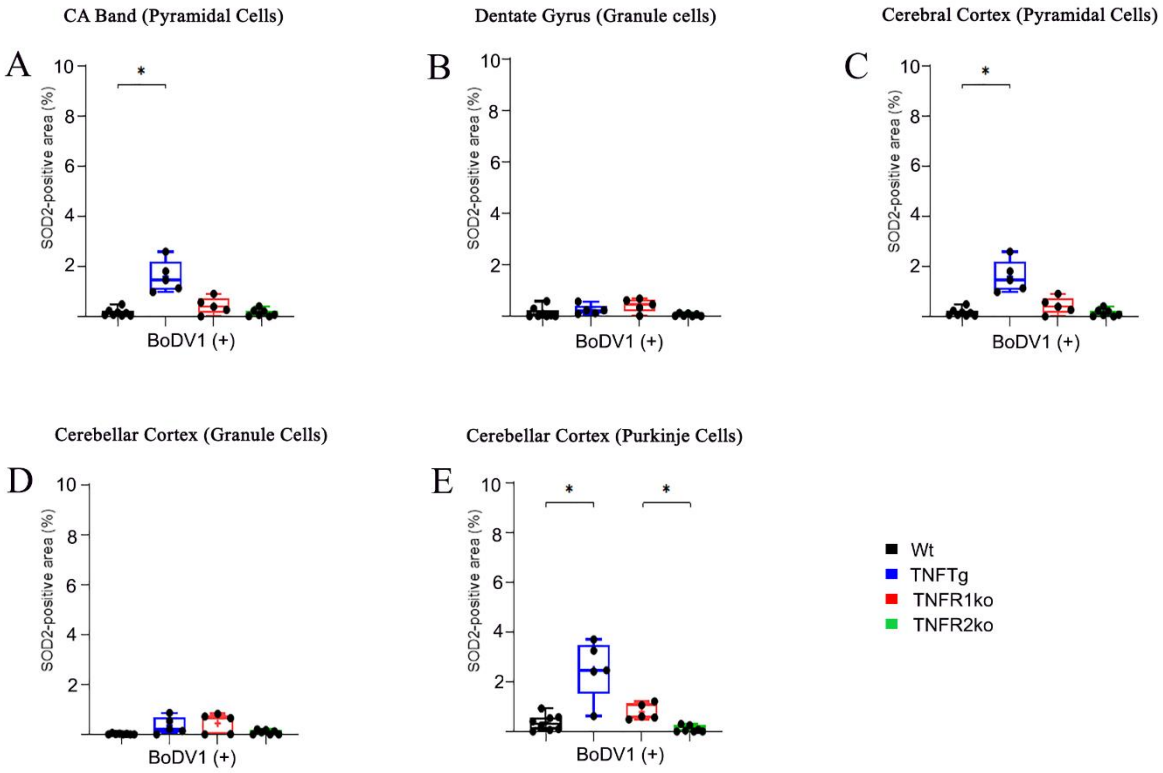

SOD2-positive mitochondria in the hippocampus, cerebral and cerebellar cortices of each mouse line [Wt (black), TNFTg (blue), TNFR1ko (red) and TNFR2ko (green) mice] after BoDV1 infection (**A-E**). No changes in SOD2 abundance in TNFR1ko mice after after BoDV1 infection. ***Wt***, wild-type; ***TNFTg***, TNF transgenic; ***TNFR1ko***, TNF receptor 1 knockout; ***TNFR2ko***, TNF receptor 2 knockout; ***BoDV1(+)***, with BoDV1 infection. P-value: 0.01–0.05 (*).

9.2 Sources of materials

Abcam, Cambridge, United Kingdom
Polyclonal rabbit anti-SOD2 antibody (ab13533)

Carl Roth Co. Ltd., Karlsruhe, Germany
Microcentrifuge
10% non-buffered formalin (P733.3)
Bovine serum albumin (BSA)
Sodium chloride (NaCl; USP, P029.3)

Department of Molecular Neurobiology, University of Groningen, the Netherlands
TNFTg mice [C57Bl/6-Tg (Grin2b-Tnf)41.3MK]
TNFR1ko mice (B6.129-Tnfrsf1a tm1Blt/J)
TNFR2ko mice (B6.129S2-Tnfrsf1btm1Mwm/J)

Engelbrecht Co. Ltd., Edermünde, Germany
Cover slips (24 x 50 mm^2)

Eppendorf, Wesseling-Berzdorf, Germany
Pipettes (10 µL, 20 µL, 100 µL, 200µL, and 1000µL)

Fluka, Buchs, Switzerland
Tween 20

Gesellschaft für Labortechnik, Burgwedel, Germany
Shaker platform (on which slides were washed in PBS)

Griffith University, Brisbane, Australia
Polyclonal rabbit anti-PEX14 antibody (gift from Denis I. Crane)
Polyclonal rabbit anti-catalase antibody (gift from Denis I. Crane)

Harlan Laboratories Co., Ltd., Indianapolis, IN, USA
Wild-type mice (C57BL/6JOlaHsd)

Heidolph Instruments, Schwabach, Germany
Magnetic Stirring Hotplate (MR 3001)

Heraeus Instruments Co. Ltd., Hanau, Germany
Centrifuge Labofuge (400R)

Invitrogen (Thermo Fisher Scientific Inc.), Dreieich, Germany
Goat anti-rabbit IgG Alexa Fluor 488 (A21206)

Leica, Berlin, Germany
Leica SM 2000R rotation microtome
Confocal laser-scanning microscope (type SPC2)

LG, Seoul, South Korea
Microwave oven (MB-392445)

Medax, Reutlinien, Germany
Thermoplate

Merck, Darmstadt, Germany
Dipotassium phosphate (K_2HPO_4)
Monopotassium phosphate (KH_2PO_4)
Sodium hydroxide (NaOH)
Citric acid ($C_6H_8O_7.H_2O$)
Sodium citrate ($C_6H_5Na_3O_7.2H_2O$)
Xylene

Mettler-Toledo, Gießen, Germany
Weighing scale

Miele, Karlsruhe, Germany
Dishwashing machine (G7883CD)

Milli Q-Millipore (Merck KGaA), Darmstadt, Germany
Biocell A10 water system

Molecular Probes (Thermo Fisher Scientific Inc.), Eugene, OR, USA
Goat anti-rabbit IgG Alexa Fluor 488

Polysciences, Hirschberg an der Bergstrasse, Germany
Mowiol (4-88)

R. Langenbrinck Co. Ltd., Emmendingen, Germany
Superfrost® plus microscope glass slides

SAV Liquid Production Co. Ltd, Flintsbach am Inn, Germany
96% Ethanol (ETO-10000-96-1)

Scotsman Ice Systems, Vernon Hills, IL, USA
Ice machine, Scotsman (AF-100)

Sigma-Aldrich, Deisenhofen, Germany
Polyclonal rabbit anti-ATP5B antibody (APA001520)
DAPI stain (4', 6-diamino-2-phenylindole)
Hydrogen chloride (HCl)
Triton X-100
N-propyl-gallate
Glycerol
Rabbit anti-ATP5B antibody (APA 001520)
Phosphate-buffered saline (1x)

Thermo Fisher Scientific Inc., Dreieich, Germany
Dulbeccos Modified Eagle Medium, low glucose, pyruvate (31885023)

Veith, Öhringen, Germany
Microtome water bath

VWR International GmbH, Darmstadt, Germany
Vortex (M10)

WTW, Weilheim, Germany
pH meter inoLab

9.3 Buffers and solutions (IF staining of FFPE brain tissue)

Phosphate-buffered saline (PBS) solution
For a 1000 ml of 10% PBS stock solution (10x):

- 43.5g sodium chloride (NaCl), 22.8g dipotassium phosphate (K_2HPO_4), and 6.8g monopotassium phosphate (KH_2PO_4) in 1000 ml distilled water
- Store solution at RT

For a 1000 ml 1% PBS solution (1x):

- 100 ml of 1% PBS stock solution and 900 ml distilled water
- Stir gently and set pH 7.4 using 0.1-1M hydrochloric acid (HCl)
- Store solution at RT

Citrate buffer

Solution A: 0.1mM citric acid (2.1g $C_6H_8O_7.H_2O$ in 100 ml distilled water)
Solution B: 0.1mM sodium citrate (14.7g $C_6H_5Na_3O_7.2H_2O$ in 500 ml distilled water)
For a 1000ml citrate buffer:

- 15 ml solution A and 85 ml solution B with 900 ml distilled water
- Set pH 6.0 using 0.1-1M sodium hydroxide (NaOH)
- Store solution at 4°C

4% PBSA/0.05% Tween 20 blocking solution
For a 1000ml 4% PBSA blocking solution;

- 40g BSA in 1000ml of 1% PBS with 500µl of 0.05% Tween 20
- Stir gently to avoid foam formation
- Store frozen

1% PBSA/0.05% Tween 20 dilution solution
For a 1000ml of dilution buffer solution:

- 10g BSA in 1000ml of 1% PBSA with 500µl of 0.05% Tween 20
- Stir gently to avoid foam formation
- Store frozen

Mowiol 4-88 solution

- 16.7 % Mowiol 4-88 (w/v) in 80 ml 1x PBS with 40 ml glycerol
- centrifuged at 15,000 rpm for 1 h
- supernatant collected and stored at -20°C

2.5% Anti-fading agent

- 2.5 g N-propyl-gallate in 50 ml PBS (1x) with 50 ml glycerol

Mounting medium

- 3 parts of Mowiol 4-88
- 1 part of anti-fading agent

DAPI (1:750 solution)

- 1 mg/ml stock solution + 750 distilled water

9.4 Mouse data sheet for the animal experiments

Appendix 5: Mouse data sheet for all 42-day-old mice of each mouse line, with or without BoDV1 infection

Mouse strain	Animal ID No.	Genetic status	Infection status
Wt	V101/11	+/+	n.i.
Wt	V102/11	+/+	n.i.
Wt	V103/11	+/+	n.i.
Wt	V104/11	+/+	n.i.
Wt	V105/11	+/+	n.i.
Wt	V106/11	+/+	n.i.
Wt	V123/11	+/+	n.i.
Wt	V5/12	+/+	n.i.
Wt	V433/12	+/+	BoDV1
Wt	V75/13	+/+	BoDV1
Wt	V77/13	+/+	BoDV1
Wt	V82/13	+/+	BoDV1

Wt	V83/13	+/+	BoDV1
Wt	V87/13	+/+	BoDV1
Wt	V95/13	+/+	BoDV1
Wt	V126/13	+/+	BoDV1
TNFTg	V120/11	tg/tg	n.i.
TNFTg	V125/11	tg/tg	n.i.
TNFTg	V126/11	tg/tg	n.i.
TNFTg	V127/11	tg/tg	n.i.
TNFTg	V6/12	tg/tg	n.i.
TNFTg	V76/13	tg/tg	BoDV1
TNFTg	V80/13	tg/tg	BoDV1
TNFTg	V84/13	tg/tg	BoDV1
TNFTg	V88/13	tg/tg	BoDV1
TNFTg	V97/13	tg/tg	BoDV1
TNFR1Ko	V259/12	d/d	n.i.
TNFR1Ko	V260/12	d/d	n.i.
TNFR1Ko	V328/14	d/d	n.i.
TNFR1Ko	V329/14	d/d	n.i.
TNFR1Ko	V330/14	d/d	n.i.
TNFR1Ko	V256/14	d/d	BoDV1
TNFR1Ko	V257/14	d/d	BoDV1
TNFR1Ko	V258/14	d/d	BoDV1
TNFR1Ko	V259/14	d/d	BoDV1
TNFR1Ko	V260/14	d/d	BoDV1
TNFR2Ko	V210/12	d/d	n.i.
TNFR2Ko	V397/12	d/d	n.i.
TNFR2Ko	V398/12	d/d	n.i.
TNFR2Ko	V399/12	d/d	n.i.
TNFR2Ko	V400/12	d/d	n.i.
TNFR2Ko	V401/12	d/d	n.i.
TNFR2Ko	V402/12	d/d	n.i.
TNFR2Ko	V403/12	d/d	n.i.
TNFR2Ko	V64/14	d/d	BoDV1
TNFR2Ko	V65/14	d/d	BoDV1
TNFR2Ko	V66/14	d/d	BoDV1
TNFR2Ko	V204/14	d/d	BoDV1
TNFR2Ko	V205/14	d/d	BoDV1
TNFR2Ko	V296/14	d/d	BoDV1
TNFR2Ko	V297/14	d/d	BoDV1

+/+ (Wt): wild-type; tg/tg: homozygote TNF transgenic; d/d: homozygous TNFR1- or TNFR2-knockout; ID no.: identification number; n.i.: non-infected; BoDV1: Borna disease virus 1-infected

Acknowledgements

I would like express my deepest gratitude to:

Prof. Dr. habil. Christiane Herden for the support, supervision, guidance, and the opportunity to work on this project.

PD Dr. Barbara Ahlemeyer for the support, supervision, guidance, and the opportunity to work on this project.

Prof. Dr. Eveline Baumgart-Vogt for the support and permission to perform all my indirect inmmunofluorescence stainings and morphometric analyses in her lab – not forgetting the warm reception into her team, and for always checking up on how this project was progressing.

Prof. Dr. Ulrich L.M. Eisel (Department of Molecular Neurobiology, University of Groningen, Netherlands) for providing the transgenic and knockout mice.

The late Dr. Helge Hudel (Dekanat of the Medicine Faculty, Justus Liebig University, Giessen) for helping with the statistical design of this study.

Administrative staff and colleagues at the Giessen Graduate Center for the Life Sciences (GGL) for the times spent together in learning, meeting new friends, and the programs offered – I really did learn a lot.

Bianca Pfeifer (Institute of Anatomy and Cell Biology) for the technical assistance and everlasting friendship.

Petra Hahn-Kohlberger (Institute of Anatomy and Cell Biology) for the technical assistance.

Silke Engel (Institute for Veterinary Pathology) for the technical assistance.

My parents [Gyasi Twum (deceased) and Doris Afram] and siblings [Nyameama (deceased), Serbeh, Serwaa and Kusi] for their support. Their prayers kept me going when things were tough, especially during the COVID19 pandemic.

Deborah (my wife) and kids (Adepa, Ohenewaa and Onyadea) for the support, love, encouragement and prayers during this entire PhD work.